CERN / LHCC 98–19
ALICE TDR 1
14 August 1998

ALICE

Technical Design Report

of the

High Momentum Particle Identification Detector

Spokesperson
J. Schukraft

HMPID Project Leader
F. Piuz

Technical Coordinator
W. Klempt

Engineering/Integration Coordinator
L. Leistam

Resources Coordinator
J. de Groot

Cover design by Fabienne Marcastel

Printed at CERN
August 1998

ISBN 92-9083-134-0

ALICE Collaboration

Alessandria, Italy, Facoltà di Scienze dell'Università:
S. Beolè, G. Dellacasa, L. Ramello, E. Scalas, M. Sitta and C. Soave.

Aligarh, India, Physics Department, Muslim University:
N. Ahmad, S. Ahmad, T. Ahmad, W. Baritak, M. Irfan and M. Zafar.

Athens, Greece, Nuclear and Particle Physics Division, University of Athens:
A. Angelis, A. Kapogiannis, G. Mavromanolakis and A.D. Panagiotou.

Attikis, Greece, Institute of Nuclear Physics, NRC Demokritos:
K. Kalfas.

Bari, Italy, Dipartimento di Fisica dell'Università and Sezione INFN:
N. Colonna, D. Cozza, D. Di Bari, D. Elia, R.A. Fini, B. Ghidini, V. Lenti, L. Liberti, R. Loconsole, V. Manzari, E. Nappi, F. Navach, F. Posa, S. Stucchi and G. Tomasicchio.

Bari, Italy, Politecnico and Sezione INFN:
F. Corsi, D. De Venuto, M. Di Ciano, G. Gramegna, A. Grimaldi, C. Marzocca and E. Monno.

Beijing, China, China Institute of Atomic Energy:
Z. Sun.

Bergen, Norway, Department of Physics, University of Bergen:
E. Andersen, K. Fanebust, H. Helstrup, A.K. Holme A. Klovning, O. Maeland, O.H. Odland and T.F. Thorsteinsen.

Bhubaneswar, India, Institute of Physics:
D.P. Mahapatra and S.C. Phatak.

Birmingham, United Kingdom, School of Physics and Space Research, University of Birmingham:
I.J. Bloodworth, D. Evans, G.T. Jones, P. Jovanović, J.B. Kinson, A. Kirk, O. Villalobos Baillie and M.F. Votruba.

Bratislava, Slovakia, Faculty of Mathematics and Physics, Comenius University:
J. Braciník, V. Černý, J. Ftáčnik, V. Hlinka, M. Ivanov, R. Janik, R. Lietava, M. Pikna, J. Pišút, N. Pišútová, B. Sitar, P. Strmeň and I. Szarka.

Budapest, Hungary, KFKI Research Institute for Particle and Nuclear Physics, Academy of Science:
E. Denes, B. Eged, Z. Fodor, G. Harangozo, T. Kiss, Z. Meggyesi, G. Palla, T. Roka, J. Sulyan, L. Szendrei, J. Sziklai, D.L. Tarjan, B.N. Vissy and J. Zimanyi.

Cagliari, Italy, Dipartimento di Fisica dell'Università and Sezione INFN:
M. Cerù, C. Cicalo, A. De Falco, A. Lai, M. Macciotta-Serpi, A. Masoni, S.A. Mauro, G. Puddu, S. Serci, E. Siddi, P. Temnikov and G. Usai.

Calcutta, India, Saha Institute of Nuclear Physics:
P. Bhattacharya, S. Bose, Sukalyan Chattopadhyay, N. Majumdar, A. Sanyal, S. Sarkar, P. Sen, S.K. Sen and B.C. Sinha.

Calcutta, India, Variable Energy Cyclotron Centre:
Subhasis Chattopadhyay, M.R. Dutta Majumdar, M.S. Ganti, T.K. Nayak, R.N. Singaraju, M.D. Trivedi and Y.P. Viyogi.

Catania, Italy, Dipartimento di Fisica dell'Università and Sezione INFN:
A. Badalà, R. Barbera, U. Becciani, C. Caligiore, M. Gulino, S. Ingrassia, A. Insolia, F. Librizzi, D. Lo Presti, A. Palmeri, S. Panebianco, G.S. Pappalardo, L. Pappalardo, C. Petta, N. Randazzo, S. Reito, F. Riggi, A.C. Russo, G.V. Russo, M. Russo, G. Saccà and A. Sciutto.

CERN, Geneva, Switzerland, European Organization for Nuclear Research:
J. Bächler, L. Barwacz, J.A. Belikov, V. Berejnoi, J.-C. Berset, R. Brun, M. Burns, M. Campbell, E. Cantatore, W. Carena, F. Carminati, J. Christiansen, C. D'Ambrosio, M. Davenport, C. Eisenberg, T. Grassi, J. de Groot, A. Di Mauro, R. Divià, C. Engster, H.G. Fischer, M. Flammier, F. Formenti, D. Fraissard, E. Futo, E. Gaumann, M. Goossens, B. Goret, C. Gregory, P.G. Innocenti, A. Jachołkowski, W. Klempt, K. Knudson, G. Lecoeur, J.C. Legrand, L. Leistam, Y. Lesenechal, C. Lourenço, M. Macowicz, T. Marszal, P. Martinengo, M. Mast, R. Monnin, M. Morel, A. Morsch, M. Mota, L. Musa, L. Pigni, F. Piuz, E. Quercigh, J. Raynaud, H. Renshall, A. Rivetti, G. Rubin, K. Šafařík, J.-C. Santiard, J. Schukraft, E. Scomparin, W. Snoeys, C. Sobczynski, P. Sonderegger, M. Spegel, D. Swoboda, P. Szymanski, J.-C. Tarlé, J. van Beelen, H. van der Velde, P. Vande Vyvre, A. Vascotto, D. Vranic, S. Wenig, P. Wertelaers and T. Williams.

Chandigarh, India, Physics Department, Panjab University:
M.M. Aggarwal, A.K. Bhati and V.S. Bhatia.

Clermont-Ferrand, France, Université Blaise Pascal and IN2P3:
J.P. Alard, R. Babut, A. Baldit, N. Bastid, G. Blanchard, M. Brossard, N. Brun, J. Castor, T. Chambon, F. Daudon, A. Devaux, P. Dupieux, B. Espagnon, J. Fargeix, P. Force, F. Manso, S. Mayade, V. Ramillien, G. Roche, O. Roig, L. Royer, P. Saturnini and G. Savinel.

Coimbra, Portugal, Departamento de Física, Faculdade de Ciências e Tecnologia:
R. Ferreira Marques, P. Fonte and A. Policarpo.

Columbus, U.S.A., Department of Physics, Ohio State University:
D. Hardtke, T.O. Humanic, M. Lisa, G. Lo Curto, B. Nilsen, G. Paić, D.M. Reichhold and E. Sugarbaker.

Copenhagen, Denmark, Niels Bohr Institute:
I. Bearden, H. Bøggild, J. Gaardhøje and B. Nielsen.

Cracow, Poland, Henryk Niewodniczanski Institute of Nuclear Physics, High Energy Physics Department:
J. Bartke, E. Gładysz-Dziaduś, E. Górnicki, M. Kowalski, K. Papiernik, A. Rybicki, P. Stefański and Z. Wlodarczyk1).

Darmstadt, Germany, Gesellschaft für Schwerionenforschung (GSI):
A. Andronic, R. Averbeck, C. Blume, P. Braun-Munzinger, P. Crochet, A. Deusser, A. Devismes, J. Eschke, N. Herrmann, B. Kolb, J. Lühning, U. Lynen, D. Miskowiec, W.F.J. Müller, C. Neyer, A. Sandoval, H. Sann, H.R. Schmidt, H. Stelzer, W. von Rüden and A. Wörner.

Frankfurt, Germany, Institut für Kernphysik, Johann-Wolfgang Göthe Universität:
C. Bormann, P. Buncic, P. Foka, M. Gaździcki, J. Günther, R. Renfordt, D. Röhrich, G. Roland, R. Stock, H. Ströbele and P. Szymanski.

Gatchina, Russia, St Petersburg Nuclear Physics Institute:
B. Komkov, V. Mylnikov, V. Nikouline, V. Samsonov, S. Volkov and A. Vorobiev.

Geneva, Switzerland, Department de Physique Nucléaire et Corpusculaire, Université de Genève:
M. Martin and L. Rosselet.

Heidelberg, Germany, Max-Planck-Institut für Kernphysik:
F. Ceretto, C. Fuchs, J. Rak and J.P. Wurm.

Heidelberg, Germany, Physikalisches Institut, Ruprecht-Karls Universität:
H. Appelshäuser, R. Baur, S. Esumi, P. Glässel, B. Lenkeit, M. Messer, A. Pfeiffer, W. Schmitz, J. Stachel, H. Tilsner, C. Voigt, S. Voloshin, J.P. Wessels and T. Wienold.

Ioannina, Greece, University of Ioannina, Department of Physics:
X. Aslanoglou.

Jaipur, India, Physics Department, University of Rajasthan:
K.B. Bhalla, A. Bharti, S.K. Gupta, V. Kumar, R. Raniwala and S. Raniwala.

Jammu, India, Physics Department, Jammu University:
P.V.K.S. Baba, S.K. Badyal, A. Bhasin, A. Gupta, V.K. Gupta, L.K. Mangotra, N.K. Rao and S.S. Sambyal.

JINR, Dubna, Russia, Joint Institute for Nuclear Research:
P.G. Akichine, V.A. Arefiev, E.V. Arkhipov, V.I. Astakhov, Alexandre Baldine, Anton Baldine, V.D. Bartenev, B.V. Batiounia, N.A. Blinov, M. Bondila, V.F. Boreiko, Z.V. Borissovskaia, Y.T. Borzunov, A.V. Chabounov, G.S. Chabratova, I.A. Chichov, V.I. Datskov, V.K. Dodokhov, L.G. Efimov, A.G. Fedounov, L.B. Golovanov, B.N. Guouskov, O.I. Iouldachev, V.G. Kadychevsky, V.S. Korolev, A.D. Kovalenko, V.L. Lioubochits, V.I. Lobanov, G.I. Lykasov, E.A. Matiouchevski, A.N. Maximov, R.R. Mekhtiev, K.V. Mikhailov, D.P. Mikhalev, I. Minaev, P.V. Nomokonov, A.N. Parfenov, I.V. Pouzynin, A.B. Sadovski, S.V. Semashko, A.E. Senner, I.A. Shelaev, A.V. Sidorov, N.V. Slavine, R.V. Slepnev, G.P. Tsvineva, A.S. Vodopianov, M.B. Yuldasheva, S. Zaporozhets and A.I. Zintchenko.

V. Diomkin2), V. Kuznetsov2), V. Shestakov2) and I. Tkatchouk2).

Ts. Baatar3), B. Khurelbaatar3) and R. Togoo3).

K.G. Akhobadze4), A.K. Djavrishvili4), T. Grigalashvili4), E.S. Ioramashvili4), A.V. Kharadze4), L. Khizanishvili4), T.V. Khuskivadze4), L.V. Shalamberidze4) and N. Shubitidze4).

V. Djordjadze5), N. Grigalashvili5), Z. Menteshashvili5), M. Nioradze5), M. Tabidze5) and Y. Tevzadze5).

Jyvaskyla, Finland, Department of Physics, University of Jyvaskyla and University of Helsinki:
J. Aysto, W. Trzaska and V. Ruuskanen.

Kharkov, Ukraine, National Scientific Centre ‘Kharkov Institute of Physics and Technology’:
G.L. Bochek, V.F. Boldyshev, I.F. Chervonny, A.N. Dovbnya, V.I. Kulibaba, N.I. Maslov, S.M. Potin, I.M. Prokhorets and A.F. Starodubtsev.

Kharkov, Ukraine, Scientific and Technological Research Institute of Instrument Engineering:
V.N. Borshchov, S.K. Kiprich, O.M. Listratenko, V.E. Starkov and M. Zamirets.

Kiev, Ukraine, Department of High Energy Density Physics, Bogolyubov Institute for Theoretical Physics, National Academy of Sciences of Ukraine:
D.E. Kharzeev, O. Pavlenko, A. Velytsky and H. Zinovyev.

Košice, Slovakia, Institute of Experimental Physics, Slovak Academy of Sciences and Faculty of Science P.J. Šafárik University:
J. Fedoršin, M. Hnatič, A. Jusko, B. Kocper, I. Králik, A. Kravčáková, F. Kriváň, I. Kuľková, M. Lupták, G. Martinská, B. Pastirčák, L. Šándor, J. Urbán, S. Vokál and J. Vrláková.

Legnaro, Italy, Laboratori Nazionali di Legnaro:
R.A. Ricci.

Lisbon, Portugal, Departamento de Física, Instituto Superior Técnico:
J. Barbosa, P. Branco, R. Carvalho, J. Seixas and R. Vilela Mendes.

Lund, Sweden, Division of Cosmic and Subatomic Physics, University of Lund:
L. Carlen, K. El Chenawi, S.I.A. Garpman, H.-A. Gustafsson, P. Nilsson, A. Oskarsson, L. Osterman, I. Otterlund, D. Silvermyr, K. Söderström and E.A. Stenlund.

Lyon, France, Institut de Physique Nucléaire de Lyon, Université Claude Bernard Lyon-I:
M. Chevallier, B. Cheynis, J.Y. Grossiord, A. Guichard, D. Guinet, G. Jacquet and P. Lautesse.

Marburg, Germany, Fachbereich Physik, Philipps Universität:
F. Eckhardt, V. Friese and F. Pühlhofer.

Mexico City, Mexico, Centro de Investigación y de Estúdios Avanzados:
T. Fearnley, G. Herrera Corral and H. Mendez.

Minsk, Belarus, Institute for Nuclear Problems, State University:
A.A. Lobko

Moscow, Russia, Institute for Nuclear Research, Academy of Science:
K.A. Chileev, S.N. Filippov, Ju.K. Gavrilov, M.B. Goloubeva, M.N. Gotra, F.F. Gouber, T.L. Karavitcheva, A.B. Kourepin, V.D. Laptev, A.I. Maevskaya, V.I. Razine, A.I. Rechetine, N.M. Sobolevsky and N.S. Topilskaia.

Moscow, Russia, Institute for Theoretical and Experimental Physics:
A.N. Akindinov, S.V. Boiarinov, V. Golovine, I.G. Grichouk, A.B. Kaidalov, M.M. Kats, I.T. Kiselev, S.M. Kisselev, I. Kisselevitch, E. Lioublev, A.N. Martemiyanov, M. Martemianov, P.A. Polozov, S.A. Pozdniakov, V.S. Serov, A.V. Smirnitski, M.M. Tchoumakov, I.A. Vetlitski, K.G. Voloshin, L.S. Vorobyev and B.V. Zagreev.

Moscow, Russia, Russian Research Center "I.V. Kurchatov Institute":
V. Antonenko, S. Beliaev, R. Cherbatchev, I. Doubovik, S. Fokine, M. Ippolitov, K. Karadjev, A.L. Lebedev, V. Lebedev, V.I. Manko, G. Mguebrichvili, T. Moukhanova, A. Nianine, S. Nikolaev, O. Patarakine, D. Peressounko, I. Sibiriak, A. Vasiliev, A. Vinogradov and M. Volkov.

Moscow, Russia, Moscow Engineering Physics Institute:
V. Grigoriev, V. Kapline, V. Loguinov and M. Strikhanov.

Mumbay, India, Physics Department, Indian Institute of Technology:
R. Varma.

Münster, Germany, Institut für Kernphysik, Westfälische Wilhelms Universität:
C. Barlag, D. Bucher, T. Peitzmann, R. Santo and H. Schlagheck.

Nantes, France, Laboratoire de Physique Subatomique et des Technologies Associées:
A. Boucham, S. Bouvier, J.P. Cussonneau, B. Erazmus, S. Giliberto, B. Guillet, H.H. Gutbrod,
M.S. Labalme, P. Lautridou, F. Lefèvre, L. Luquin, L. Martin, V. Métivier, A. Rahmani, O. Ravel,
T. Reposeur, F. Retiere, C.S. Roy and D. Roy.

Novosibirsk, Russia, Budker Institute for Nuclear Physics:
A.R. Frolov, I.N. Pestov and M.A. Tiounov.

Oak Ridge, U.S.A., Instrumentation and Controls Division, Oak Ridge National Laboratory:
C.L. Britton, W.L. Bryan, M.N. Ericson, M.J. Paulus, M.L. Simpson, J.W. Walker and A.L. Wintenberg.

Orsay, France, Institut de Physique Nucléaire, Université de Paris-Sud:
L. Bimbot, M.P. Comets, P.F. Courtat, R. Douet, B. Genolini, H. Harroch, D. Jouan, L. Kharmandarian,
Y. Le Bornec, M. Mac Cormick, J. Peyré, J. Pouthas and N. Willis.

Oslo, Norway, Department of Physics, University of Oslo:
L.M. Ingebrigtsen, G. Løvhøiden, B. Skaali and D. Wormald.

Padua, Italy, Dipartimento di Fisica dell'Università and Sezione INFN:
F. Antinori, F. Brandolini, N. Carrer, T. Grassi, M. Morando, A. Pepato, F. Scarlassara, G. Segato,
F. Stanco and E. Zanoni.

Prague, Czech Republic, Institute of Physics, Academy of Science:
J. Mareš, E. Mihoková, M. Nikl, K. Píška, K. Polák and P. Závada.

Protvino, Russia, Institute for High Energy Physics:
A.M. Blik, M. Bogolyubsky, G. Britvitch, S. Erine, G.V. Khaoustov, I.V. Kharlov, V.N. Kolossov,
V. Lichine, S.A. Sadovski, V.D. Samoilenko, P.A. Semenov, V.I. Suzdalev, V. Tikhonov and A. Zviagine.

Řež u Prahy, Czech Republic, Academy of Sciences of Czech Republic, Nuclear Physics Institute:
V. Hanzal, J. Hošek I. Hrivnačova, V. Kuschpil, A. Kugler, V. Petraček, M. Šumbera, A. Tlustý,
V. Wagner and D. Zakoucky.

Rome, Italy, Dipartimento di Fisica dell'Università 'La Sapienza' and Sezione INFN:
S. Di Liberto, A.M. Mazzoni, F. Meddi, D. Prosperi and G. Rosa.

Saclay, France, Centre d'Etudes Nucléaires, DAPNIA/SPhN:
A. Baldisseri, H. Borel, J. Gosset, F.M. Staley and Y. Terrien.

Salerno, Italy, Dipartimento di Fisica Teorica e S.M.S.A., Università di Salerno and Sezione INFN:
G. Grella, M. Guida, G. Romano and T. Virgili.

Sarov, Russia, Russian Federal Nuclear Center (VNIIEF):
S. Abramovitch, V. Basmanov, E. Fomouchkine, V. Ianowski, R. Ilkaev, L. Ilkaeva, A. Khlebnikov,
S. Nazarenko, V. Pounine, S. Poutevskoi, G.G. Savkin, I. Selin, I. Vinogradov and A. Zhitnik.

St Petersburg, Russia, Institute for Physics of St Petersburg State University, Mendeleev Institute for Metrology and Meson Scientific Association:
L.Y. Abramova, V.S. Alexandrov, V.M. Baratov, A.A. Bolonine, M.A. Braun, V.M. Dobulevitch, G.A. Feofilov, O.N. Godissov, S. Guerassimov, S.N. Igolkine, M.I. Ioudkine, A.A. Kolojvari, V. Kondratiev, I.A. Novikov, S.V. Potapov, O.I. Stolyarov, T.A. Toulina, F.A. Tsimbal, F.F. Valiev, V.V. Vetchernine, L.I. Vinogradov and L.F. Vitouchkine.

Strasbourg, France, Institut de Recherches Subatomiques:
L. Arnold, M. Ayachi, J. Baudot, J.D. Berst, J.P. Blondé, J.P. Coffin, W. Dulinski, G. Guillaume, L. Guthneck, L. Hebrard, S. Higueret, Y. Hu, F. Jundt, C. Kuhn, J. Lutz, A. Michalon, F. Rami and C. Suire.

Trieste, Italy, Dipartimento di Fisica dell'Università and Sezione INFN:
V. Bonvicini, A. Gregorio, A. Rachevski, A. Vacchi L. Valentincic and N. Zampa.

Turin, Italy, Dipartimento di Fisica Sperimentale dell'Università and Sezione INFN:
B. Alessandro, R. Arnaldi, R. Astengo, G. Bonazzola, E. Botta, L. Busso, P.G. Cerello, E. Chiavassa, P. Cortese, F. Daudo, N. De Marco, R. Farano, A. Feliciello, S. Gallian, M. Gallio, G. Giraudo, P. Giubellino, A.R. Hernandez Montoya, M. Idzik, A. Marzari-Chiesa, M. Masera, G. Mazza, B. Minetti, A. Musso, D. Nouais, A. Piccotti, L. Riccati, A. Rivetti, F. Tosello and E. Vercellin.

Utrecht, The Netherlands, NIKHEF and Subatomic Physics Department of the Utrecht University:
M. Botje, A. Buijs, A. De Haas, R. Kamermans, P.G. Kuijer, C.J. Oskamp, A. Van Den Brink and N. Van Eijndhoven.

Warsaw, Poland, Soltan Institute for Nuclear Studies:
D. Czerwinski, A. Deloff, K. Karpio, S. Kozak, L. Lukaszek, H. Malinowski, T. Siemiarczuk, G. Stefanek, L. Tykarski and G. Wilk.

Wuhan, China, Institute of Particle Physics, Huazhong Normal University:
X. Cai, Y. Hu, F. Liu, L. Liu, H. Wang and D. Zhou.

Yerevan, Armenia, Yerevan Physics Institute‡):
R. Asatryan, M. Atayan, R. Avakian, V. Danielyan, V. Gavalian, A. Grigorian, S. Grigoryan, H. Gulkanyan, R. Hakobyan, V. Kakoyan, S. Mehrabyan, L. Parlakyan, R. Shahoyan and H. Vardanyan.

Zagreb, Croatia, Ruder Bošković Institute:
D. Ferenc, A. Ljubičić and T. Tustonic.

‡) Applying to join ALICE.
1) Institute of Physics, Pedagogical University, Kielce, Poland.
2) Research Centre for Applied Nuclear Physics (RCANP), Dubna, Russia.
3) Institute of Physics and Technology, Mongolian Academy of Sciences, Ulaanbaatar, Mongolia.
4) Institute of Physics, Georgian Academy of Sciences, Tbilisi, Georgia.
5) High Energy Physics Institute, Tbilisi State University, Tbilisi, Georgia.

Acknowledgements

We warmly acknowledge for their participation in the RD26 and HMPID projects:
Y. Andrès, M. Bosteels, A. Braem, A. Breskin, D. Carminati, P. Carrie, G. Cerutti, R. Chechick, E. Chesi, C. Coluzza, A. D'Auria, C. David, J.M. Delabré, A. Gandi, G. Lenzen, G. Lion, P. Majewski, C. Millerin, A. Placci, R. Puntaferro, E. Rosso, C. Schillinger, T. Scognetti, J. Seguinot, S. Sgobba, I. Sorin, V. Valentino, J. Vávra and T. Ypsilantis.

The Editorial Board, E. Nappi[1], G. Paic[2] and F. Piuz[3], is also indebted to:
I. Canon, M. Jouhet, S. Leech O'Neale, F. Marcastel and C. Vanoli form the Desktop Publishing Service, for their professional help with the editing.

The collaboration wishes to thank all the technical and administrative staff (in particular S. Barras and S. Stappers) involved during the preparation of this TDR.

---

[1] Eugenio.Nappi@cern.ch

[2] Guy.Paic@cern.ch

[3] Francois.Piuz@cern.ch

Contents

1 Introduction

1.1 The ALICE experiment

ALICE (A Large Ion Collider Experiment) [1] is an experiment at the Large Hadron Collider (LHC) optimized for the study of heavy-ion collisions, at a centre of mass energy ~ 5.5 TeV. The prime aim of the experiment is to study in detail the behaviour of matter at high densities and temperatures, in view of probing deconfinement and chiral symmetry restoration.

The detector consists essentially of two main components: the central part, composed of detectors mainly devoted to the study of hadronic signals and dielectrons in the pseudorapidity range $-1 < \eta < 1$, and the forward muon spectrometer, devoted to the study of quarkonia behaviour in dense matter. The layout of the ALICE set-up is shown in colour Fig. 1.i. The first technical challenge is imposed by the large number of particles created in the collisions of lead ions. There is a considerable spread in the presently available predictions for the multiplicity of charged particles produced in a central Pb–Pb collision. The design of the experiment has been based on the highest value, 8000 charged particles per unit of rapidity, at mid rapidity. This multiplicity dictates the granularity of the detectors and their optimal distance from the colliding beams.

The detailed characterization of ion–ion collisions requires particles to be measured and identified over a large range of momenta and masses. This second challenge has determined the rather complex particle identification scheme of ALICE, as described in the next section.

1.2 Particle identification in ALICE and the HMPID

The goals of ALICE involving particle identification are: the measurement of global event characteristics like event topology, momentum spectra of identified particles, particle correlations (HBT), and particle ratios; the measurement of the ϕ decay in the KK channel; the detection of charm. The ALICE PID system has three detectors that participate in the particle identification with a full coverage of the central ALICE barrel — ITS, TPC and TOF — and a single-arm detector, the High-Momentum Particle IDentification (HMPID), devoted to the identification of the high-momentum particles, i.e. pions, kaons and protons in the range from 1 to 5 GeV/c.

The ITS and TPC identify, via the dE/dx measurement, up to $p \sim 600$ MeV/c while the TOF will cover up to 1.2–1.4 GeV/c, overlapping well with the dE/dx detectors. These detectors will allow the measurement of several signals on an event-by-event basis.

The HMPID is devoted to the detection of the particles in the momentum range above the one covered by the other detectors. Since for most particles the expected yield is rather low above $p \sim 1$ GeV/c, the HMPID is conceived as a single-arm detector that measures the spectra of particles in an inclusive manner, with the possibility to build classes of events using the event-by-event characterization done at lower momenta by the barrel detectors. The axonometric view of the HMPID detector in the ALICE set-up, together with the spaceframe that supports the HMPID, the TPC, and the time-of-flight barrel, is shown in colour Fig. 1.ii.

Not many detectors can provide the required momentum range for particle identification in the ALICE central barrel. We can envisage to use either a time-of-flight with very good time resolution (≤ 100 ps) or a ring-imaging technique using Cherenkov light. Since the time-of-flight alternative, using scintillators and photomultipliers, is both onerous and difficult in the radiation and magnetic environment of ALICE and since no other method is for the time being capable of similar resolutions, we have decided to adopt a

RICH, for which a specific R&D project has been developed (see Chapter 2). The specificity of this detector is that it employs for the first time, in a detector of that size, the concept of two-dimensional electronic readout with CsI photocathodes for the conversion of the Cherenkov photons. The high readout rate of this detector also allows particle identification at much higher rates than foreseen for Pb–Pb collisions, an important feature for the pp operation.

In Fig. 1.1 we show the front and lateral views of the HMPID, including some relevant geometrical dimensions.

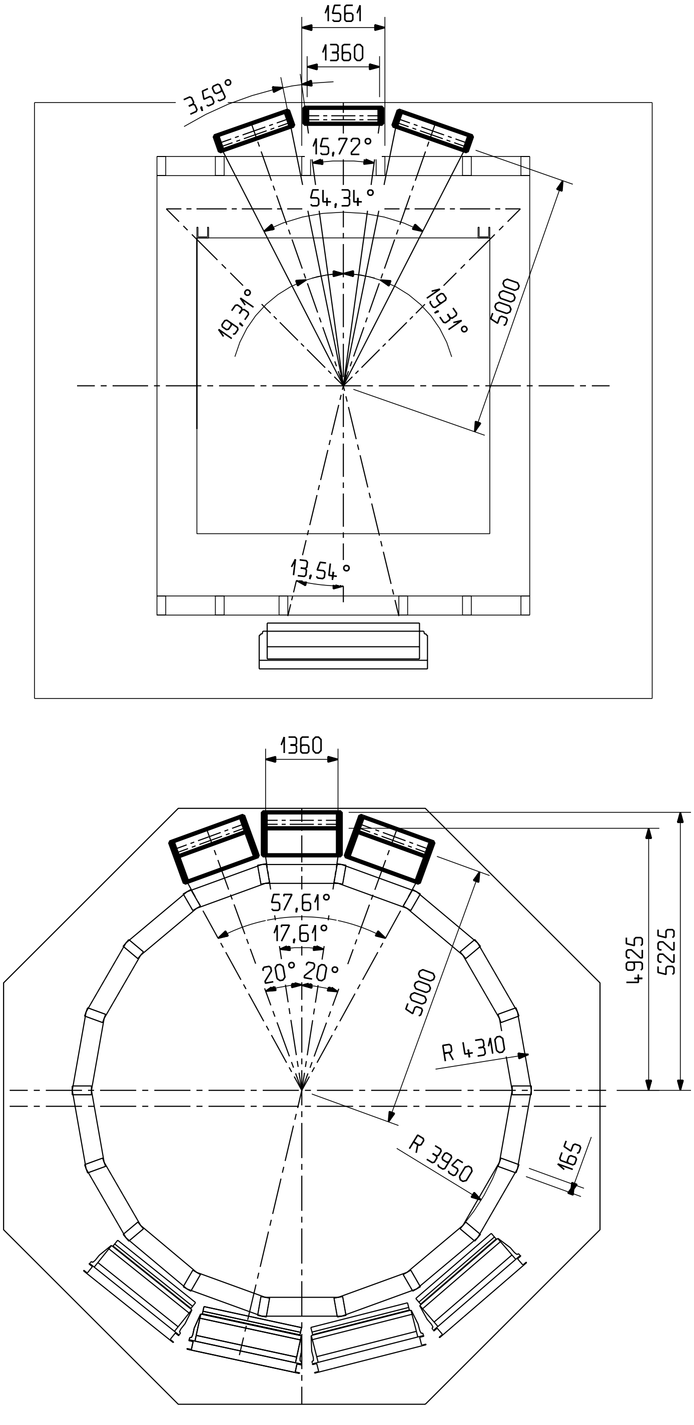

Figure 1.1: Side and front view of the HMPID, shown in the upper part of the figures. The boxes in the lower parts represent the PHOS calorimeter.

1.3 Physics of the HMPID

While the low-p_t particle spectra (up to around 1 GeV/c) provide information about the temperature of the formed medium, through thermal particle emission, in the high-p_t region, accessible through the HMPID, particle production becomes dominated by hard processes. This is a particularly interesting observable since initial hard production can be calculated in the framework of perturbative QCD, and the calculations can be verified using the data collected in pp collisions.

Detailed information on the density of the medium produced in a Pb–Pb collision can, in principle, be obtained by studying the energy loss of high-energy partons traversing that medium. Partons are usually studied, in pp collisions, via jets using calorimetry. In heavy-ion collisions, the background from the underlying event makes jet recognition difficult and leads to a bad energy resolution for jets with less than ~ 100 GeV. Furthermore, the lost energy is mainly carried by soft gluons radiated close to the jet axis, making calorimetry measurements rather insensitive to jet quenching.

There is, however, an alternative way to study this interesting phenomenon. The suppression of large E_t jets naturally leads to the suppression of large p_t particles. A clear advantage of this method is the large production rate of such particles. Therefore, the measurement of the momentum spectra of identified particles at large momenta allows, with a moderate experimental effort, the study of the effect of jet quenching. The comparison of the high-p_t spectra of identified particles measured in Pb–Pb collisions with the calculated curves, and with the spectra obtained from pp data, will be very sensitive to the medium-induced energy loss of high-energy partons [2].

Figure 1.2a illustrates the drastic effect of jet quenching on the the proton p_t distribution, made visible through the ratio between the Pb–Pb and the pp spectra.

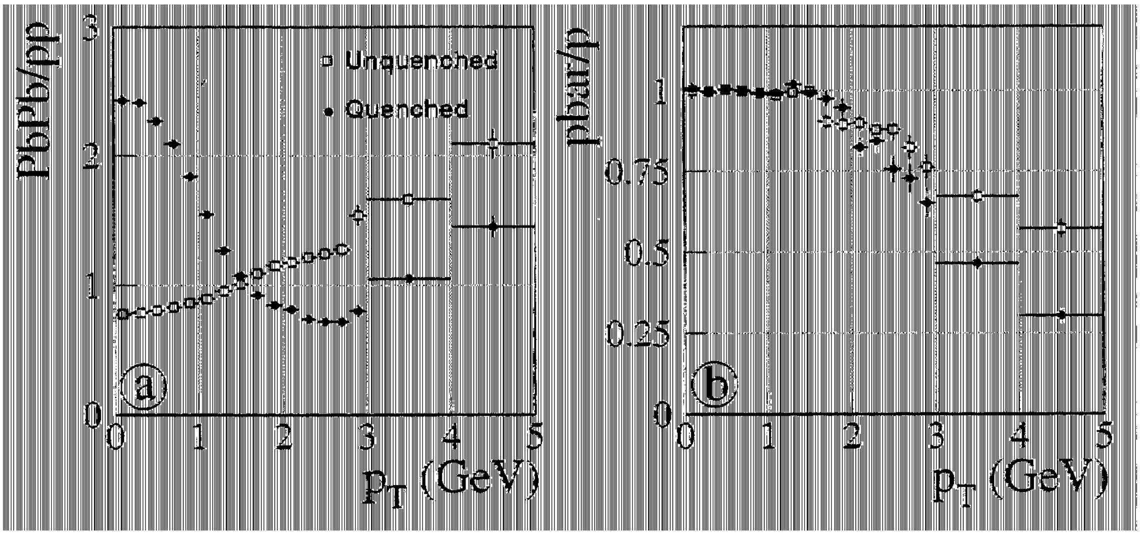

Figure 1.2: Expected influence of jet quenching on the ratio of proton p_t spectra between Pb–Pb and pp collisions (a) and on $\overline{\mathrm{p}}/\mathrm{p}$ ratio in Pb–Pb collisions (b). The statistics corresponds to 10^7 pp and 5×10^4 central Pb–Pb collisions.

The comparison of proton and antiproton spectra will also give information on the jet quenching in dense matter [3] . At high p_t the origin of the proton and antiproton spectra are not the same. The quark jets (containing more likely a valence quark) lead more often to proton than antiproton production, while the gluon jets have equal probability to produce either particle. Therefore, the protons and antiprotons may be used to 'tag' the quark and gluon jets, respectively. To that basic asymmetry in production is added the fact that the gluons, owing to their larger colour charge, lose more energy in a dense medium than quarks, thus suppressing the antiproton spectra at large p_t. The predicted difference in yields above 3 GeV/c is about a factor of two (see Fig. 1.2b), easily accessible by the HMPID performance.

The study of particle correlations at high momenta gives information on the evolution of the size of the emitting source as a function of the transverse mass of the different particles. This is of particular importance since the correlations in expanding systems provide information about the dynamical evolution of the system, e.g. proper time of decoupling, duration of particle emission, and presence of collective flows. Furthermore, it is also desirable to cover the possibility for a drastic change in the measured radii at high momenta — indicating a non-equilibrated early stage with a small radius.

1.4 A Ring-Imaging Cherenkov (RICH) detector using CsI photocathode

1.4.1 General remarks

The first choice to be made when designing a RICH detector for particle identification is the type of radiator and geometry to be used. The momentum limit for particle identification determines the choice of the radiator medium.

For the momentum range of interest in ALICE (1 to 5 GeV/c), and the particles we want to identify (π, K and p), only liquids have an adequate refractive index. The type of liquid is also restricted by the range of the Cherenkov photon detection, in our case limited to the far ultraviolet photons ($\lambda \leq 200$ nm). Only one liquid, C_6F_{14}, satisfies the requirement of transparency to Cherenkov photons in this range.

As far as the geometry is concerned, there is a choice between two main types of RICH detectors:

- those with focusing properties, where the photons emitted along the track in the radiator medium are subsequently focused, usually by a mirror, onto the photon detection plane, which is at the same time the focal plane of the detector;
- those that do not use focusing devices but, instead, have a particle path through the detector which is small with respect to the distance from the radiator to the photon detection plane as shown in colour Fig. 1.iii.

In our case we are forced for several reasons — particle density, space considerations, photon absorption, etc., to choose the latter solution, called also the ‘proximity focusing’.

Another vital choice is the choice of the photon detector. Considering the surface, the price, and the particle densities involved, the only realistic candidate is a solid photocathode consisting of CsI in conjunction with a MWPC. This technique allows for a detector of considerable simplicity and adequate performance in the ALICE environment.

Although in ALICE we are confronted with high charged particle densities hitting the detector (more than 80 particles/m^2 in the highest multiplicity events), the low counting rate ($\leq 10^4$ Hz) allows a long integration time to be used on the induced charge signal. Therefore, we can operate at a rather low gas gain, particularly well suited for the CsI operation. In colour Fig. 1.iv we show an event recorded with the fully equipped prototype (proto-2) module, that represents two-thirds of the final one.

1.4.2 The HMPID layout in ALICE

The HMPID detector consists of seven modules in a calot-like arrangement at the top of the ALICE set-up as shown in Fig. 1.1. The adopted layout is dictated by physics requirements and by technical constraints. The latter will be explained in detail in Chapter 3 and we shall review here only the aspects connected to the physics. The range of positive identification (i.e. the range where the particles will emit Cherenkov light) starts at different momenta for different particle masses. For instance, the lower limit for kaon identification will be ~ 1.2 GeV/c and the lower limit for proton identification will be ~ 2 GeV/c. Both limits allow a good overlap with the capability of the time-of-flight system.

Mainly for reasons of particle density, it was important to locate the detector as far as possible from the interaction point, close to the inner radius of the L3 magnet. In order to ensure the best tracking accuracy (see Chapter 4), no detector or constructive element is planned in between the outer wall of the TPC and the HMPID.

The size of the detector is determined by the following factors:

- the cross section for high-momentum particle production is too small to allow an event-by-event analysis: only inclusive measurements are possible;
- the measurement of correlations between high-momenta particles imposes a minimum detector size both in the beam direction and in the azimuthal angle coverage, to allow the detection of small source sizes, corresponding to rather large momentum differences in the relative momenta of the particles.

1.5 Overview of the HMPID design and main results

1.5.1 R&D, prototypes, and test results

The use of large-area CsI photocathodes as a photo-converter element in a RICH detector, as proposed for the HMPID in 1993, was a novel concept. The preliminary research work was launched in the framework of the CERN RD-26 project and a 1 m^2 prototype (proto-2) has been completed and tested in the framework of the ALICE collaboration. In the following we give an overview of the main results obtained during this period.

1.5.1.1 CsI photocathode

CsI photocathodes of large areas, up to half a square metre, can be produced with high and reliable Quantum Efficiency (QE) performance by using standard and affordable technologies:

- the substrate, that acts also as the pad-segmented cathode of a wire chamber, can be manufactured using industrial Printed Circuit Board (PCB) techniques applying specific features such as surface polishing and use of nickel layer;
- the CsI evaporation is performed using Joule effect under a vacuum of a few 10^{-6} Torr. A key improvement in QE on such substrates was obtained by post treatment, the effect of which is illustrated in Fig. 2.8 on page 21. It consists of performing the CsI evaporation on a substrate held at 60 °C, maintaining this temperature under vacuum during eight hours after evaporation.

The CsI photocathode is operated at atmospheric pressure as the cathode of a wire chamber. It was shown that the ratio between the QE value measured at atmospheric pressure and the one in vacuum is a function of the gas species and of the reduced field value at the cathode surface, E/p (V/cm Torr^{-1}). CH_4 was found to achieve the best ratio, close to 0.9, at the field value to be used in the wire chamber (see Fig. 2.6 on page 20).

1.5.1.2 Single-electron detection using CsI pad cathode in a MWPC

The chamber performs the detection of Cherenkov single photoelectrons and minimum-ionizing particles (MIP). Since a 2-dimensional readout pattern is mandatory, signals induced on pads are measured. The cathode-to-anode gap has been chosen to be 2 mm, a compromise between anode/cathode coupling, MIP primary deposition, and layout arguments. The main concern was to demonstrate a stable operation of the chamber at a gain insuring maximum photoelectron yield and maximum single-electron detection efficiency while mastering the problem of the feedback photons in a chamber with an ‘open geometry’ configuration. The number of feedback photons N_{pf} emitted by primary avalanches is proportional to the size of the avalanche, according to $N_{\mathrm{pf}} = k \times G$ where k is a constant depending on the gas medium and G the chamber gain. The fraction of N_{pf} converted by the CsI photocathode leads in cases of large avalanches to the smearing of the Cherenkov signal and the creation of an uncorrelated background. Both effects increase the pad occupancy per ring pattern. Also, at high G diverging processes may occur when N_{pf} approaches 1, in case of highly ionizing events, possibly damaging the chamber. The pre-requisite to satisfy the previous requirements is to build a charge sensitive front-end electronics (see Chapter 3). Then, the choice of the operating gas is a key feature. Following gas mixtures studies, the present choice is still pure CH_4. The main results are presented, as a function of the single-electron mean pulse height in Fig. 2.36a. The lower curve shows that the mean number of Cherenkov photoelectrons reaches a plateau at a value of 16 per ring while the total number of electrons and of pad hits per event increases with the gain, as expected from feedback photon contribution. In Fig. 2.36b, one sees that the relative photon feedback yield shows a minimum at a gain in the plateau. Figure 2.35 on page 48 indicates a single-electron detection efficiency larger than 90% for A_0 above 30 ADC channels, providing a significant plateau length with stable operation. The effect of a small admixture of iC_4H_{10} in CH_4, as shown in Fig. 2.60 on page 65, results in a reduction by 50% of the feedback photon yield at high gain but a drop of 10–20% of the photoelectron yield.

We have also established that a magnetic field, up to about 1 T, parallel to the photocathode, does not affect the photoelectron yield (see Fig. 2.43 on page 54).

1.5.1.3 Results obtained with the 1 m^2 prototype (proto-2)

A full-scale prototype, representing two-thirds of a final HMPID module, was assembled and equipped with four CsI photocathodes 64×38.4 cm^2, two radiator trays, 133×41.3 cm^2, and 15 360 channels of pad front-end (FE) electronics. It was exposed at PS/SPS test beams under single- and multiparticle irradiation up to a track density locally higher than the one expected in ALICE. A large amount of data was recorded under various operating conditions for further pattern recognition studies. The operation of the chamber was very stable up to the maximum gain at which we want the detector to be operated, in an irradiation flux two orders of magnitude larger than the one expected in ALICE. The mean value of the photoelectron yield measured at the plateau for the four proto-2 photocathodes was 14.9 ± 1.5, using a 10 mm thick C_6F_{14} radiator. The uniformity of the photoelectron yield was always found satisfactory (see Fig. 2.54 on page 60).

1.5.1.4 Angular resolution of the reconstructed Cherenkov photons

The intrinsic angular resolution obtained with single-particle events was studied as a function of many parameters: chamber gain, gas species, radiator thickness, incidence angle and ring radius. Only the ring radius affects the single-photon angular resolution, as seen in Fig. 2.63 on page 69. From a radius of 100 mm, this resolution flattens at a value of 7–8 mrad. Surprisingly, all the other parameters are of little influence on this value, as seen in Figs. 2.64 on page 70, 2.65 and 2.66 on page 71. The corresponding ring resolution is of 2 mrad with a 10 mm thick radiator and particles at β close to 1.

1.5.1.5 Stability of the CsI photocathodes

During the R&D period, 32 large photocathodes (PCs) were produced and evaluated using RICH prototypes. As seen in Fig. 2.55 on page 60, a significant step in the QE performance was achieved from the 19th PC onwards, when the new pad substrate technology was adopted. The spread in QE values decreased substantially for the last produced PCs. That might reflect the greater care taken in the protection of the PCs against exposure to air during transfer and mounting on the detector. The stability of the QE as a function of time was checked on several PCs kept under continuous argon flow and evaluated at the beam periodically. A QE drop of about 5% has been observed over a four-year period (see Fig. 2.56 on page 62).

1.5.2 Detector description

In the first part of Chapter 3, the design and the prototyping studies of all the elements of a CsI-RICH module are described. The main elements of a CsI-RICH module are sketched in Fig. 1.3.

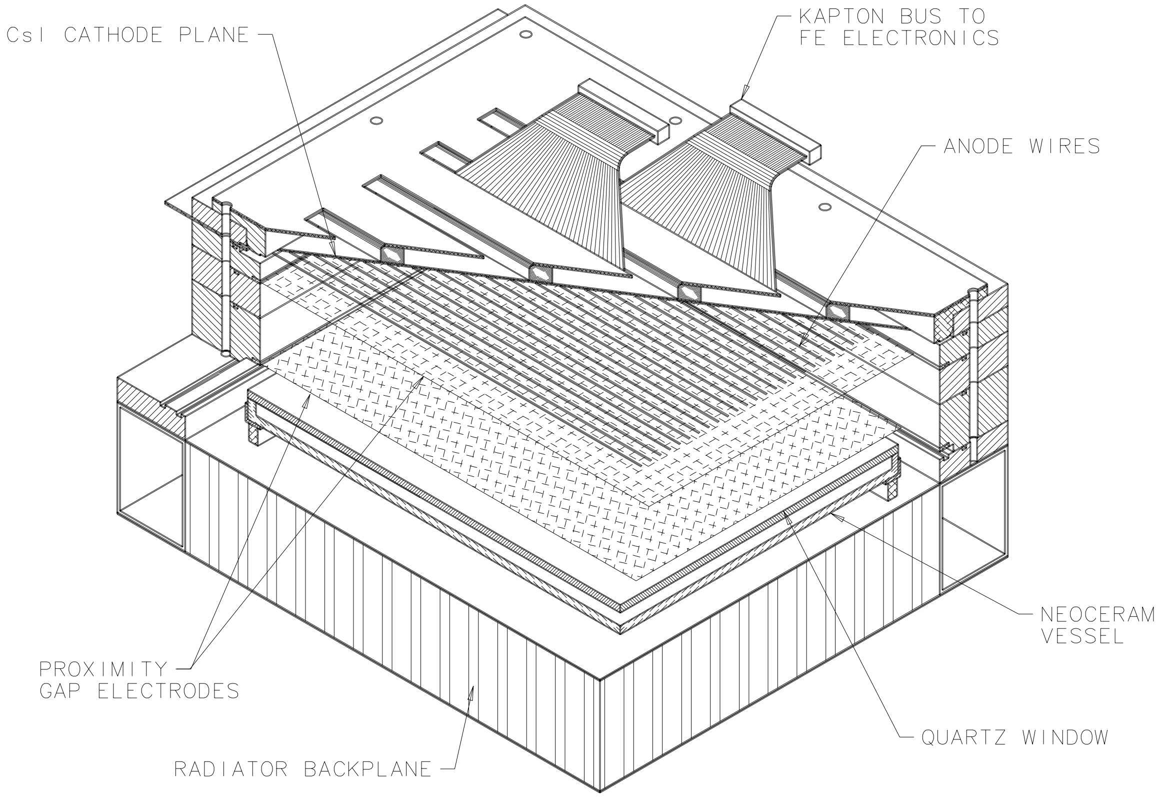

Figure 1.3: Artist's rendering of a HMPID module showing the various detector components, including the Kapton bus lines which carry the signals to the GASSIPLEX amplifiers (not shown).

- The photodetector is a conventional 2 mm gap MWPC with anode wires 20 μm in diameter and a pitch of 4 mm. One of the cathodes is a wired electrode (2 mm pitch, 100 μm diameter), while the second, where the CsI is deposited, is pad segmented. The pad size is 8×8 mm^2. The module has been designed in such a way that the CsI pad panels are stand-alone elements, easily detachable for CsI processing operations, while ensuring a reproducible and accurate chamber geometry, such as the cathode-to-anode gap of 2 mm within $\pm$50 μm (see Figs. 3.1 and 3.2 on page 84).
  The pad panels, made of light and stiff composite materials, hold on one face the pad PCB with the CsI layer and on the other the front-end electronics (FEE). The connections between the pads and the FEE inputs are made by flexible Kapton foils soldered at the back of the pad plane (see Figs. 3.4 and 3.5 on page 87).
- The CsI photoelectric threshold of 210 nm imposes severe UV-transmission specifications on the liquid radiator, C_6F_{14}, and on its container. The latter consists of a tray made of a glass-ceramic material with a 133×41.3 cm^2 silica window. The constituting materials have comparable dilation coefficients to ensure a perfect sealing of the glued assembly. The tray, designed to hold a hydrostatic pressure equivalent to 120 mbar, has been successfully tested up to 130 mbar.
- A C_6F_{14} circulation system has been built to purify, circulate, fill, and empty the two prototype radiator trays, remotely and safely. It is based on a gravity flow principle ensuring simple, passive, and safe operation, fully protected against overpressure.

- The front-end pad electronics has been designed by benefiting from the low interaction rate, 1–100 kHz, specific to the ALICE operation. It allows the use of a charge-sensitive preamplifier with a long integrating time, providing high sensitivity, and a multiplexed analog operation, saving digitizing channels. The system is based on the ASIC CMOS front-end chip GASSIPLEX, providing 16 analog multiplexed channels. The noise figure of the charge amplifier is 630 e r.m.s. at 0 pF. A filter stage, adapted to the long-tailed input current shape delivered by a wire chamber, ensures a base line restoration in 3 μs at 0.5% of the peak amplitude. A shaper stage sets the peaking time to 700 ns. The chip is operated in Track and Hold mode storing the charges into capacitors by means of an external trigger signal sent at the peak amplitude.
- A system has been built to evaporate the CsI by Joule effect on panels of 70×50 cm^2 and to perform the post-treatment by heating at 60 °C, under a vacuum of a few 10^{-6} Torr. The system allows the CsI photocathodes to be taken out without contact with air.
  The QE across the surface of the photocathodes can be evaluated in situ by means of a device, located in a vessel appended to the evaporation chamber, that measures the direct photocurrent emitted by local irradiation with monochromatic UV beam.

In the second part of Chapter 3, the system aspect of the HMPID is described, detailing the assembly and test procedures of the seven modules as well as the final schematics of the electronics and of the gas and liquid supplies.

1.5.3 Detector performance

We have studied the HMPID performance in the ALICE environment, under the highest particle densities currently predicted.

A complete simulation of the radiation environment of ALICE has been undertaken using the GEANT and FLUKA simulation programs, as well as the response of the RICH detectors assuming the design established in this document. The simulation shows that we shall be confronted with an important flux of charged particles, only about 30% of which is due to primary particles. The remaining part of the flux is due to secondary particles of different origins (see Table 4.2 on page 157). The neutron flux in the detector, although large, creates relatively few interactions. However, they result in an important energy deposition. Taking into account the response of the detector to charged particles and to the Cherenkov photons created in the radiator liquid and in its quartz window, the occupancy has been calculated to be about (10 ± 2)%.

We have developed a pattern recognition technique, based on a modified Hough transform method, which has been applied to samples of ‘synthetic’ data, created from the superposition of single events taken at the SPS, with 350 GeV/c pions at perpendicular incidence. Randomly overlapping between 10 and 50 particles/m^2, the corresponding occupancy varied from 2% to 12%. The highest value corresponds to the occupancy anticipated for the highest multiplicity ALICE events, according to the simulation.

The applied pattern recognition method was robust enough to identify the Cherenkov ring patterns and to determine the mean photon angle with satisfactory resolution. The best resolution was achieved for the smaller rings — an important indication for the final chamber design. The quality of the pattern recognition can be appreciated in Fig.1.4, for the largest occupancy expected in ALICE. The Gaussian fit gives a resolution of 6.2 mrad. Translated into identification range for π/K, it corresponds to an upper limit of 2.5 GeV/c. In the case of lower occupancies, either for more peripheral Pb–Pb collisions or for lighter nuclei (e.g. Ca–Ca), the identification limit is beyond 3 GeV/c.

We have also studied the matching of tracks recorded in the ITS and in the TPC (and extrapolated to the HMPID) with charged-particle impacts in the MWPC cathode. A matching efficiency of about 96% in the environment of 100 particles/m^2 has been achieved in the simulation.

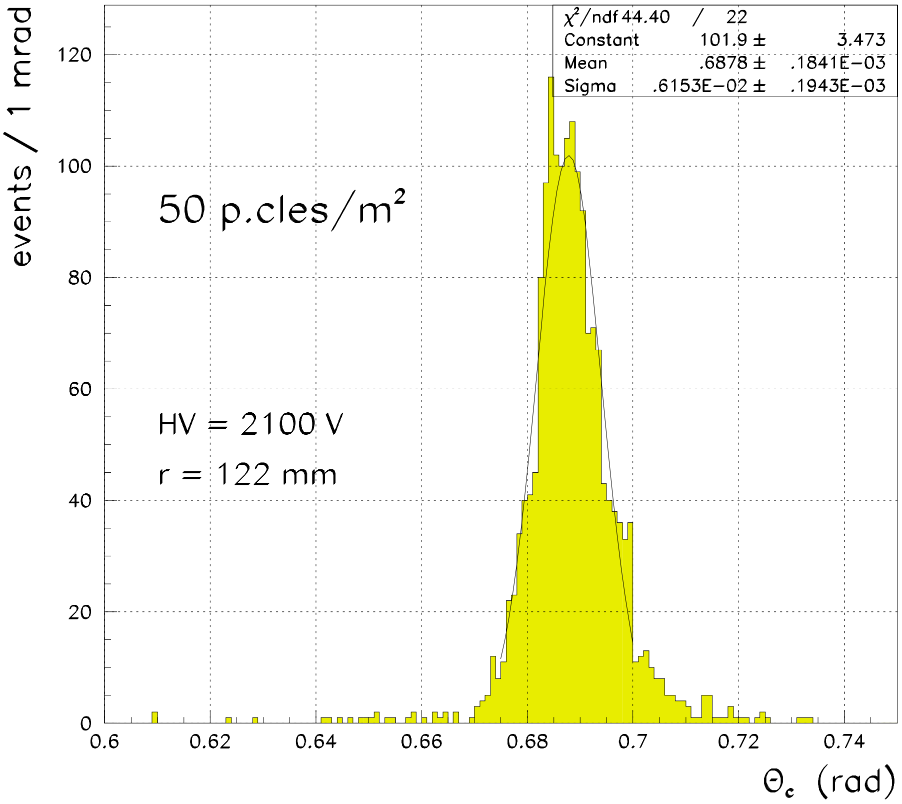

Figure 1.4: Cherenkov angle distribution at 50 particles/m^2, for the sample (4) described in Table 4.5 on page 160.

The current detector design and the performance demonstrated with a large prototype met essentially all the requirements set in the Technical Proposal [1] for the HMPID. Nevertheless, we intend to use the time available before the start of construction (in 2000) to further optimize and improve the HMPID system.

figure 1.i

figure 1.ii

figure 1.iii

figure 1.iv

2 R&D, Prototypes, Test Results

Introduction

In the late eighties, the interest for solar-blind single-photon detectors was revived by independent works studying the possibility of using CsI-based wire chambers of large area. High quantum efficiency (QE) values were reported in Refs. [1, 2] for CsI- and TMAE-coated films in CH_4 and stable operation of CsI-based gaseous photomultipliers under high gain was achieved. The growing availability of sophisticated integrated electronics opened the possibility of instrumenting wire chambers with large areas of pad-segmented cathodes using sensitive and low-noise front-end amplifiers of convenient volume, and at an affordable cost.

During the same time, the HEP community started to propose new experimental facilities dedicated to the future colliders SLAC, RHIC, and the LHC. The development of CsI RICH detectors designed to achieve particle identification in various momentum ranges was therefore undertaken by many research teams and included a common feature, the possibility to operate in high-density particle environments.

This situation led to the launching in 1992 of a CERN R&D project, RD-26 [3], aimed at studying the ‘Development of a large-area advanced fast RICH detector for particle identification at the Large Hadron Collider operated with Heavy Ions’. Several groups joined RD-26, proposing CsI RICH detectors to be integrated into the following large experiments: HADES at GSI Darmstadt, Babar at SLAC, HERA-B in Hamburg, ALICE at LHC. In addition, basic research work on CsI thin films was undertaken, in the collaboration, by specialized laboratories such as the Weizmann Institute, Ecole Polytechnique Palaiseau and EPF Lausanne [4].

A wide variety of research work has been performed in these laboratories both on matters of common interest such as CsI layer processing, chamber optimization, front-end electronics etc. and on more specific topics such as radiator systems, pattern recognition, etc. A part of the information can be found in the RD-26 Status Reports issued every year [5] as well as in review papers [6] and proceedings of workshops dedicated to RICH detectors and photodetection [7].

After four years of developments in RD-26, three large experiments have adopted the use of CsI RICH detectors as part of their apparatus: HADES [8], ALICE [9] and COMPASS/NA58 [10]. A detector of about half a square metre of CsI photocathode has been built and successfully operated in the NA44 experiment [11]. In the next section, we shall report on the studies related to ALICE detectors. Different options were adopted for other detector systems like HADES [8].

2.1 Basic CsI RICH components

The design of a CsI-RICH detector is based on the following requirements:

i) produce a CsI thin film of large area deposited on the cathode of a MWPC providing a high QE in the wavelength range below 210 nm (photoelectric threshold);
ii) ensure that an efficient detection of single electrons is obtained under stable operation of the MWPC having CsI-covered cathode and open geometry;
iii) make a detector system, with radiator and gaseous media highly transparent to UV light, allowing the generation and propagation of Cherenkov photons with wavelength below the 210 nm threshold.

We shall first discuss these basic features in general terms of their physical properties as well as their implications on the design of a RICH detector.

2.1.1 The CsI thin film

Combined with vacuum or gaseous electron multipliers, CsI photocathodes provide an efficient mean for UV photon imaging over a considerable spectral range [12]. It is limited in the short wavelengths by optical window or gas absorption and reaches a cut-off at a wavelength around 210 nm ($E_{\mathrm{g}} \sim 6$ eV). Of all alkali halides, CsI has the largest quantum efficiency. This is due to its low electron affinity ($E_{\mathrm{a}} = 0.1 \div 0.2$ eV) and to its exceptionally large electron escape length, which is 16 nm for 1 eV electrons [13]. Indeed, the QE of CsI surpasses that of all known solid UV photocathodes. It is comparable to that of TMAE (tetrakis (dimethylamine) ethylene) vapours in the short wavelengths but is smaller by about a factor of two above 190 nm. Compared to gas photoconversion, affecting the time response, occupancy and localization properties of the photodetector, CsI-based devices have the advantage of surface conversion and emission. The latter is of prime importance for operation at very high photon flux and for the ultimate localization and timing under oblique photon incidence.

CsI films are simple to prepare and are rather stable when exposed to ambient air. A low sensitivity to exposure at oxygen is indeed expected for material having $E_{\mathrm{g}} + E_{\mathrm{a}} > 6$ eV [14]. This specific property is the key feature for the processing of large areas of CsI thin films. It will be reported in the next sections that such a processing implies a series of manipulations and transfers from the evaporation station to the photodetector that would be impossible in the high vacuum conditions imperatively needed in the processing of bi-alkali halide photocathodes operating in the visible range.

Finally, the relatively low volume resistivity of CsI thin film (< 500 nm thickness), of the order of $10^{10} - 10^{11}$ Ω cm [15], makes possible their stable operation at high radiation fluxes under high gaseous multiplication conditions.

2.1.1.1 Preparation of the CsI film

The CsI films are usually prepared by resistive vacuum deposition, the substrates being kept either at room temperature or heated, as will be discussed later. In the processing of CsI layers, some physical features of this compound have to be taken into account:

- melting and boiling temperatures at 621 and 1280 °C, respectively;
- insulator compound with poor thermal conductance;
- high vapour pressure at melting point (0.1 mbar at 621 °C).

According to Maier-Komor [16], these features favour a dissociation of the CsI molecules during thermal evaporation when too high a temperature is reached at local points as supported by the observation of a non-stoichiometric composition of CsI thin films [17]. This suggests to use the electron gun evaporation with a cooled crucible and well-controlled surface evaporation. However, a large proportion of the users adopted the easier thermal evaporation. To palliate the above effects, the evaporation boat is prepared by pre-melting the CsI powder or small crystal pieces under vacuum, ensuring a good thermal contact between the boat and the load for future use. To eliminate the presumably contaminated superficial layer of the pre-molten CsI load, the deposition under vacuum is started by a short release on a rotable shutter and only then pursued on to the substrate.

It was found that the physical form and purity of the raw CsI material might play some role in the photoemission properties of the photocathode, probably due to the concentration of impurities. Anderson et al. [18] reported on significantly superior QE values, starting from large CsI crystals. We have not observed such an enhancement and have subsequently employed, as most of the users, CsI powder of different purities.

CsI is also known as a hygroscopic compound: exposed to moist air, its surface becomes whitish. Many compounds are formed from chemical and photo-reaction of water vapour with the CsI surface, such as cesium hydroxide (CsOH), oxide (Cs_2O), iodate ($CsIO_3$) and hydrogen iodide multihydrate ($HI \cdot (nH_2)$). All of them will degrade the CsI QE by poisoning the surface and the CsI bulk after diffusion. In the case of free cesium, fast oxidation is observed. Therefore, it is advisable to perform the deposition of CsI film in the best possible vacuum. In addition, it is essential to get the substrate surface free of moisture, requiring a heavy outgassing, preferably at the highest temperature tolerated by the substrate under vacuum.

In practice, as reported by different groups, the pressure during the evaporation may range between 1.0×10^{-4} and 5.0×10^{-7} Torr without any clear indication of great influence on the photocathode performance. However, since the QE evaluation of a fresh photocathode is usually carried out a short time period after its production, it is likely that all the early contaminations influence the ageing properties of the film, affecting the rate of chemical reactions in the longer term.

No visible influence on the photocathode performance has been seen by varying the evaporation rate between 1 and 50 nm/s in the 1.0×10^{-5} to 5.0×10^{-7} Torr vacuum range.

2.1.1.2 Evaluation of the CsI film

The two major parameters of a CsI film, relevant to its application as RICH photocathode, are the QE as a function of the wavelength of the incident photon and the long-term stability versus external agents (chemical contamination, radiation, etc.). It is expected that the optimization of these two variables will depend on a variety of physical and technical parameters such as evaporation procedures, substrate composition, microstructures, etc.

The QE measurements of CsI films can be carried out in vacuum and in gas media. The studies are usually made in three different modes:

a) measuring a DC photocurrent in vacuum or gas under relatively low electrical fields;
b) counting pulses in CsI-based wire chambers, under gas multiplication at moderate-to-high fields;
c) counting particle-induced photoelectrons in a CsI-based UV detector using Cherenkov emission.

QE measurements under vacuum

The results presented in this section are obtained using method a), studying small-area CsI samples with a monochromatic UV beam in a laboratory vacuum vessel. The QE differential curves will serve as a reference for comparison with results obtained with large photodetectors operated under gas with single Cherenkov photon counting, method c).

Among the numerous studies performed on the subject (see references quoted in Refs. [4, 6, 7]), we shall refer only to the ones performed at the Weizmann Institute by Malamud et al., [19]. A versatile apparatus was built in that institute, schematically shown in Fig. 2.1, where the following operations can be performed in sequence:

- resistive CsI film deposition under high vacuum and controlled by quartz balance;
- in situ exposure to a monochromatic collimated beam using a D_2 Hamamatsu DC-lamp and measurement of the induced photocurrent using a Keithley picoammeter;
- adjustable substrate temperature for film conditioning;
- measurement of the incident photon flux by deviating the UV beam by means of a rotable mirror on a calibrated photomultiplier (Hamamatsu R1460).

Two reasons made that instrument the most appropriate for our purposes:

a) the full sequence of operations and measurements is achieved in the same vacuum vessel, the CsI films are studied under optimal condition of cleanliness warranting excellent reproducibility;
b) the problem of measuring the absolute photon flux in the $150 \div 210$ nm range was mastered by calibrating commercial phototubes against a NIST reference (see Breskin in Ref. [4]).

All of our optimization studies on substrates and post treatment were done in close collaboration with the Weizmann group.

Figure 2.2 shows the differential CsI QE curve obtained in vacuum by averaging a large number of measurements. The error is evaluated to ±5%. The CsI films, 500 nm thick, were deposited on a polished stainless-steel substrate, held at 50°C and submitted to the post treatment described below. That curve will be taken as a reference curve and referred to as ‘QE-RD-26’. On the same figure is shown the best result obtained by Seguinot et al. [2] with a significantly higher QE value. It was not possible to reproduce such a good result in our set-up.

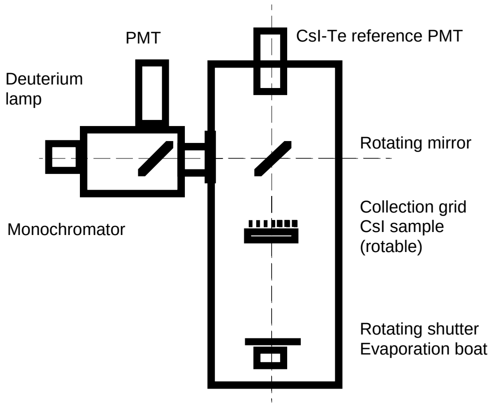

Figure 2.1: Scheme of the set-up used to measure the QE of CsI evaporated on small samples. After coating, the sample is rotated by 180 °, under vacuum, to be illuminated from the top by the UV collimated beam.

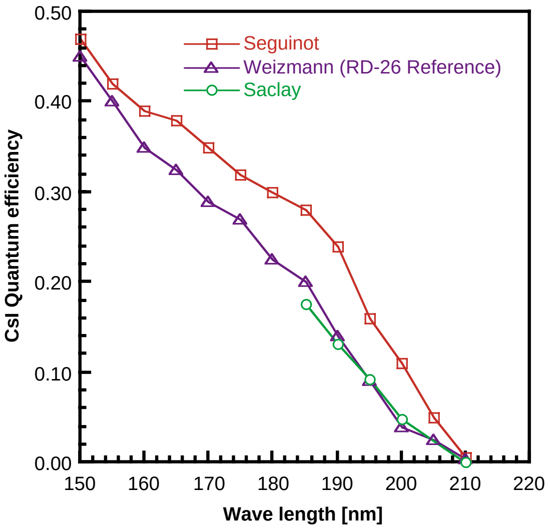

Figure 2.2: Measurements of the CsI QE as a function of wave length: a) Seguinot et al., best result from Ref. [2]; b) Weizmann, average curve [19]; c) Besson et al. [4]. Measurements a) and b) were made under vacuum.

Influence of the polarization and of the angle of incidence

The measurements described were performed using unpolarized UV beams at normal incidence while Cherenkov photons to be counted in a RICH detector are emitted in a p-polarized state and are expected to impinge on the CsI surface at large angle, 60–70 degrees. As shown in Fig. 2.3 the polarization state does not affect the reflection coefficient at normal incidence but does so significantly in the 60–80 degree range according to the polarization state. Hence, the QE measured by both methods — lamp or Cherenkov emission — has to be first corrected for that effect before comparison. In addition, the Fresnel relations used to calculate the reflection coefficients are applicable to a specular surface. If the roughness of the physical CsI surface is such that its normal at the impinging point is no longer in the polarization plane of the incident photon, the polarization vector is then decomposed into p- and s-components, meaning a more important probability of reflection than the pure p-component. Therefore, the surface roughness of the CsI films was investigated (see Section 2.1.1.5) to check the validity of the specular assumption.

A direct measurement of the CsI QE versus the incident angle by Mine et al., shown in Fig. 2.4 [20], indicates a decrease of the QE as a function of the incident angle which becomes more pronounced at larger wavelength. A test set-up, to pursue studies of small CsI samples, will be completed at CERN in autumn 1998. It is described in Section 2.1.1.6.

QE measurements under gaseous media

The use of a solid photocathode in a MWPC imposes the evaluation of its quantum response under gas which is generally smaller than the QE measured under vacuum. Indeed, the collection efficiency of photoelectrons emitted into gas depends on the gas composition and pressure (p) [21], and can be considerably reduced by elastic backscattering from gas molecules. Also the electric field in the photocathode vicinity plays an important role: at high field values the backscattering effect is almost totally suppressed [22]. The effect can be explained by the difference between inelastic and elastic collisions with gas molecules: in the first case the photoelectron trajectory is only slightly perturbed, while in the latter it is completely randomized, resulting in the backscattering towards the photocathode owing to the large mass difference between an electron and a gas molecule. This effect puts constraints on the detector operating conditions since the usually low reduced electric field E/p at the photocathode imposes a limited choice of gases. With the chamber geometry and operating voltage in use, the E/p value is 4 V/cm Torr^{-1} at the surface of the photocathode.

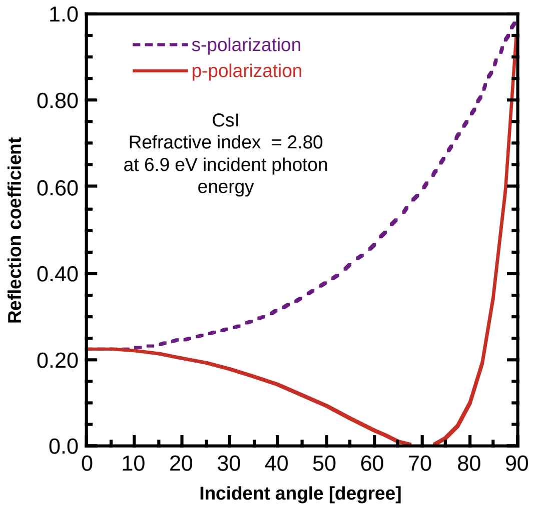

Figure 2.3: Reflection coefficient of a CsI layer as a function of the incident angle for s- and p-polarized light beam. Calculated from Fresnel relations for a specular surface.

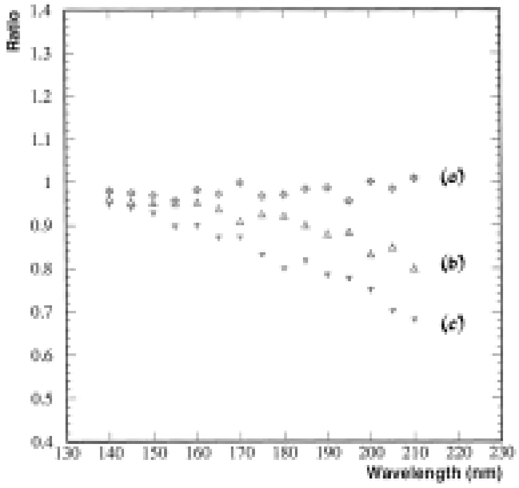

Figure 2.4: Ratio of the CsI QE measured under vacuum at an incident angle to that measured at normal incidence as a function of wave length. The angles are: curve a) = 15°, b) = 45°, c) = 55° [20].

This effect has been extensively studied in the framework of the RD-26 project and all details about experimental set-up, measurement procedures, and results can be found in Ref. [23]. The CsI photoemission into gaseous media has been investigated, both, in laboratory using a UV source and in beam test, with a RICH detector using He-, Ar- and CH_4-based mixtures [24].

In the UV tests both the single pulse counting and the DC current recording techniques were used. The single pulse counting technique allows the field to be varied at the vicinity of the CsI surface while maintaining the pulse detection efficiency. Thus we can compare the photoelectron collection efficiency measured at low electric fields, under 'charge collection mode', to the one observed in high electric fields, under 'charge multiplication mode' (relative QE measurement). Using the DC current recording, an absolute evaluation of the photoelectron collection efficiency is obtained by the ratio of the photocurrents measured in gas to that measured in vacuum, where the backscattering effect is absent.

The photoemission measured in He/CH_4 (95/5) mixture by pulse counting on the charge collection plateau is about 60% less than on the charge multiplication plateau [25]. The photocurrent measured in DC mode, in the same gas mixtures, below the multiplication threshold, is reduced by the same factor with respect to vacuum (Fig. 2.5). Therefore, we deduce that at high electric fields, above a gas amplification of 100, the same photoelectron yield as in vacuum is obtained.

In CH_4, the photoelectron collection efficiency in the charge collection mode, derived from the pulse counting, is about 90% of the value in the multiplication mode [25]. Also, in this gas, the gas-to-vacuum photocurrent ratio (~ 0.9 below multiplication, Fig. 2.6) is almost equal to the reduction factor estimated with the single-pulse counting technique. These experimental findings support the assumption that gas effects on the photoelectron collection efficiency are suppressed under charge multiplication.

Ar-based mixtures were studied only with the DC current recording technique. Pure Ar shows the same behaviour as He-based mixtures while in Ar/CH_4 (50/50) the photoelectron collection efficiency approaches that of pure CH_4.

A Monte Carlo program simulating the photoelectron transport process from the photocathode to the anode has been implemented to reproduce and interpret the laboratory measurements [25]. The results are shown in Figs. 2.5, 2.6, 2.7 together with the respective measured gas-to-vacuum photocurrent ratios. The photoelectron collection efficiency is determined primarily by the ratio of elastic and inelastic collision frequencies: the larger the rate of inelastic collisions the lower the backscattering probability.

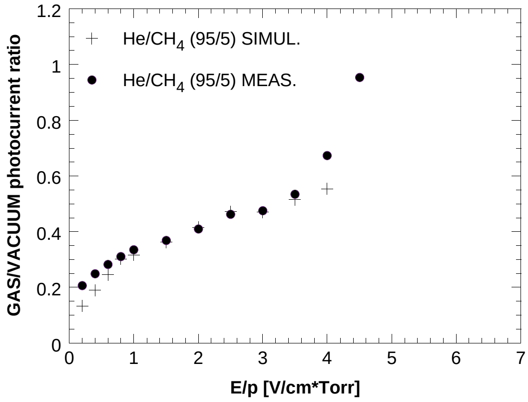

Figure 2.5: The ratio of the photocurrent from CsI, at 185 nm, in He/CH_4 (95/5) at 800 Torr, to that in vacuum (measured at the same absolute electric field) and the simulation results as a function of E/p at the photocathode surface.

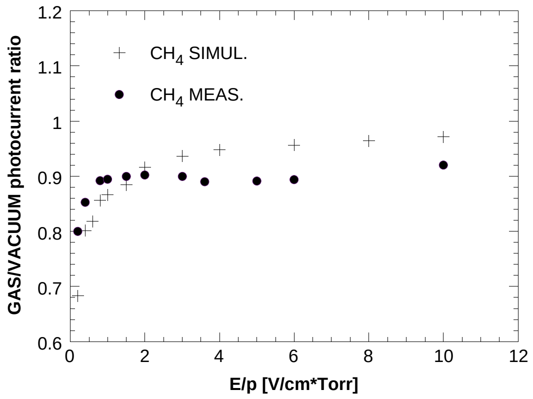

Figure 2.6: The ratio of the photocurrent from CsI, at 185 nm, in CH_4 at 800 Torr, to that in vacuum (measured at the same absolute electric field) and the simulation results as a function of E/p at the photocathode surface.

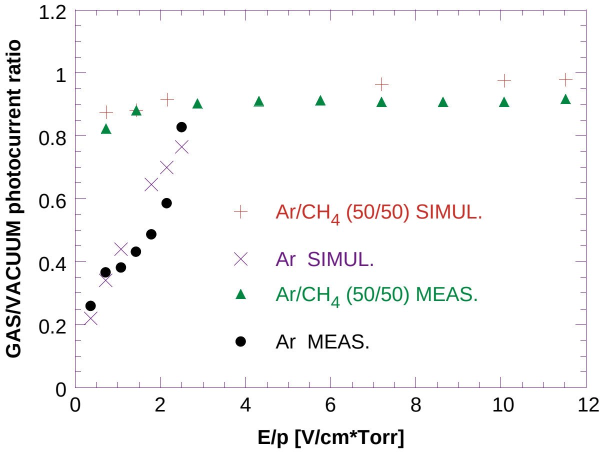

Figure 2.7: The ratio of the photocurrent from CsI, at 185 nm, in pure Ar and Ar/CH_4 (50/50) at 800 Torr, to that in vacuum (measured at the same absolute electric field) and the simulation results as a function of E/p at the photocathode surface.

Therefore the backscattering effect is particularly evident with noble gases where the lack of rotational and vibrational excitation levels makes the elastic channel the only one available at photoelectron energies below gas ionization thresholds. When the electric field at the photocathode surface reaches values high enough to start avalanche multiplication or there are polyatomic (hydrocarbon) gases, several inelastic channels become available, resulting in a suppression of the backscattering.

This study allowed us to verify the optimization of the MWPC operating conditions from the point of view of the Cherenkov photon total detection efficiency, confirming CH_4 as the best gas, since the electric field requirements for maximal photoelectron collection match well the high-voltage ranges providing a stable operation of the chamber.

2.1.1.3 Post treatment

So far, all teams involved in the processing of CsI films have followed the above evaporation procedures, considered necessary in order to produce photocathodes stable in time, but not expected to drastically change the QE performance. More controversial are the influence of the substrate and the conditioning. The conditioning, initially described by Anderson [26], consists in heating the photocathode, kept under vacuum after the evaporation to 50 – 60 °C for 4–6 hours. In addition, different configurations were tested such as flushing the vessel with CH_4 or C_2H_6 during the heating, varying the substrate temperature or the duration of the process. In Fig. 2.8, the enhancement of the QE with time is illustrated by a measurement made in the Weizmann set-up using a PCB substrate. A drastic increase in the QE was observed, mainly in the long wavelength range (> 190 nm), after heating the film to 60 °C for 5 hours compared with measurements taken just after the evaporation. In addition, the films appear to have a better stability following exposure to air after conditioning. Such an effect was systematically reproduced by Breskin on a large number of different substrates, PCB included [27].

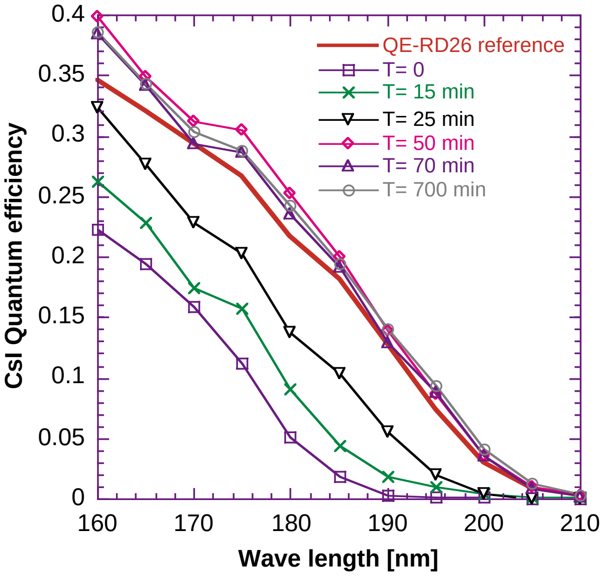

Figure 2.8: Effect of the heating of the CsI sample after evaporation at 60 °C under vacuum. From $T = 0$ (the end of evaporation), an enhancement of the QE with time is observed. Measurements made at the Weizmann Institute using a CERN PCB substrate.

Following these tests on small samples in vacuum, a post treatment was systematically applied in the production of the large PCB photocathodes aimed at equipping the RICH detector. The post treatment consisted in evaporating on the pad cathode held at 50 °C and in keeping under vacuum the fresh film at the same temperature for 6 to 12 hours. The positive influence of that treatment is illustrated later in Section 2.3.2.3 showing a substantial increase of the QE in our production of large photocathodes.

It should be mentioned that the positive influence of the post treatment was not observed by some authors [28]. A tentative explanation could be found in the fact that different substrates were used, such as aluminium, known for their peculiar surface structure usually porous and oxidized. Although several large photocathodes of high quality were later produced with a good yield, it is felt that deeper understanding of the processing should be still acquired in order to ensure a better control in the production of the 48 photocathodes needed in the HMPID system. For that purpose, an extension of the HMPID evaporation vessel has been built, described in Section 3.1.5, allowing for the evaluation of the photocathode immediatly after its processing.

2.1.1.4 Exposure to air and ageing of small samples

After having reached the nominal QE value by applying the post treatment, J. Almeida et al. [29] exposed the sample to air and measured the variation of the QE with time. In Fig. 2.9, it is seen that a short exposure to air, less than 30 minutes, does not affect the QE.

Two processes are known to damage a CsI film: the exposure to a direct photon flux and the impact of ions when used in a MWPC. We shall not discuss the first case since it necessitates photon density of 10^{11} mm^{-2} s^{-1}, far from our Cherenkov application, but we shall report on some investigations performed on the second one by Breskin et al. [7] and Krizan et al. [30].

Ageing studies of CsI photocathodes were done in a MWPC detector, having an anode plane made of 20 μm wires, with 2 mm spacing, placed 2 mm away from the cathodes and filled with pure methane. The chamber was illuminated with an Hg(Ar) lamp through air (dominant wavelength 185 nm) and the photocurrent was collected from both cathodes.

The photocathode ageing under a gas gain of 10^5, was measured by monitoring the decay of the photocurrent. The illuminated area was 100 mm^2 and the total current density was limited to 0.05 nA/mm^2, in order to avoid local space charge problems. The decay induced by photons only, measured at gain equal to 1, is of the order 20% after accumulated charge of 25 mC/mm^2. As shown in Fig. 2.10, no visible drop of QE was observed by R. Chechik et al. (private communication) up to a 2.2 mC/cm^2 accumulated charge during a UV irradiation done at a chamber gain of 10^5 in CH_4 using an aluminized stainless steel substrate.

A summary of the status of CsI ageing studies can be found in [7] (Uppsala p. 116–136). Krizan et al. [31], observed some drop of QE obtained with CsI deposited on different substrates (Sn).

As reported in Section 2.3.2.7, the rate integrated over one month of Pb operation is expected to amount at 0.15 mC/cm^2.

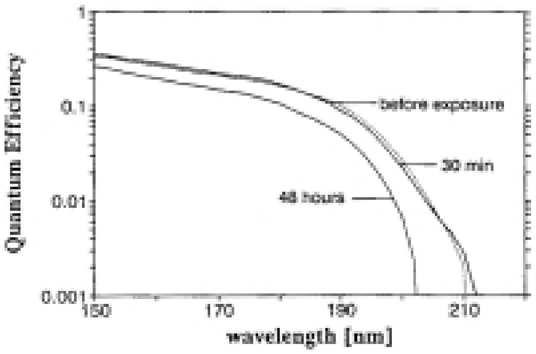

Figure 2.9: The decay of the QE of CsI layers evaporated on Ni/Au coated PCB under exposure to air at a relative humidity of 35% [29].

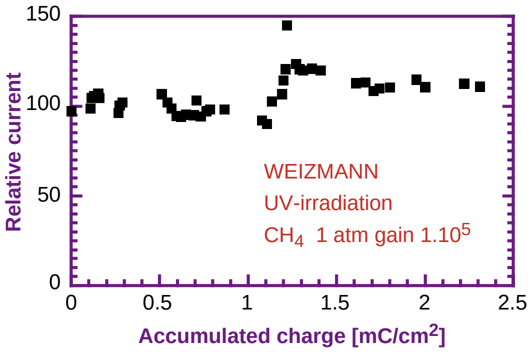

Figure 2.10: Ageing test under ion charge impact (R. Chechik et al., private communication).

2.1.1.5 Substrate and microstructural studies

Microstructural studies were undertaken in the RD-26 collaboration in an attempt to characterize CsI films by the observation of specific features using different physical probes. The aim was to correlate such features to a QE evaluation of the film and to serve as a quality control procedure. In addition, these studies are necessary in order to understand the underlying physicochemical ageing process. We shall report here only most important results. Some of these studies are still in progress thanks to a new instrument described in Section 2.1.1.6.

X-ray diffraction pattern (XRD)
The XRD probe has shown the effect of the copper substrate promoting the dissociation of the CsI [32]. In Fig. 2.11, a XRD pattern of CsI film deposited on Cu/Au is compared to the one obtained with a film deposited on a Ni/Au substrate. CsI lines are only observed on Ni/Au and are absent on Cu/Au where only some Cs lines are visible. It was also observed that the CsI film has a preferential crystallographic orientation along the $\langle 200 \rangle$ line.

CsI films were also observed under EDX and Auger probes in order to search for superficial contaminants. Carbon is found in variable thickness but essentially originating from the passage to air of the film before the measurement.

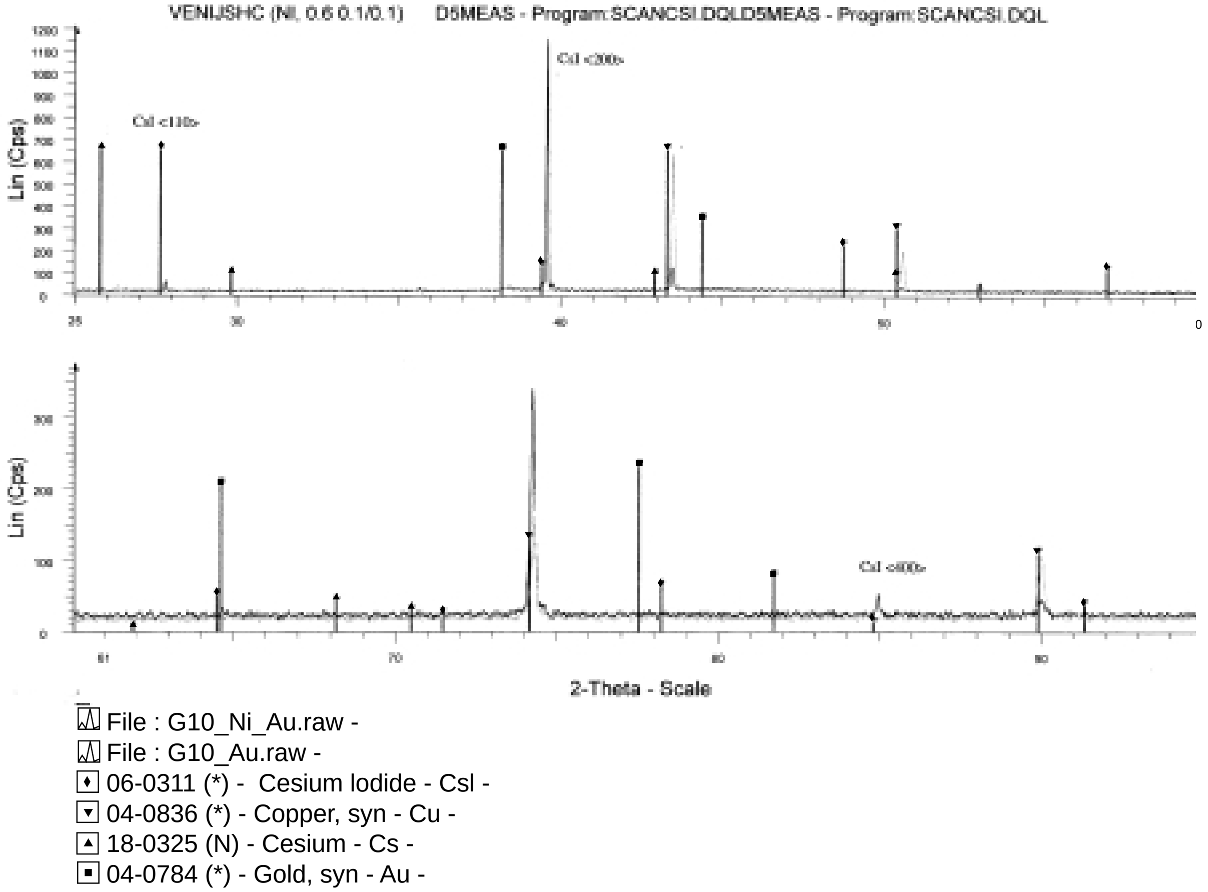

Figure 2.11: X-ray diffraction pattern of CsI coating (thickness 500 nm) on G10/Cu/Ni/Au and G10/Cu/Au substrates. The CsI peaks are visible only on the first substrate. Pronounced Cu peaks are visible on G10/Cu/Au.

Photoemission spectromicroscopy (PEEM)
These studies were performed by C. Coluzza and his team from the EPF Lausanne [17,29,33,34]. They provide an image with a high lateral resolution of the primary and secondary electron emission of an area of $80 \times 80\ \mu\mathrm{m}^2$ of the sample using different excitation sources. The ESCA-300 instrument is using a source of AlK_α X-ray photons (1486.7 eV) for the excitation of Cs3d and I3d core level. Secondary electrons of very low kinetic energies (< 10 eV) were obtained by using a VUV deuterium lamp and some measurements were performed at the ELETTRA Sincrotrone in Trieste. These studies have demonstrated that inhomogeneities are found in the Cs to I stoichiometry up to the highest lateral resolution obtained with the scanning tunelling microscope (100 nm range). A correlation has been found between the region enriched in I and a stronger secondary emission. The CsI dissociation due to copper-based substrate was also demonstrated.

Surface morphology
Surface morphologies were extensively studied using the Scanning Electron (SEM) and the Atomic Force (AFM) Microscopes. The textures of the films were analysed after varying substrate, evaporation procedure and other parameters. The growth of the film on the substrate starts from well-separated nucleation spots to reach a homogeneous coverage when the film thickness is larger than 100 nm. The process is described as a columnar growth [35] and the film surface appears as composed of grains more or less faceted. Extreme cases with macroscopic fractures and bad adhesion are observed on films evaporated on Cu substrates (Fig. 2.12a). Finding the parameters responsible for the size of the grains is a puzzling question. Is it a substrate- or an evaporation-related effect? In Fig. 2.13 one can see surface morphologies for different film thicknesses, showing the effect of the nucleation on the film coverage. CsI layers become continuous from a thickness larger than 100 nm. Only recently we have made SEM observations keeping the CsI film fully protected against air exposure from the evaporation vessel to the SEM vacuum chamber.

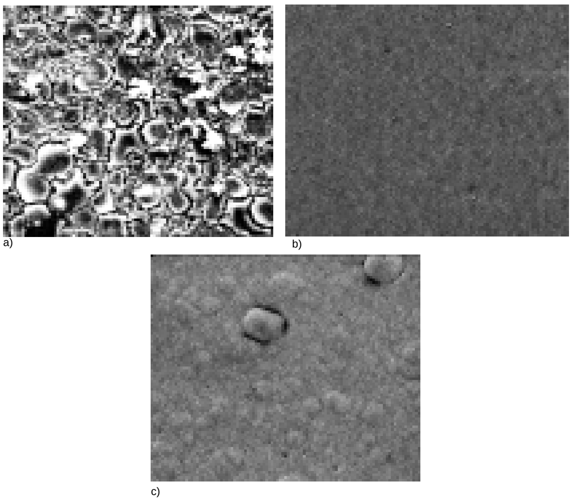

Figure 2.12: SEM images: $\times 2500$. CsI layers, 500 nm thick, deposited on various substrates: a) G10/Cu/Au, b) glass/Ni/Au, c) G10/Cu/Ni/Au.

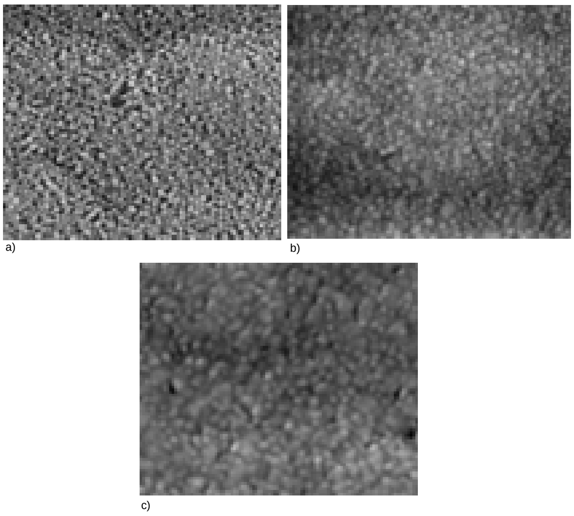

Figure 2.13: SEM images: $\times 25\ 000$. CsI layers deposited on G10/Cu/Ni/Au substrate at different thickness. a) 20 nm, b) 90 nm, c) 400 nm.

In Fig. 2.14, the texture of the non-exposed film is compared to the one observed after controlled exposures to a moist inert gas in the SEM chamber. Initially, the size of the grain is small, of the order of several hundred nanometers and increases significantly after a short exposure to moisture. The grains are also more faceted. After a longer exposure, the film becomes discontinuous and is composed of very large isolated grains.

That sequence is also shown on a thinner film, initially discontinuous, in Fig. 2.14d,e. These studies will be pursued using the experimental set-up ASSET, described in the next section, where the QE of the samples will also be measured.

In Fig. 2.15 we show a photo taken with the AFM at the Weizmann Institute. The surface profile and the lateral grain size obtained with this instrument allow the quantification of the specularity of the CsI surface and the derivation of the optical model needed to describe the reflective properties of the film (see Section 2.4). The surface roughness is found to be of the order of ±20 nm and the lateral grain size to be 200–400 nm.

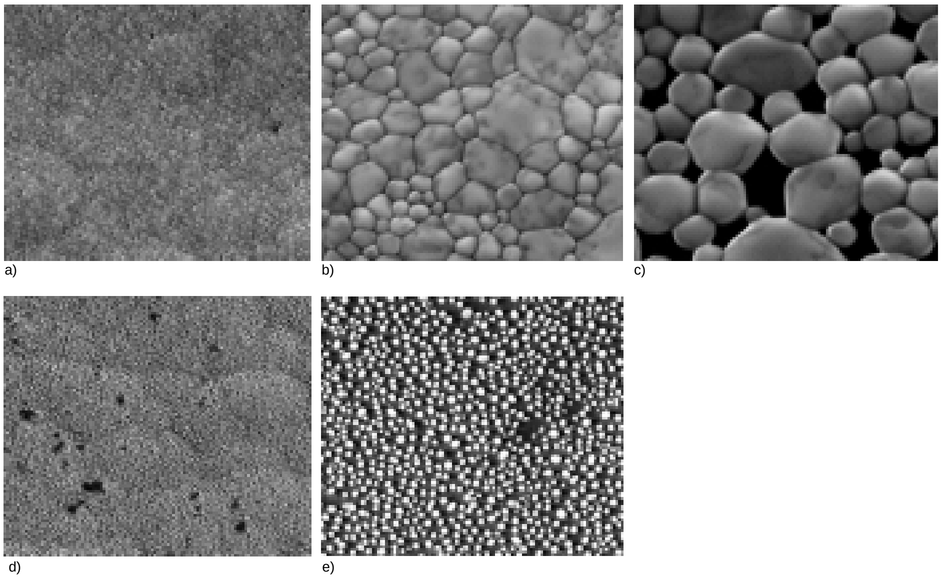

Figure 2.14: SEM images: $\times 10\ 000$. Influence on the morphology of a CsI film of an exposure to argon at a relative humidity of 80% during a time T. Substrate: G10/Cu/Ni/Au. Series a, b, c: thickness 400 nm. a) $T = 0$, b) $T = 3$ min., c) $T = 5$ min. Series d, e: thickness 20 nm. d) $T = 0$, e) $T = 1$ min.

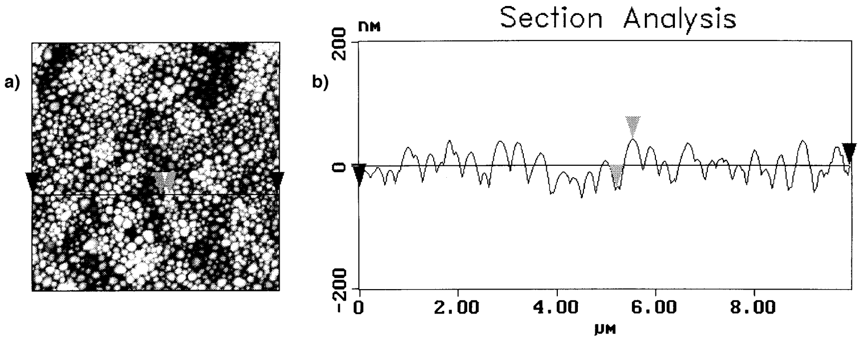

Figure 2.15: a) Atomic Force Microscope image of a CsI layer, 500 nm thick, deposited on a G10/Cu/Ni/Au substrate and b) roughness profile.

2.1.1.6 ASSET: A Small Sample Evaporation and Test facility

ASSET is a laboratory set-up to characterize small samples of CsI film (1–10 cm^2) by performing in the absence of exposure to air the sequence of operations and tests, i.e. evaporation, conditioning, QE evaluation, and storage in a container allowing clean transfer to any external measuring device, SEM, X-ray, etc. We shall be able to improve our present QE performance and possibly reach the higher values already demonstrated by several authors as best results. (See in Fig. 2.2, Seguinot et al. and also Krizan et al., Anderson et al. in Ref. [4]).

As seen in Fig. 2.16, the set-up is composed of two vessels, one used for film processing, the other for QE evaluation. They are separated by a vacuum valve to isolate one vessel from the other. An arm makes a linear transfer of the sample from one vessel to another and can also be rotated to vary the orientation of the substrate with respect to normal incidence. The angular effect on the growth of the CsI film and on the QE measured for inclined photons can thus be studied.

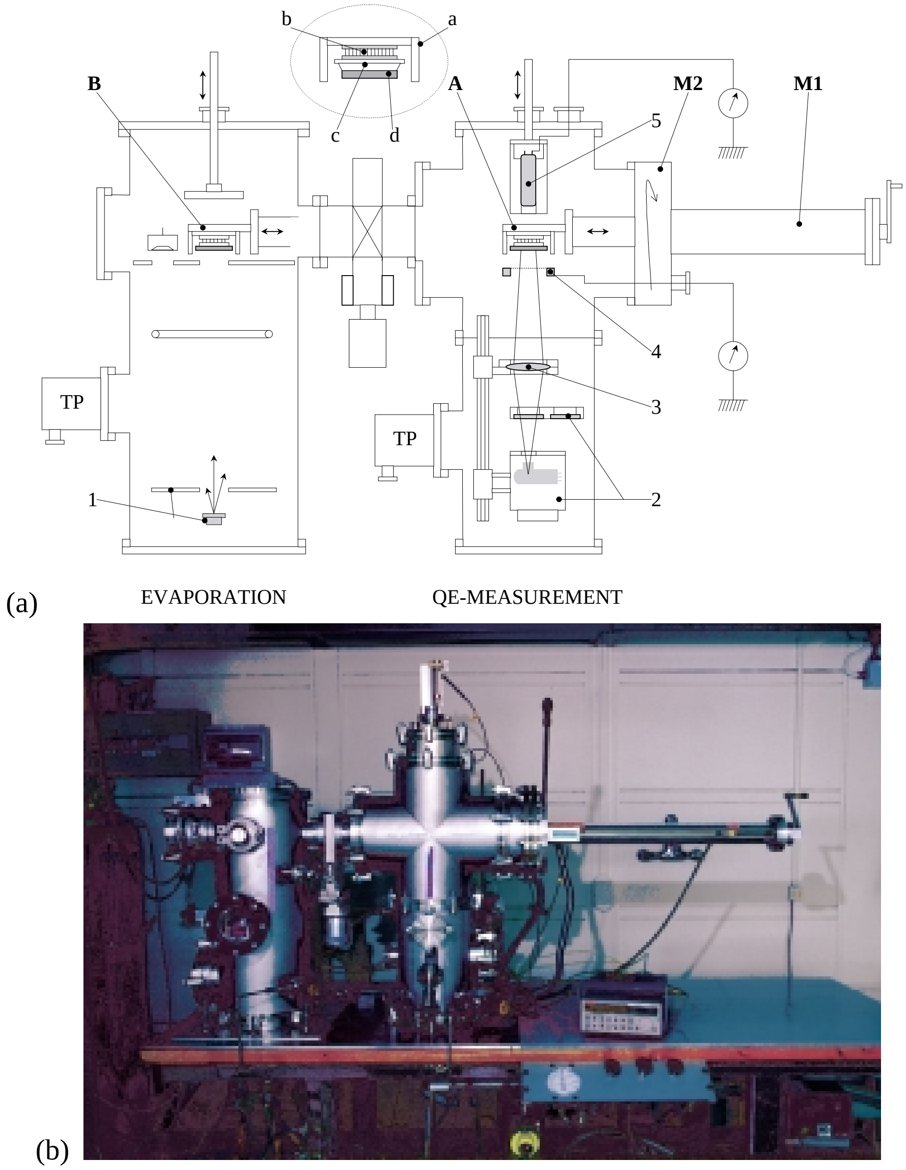

Figure 2.16: (a) Schematic of the ASSET system. The sample holder can be shifted from position B (evaporation vessel) to position A for QE measurement. M1 performs the linear transfer and M2 the sample orientation. Sample holder (seen in the expansion): a) protective box for transportation, b) Peltier elements for thermal cycle, c) insulation, d) substrate. In the evaporation vessel: 1) boat and shutter. In the QE measurement vessel: 2) UV lamp housing and interferential filter wheel; 3) CaF_2 lens; 4) photocurrent collection grid; 5) PM for photon flux calibration. (b) View of the ASSET system. The sample is coated with CsI in the evaporation vessel on the left side. Then, after operating the linear transfer arm seen on the right side, the sample is shifted from the evaporation vessel to the QE measurement vessel on the right side. The UV source is located inside and at the bottom of that vessel. One sees on the top the housing of the photomultiplier used for photon flux calibration.

Evaporation chamber
Three sources are available, supplied by independent high-current power units (12 V, 200 A, Sorensen model DCR 10-170B) to perform sequentially the evaporations of a clean substrate (Al, Au, etc.), a CsI film, and a protective coating (alkali halides). Each source has a manual shutter. A quartz crystal balance (Inficon model XTM/2) assures the monitoring of the thickness and rate of deposition of the films. The evaporation chamber is also equipped with a high-voltage glow discharge unit, to provide careful cleaning of the surfaces before evaporation by ion etching.

The linear transfer arm allows a 180 ° rotation, so that CsI can be evaporated on a tilted sample.

Test chamber
The QE of the CsI sample is obtained by measuring the photocurrent emitted by exposure to a monochromatic UV beam. The source is placed in the vacuum vessel. It is a deuterium lamp (Oriel model 63163) enclosed in a water-cooled aluminium box holding a wheel with four interference filters at 170, 180, 190 and 200 nm of ± 10 nm band width. After retracting the sample from the beam axis, the UV photon flux is evaluated by using a calibrated photomultiplier (Hamamatsu, R 1460) shifted along the beam axis and brought to the same location as the sample. The box is clamped to an optical rail that supports a diaphragm and a 50 mm $\mathrm{CaF_2}$ lens providing a collimated beam of 4 mm diameter. A Rochon prism can be inserted to provide a polarized beam. The photocurrent is collected by a grid made of 15 μm diameter golden tungsten wires 1 mm spaced and held by a second rotary arm that can move the grid assembly out of the path of the arm when the sample is transferred into the evaporation chamber. A sapphire feedthrough is used to bring the photocurrent to a Keithley picoammeter.

Our programme is to repeat and improve some of the measurements described in Section 2.1.1.2: polarization and incident angle dependences; Section 2.1.1.3: post treatment; Section 2.1.1.4: ageing; Section 2.1.1.5: micro-structures in a set-up avoiding the exposure of the CsI film to air.

2.1.2 Single-electron detection using pad cathode readout in MWPC

2.1.2.1 The photodetector: choice of the geometry of the photodetector with pad CsI cathode

Given the high multiplicity expected in the HMPID photodetectors, a 2-dimensional readout is mandatory. Therefore we have considered only MWPC having a cathode readout segmented into pads. The pads will then be the only elements to be instrumented with electronics.

The photodetector has to locate as efficiently and accurately as possible single electrons emitted by the CsI film deposited on the pad cathode. In the case of single electrons, very small signals have the highest probability of being generated owing to the expected exponential pulse-height (PH) distribution, the small avalanche size, and the loss due to the anode/cathode coupling. Increasing the chamber gain to remedy this situation, has several limitations. The main one originates from the photon feedback (pf) mechanism. Depending on the chamber gas in use, the primary avalanche isotropically emits photons, which can in turn re-emit single electrons by hitting the CsI photocathode. Their number, N_{pf}, is taken to be proportional to the total avalanche charge Q_0, that is the chamber gain G in case of a single electron, according to

$$N_{\mathrm{pf}} = K_{\mathrm{pf}} \cdot G \; . \tag{2.1}$$

Such a feedback can diverge at too high gain ($N_{\mathrm{pf}} \approx 1$) and is also responsible for a background uncorrelated to the Cherenkov candidates.

Another limitation in gain is related to ageing since the impact on the photocathode of the ion clouds produced from each avalanche is the main source of degradation of the CsI film. Discharges, initiated by charging the CsI, could possibly occur at very high local irradiation rates even though CsI is proven to be a poor insulator.

The pad signal amplitude at a given gas gain can be increased by reducing the distance anode-to-pad in order to maximize their coupling: since, in our situation, that gap should be as small as a millimetre, or less, such a choice leads to undesirable technical problems in the feasibily and stability of large chamber area. Another way to gain in signal amplitude is to operate the FE pad electronics at the largest integrating time compatible with the expected local event rates.

We adopted the latter choice since the interaction rate expected at ALICE is maximum 100 kHz when running the experiment in proton mode and a few kHz in lead mode. It will be shown that such rates allow a long enough integration time of the FE electronics, > 700 ns, to get sufficient signal induced on the pads for efficient single-electron detection by still keeping a low anode-to-cathode coupling geometry thanks to the low detection threshold of the FE electronics in use. Hence, a 2 mm distance between anode and cathode has been adopted. In Section 3.1.1 the importance of that choice to ease the chamber construction is demonstrated. However, care should be taken not to increase the gap too much since the chamber is sensitive not only to single photoelectrons but also to particles depositing an amount of primary ionization proportional to the gap thickness.

The determination of the pad size is a compromise between the localization accuracy and the number of pad channels to be instrumented. Due to the low operation rate to be met in ALICE, the use of an analog multiplexed readout electronics is possible allowing for accurate localization by using charge centroid determination.

The smaller the pad size the more accurate centroid finding can be achieved, due to a larger fraction of clustered event patterns. However, a too small pad size would affect the detection efficiency.

The choice of a pad size of 8×8 mm^2 and of an anode pitch of 4 mm is indeed a compromise between the price of the electronics and the localization accuracy.

2.1.2.2 Chamber gain

In a MWPC geometry, shown in Fig. 2.17, a single electron extracted at the abscissa x of the cathode 1 (lower), generates an avalanche of charge Q_0 concentrated, in the case of low gain and no secondary photonic effect, at a point of the sense wire defined by the angle α. In the motion of Q_0 towards the cathode 1 during a time t, the charges $q_-(t)$, $q_{+1}(t)$, $q_{+2}(t)$ are induced on the sense wire, cathode 1 (lower) and 2 (upper), respectively. According to Vávra's nomenclature [36], these quantities are referred to as 'visible gain' when measured at $t_{\rm integ}$, while Q_0 is the total gain reached when $t_{\rm integ}$ equals the total ion drift time, ($>$ 10 msec). In order to evaluate the photon feedback yield (Eq. 2.1), Q_0 must be deduced from $q_{+1}(t)$ measured at $t_{\rm integ}$.

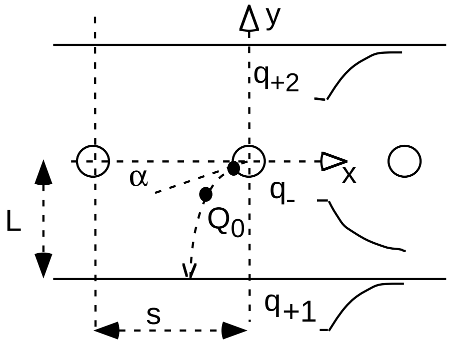

Figure 2.17: Schematics of the charges q induced by the motion of a charge Q_0 in a MWPC geometry.

For that purpose, a first correction factor for $q_-(t_{\rm integ})$ is obtained from the equation of motion of Q_0 in the MWPC field structure, assuming a known constant ion mobility. An example of such a curve is shown in Fig. 2.18 for the case of methane, indicating an increase by a factor of approximately 2 in signal amplitude between $t_{\rm integ} = 20$ and 600 ns for the same gap. Operating our FE electronics at $t_{\rm integ} \approx 1\ \mu$s, we have taken the value of $q_-(t_{\text{integ}})/Q_0$ equals 0.5. A second correction factor takes into account the fraction, q_{+1}/q_- of the charge induced on the pad cathode. When the gap is small, this factor depends on the angle α, that is on the location of the electron emission. Arnold et al. [37] have measured a 15% variation for a 0.67 mm gap, which is the order of magnitude of the error expected when determining Q_0 by measuring $q_{+1}(t)$ without knowing the location of emission. However, the spatial extension of Q_0, assumed to be punctual in the calculation, should reduce the spread of $q_{+1}(t)/Q_0$.

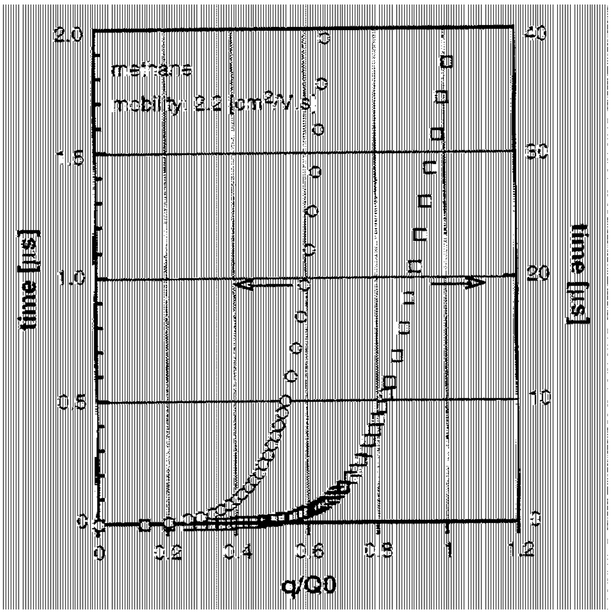

Figure 2.18: Time dependence of the ratio of the charge q induced at the anode wire to the total charge Q_0 moving towards the cathode calculated in methane in a 2 mm gap MWPC geometry. The plot on the right indicates that Q_0 is fully collected in about 40 μs; the one on the left, that after 1 μs, 60% of the Q_0 value is induced at the anode wire.

2.1.2.3 Charge distribution on the pad cathode and avalanche position evaluation

The evaluation of the distribution of the induced charge on the cathode plane is an electrostatic problem which can be solved by considering the signal induced on the electrodes by a positive point charge as a function of spatial coordinates. For a given MWPC geometry, different models provide the parametrization of the geometrical spread of induction [38–41]. In particular, that of Gatti [38] describes the distribution of the induced charges along the anode wires taking into account the signal finite sampling related to the cathode strip segmentation, the capacitive coupling among strips, and the amplifier white noise. In that model the fraction $\Gamma(\lambda)$ of the total charge at a given normalized coordinate $\lambda = x/D$ in the sense wire direction (where D is the anode-cathode gap), is:

$$\Gamma(\lambda) = K_1 \frac{1 - \tanh^2(K_2\lambda)}{1 + K_3 \tanh^2(K_2\lambda)} , \tag{2.2}$$

where K_1, K_2, K_3 are parameters depending on the chamber geometry.

Mathieson et al. [42] have demonstrated that, in a chamber with symmetric gap, the charge distribution may be considered approximately symmetrical in the two directions, perpendicular and parallel to the wires, and that $\Gamma(\lambda)$ may be conveniently described in terms of K_3 only, the three parameters being related by the following relations:

$$K_2 = \frac{\pi}{2}(1 - \frac{1}{2}\sqrt{K_3}) , \tag{2.3}$$

$$K_1 = \frac{K_2\sqrt{K_3}}{4\arctan(\sqrt{K_3})} \; . \tag{2.4}$$

The free parameter K_3 may vary between 0 and 1 depending on the wire diameter and on the ratio of D and the wire pitch [43]. Figure 2.19a shows the induction shape obtained with $K_3 = 0.68$, corresponding to the proto-2 geometry.

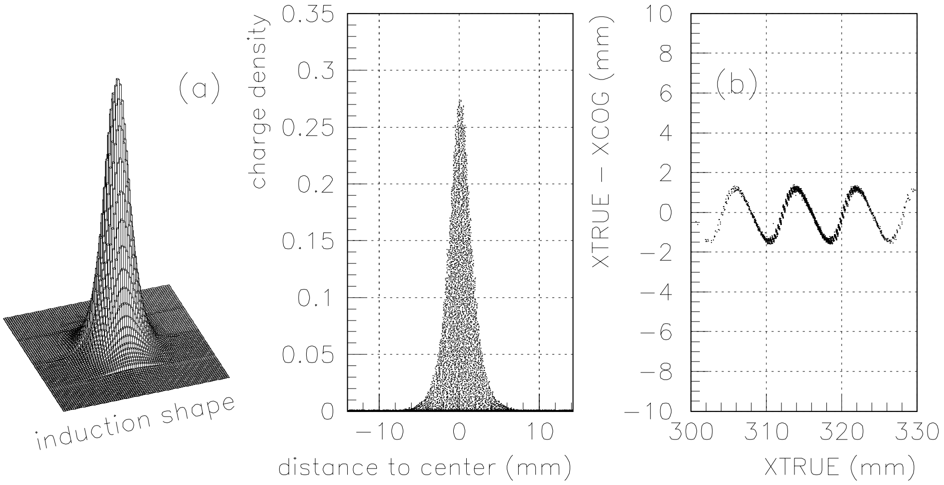

Figure 2.19: (a) Two-dimensional shape (left) and projection in one direction (right) of the charge distribution on the pad cathode. (b) Non linearity in the residuals distribution as a function of the true particle impact on 8 mm pads (the edges of the central pad are positioned at 312 and 320 mm).

Depending on the total charge developed in the avalanche (and on the pad size), in some fraction of the events the signal will be shared on more pads. In that case the average position of the avalanche, in the direction parallel to the wires, can be estimated with the centre of gravity (or *centroid*) of the charge distribution:

$$x_\mathrm{c} = \frac{\sum_i (Q_i - B)x_i}{\sum_i (Q_i - B)} \tag{2.5}$$

for $Q_i > B$, where x_i and Q_i are, respectively, the cluster i-th pad x coordinate and measured charge; $B = b\sum_i Q_i$ is a threshold level allowing the influence of electronic noise to be reduced. The value of b has to be determined empirically so as to eliminate the contributions from small pulse-height channels, where the noise signal can be predominant, but also to avoid loss of information, if b is too high. With accurate studies, Piuz et al. [44] have pointed out that the influence of the parameter b on the evaluation of the localization accuracy has a periodic dependence on the avalanche position, with period equal to the pad width. In particular, the largest error corresponds to positions at 1/4 or 3/4 of the pad, while the maximal accuracy is obtained when the avalanche is in the middle of the pad or at the edge between two pads (Fig. 2.19b). A value of $b = 0.015$ seems to be a reasonable compromise to achieve better localization. The y_c coordinate, perpendicular to the anode wires, is discrete since it corresponds to the position of the wire on which the avalanche has developed, a position that can be deduced from the cluster shape and the induced signal distribution.

2.1.2.4 Detector response to single electron

Modelling

The shape of the pulse-height distribution obtained from Single-Electron Pulse-Height Detection (SE-PHD) is usually found to be purely exponential at low gas amplification whatever the gas mixture, obeying the Furry distribution:

$$P(A) = \frac{1}{A_0} \cdot \exp - \left(\frac{A}{A_0} \right) , \tag{2.6}$$

where A and A_0 are the current and the average pulse heights, respectively. If A_{th} is the detection threshold of the FE electronics, the single-electron detection efficiency is simply given by:

$$\epsilon_{\mathrm{det}} = \exp - \left(\frac{A_{\mathrm{th}}}{A_0} \right) . \tag{2.7}$$

The knowledge of that distribution is essential for further simulation of the detector behaviour. The mean value of the SE-PHD has been taken as the parameter characterizing the photodetector response all along our tests. In the following, these quantities are expressed in ADC channel units, easily converted into charge unit (fC) by means of an electronics calibration.

The departure from the exponential Furry shape indicates that a fraction of the avalanches originate from more than one single electron. The mechanisms responsible are discussed in the next section. In that case, a more general pulse-height generator to fit the experimental distributions is a normalized Polya distribution [45] characterized by two parameters, A_0 and θ, according to

$$P(A) = \frac{1+\theta}{A_0 \cdot \Gamma(1+\theta)} \cdot [\frac{A}{A_0}(1+\theta)]^{\theta} \cdot \exp -[\frac{A}{A_0}(1+\theta)] \qquad \text{with} \qquad 0 < \theta < 1 \, . \tag{2.8}$$

or

$$P(A) = \frac{(1+\theta)^2}{A_0 \cdot \Gamma(1+\theta)} \cdot [\frac{A}{A_0}(1+\theta)]^{\theta} \cdot \exp -[\frac{A}{A_0}(1+\theta)] \qquad \text{with} \qquad -1 < \theta < 0 \, . \tag{2.9}$$

In the case of $0 < \theta < 1$, $(1+\theta)$ is the averaged number of primary electrons per avalanche. In the case of low amplification, the Polya distribution turns to a simple exponential distribution (Furry law).

These distributions are represented in Fig 2.20.

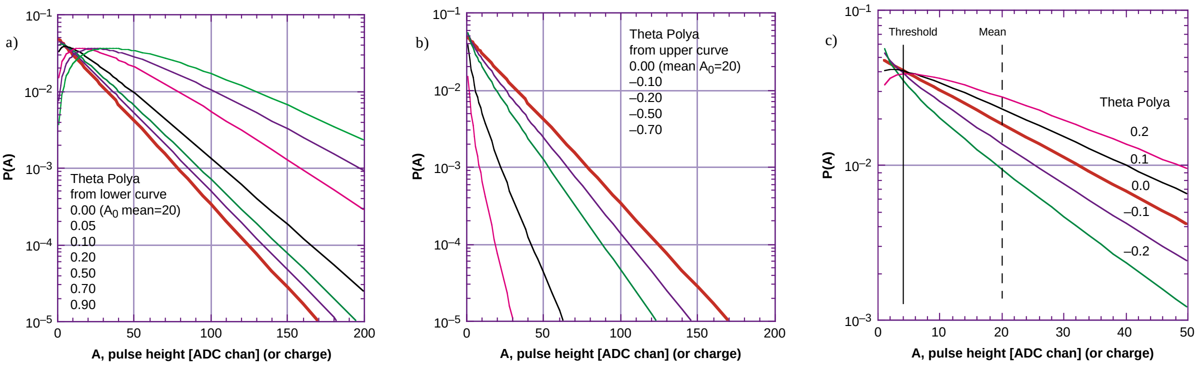

Figure 2.20: Representations of Polya distributions calculated from formulas Eqs. 2.8 and 2.9 with the mean single-electron pulse-height, $A_0 = 20$ ADC channels. In (a) and (b), positive and negative θ values are taken, respectively. (c) indicates the parts of the spectra experimentally recorded when applying a threshold cut at 4 ADC chan. At values $-0.2 \leq \theta \leq 0.2$ we observe mainly a change in the slope of the exponential.

Examples of measured SE-PHD

In standard operation of wire chambers (no CsI cathode), secondary electrons are generated from the conversion in the chamber gas of photons emitted by de-excitation processes from the primary avalanche. These secondary-emission photon mechanisms are quite complex depending on the gain and the gaseous species involved. In practice, while increasing the chamber gain, the exponential Furry distribution is modified into a Polya distribution having θ value either positive or negative.

Mixtures exclusively composed of hydrocarbon gases (CH_4, C_2H_6, iC_4H_{10}) lead to a concave shape, associated with a positive θ value. Noble gases are generally emitting energetic photons, usually absorbed by the admixture of a 'quenching' component, typically a hydrocarbon gas. It is observed that a convex shape characterizes poor quenching property, typical of noble-gas-based mixtures (argon, helium), associated with a negative θ value [36].

In addition to the gaseous generation from the primary avalanche in poorly-quenched mixtures, secondary electrons are also produced by feedback photons when CsI coated cathodes are used. In the case of CH_4, photons are emitted from excited carbon atoms according to three lines at 156, 166, 193 nm in the ratio 30, 57, 13 [46]. In absence of quenching admixture, CH_4 is transparent to these photon energies leading to a photon feedback yield of $N_{\mathrm{pf}} = 7.7 \times 10^{-6} \times G$ [47], where G is the gain of the primary avalanche (Eq. 2.1). Therefore, the Polya model cannot be applied as described above since θ is not anymore a constant but a function of the individual avalanche gain i.e. of the induced pulse height: the higher the individual amplification, the more feedback photons produced.

This is illustrated in Fig. 2.21 by SE-PHDs measured in different gas mixtures with CsI-coated cathodes. Standard Polya fits are applied to the spectra providing A_0 and θ values. The Furry curve of mean A_0 are superimposed on the measured spectra. Contrary to what is seen in Fig. 2.20, in case of negative θ, high PHs are found in excess to the Furry curve with a poorly quenched mixture. In turn, using the less transparent iC_4H_{10} cuts off two of the three carbon lines (see transmission curve in Section 2.1.3) and the SE-PHD (Fig. 2.21d) has a positive θ but shows a lack of high PHs with respect to the Furry curve, illustrating its known 'quenching' ability.

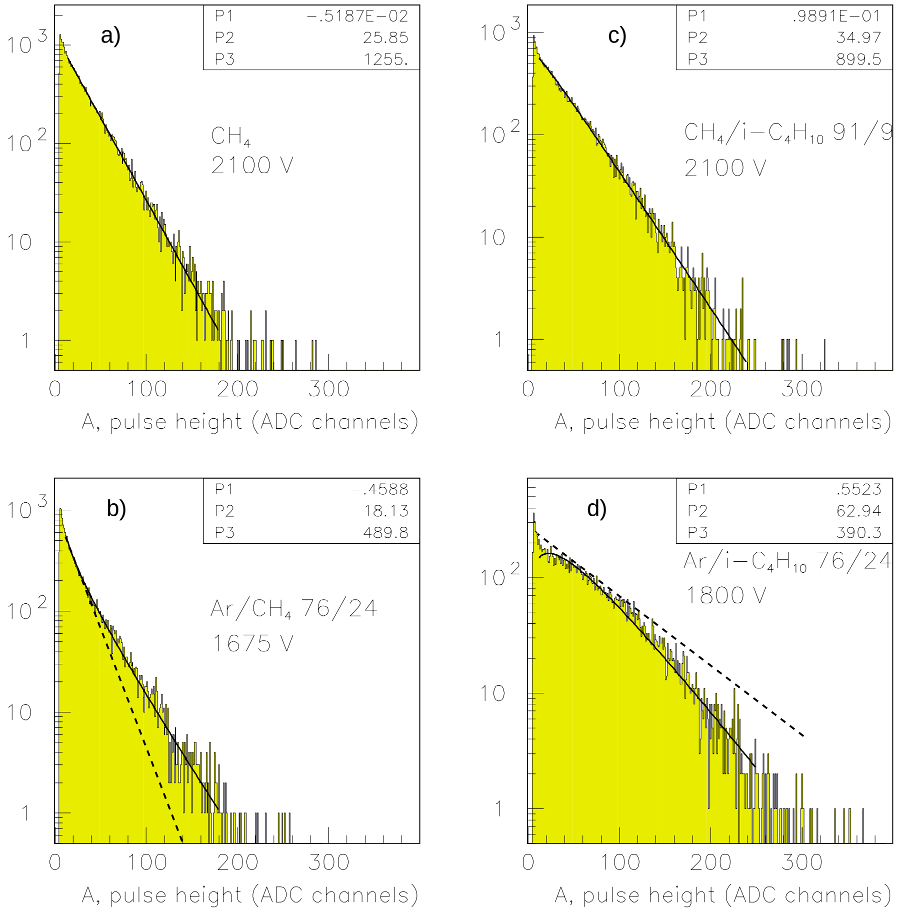

Figure 2.21: Single-electron pulse-height in different gas mixtures. A fit with the Polya distribution function is shown, with parameters P1: θ and P2: A_0. In b) and d) hatched lines are the Furry curves with mean A_0.

In our experimental geometry and at a maximum gain of 5×10^5, the yield of photoelectrons in CH_4 is expected to be 0.3 – 0.4 per avalanche, assuming QE between 0.2 and 0.3 and a the solid angle for electron emission of about 1.5 π srad.

2.1.2.5 Evaluation of the photon feedback yield

A method for evaluating the photon feedback yield in any gas mixture has been developed [48] and currently applied to check the critical parameter $K_{\mathrm{pf}} = 7.7 \times 10^{-6}$ proposed by Arnold et al. [47] for hydrocarbon mixtures.

For this purpose, a pad cathode was half-covered with CsI and photoelectrons were extracted using a well-collimated UV source (deuterium lamp) from two spots, distant by about 10 cm, one coated with CsI and the other one not coated, in order to compare the resulting SE-PHDs. The two spots are located along the same sense wire, used as a trigger for the pad electronics in both cases. Measurements, shown in Fig. 2.22, were obtained using a MWPC with a pad size of 8×8 mm^2, 2 mm anode to cathode distance, 4 mm anode pitch and CH_4, iC_4H_{10}/CH_4, Ar/CH_4 as gas mixtures. The SE-PHDs measured at the two spots at different voltages were fitted to Polya distributions providing the θ values plotted in Fig. 2.23a. Indeed, the adjunction of CsI results in making the θ values more negative than the one obtained with bare cathodes. To simulate these measurements, by varying K_{pf}, a proportion of photon feedback photons is added to a primary SE-PHD obtained from the fit of the no-CsI SE-PHDs until the θ value measured at the CsI spot is reproduced. Figure 2.23b shows the simulated θ values obtained for different K_{pf} values. A reasonable agreement with the measurements is obtained for a K_{pf} value of 7×10^{-6}, close to the one quoted in [47].

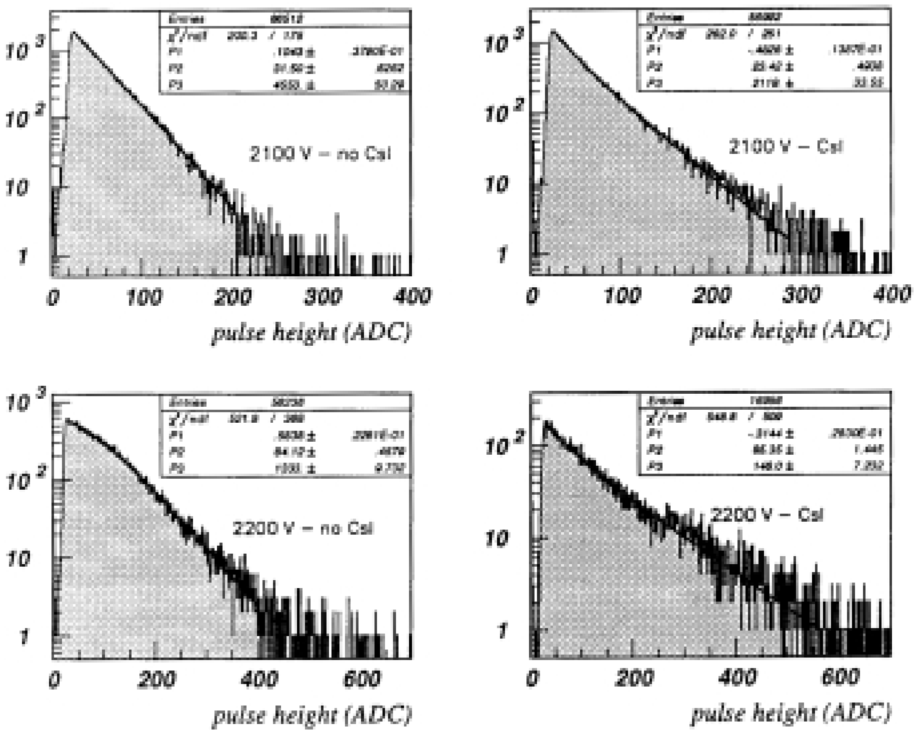

Figure 2.22: PH spectra of single electrons emitted from a cathode spot surrounded (right column) or not (left column) by a CsI coating, measured at two chamber gains in CH_4. The constant θ and A_0 of the Polya fit are the values P1 and P2 , respectively.

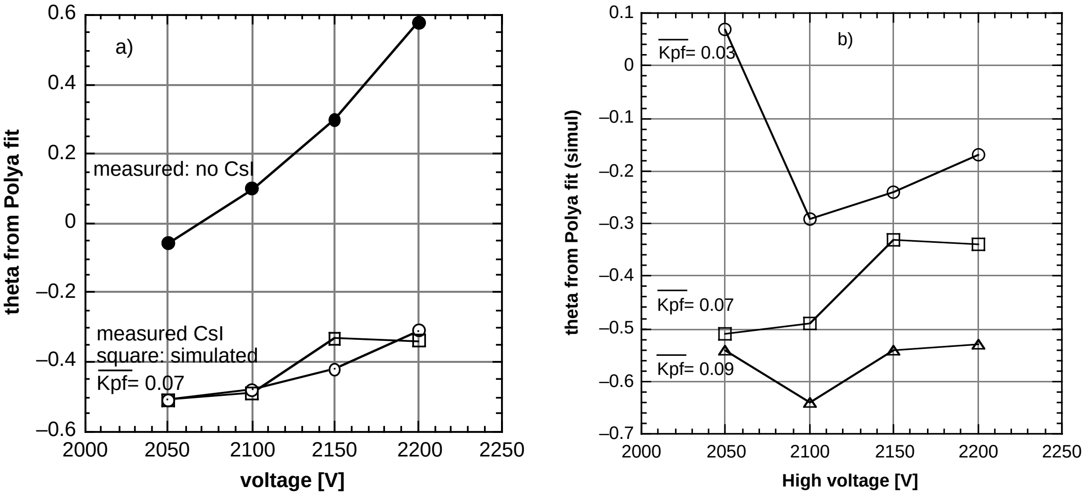

Figure 2.23: a) Having simulated SE-PHDs at different values of the feed back constanf $K_{\rm pf}$ and made the Polya fits, the corresponding θ values are plotted as a function of the chamber gain. b) Plot of the θ values obtained from spectra measured at the two spots (CsI and no-CsI). For the presented set of CsI data the best fit is obtained with $\overline{K_{\rm pf}} = 0.07$. In these plots, $\overline{K_{\rm pf}}$ is expressed in experimental charge unit (ADC channel). This value corresponds to $K_{\rm pf} = 7 \times 10^{-6}$.

In conclusion, the Polya distributions are used as convenient analytical tools only for the purpose of fitting SE-PHDs, without attributing its usual physical meaning to the θ constant. For simulation purposes, a Monte Carlo generation is used, based on the feedback constant, $K_{\rm pf} = 7.7 \times 10^{-6}$ and a Furry curve with mean A_0.

However, for a pure methane, the Polya curve corresponding to small θ values, (0.1 − 0.2), still shows a quasi-exponential behaviour but of a different slope than the Furry curve, as seen in Fig. 2.20c. In addition, the tiny maximum expected at very low PH is usually masked by the applied threshold making it hardly visible in the SE-PHD.

2.1.3 Measurements of basic physical RICH parameters

Besides the CsI photodetector, the Cherenkov radiator medium is the other major element constituting the CsI RICH. Given the momentum range under study at ALICE, 1 to 5 GeV/c, only a liquid radiator could be considered. Liquid C_6F_{14} was selected for the achievable Cherenkov angular resolution, tolerable technical constraints, and affordable cost. In addition, its UV transparency threshold, at about 165 nm, presents an acceptable match to the CsI QE curve (Fig. 2.24a,d).

The main physical properties of C_6F_{14} are reported in Section 3.1.3.2. The remaining components, the chamber gas and the window containing the liquid, should have UV transparencies at least comparable to the that of the liquid C_6F_{14}. Pure CH_4 satisfies such requirement while iC_4H_{10}, if not pure enough, or contaminated by water vapour and oxygen, might reduce the transparency range (Fig. 2.24c,d). The purity control of the chamber gas aims to guarantee that the fractions of O_2 and H_2O are kept at the lowest level also in order to minimize the contamination of the CsI photocathode. High-quality primary gases are used (class 38 to 45). The impurity checks are performed with commercial instruments from Hermann-Moritz for O_2 and Shaw for H_2O. In the case of C_6F_{14} or iC_4H_{10}, the achievement of optimum transparency necessitates active filtering; in particular the options for the C_6F_{14} purification system will be described in Section 3.1.3.4.

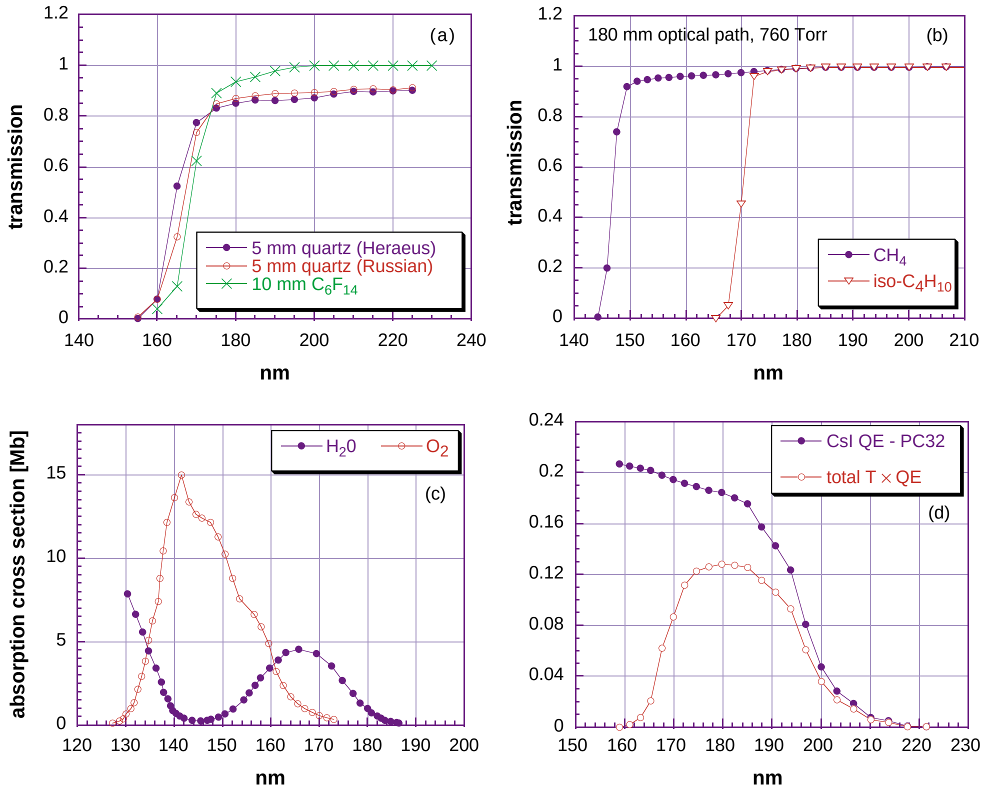

Figure 2.24: (a) Measured UV transmission of 10 mm C_6F_{14} and 5 mm quartz plates (not corrected for reflection losses). (b) UV transmission of CH_4 and iC_4H_{10}, calculated from [49] and [50] respectively, for a photon path of 180 mm equivalent to a distance travelled in a proximity gap of 103 mm by Cherenkov photons emitted in C_6F_{14} by $\beta = 1$ particles. (c) UV absorption cross section of oxygen [51] and water [52]. (d) PC32 QE evaluated from simulation (Section 2.4.2) and the convolution with the total media transmission.

The window of the radiator vessel containing the liquid C_6F_{14} raises some problems since the final area of the container will be half a square metre. High-quality synthetic quartz, such as a Suprasil-Standard UV Grade from Heraeus, has an acceptable transparency, considering the C_6F_{14} cut-off, and, in addition, it can be delivered with the necessary polishing in plates of size 45×45 cm^2, 5 mm thick. Figure 2.24a shows the UV transmission of quartz samples, from Heraeus and St Petersburg Optical Institute. The C_6F_{14} and quartz transparencies were measured at CERN using a dedicated set-up put at our disposal by A. Braem, CERN.

The quartz window refractive index has been measured by the supplier Heraeus and fits with the following parametrization, which can be found also in Ref. [52]:

$$n_{\mathrm{qz}}^2(E) - 1 = \frac{F_1}{E_1^2 - E^2} + \frac{F_2}{E_2^2 - E^2} \ , \tag{2.10}$$

where E_1 = 10.666 eV, E_2 = 18.125 eV, F_1 = 46.411 eV^{-2} and F_2 = 228.71 eV^{-2} .

2.1.3.1 C_6F_{14} refractive index

The radiator refractive index and its dispersion are basic parameters for the Cherenkov angle reconstruction and the evaluation of the achievable angular resolution. The radiator refractive index is related to its physical properties by the Lorentz–Lorenz equation [52]:

$$\frac{n^2 - 1}{n^2 + 2} = \alpha f(E) \ ; \tag{2.11}$$

$f(E)$ is the molar refractivity (in terms of the energy E) and $\alpha = 0.3738\rho/M$ where ρ is the density (in g·cm^{-3}) and M is the molecular mass.

In the far-UV range, 150–200 nm, only a few measurements are available (Fig. 2.25) [52, 53]. The oldest measurement, from J. Seguinot and T. Ypsilantis, was limited to the range 195–250 nm; in Fig. 2.25 an extrapolation up to 160 nm is shown, according to the relation used to fit the experimental data, which has a linear behaviour with energy:

$$n(E) = a + b \cdot E \, , \tag{2.12}$$

with $a = 1.2177$ and $b = 0.00928$ eV^{-1}. Such a curve does not reproduce our beam-test data: at the average wavelength of detected Cherenkov photons of 181 nm the index is 1.28127, a value corresponding to an average ring radius of 144.5 mm (for $\beta = 1$ particles and a proximity gap of 103 mm), instead of the observed 156 mm (Fig. 2.34k). The value needed to obtain the right ring radius (and to reconstruct correctly the Cherenkov angle), at the average detected wavelength, is $n = 1.2948$. The index dispersion was adjusted in order to get, in simulated events, the correct spread of the ring radius and the reconstructed Cherenkov angle distributions (Section 2.3.2.5). Indeed a and b have been estimated with a trial and error method, taking into account all the tunable parameters (namely the photon feedback and the CsI quantum efficiency); the estimated values giving the best fit to data are: $a = 1.177$ and $b = 0.0172$ eV^{-1}. The corresponding curve is shown in Fig. 2.25, where also the recent DELPHI measurements at 27.5 °C are reported (data published by courtesy of E. Fokitis, S. Maltezos and P.G. Moyssides [53]).

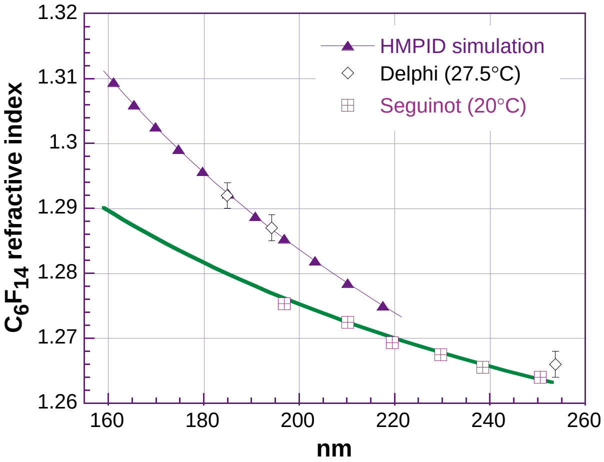

Figure 2.25: The C_6F_{14} refractive index. The Seguinot [52] and DELPHI [53] values come from measurements, while the HMPID curve has been used in a Monte Carlo simulation to reproduce RICH beam-test data. The fit to the Seguinot data with: $n = 1.2177 + 0.00928 \cdot E$ (eV) is also shown.

Even taking into account the correction for the different temperatures to which the two sets of data refer (Eq. 2.11), their agreement is still good. Indeed the experimental error quoted for the DELPHI index corresponds to an uncertainty of about 4 °C, using a coefficient dn/d$T = -5 \times 10^{-4}$ °C^{-1} given by the supplier. On the other hand the system monitoring the temperature at the experimental radiator vessel inlet and outlet has indicated a gradient of ~ 2.5 °C at an ambient temperature, measured at the inlet, of 22.5 °C (the heating is very probably due to the front-end electronics dissipating about 100 Wm^{-2}).

Another factor that could play an important role is the purity of the liquid (Section 3.1.3.2).

These remarks prompted the construction of a dedicated monitoring apparatus to measure the C_6F_{14} refractive index that will be part of the ALICE C_6F_{14} circulation system. That device is under development and will be available in 1999.

2.2 Overview of the CsI-RICH prototypes and modules

The first constraint for the HMPID module layout is that its full size is reached by particles with incident angle in the range $\pm 10^\circ$, taking into account the overall tilt of the modules, as shown in Chapter 1, Fig. 1.1 on page 2. Given the distance to the vertex, a 1.33×1.28 m^2 sensitive area fulfils that requirement.

A second constraint is given by the size of our present CsI evaporation station that allows for handling substrates of a maximum area of about 60×60 cm^2 to minimize the investment on that device. Since no severe requirement is imposed on the detector dead zone, the whole CsI photocathode area has been partitioned into panels of size 60×40 cm^2 as shown in Fig. 2.26.

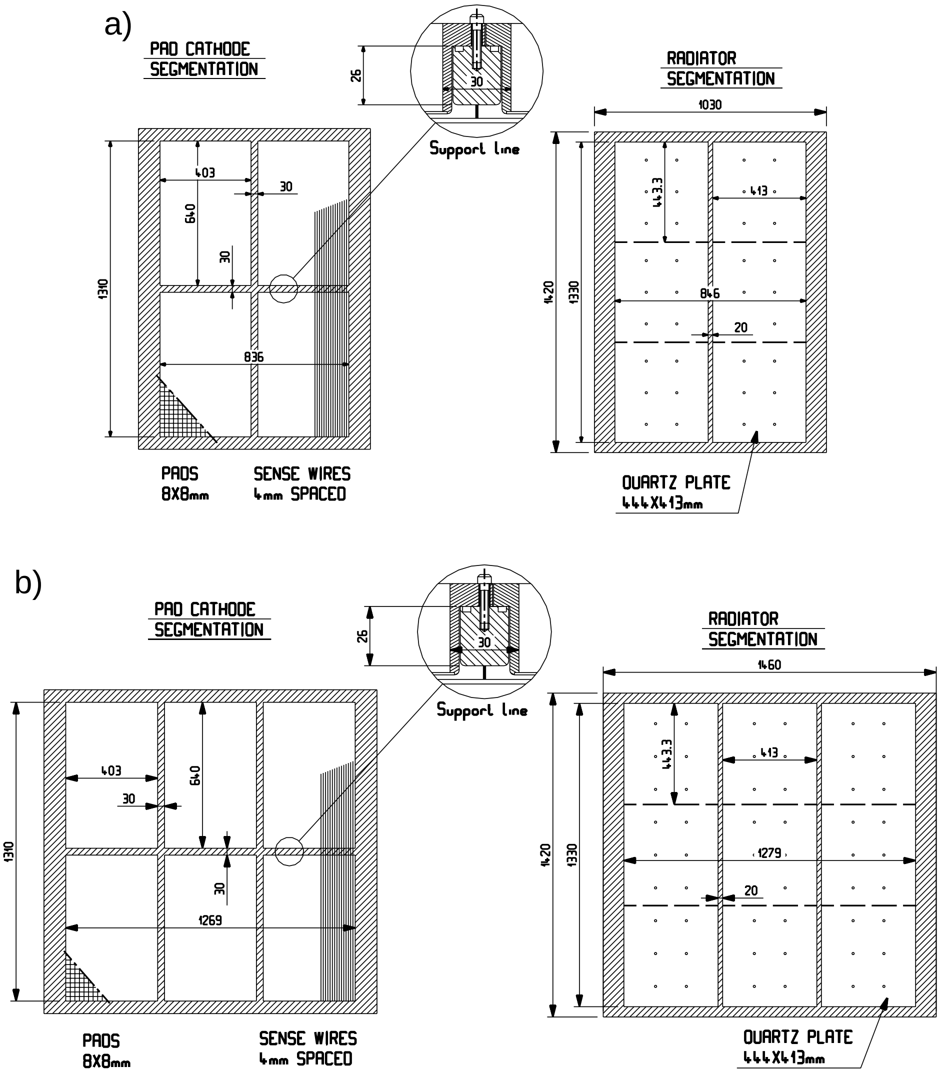

Figure 2.26: Schematic layout of proto-2 (a) showing the CsI pad panel and radiator trays segmentations. Proto-2 corresponds to 2/3 of a full size HMPID module which is shown in (b). The dead zones represented by the crossing rods correspond to 5% of the total area.

A third constraint is that the pad panel has to be easily detachable from the detector in order to perform the processing of the CsI film followed by several mounting and dismounting operations. Therefore, one has to make it as an independent element with flatness and stiffness such that the chamber gap is not affected by these operations.

The choice of a 2 mm anode-to-cathode gap satisfies the previous requirement. In fact, a ± 40 μm tolerance, i.e. $\pm 2\%$ of the gap, in the machining of the frame and the flatness of the panel is sufficient to guarantee a uniform behaviour of the chamber. Such mechanical specifications are still practicable with simple and affordable technologies. Also, the diameter of anode wires can be kept at $20\ \mu$m to simplify the weaving and ensure the stability of the anode plane. The dead zones hence created to hold the CsI pad panels ease in turn the segmentation of the radiator array, made out of three independent trays overlapping the sensitive pad areas.

During the development phase (RD-26), three early small prototypes were built in order to define the wire chamber geometry and the associated FE electronics [54–56]. They were used to evaluate our first CsI photocathodes of 26×10 cm^2 area [57]. Subsequently, two large prototypes were assembled, referred to as proto-1 and proto-2 (see Fig. 2.27).

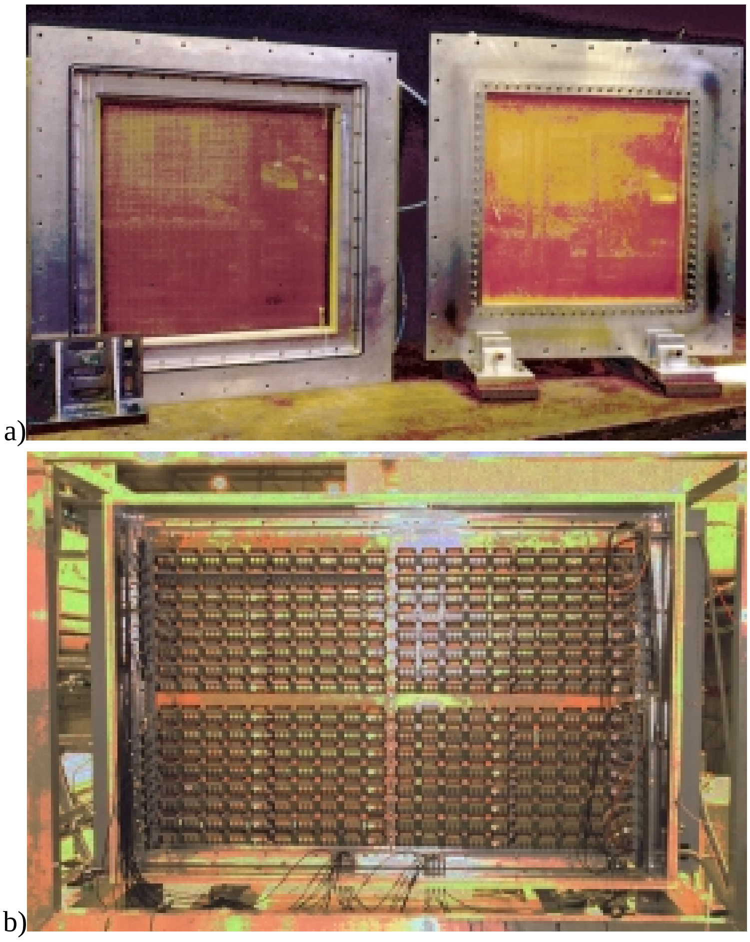

Figure 2.27: a) View of proto-1. On the left side, one sees the photodetector with a pad panel of 56×60 pads and on the right side the radiator vessel enclosed by a quartz plate of 440×460 mm^2. b) Proto-2 viewed from the pad panel side. The four independent pad panels instrumented with GASSIPLEX chips can be distinguished.

With proto-1, pad CsI-photocathodes of size up to 50×50 cm^2 were studied at the test beam using small C_6F_{14} or NaF radiators convenient for single-particle tests. Proto-2 is already a part of a final HMPID module, (two-thirds of the full size). All the essential elements, the anode length, pad CsI-photocathodes (64×38.4 cm^2), FE electronics and radiator trays (133×41.3 cm^2) are implemented in their final version. Proto-2 was tested under single and multiparticle irradiation. All the papers published in the HMPID group during the R&D phase, related to beam-test results or system descriptions, are found under references [58–64]. The detailed description of proto-2 and its equipment is found in Section 3.1 since there were no major conceptual differences between proto-1 and proto-2 except the area.

Table 2.1 summarizes the main geometrical parameters and equipment of the differents prototypes tested during our R&D period. For all of them, the pad size was of 8×8 mm^2 and the anode pitch of 4 mm.

Table 2.1: Main geometrical parameters of the CsI RICH prototypes

Proto	gap (mm)	CsI PC size (pad)	No. FEE channels	CsI PC size (cm^2)	Radiator medium	Radiator area (cm^2)
Small-1	var.	24×12	288	19.2×9.6	NaF	20
Small-2	2	32×12	384	25.6×9.6	NaF, C_6F_{14}	20
Proto-1	2	40×36	1 440	32.0×28.8	NaF, C_6F_{14}	20
		60×56	3 360	48.0×44.8		
Proto-2	2	80×48	15 360	64.0×38.4	C_6F_{14}	6×20
		(4 times)		(4 times)		5500
						2×5500

2.3 CsI RICH performance

2.3.1 Test beam facilities and test layouts

All our CsI RICH tests were carried out at two test beam facilities: T11 at the East Hall and H4 at the SPS, North Area.

2.3.1.1 T11 test set-up: proto-1, partial proto-2

At T11, the slow PS-extraction on a target provides a secondary beam composed of mixtures of protons/pions using positive magnet polarities or pions/electrons with the other polarity. The available momentum ranges from 1.0 to 3.5 GeV/c with a $\Delta p/p$ of 1%, the duration of the burst is 300 ms.

Figure 2.28 shows our set-up. Two crossed plastic scintillator doublets (PM1,2–PM3,4), 2 m apart define our trigger geometry covering an area of 1 cm^2 of the detector with a beam divergence ≤ 1 mrad. The beam rate was set to 10 kHz/cm^2. A Time-of-Flight (ToF) array composed of two scintillators, 10 m apart , was used to identify pions from protons present in the beam (Fig. 2.29).

The six-fold coincidence of these scintillators defines the physics trigger signal and the ToF identification used at the software level. The CsI RICH is placed on a table allowing for X/Y translation and vertical rotation. The anode wires are horizontal in the set-up.

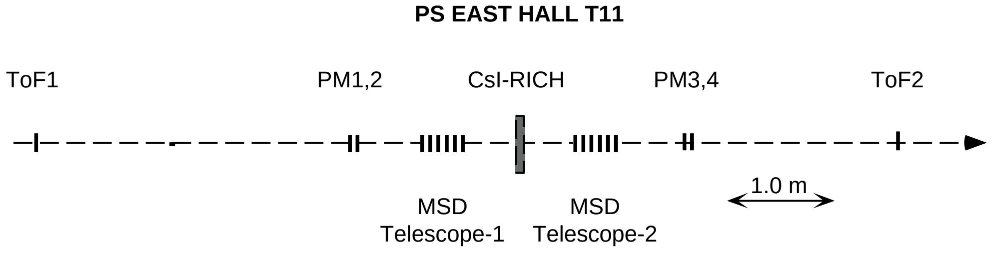

Figure 2.28: Experimental layout used at the PS/T11 test beam.

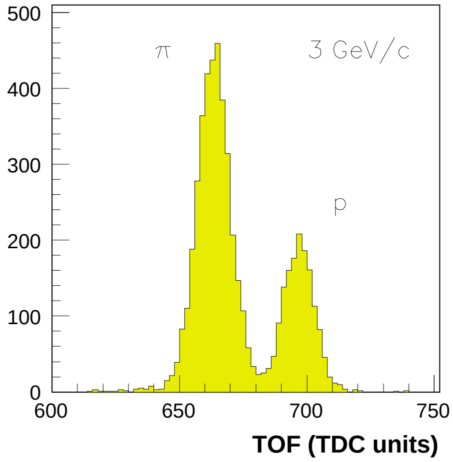

Figure 2.29: Time-of-flight spectrum obtained at the PS/T11 test beam (pi /proton).

In order to study the pad response, the detector was interleaved between two telescopes composed of six planes of microstrip silicon detectors of 50 μm pitch providing an accurate localization, 15 μm r.m.s., of the particle impacts in the pad plane.

The gas mixtures were supplied from primary sources of purity better than 99.98 %. Copper tubes were used and the mixture was circulated through Oxysorb and Hydrosorb cartridges. The flow was usually 30–40 l/h. The contaminations were continuously controlled by a Hermann–Moritz oxymeter and a Shaw hygrometer to the ppm level at the output of the detector. While not in operation, the detector was kept under constant argon purge.

The radiator array is fixed to the plate closing the detector. Its position can be adjusted relative to the CsI photocathode plane, allowing for varying in situ the Cherenkov radius. Two kinds of radiating media could be installed. One was a circular plate of NaF, 50 mm diameter, 10 mm thick. The second one was a vessel circulated with C_6F_{14}. The output window was made of a quartz Suprasil plate of 3 mm thickness, 50 mm diameter. The effective thickness of C_6F_{14} could also be adjusted continuously from 0 to 15 mm by moving an opaque foil inside the liquid screening the Cherenkov photons emitted before it. The total volume of liquid was 1 litre. The tightness was achieved with Viton O-rings.

The C_6F_{14} was supplied by 3 M company (DELPHI RICH supplier). It was circulated by using a magnetic circulator at a flow of 0.5 l/h through fully metallic tubings. Several filters were necessary to achieve the best UV transparency: we used a molecular sieve and activated copper. The best results, corresponding to Fig. 2.24(a) were achieved with the molecular sieve alone. A test cell equipped with two CaF_2 windows was inserted in the C_6F_{14} circuit in order to measure the UV transparency.

The first small RICHs and proto-1 were tested at T11 to study CsI photocathodes of size 30×30 cm^2. In 1997, the four final large photocathodes were successively evaluated using proto-2 with small radiators.

The elements of the electronics system in use are described in Section 3.1.4. The pad panel of proto-1 was equipped with 6 boards of 15 GASSIPLEX, corresponding to 240 channels per board. A scheme of the DAQ system is shown in Fig. 2.30.

2.3.1.2 H4 test set-up: proto-2

Since 1997 ALICE groups have been carrying out tests in the SPS H4 beam line. It can receive standard hadron SPS beams up to 450 GeV/c and runs dedicated extracted lead beams at 158 GeV/c per nucleon. The zone is shared with the NA57 experiment. It was foreseen to perform here the final test of the large proto-2 under multiparticle events of high density obtained by interaction on target.

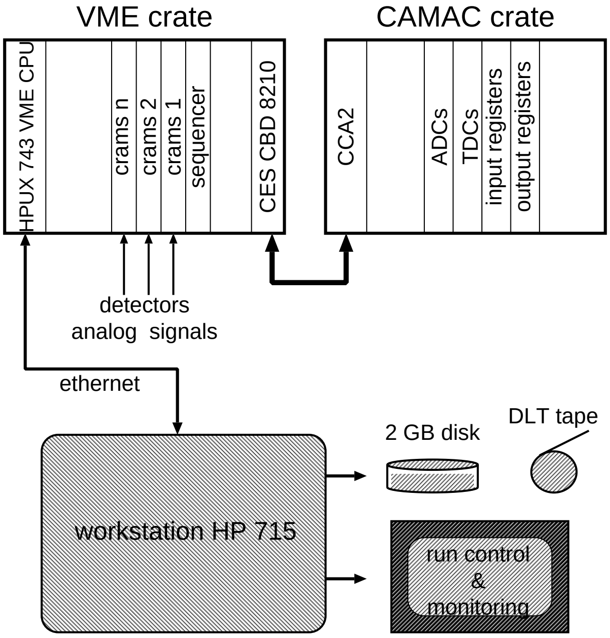

Figure 2.30: Schematic of the DAQ system used at the PS/T11 test beam line. The VME modules used to perform digitization and zero suppression are CAEN-CRAMS V550 and a Sequencer Unit V551.

The layout of the experimental set-up is shown in Fig. 2.31. Starting from upstream, it is composed of the following elements:

a) A first scintillator doublet providing beam coincidence in a sensitive area of 5×5 mm^2.
b) A veto array for upstream interactions made of four scintillators 20×20 cm^2 providing two- or four-fold coincidences as veto signals. The array has a hole in its middle to let the beam pass through.
c) A target holder, remotely controlled with several targets Be, Pb and MT.
d) An interaction array, identical to the veto array, providing various interaction trigger signals (two- and four-fold coincidences).
e) A telescope of four pad chambers used to reconstruct the trajectories of the secondaries emitted by the target. Its final configuration is seen in Fig. 2.31 and the chamber acceptances listed in Table 2.2: The projected acceptance of that telescope covers only half of the proto-2 area. Results are shown and analysed in Section 2.3.2.6.
f) The large proto-2, located on a movable stage with remote control in horizontal and vertical motions. The anode wires are horizontal.
g) A second scintillator doublet providing beam coincidence with a sensitive area of 5×5 mm^2.

For these tests, proto-2 was equipped with four large CsI photocathodes, with one and subsequently two full-size C_6F_{14} radiator trays.

Gas mixtures were supplied to proto-2 by a system identical to the one described at the T11 test set-up. In addition to the contaminant control, a system to detect traces of electronegative gas was implemented, with the aim to monitor possible leaks of the C_6F_{14} from the radiator trays surrounded by the chamber gas. The prototype of the ALICE C_6F_{14} circulation system, described in Section 3.1.3 was put in operation feeding one or two radiator trays.

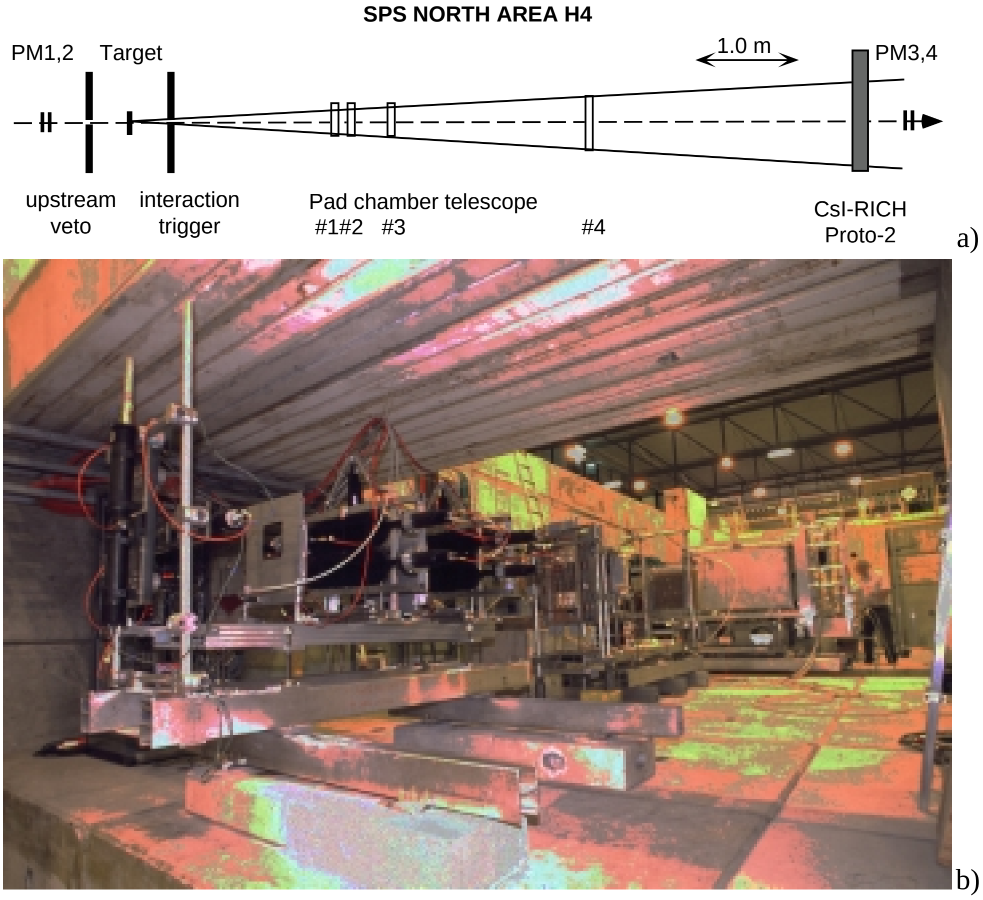

Figure 2.31: a) Experimental layout used at the SPS/H4 test beam. b) General view of the test set-up at the SPS H4 beam line. Following the trigger array and the pad chamber telescope, proto-2 is installed on a translation stage.

Table 2.2: Geometrical parameters of the telescope pad chambers

MWPC	Anode wire	Coord. centroid	Pad size (mm^2)	Pad cathode size (pads)		
				X		Y
1	vertical	Y	8×8	30	×	32
2	horiz.	X	8×8	32	×	30
3	horiz.	X	8×8	40	×	36
4	horiz.	X	8×8	56	×	60

The elements of the electronics system in use are described in Section 3.1.4. Each pad panel was equipped with 8 rows of 2 GASSIPLEX-1.5 15-chip boards plugged in a horizontal position such that the readout is propagated in a direction parallel to the anode wires. The readout was organized by horizontally daisy-chaining boards belonging to 2 adjacent pad panels, forming a super-row of 60 chips, i.e. 960 channels. This way, a total of 16 super-rows were read out by 8 CAEN V550 modules, i.e. 15 360 channels. The behaviour of this system is reported in Section 3.1.4.

The pad telescope chambers were also read out by the same electronics, adding eight V550 modules. The DAQ system is the same as the one of the T11 test set-up. The low voltage and current supplying the GASSIPLEX and the HV current of the chamber were constantly monitored.

2.3.2 Results from the PS and SPS beam tests

2.3.2.1 Introduction

The goal of these tests is to understand and optimize the detector in order to achieve the best angular Cherenkov resolution and:

a) to guarantee a stable and sustainable operation of the detector under the expected ALICE conditions of irradiation;
b) to demonstrate that the pattern recognition of very dense events (50 particles per square metre) is achievable.

We have concentrated the analysis, modeling and simulation studies after the experimental results (see Section 2.4). The reader may wish to start reading that section first.

The performance of a RICH detector is characterized by the well-known equation [52]:

$$N_{\mathrm{phel}} = L \cdot N_0 \cdot \sin^2 \theta_{\mathrm{c}} \ , \tag{2.13}$$

where

$$\cos \theta_{\mathrm{c}} = \frac{1}{n\beta} \ , \tag{2.14}$$

$$N_0 = 370 \cdot \epsilon_{\mathrm{det}} \cdot \int QE(E) \prod_i T_i(E) \mathrm{d}E \ . \tag{2.15}$$

Here N_{phel} is the number of Cherenkov photoelectrons, L is the radiator thickness, θ_{c} is the mean Cherenkov angle over the detected photon energy spectrum (established by the traversed media transmissions T_i), ϵ_{det} is the single electron detection efficiency and N_0 is the detector factor of merit.

That number has to be as large as possible since the Cherenkov ring angular resolution is expressed as $\sigma_{\mathrm{ring}} = \sigma_{\mathrm{phel}}/\sqrt{(N_{\mathrm{phel}})}$, where σ_{phel} is the angular resolution per Cherenkov photoelectron. In turn, σ_{phel} is determined by variables intrinsic to the detector layout that are in our case the radiator chromaticity, the radiator thickness (since we have no focusing geometry), and the localization accuracy of the photoelectrons.

As shown in a ring pattern in Fig. 2.32, every single electron is identified as a pad cluster providing submillimetric localization along the wire direction if its size is ≥ 2 pads. Given our large pad size, a compromise is to be found between high localization accuracy, requiring large cluster area, and accurate photon counting, requiring small clusters well separated to avoid overlap. Of course, the larger the Cherenkov radius, the less the statistical geometrical overlap with limitations imposed by the pattern recognition as seen in Fig. 2.33.

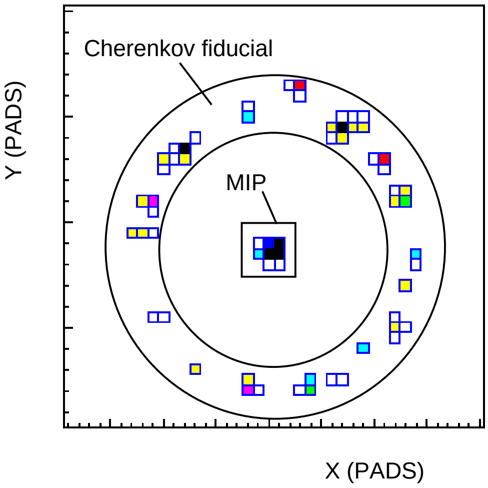

Figure 2.32: Single Cherenkov ring event with the three zones used for cluster finding.

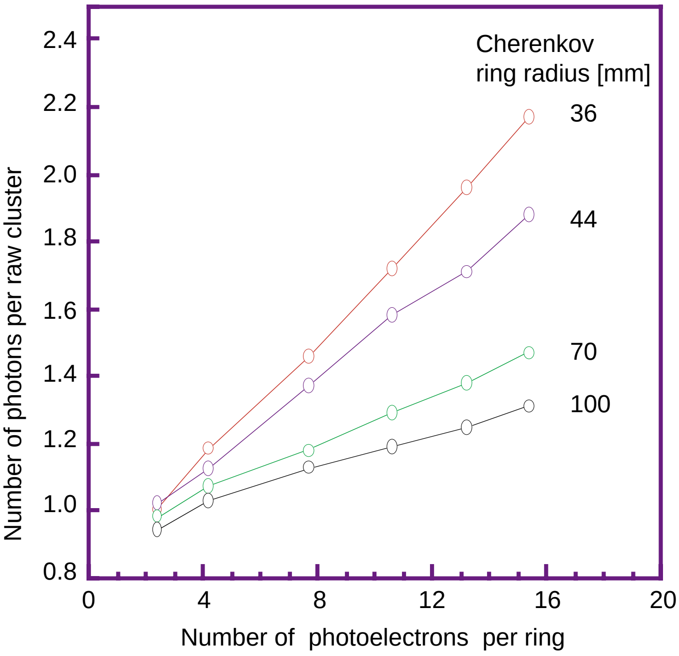

Figure 2.33: Simulated probability for geometrical overlap of Cherenkov clusters as function of the number of clusters per ring for different ring radii. (No photon feedback contribution.)

In addition, specific to the use of CsI photocathode, one expects a number of photoelectrons produced by photon feedback to contaminate the Cherenkov pattern by cluster overlap.

These remarks determine the variables to be extracted from the experimental data and used in the data analysis codes. Let us first introduce these variables to present typical experimental data while the data analysis code detailing their definitions is found in Section 2.4.

As seen in Fig. 2.32, the pad array is divided into three zones: a zone surrounding the particle impact, a Cherenkov fiducial ring zone, and the rest of the pattern corresponding to background hits. They are referred to as MIP, fiducial, and background zones, respectively. The variables listed below can be independently analysed for the three zones of the pad array:

a) N_{pad}: is the total number of hit pads (threshold dependent) per ring.

b) N_{raw}: the number of raw clusters per ring: a raw cluster is defined as a pad pattern having all pads adjacent by at least one edge. Above a certain size, it might be formed of several overlapping single patterns.

c) N_{res}: the number of resolved clusters per ring: a resolved cluster is assumed to correspond to a single Cherenkov photoelectron according to deconvolution algorithms.

d) N_{tot}: total number of single electrons (Cherenkov and photon feedback) inside a fiducial Cherenkov area.

Since the mean single electron PH, A_0, is obtained from resolved clusters, the ratio of the total pad PH measured inside the ring fiducial zone over A_0 provides N_{tot} whatever the cluster overlaps are.

2.3.2.2 Main results

Experimental distributions

For evaluating CsI-photocathodes, the standard test procedure was to take the following sequence of measurements using single particle events:

a) pedestal measurement at every run;

b) at a given radiator thickness, make an HV scan;

c) at a given HV, make a radiator thickness scan (when the convenient radiator set-up is installed).

Different impact position, incident angles, ring radius, gas mixtures, beam rates were taken as primary conditions for the scans. Empty radiator runs were also useful for studying the detector response to MIPs in the absence of Cherenkov events. In order to control the stability of the PCs, such measurements were repeated periodically over a long period of time (four years maximum).

At first, we show in Fig. 2.34 the basic distributions characterizing a run. In particular, in the plot (e) that is a zoom-in at low PH values of the SE-PHD shown in (d), the steep edge of the distribution represents the mean threshold value achieved by the FE electronics. As discussed in Section 3.1.4, this value is of 3–5 ADC channels, corresponding to 4–5 times the sigma of the noise distribution. Then according to Eq. 2.7, applicable in case of single-electron PH spectrum, the single-electron detection efficiency is represented in Fig. 2.35 as a function of the single-electron mean PH.

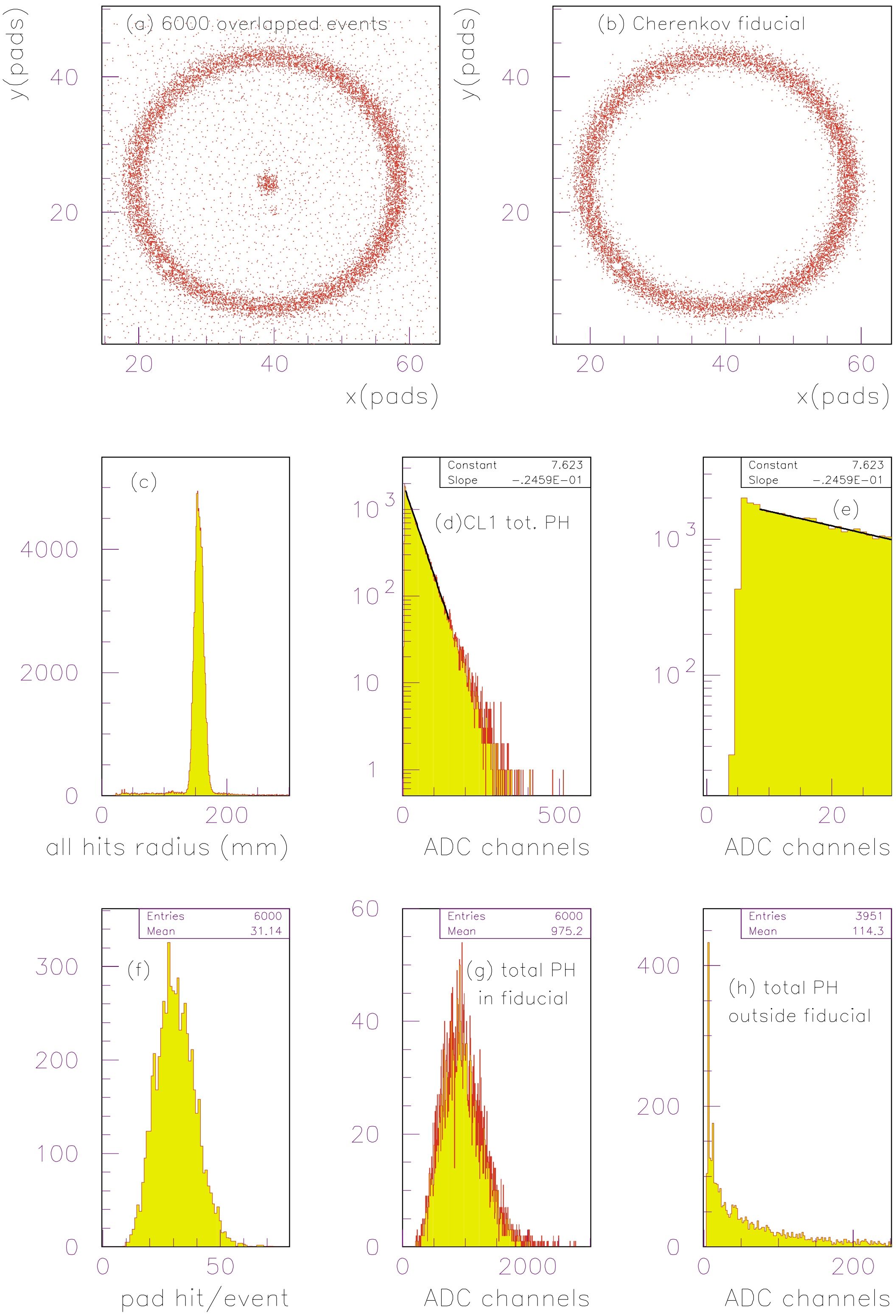
(a) 6000 overlapped events
y(pads)
40
20
20
40
60
x(pads)
(b) Cherenkov fiducial
y(pads)
40
20
20
40
60
x(pads)
(c)
4000
2000
0
0
200
all hits radius (mm)
Constant 7.623
Slope −.2459E−01
(d)CL1 tot. PH
10^3
10^2
10
1
0
500
ADC channels
Constant 7.623
Slope −.2459E−01
(e)
10^3
10^2
0
20
ADC channels
Entries 6000
Mean 31.14
(f)
300
200
100
0
0
50
pad hit/event
Entries 6000
Mean 975.2
(g) total PH
in fiducial
60
40
20
0
0
2000
ADC channels
Entries 3951
Mean 114.3
(h) total PH
outside fiducial
400
200
0
0
200
ADC channels

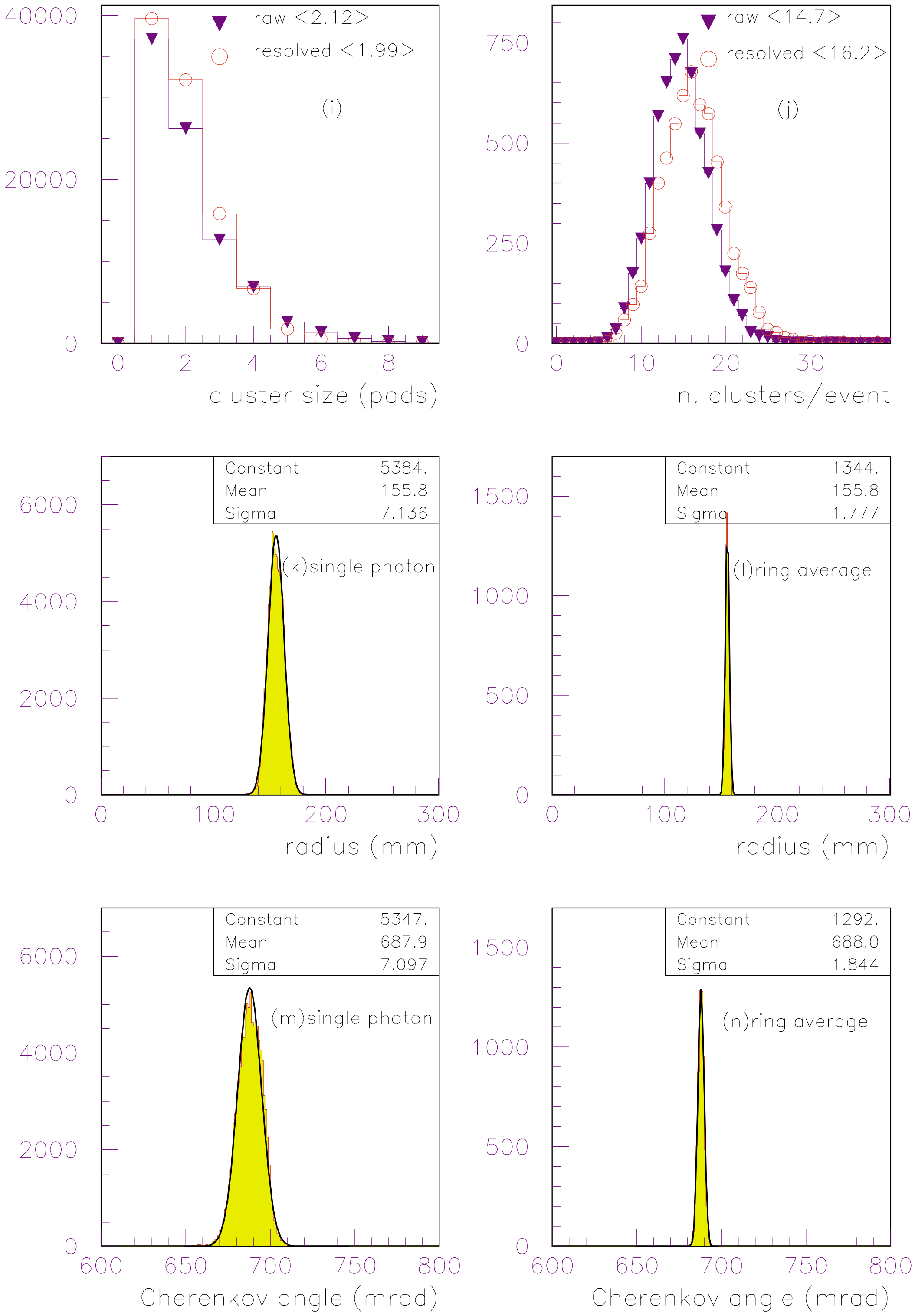

Figure 2.34: RUN2075, SPS beam test, 350 GeV/c π, PC32, 2100 V, 6000 events: two-dimensional display of (a) fully overlapped events and of (b) Cherenkov fiducial zone; (c) hits distance from MIP impact, showing the low background level; (d) single-electron PH spectrum and (e) the lower part of the same spectrum with the PH threshold in evidence; (f) number of hit pads and (g) total PH in fiducial per event; (h) total PH outside the Cherenkov fiducial; (i) size and (j) frequency of raw and resolved clusters in fiducial; (k) single-photon and (l) ring average radius distributions; (m) single-photon and (n) ring average reconstructed Cherenkov angle distributions. One ADC channel corresponds to 0.17 fC.

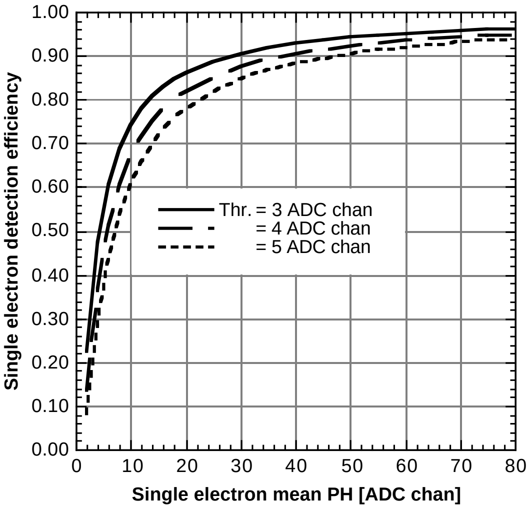

Figure 2.35: Single-electron detection efficiency as a function of the single-electron mean PH calculated at different experimental FEE thresholds.

HV scan

Figure 2.36 shows the characteristic plots derived from the previous distributions in case of an HV scan. All values are plotted versus the single-electron mean PH, A_0, in order to normalize all results to the chamber gain whatever the experimental conditions are, such as different gas pressure, gas mixtures, gap, etc.

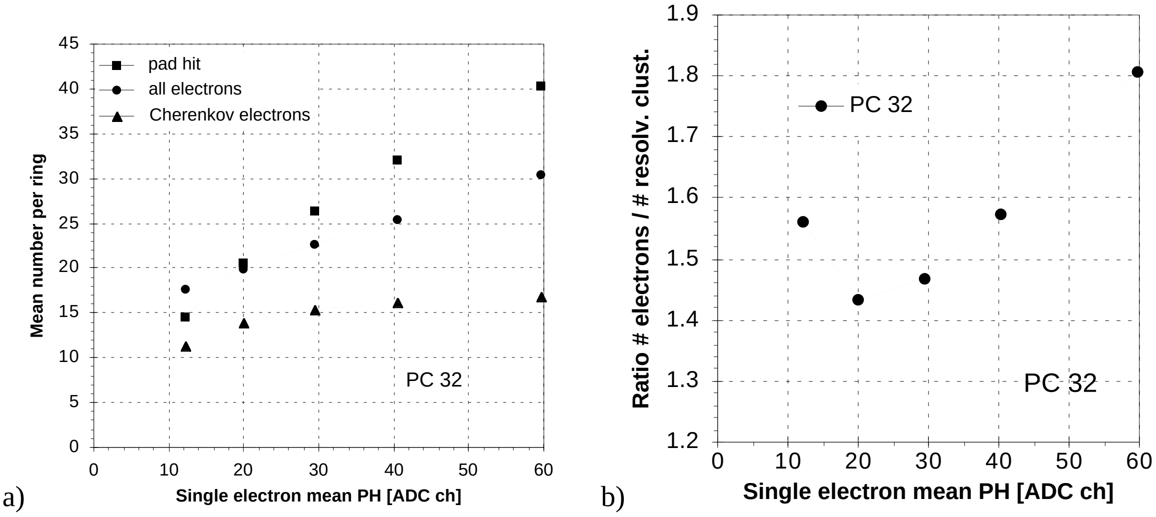

Figure 2.36: Experimental conditions: proto-2, PC32, 10 mm C_6F_{14} radiator, CH_4, pions 350 GeV/c. a) Plots of the mean number per ring of pad hits (N_{pad}), electrons (N_{tot}) and Cherenkov electrons (N_{res}) as a function of the single-electron mean PH. b) Ratio $N_{\mathrm{tot}}/N_{\mathrm{res}}$, number of electrons per cluster. One ADC channel corresponds to 0.17 fC.

One can notice in Fig. 2.36a that N_{res} tends to reach a plateau of 15–16 Cherenkov photoelectrons per ring, while the total number of electrons N_{tot} increases almost linearly with the chamber gain. Such a linear dependence is expected since the feedback photons add a contribution to the total pad PH that increases linearly with the chamber gain (Eq. 2.1). The reason why N_{res} is flat (as expected at the full detection efficiency plateau, Fig. 2.35) can be given by the feedback photons emission from the primary avalanches. Since the distance of the anode to the pads is small (2 mm) compared to the pad size ($8 \times$

8 mm^2), the feedback photons are emitted in a solid angle such that there is a high probability that the feedback photon is converted at the same pad as the primary one, hence overlapping the same cluster. In addition, the wider the emission angle of the feedback photon, the more probable it will be lost by reflection on the dielectric surface of the CsI photocathode (Fig. 2.3).

Such a feature has, a beneficial effect on the detection efficiency since a fraction of events is composed of two photoelectrons, but, the feedback photons contribute also to increase the pad pattern occupancy by enlarging the size of the clusters and their number. That is illustrated in Fig. 2.36a on the graph showing $N_{\rm pad}$, the number of pad hits per ring, monotically raising with the chamber gain. Finally, Fig. 2.36b shows the ratio of the total number of electrons to the number of Cherenkov resolved clusters, providing the number of photo electrons per cluster. This number is a close evaluation of the fraction of feedback photons however convoluted with a small contribution of primary Cherenkov clusters geometrically overlapped (Fig. 2.33 and Section 2.4.1). The rise of $N_{\rm tot}/N_{\rm res}$ observed in Fig. 2.36b at low amplification reflects that the selection by tresholding of large-sized avalanches enriches relatively the feedback photon contribution. In the next paragraph, we shall investigate the possibility of reducing $N_{\rm tot}/N_{\rm res}$ value, i.e. pad occupancy, by using different gas mixtures.

The influence of gas mixtures on photoelectron yield and photon feedback

It has been seen in Section 2.1.1.2 that the operation of a CsI photocathode in a gas medium at atmospheric pressure results in the loss of photoelectrons depending on the gas species and the reduced field E/p value at the surface. Therefore, we shall make a distinction between the CsI QE measured in vacuum and the photoelectron yield of a photocathode evaluated in a MWPC.

Pure CH_4 was used as basic chamber gas since it was known that noble-gas-based mixtures were decreasing the photoelectron yield. In addition, its excellent UV transparency was quite attractive. However, this good transparency makes its contribution to photon feedback non-negligeable due to the three emission lines at 156, 166, 193 nm. Later results from GALICE simulation showed how important the conversion of slow neutrons in a hydrogenated gas could be. These very heavily ionizing events (MeV local deposition) might be responsible for damaging the chamber. We present a study of the influence of the gas mixtures on the photoelectron yield and associated photon feedback ratio to investigate a possible optimization.

The measurements were obtained with proto-1 equipped with PC-24 and the small C_6F_{14} radiator adjusted at 10 mm liquid thickness. The detector was installed at H4 (pion 350 GeV/c). The C_6F_{14} transparency was carefully monitored and found stable all along the runs.

In Fig. 2.37, $N_{\rm res}$ and the ratio $N_{\rm tot}/N_{\rm res}$ are plotted as a function of A_0, respectively for the different gas mixtures, CH_4, CH_4-iC_4H_{10}, Ar-CH_4, Ar-iC_4H_{10}, Ar-CH_4- iC_4H_{10}. iC_4H_{10} is known for its efficient quenching property.

Figure 2.37a shows that the photoelecton yield is maximum using pure CH_4, and decreases when increasing the iC_4H_{10} fraction in the mixture. Compared to pure CH_4, the photoelectron yield loss is 13% by adding 10% iC_4H_{10} and 75% in Ar-iC_4H_{10}/52-48 %. A part of that loss can be attributed to worse iC_4H_{10} UV transparency since the iC_4H_{10} in use (98.7% purity) in our test was not purified by Oxysorb cartridges. The ‘noble-gas backscattering effect’ (see Section 2.1.1.2) can be evaluated by comparing mixtures having about the same iC_4H_{10} fraction, that is CH_4-iC_4H_{10}/94-6 and Ar-CH_4-iC_4H_{10}/73-20-7 where the loss is 20%. Ar-CH_4 mixtures seem able to achieve the same plateau as CH_4 but it will be seen that, owing to the poor quenching of CH_4, the feedback yield is so high that the cluster resolution is degraded. In addition, microdischarges were observed at such a rate that the use of these mixtures is out of the question for stable operation.

Figure 2.37b shows the variation of the ratios $N_{\rm tot}/N_{\rm res}$ as a function of A_0. As said above, $N_{\rm tot}/N_{\rm res}$ quantifies the fraction of photon feedback per ring in the Cherenkov fiducial zone. First, a rapid increase of the photon feedback yield is observed in Ar-CH_4 mixtures already at low gain making these mixtures useless even with 50% CH_4. For the other mixtures, the $N_{\rm tot}/N_{\rm res}$ curves show a minimum in the 20 to 30 ADC channel A_0 range. In fact the falling part on the left of the plots comes from the lack of efficiency at low A_0 as seen in Fig. 2.37a. The lowest minimum value, 38%, is obtained with CH_4/iC_4H_{10} mixtures for A_0 up to 40 ADC channels providing full single-electron detection efficiency. Although a comparable minimum is achieved in pure CH_4, it is obtained at lower A_0 to reach 60% at A_0 equals 40 for full efficiency. Finally, the ternary and the Ar-iC_4H_{10} mixtures show a ratio remaining constant while increasing A_0 to higher values but, as seen in Fig. 2.37a, the photoelectron yield might be too low.

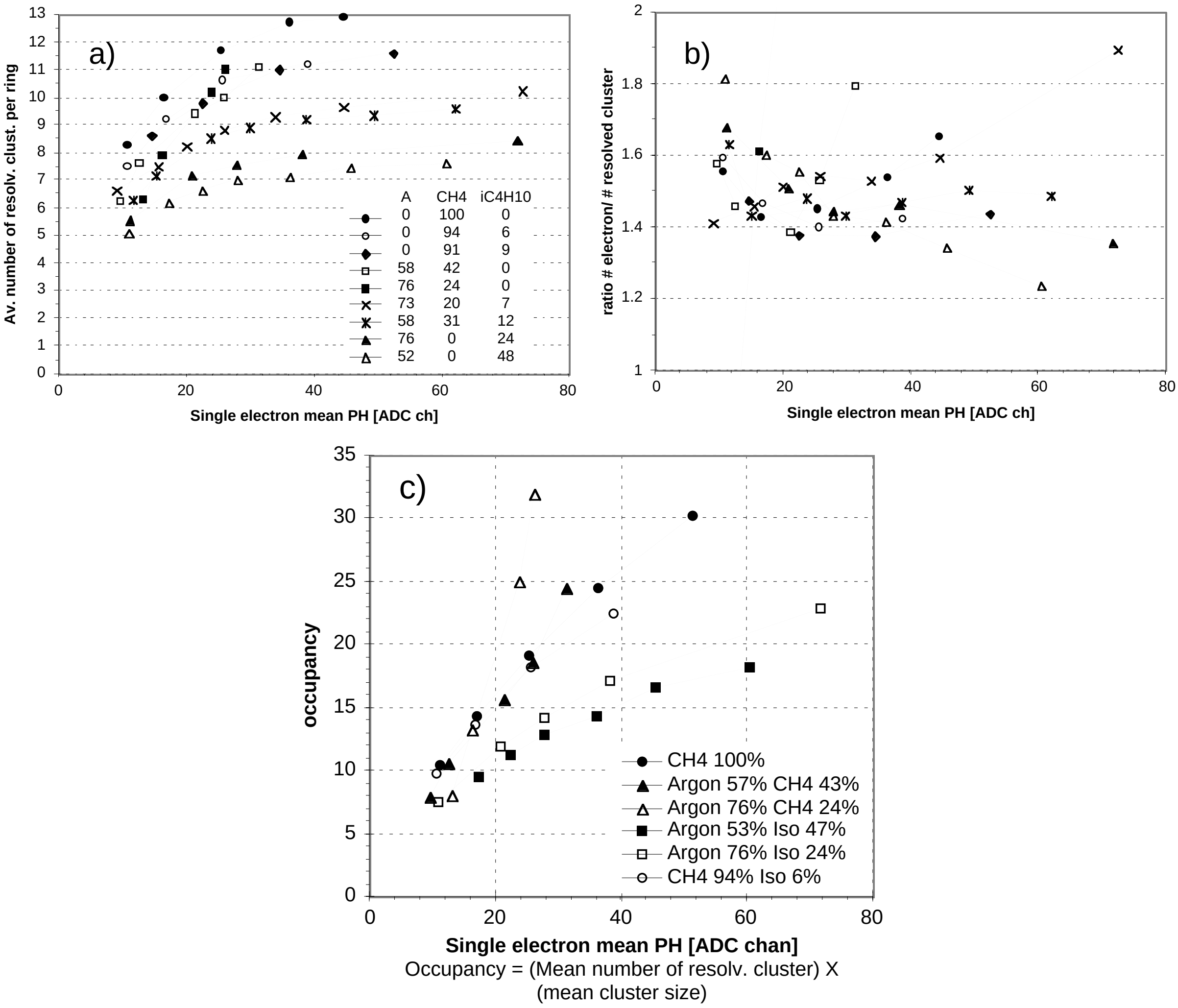

Figure 2.37: Experimental conditions: proto-1, PC24, 10 mm C_6F_{14} radiator, CH_4, pions 350 GeV/c. Gas mixtures study. a) Plots of the mean number per ring of pad hits (N_{pad}), electrons (N_{tot}), and Cherenkov electrons (N_{res}) as a function of the single-electron mean PH. b) Ratio $N_{\mathrm{tot}}/N_{\mathrm{res}}$, number of electron per cluster. c) Occupancy plot for different gas mixtures. One ADC channel corresponds to 0.17 fC.

As seen in Fig. 2.37c, the different gas mixtures can also be compared by plotting an occupancy factor defined as the product N_{res} times the corresponding mean cluster size. Argon-isobutane mixtures achieve the smaller occupancy to the cost of a reduced N_{res} value.

In conclusion, the best mixture from the point of view of detector performance seems to be CH_4-iC_4H_{10}, although the large hydrogen content increases the neutron conversion. These questions will necessitate further investigations with alpha sources. Another candidate, half-hydrogenated, could be Ar-CH_4-iC_4H_{10}/58-31-12 the properties of which are compared in Table 2.3.

Table 2.3: Effect of the gas composition on the photoelectron and photon feedback yields

Gas mixture	$N_{\rm res}$	$N_{\rm tot}/N_{\rm res}$ (%)
CH_4	12.8	60
CH_4-iC_4H_{10}/91-9	11.2	45
A-CH_4-iC_4H_{10}/58-31-12	9.2	40

MIP detection and associated background

The background generated at the passage of the MIPs through the detector essentially originates from the feedback photons emitted by the primary avalanche and converted at the CsI PC. Other contributions are the delta electrons or interactions occurring in the MWPC gap and secondary photonic effects occurring in the proximity gap, not influenced by the field in collection gap $E_{\rm coll}$ (colour Fig. 1.iii), such as Cherenkov light emitted by delta electrons created in the C_6F_{14} and the quartz window. None of the elements in use are scintillating in the operating wave length range.

In order to study the pad patterns specific to the MIPs alone in absence of Cherenkov events, the measurements presented now were taken after emptying the radiator in proto-2. The beam spot size at the chamber was of a few tens of mm^2 (pion, 350 GeV/c).

Figure 2.38a,b show primary cluster size and Landau PH distributions, (c) the mean primary particle cluster size as a function of the chamber voltage, relevant to further pad occupancy discussion and (d) the variation of the Landau peak versus HV, indicating a proportional regime.

The 2-D plots of colour Fig. 2.i show a substantial amount of hits outside the region where the beam particles cross the chamber. The upper curve in Fig. 2.39a shows the total number of separated clusters per event that can be split into two contributions. A small contribution comes from secondary interactions that are identified by the external pad chamber telescope. It accounts for 0.2/primary, independent of the chamber HV. Their occurrence, already low at the SPS beam energy, will be negligible at the much lower momentum range in ALICE. The larger fraction is identified as the feedback photon contribution as their PH distribution is found exponential and comparable to the one obtained at the same gain for the Cherenkov single photoelectrons, as shown in Fig. 2.40a,b. Let us remark that the small number of photoelectrons per particle, shown in Fig. 2.39b accounts only for separated clusters, remembering that the majority of them overlap the large primary cluster as discussed above.

The distances from the MIP impact to these separated clusters found outside of a zone corresponding to the MIP primary cluster size is plotted in Fig. 2.41. That distribution extends up to large values not compatible with a model where the emitting source is located at the anode wire only. One has to assume emitting sources more distant from the pad plane like parasitic Cherenkov light or reflections at the quartz surfaces. The influence on the centroid localization of the particle by the feedback clusters overlapping the primary one has been evaluated by simulation, Fig. 2.42. After correction of the intrinsic centroid error, a r.m.s. error for the coordinate along the wire is of 250 μm while the r.m.s. error in the orthogonal direction is dictated by the 4 mm wire pitch [65].

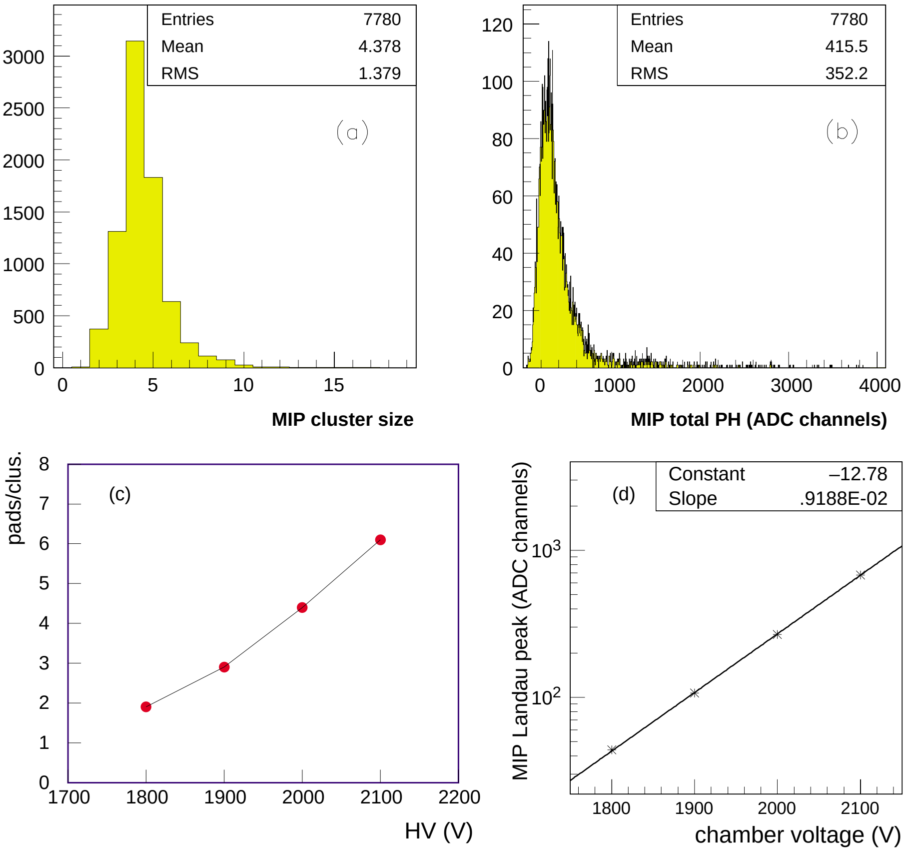

Figure 2.38: MIP studies with proto-2, PC31, CH_4, empty radiator, 350 GeV/c pion. a) Cluster size distribution. b) Landau PH distribution at 2000 V. c) Primary cluster size as a function of HV. d) MIP Landau peak as a function of HV.

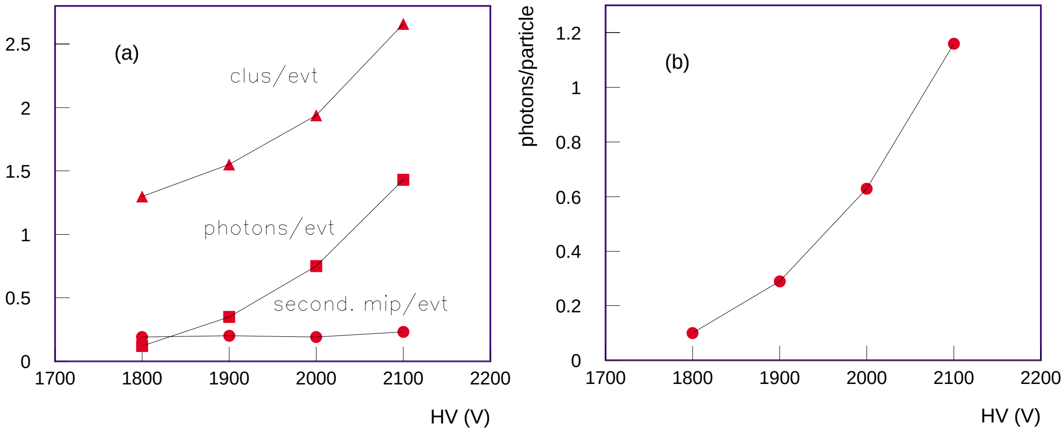

Figure 2.39: MIP studies with proto-2, PC31, CH_4, empty radiator, 350 GeV/c pion. Background associated to MIP primary clusters. a) number of clusters per event vs. HV. b) number of feedback electrons per particle vs. HV.

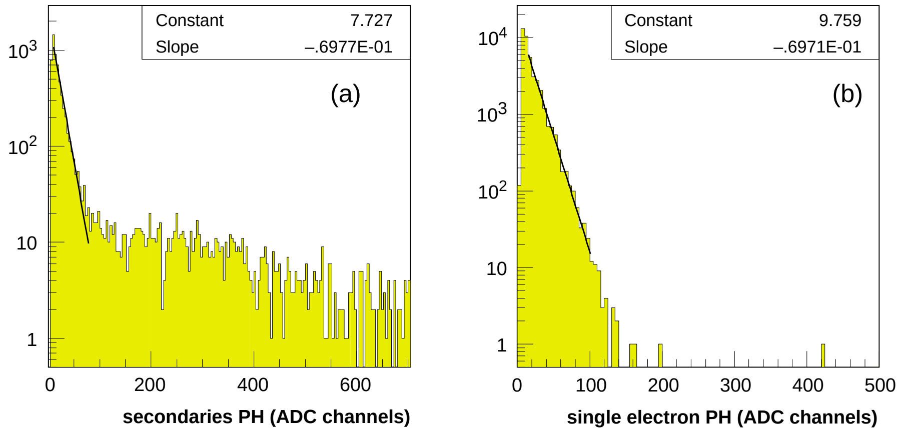

Figure 2.40: MIP studies with proto-2, PC31, 2000 V, CH_4, empty radiator, 350 GeV/c pion. a) PH spectrum of secondary clusters associated to a MIP cluster. b) For comparison, PH spectrum of single Cherenkov photoelectrons at the same voltage. One ADC channel corresponds to 0.17 fC.

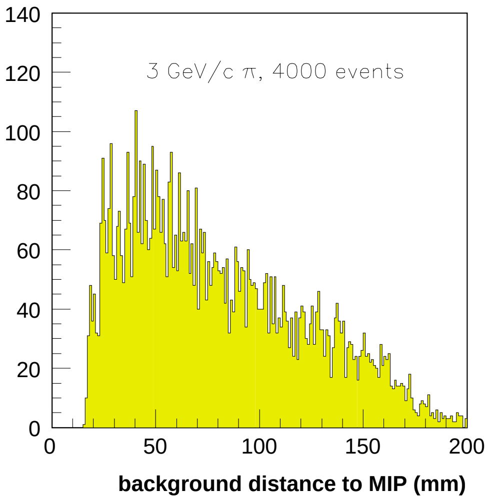

Figure 2.41: MIP studies with proto-1, PC24, 2050 V, CH_4, empty radiator, 3 GeV/c pion. Distribution of the distances of secondary clusters to the impact of their primary MIP.

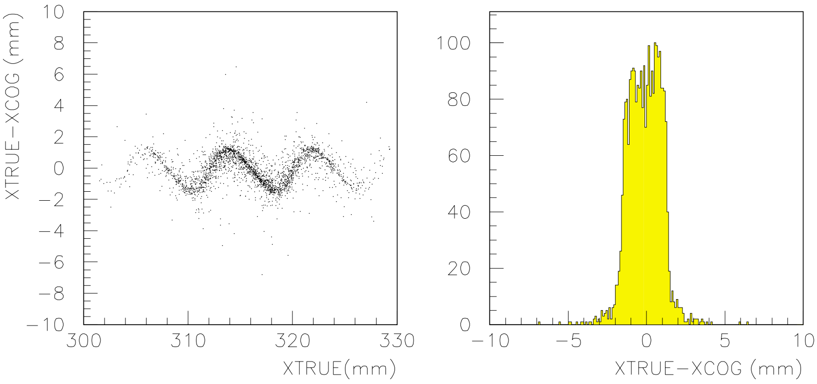

Figure 2.42: Smearing due to feedback photoelectrons of the residual distribution (compare to Fig. 2.19b).

Influence of magnetic field on the photoelectron yield

In the event of operating the CsI RICH in a magnetic field parallel to the plane of the photocathode, photoelectrons emitted nearly at rest from the CsI photocathode are submitted to the resulting force of crossed electrical and magnetic fields. Depending on the energy and emission angle of the photoelectron, the curling of the electron trajectory during the first mean free path in the gas could be such that it could be sent back to the photocathode and re-trapped. Since, to our knowledge, the distributions of the energy and emission angle of the photoelectron are not available, a direct test was set installing proto-1 inside the GOLIATH magnet at NA57 providing a field adjustable from 0 to 1.5 T parallel to the photocathode. The particles used were pions of 350 GeV/c at the H4 beam line. Proto-1 was equipped with PC-24 and a small C_6F_{14} radiator adjusted at 10 mm liquid thickness. The chamber was flushed with CH_4. Figure 2.43 shows the variations of $N_{\rm pad}$, $N_{\rm res}$ and $N_{\rm tot}$ as a function of the magnetic field measurements taken at the same gas gain: a slight decrease is observed reaching 8% at 0.9 T. Figure 2.44 shows the variations of $N_{\rm res}$ versus A_0, that is decreasing the electrical field at the photocathode surface. It can be seen that the curves remain parallel at different magnetic fields down to the minimum electrical field. The E/p range under test ranges from 3.8 to 4.2 V/cm Torr^{-1}. In conclusion, the operating magnetic field at ALICE, that is 0.2 T, is not expected to affect the performance of the CsI-RICH.

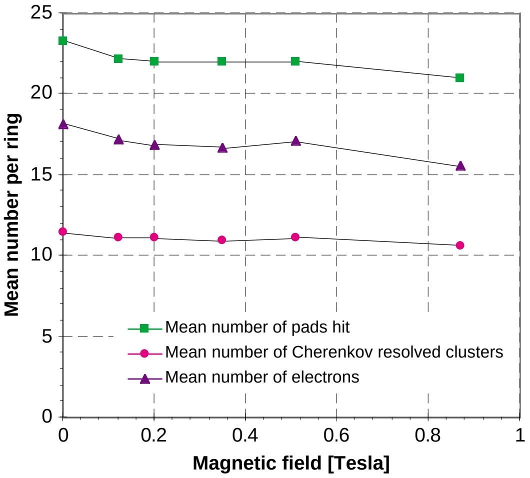

Figure 2.43: Measurements of the performance of a CsI photocathode placed parallel to a uniform magnetic field. Experimental conditions: proto-1, PC24, $HV = 2200$ V, CH_4, 10 mm C_6F_{14} radiator, pion 350 GeV/c.

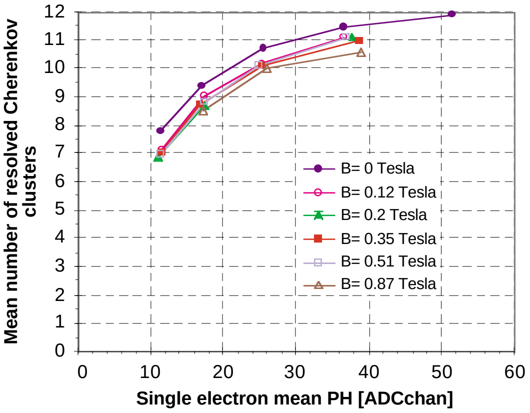

Figure 2.44: Measurement of the photoelectron yield ($N_{\rm res}$/ring) of a CsI photocathode varying the chamber gain at different intensities of the magnetic field. Part of the drop respective to the no-field value originates from an increase of the common noise induced by the magnet operation. Experimental conditions: proto-1, PC24, CH_4, 10 mm C_6F_{14} radiator, pion 350 GeV/c. One ADC channel corresponds to 0.17 fC.

CsI QE evaluation using Cherenkov measurements

The knowledge of the spectrum of the Cherenkov radiation, which constitutes a well-calibrated UV source, can be exploited to evaluate the CsI differential QE with two different approaches. The first one is based on the simulation of Cherenkov events aiming at the 'tuning' of the quantum response through the reproduction of experimental test-beam measurements; it will be described in Section 2.4. The other method allows a direct measurement of the CsI QE curve making use of the large dispersion of the refractive index of a NaF radiator (Fig. 2.45) [66].

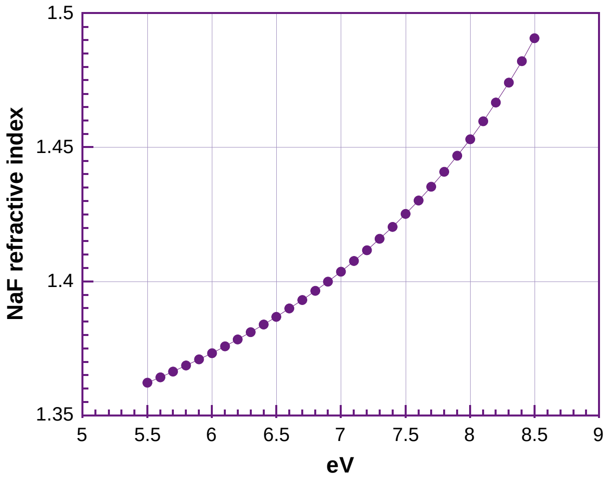

Figure 2.45: The NaF refractive index [66].

The number of photons having an energy within E, $E + \mathrm{d}E$, incident on the photocathode, can be calculated as:

$$N_{\text{phot}}(E) = 370\,L \int_{E}^{E+\mathrm{d}E} \sin^2\theta_{\text{c}}(E) \prod_i T_i(E)\mathrm{d}E \tag{2.16}$$

where L is the radiator thickness, θ_{c} is the Cherenkov angle and T_i is the transmission of the i-th traversed medium (Fig. 2.46).

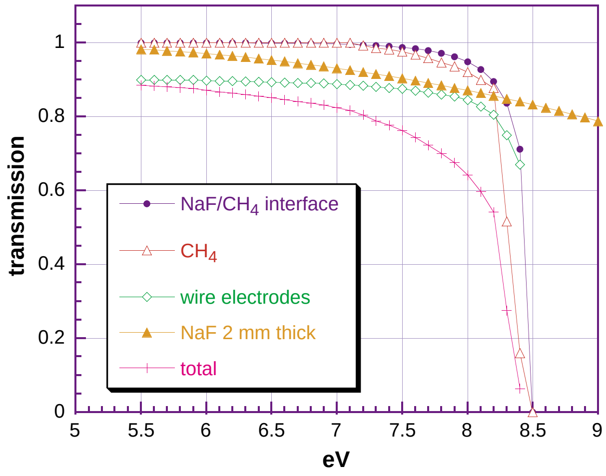

Figure 2.46: Transmission of media in the NaF RICH detector for 2 GeV/c protons, 2 mm radiator thickness and 28 mm proximity gap.

In the case of 2 GeV/c protons the spectral acceptance extends up to 8.5 eV, limit set by the CH$_4$ UV cut-off, while with 3 GeV/c protons it is limited to 7.9 eV by total internal reflection at the NaF/CH$_4$ interface, according to the relation $n_{\max} = \sqrt{1+\beta^{-2}}$. In both cases the lower limit is set by the CsI photoelectric threshold.

Given the radiator thickness and the proximity gap, it is possible to determine in the detection plane circular fiducial areas such that when a photon is counted in the n-th zone its energy falls in a bin of width ΔE centred at E_n. Figure 2.47 shows the relation between the radial distance of photon impact to the centre of the ring calculated for 2 GeV/c protons, proximity gap of 28 mm, and emission point in the middle of a 2 mm NaF radiator.

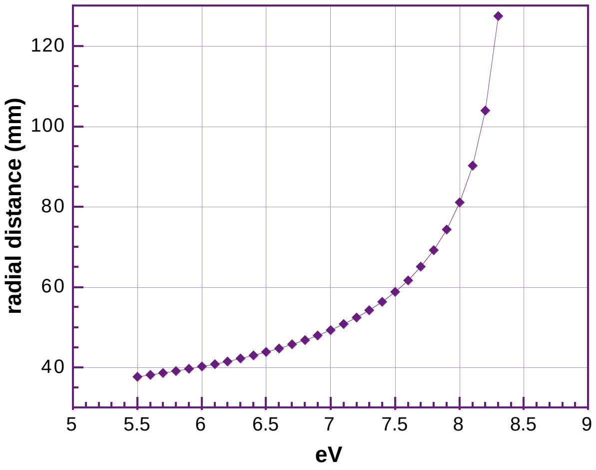

Figure 2.47: Cherenkov photons' distance from the ring centre as a function of photon energy.

Assuming that all the quantities depending on energy are constant in each energy interval of width $\Delta E = 0.1$ eV, the QE can be calculated with the approximated relation:

$$QE(E_i) = \frac{N_{\mathrm{phel}}(E_i)}{370\,L\sin^2\theta_{\mathrm{c}}(E_i)\prod_j T_j(E_i)\Delta E\epsilon_{\mathrm{det}}}\,, \tag{2.17}$$

where $N_{\mathrm{phel}}(E_i)$ is the number of photoelectrons counted in the i-th interval and ϵ_{det} is the single-electron detection efficiency. The accuracy of this method is limited by the spread of the photon emission along the particle path in the radiator. It results in a fraction of overlap between photons belonging to adjacent energy bins. To minimize this effect a radiator as thin as possible has to be used allowing narrower energy bins to be used. We present the results obtained using proto-1 equipped with PC24 and a NaF radiator 2 mm thick. Several runs have been taken in different combinations of proton beam momenta (2 and 3 GeV/c) and proximity gaps (24.5, 28, 33, 43 and 48 mm) to investigate various spectral ranges and photocathode regions. In Fig. 2.48 are reported the average QE curve and, for comparison, the CsI QE measured at the Weizmann Institute.

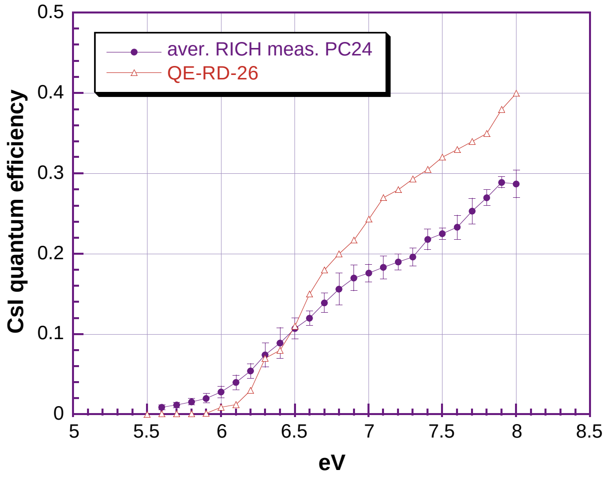

Figure 2.48: PC24 measured differential QE and the RD-26 QE obtained at the W.I.S. from photocurrent measurements on a small sample under vacuum (QE about 10% higher than the one measured in CH_4; Section 2.1.1.2.).

The measured differential QE is overestimated, owing to the feedback contribution to the total photon counting in each energy interval. This contribution is particularly evident in annular regions corresponding to Cherenkov photon energies below or close to the CsI photoelectric threshold (6 eV): photon counts larger than expected can only be associated with feedback photons, the energy of which is larger than that correlated to the hit fiducial zone.

After a suitable correction of the measured QE, we were able to reproduce, by means of the simulation described in Section 2.4, various sets of experimental data relative to the proto-1/PC24 equipped not only with NaF but also with C_6F_{14} radiator. This is a good cross-check of the validity of the measured QE, since the different set-up produces also a different photon spectrum.

2.3.2.3 Overall performance of the prototypes

Operation of the detector, chamber current

Despite the presence of a semi-insulating CsI layer, the commissioning of a new photocathode has never required any conditioning time: the working voltage is reached in less than one hour with a very low dark current (less than 10 nA) and very rare ‘microdischarge’ events when CH_4 or CH_4-iC_4H_{10} mixtures are used. The noble-gas-based mixtures are more unstable under local beam irradiation at 10^4cm^{-2}s^{-1} rate where voltage trips are observed.

When a breakdown occurs, it is essentially caused by an anode wire coming loose due to a weak soldering. Letting such a wire at a floating potential by removing its connection to the HV supply was found sufficient to restore the normal operation of the whole chamber.

The dark current delivered by the 1 m^2 area of proto-2 is 1–2 nA and stable during beam operation. Local beam irradiation up to 2×10^4cm^{-2}s^{-1} can be sustained. Such a rate is several orders of magnitude larger than the local rate expected at ALICE (10–50 particles cm^{-2}s^{-1}). Figure 2.49 shows a sequence of the chamber current recorded by the HV slow-control system between and during the bursts.

Figure 2.50 shows the gap configuration that is traversed by the relativistic charged particles (MIP). In order that the only part of the primary ionization deposited at the passage of the MIPs be the one restricted to the 4 mm thick MWPC gap, the fraction deposited in the large proximity gap is drifted towards the collection electrode raised at a positive voltage, $V_{\rm coll}$. Most of the primary ions are collected by the grounded MWPC cathode. However, if $E_{\rm mwpc}$ and $E_{\rm coll}$ are the fields in the MWPC and proximity gap, respectively, some primary electrons lying close to that transparent wired electrode may sneak from the proximity into the MWPC gap depending on the ratio $E_{\rm coll}/E_{\rm mwpc}$. That contribution has to be kept small since it unnecessarily increases the MIP avalanche size. The effect of $E_{\rm coll}$ was evaluated by measuring the current in the chamber irradiated by particles at a rate of 9×10^3 per burst. As shown in Fig. 2.51, the chamber current decreases and stabilizes at a constant value when $V_{\rm coll}$ is larger than 150 V.

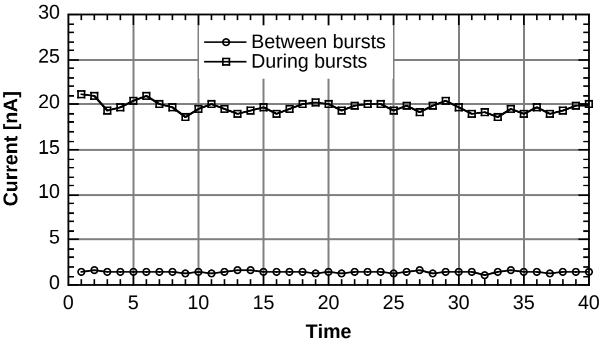

Figure 2.49: Sequence of chamber current values recorded between and during bursts of 10 000 particles. Each point is the mean of 40 bursts. $HV = 2050$ V, 10 000 particles/burst.

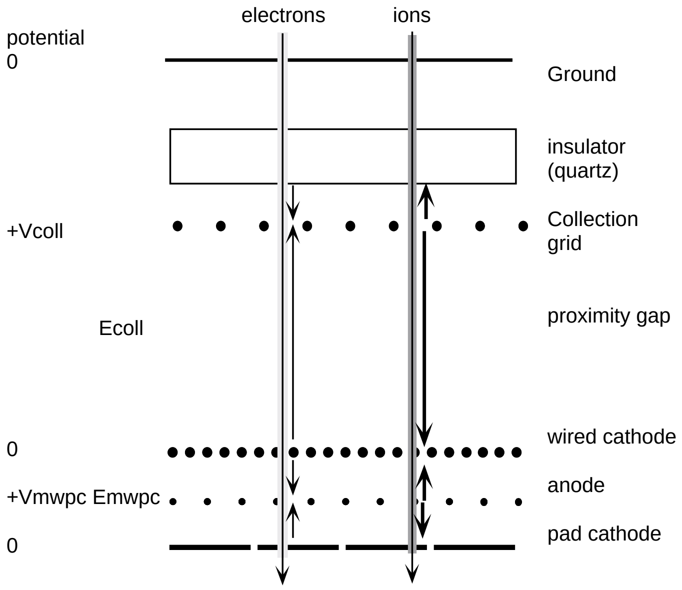

Figure 2.50: Electrical field configuration in proto-2 and primary deposition.

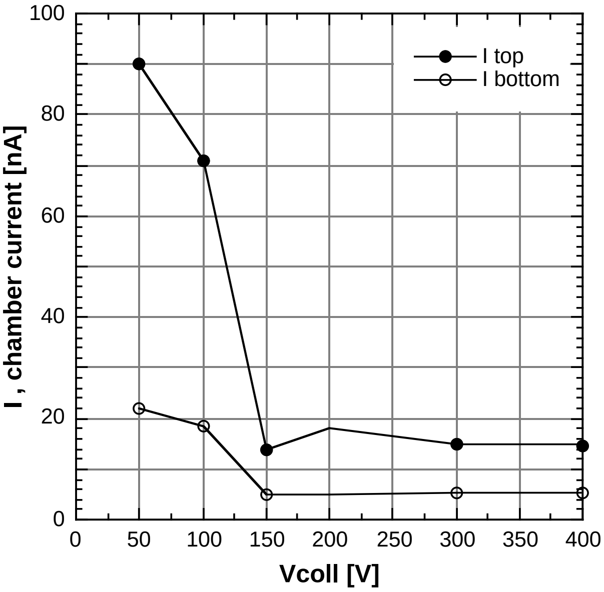

Figure 2.51: Influence of $V_{\rm coll}$ on the chamber current. PC32. $HV = 2050$ V, 10 000 particles/burst. $I_{\rm top}$ is measured in the half of the chamber crossed by the direct beam. $I_{\rm bottom}$ is the other half.

In Fig. 2.52, we show the variation of the single-electron mean PH, A_0, as a function of the chamber voltage for the different gas mixtures that were tested. The working voltage ranges start at an A_0 value of 10–15 ADC channels. Remembering that the FE electronics threshold, $A_{\rm th}$, is of 2 ADC channels, single-electron detection efficiencies are obtained as exp-($A_{\rm th}/A_0$).

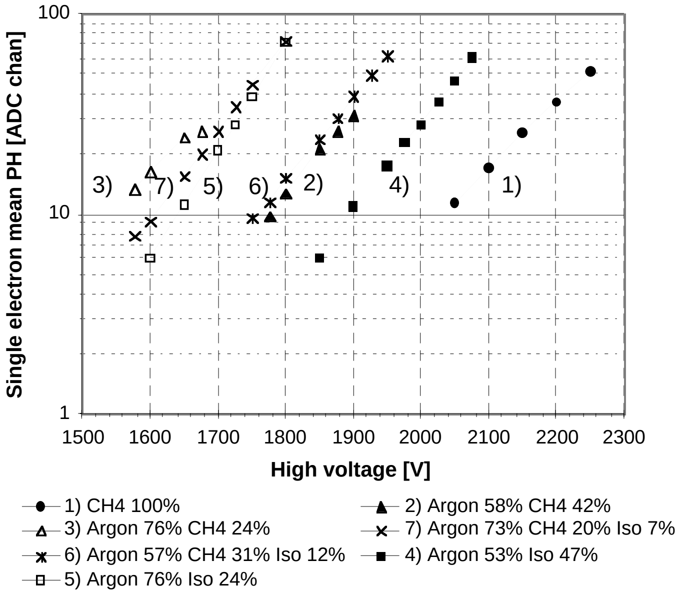

Figure 2.52: Variation of the mean single-electron PH A_0 as a function of the chamber voltage for different gas mixtures. Measurements were obtained from proto-1 using PC24, 10 mm C_6F_{14} radiator at H4/SPS, pion 350 GeV/c. One ADC channel corresponds to 0.17 fC.

Gain and photon yield uniformity

The detector is usually circulated at a flow rate of 40 l/h, that is a change of one chamber volume every 3 hours for proto-2. Given the impedance of the gas outlet pipes, the chamber is typically overpressured by 5–8 mbar. The sagittas of the pad planes induced by that overpressure were measured as a function of gas flow to be 200 μm at the centre of a pad panel at 40 l/h. To evaluate the effect of chamber gap deformation, the gain uniformity is obtained by plotting single-electron PH distributions for selected areas of the pad panel, e.g. corresponding to each quarter of a Cherenkov ring. As seen in Fig. 2.53, a coarse scan can be achieved by taking runs at different positions of the ring centre.

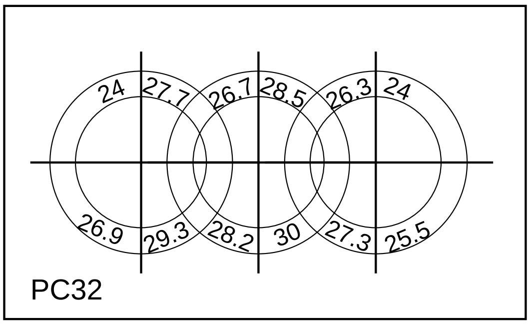

Figure 2.53: Evaluation of the uniformity of the chamber gain across PC32 in proto-2. The numbers correspond to the mean PH spectrum measured in 90° sectors of the Cherenkov fiducial zones. $HV = 2050$ V.

In order to evaluate the uniformity of the photoelectron yield of a CsI photocathode, pad patterns of rings are overlapped to create a 2-dimensional hit density plot that allows in turn to plot the hit density per unit angle versus azimuthal angle of the ring. Such a plot is shown in Fig. 2.54, indicating a uniform response all around the ring. Since the ring radius is large, repeating the operation at different locations over the pad panel allows almost the whole photocathode area to be scanned. The variation of the azimuthal density was never found to be larger than 10%, demonstrating a satisfactory uniformity of the response of the PC over its whole area.

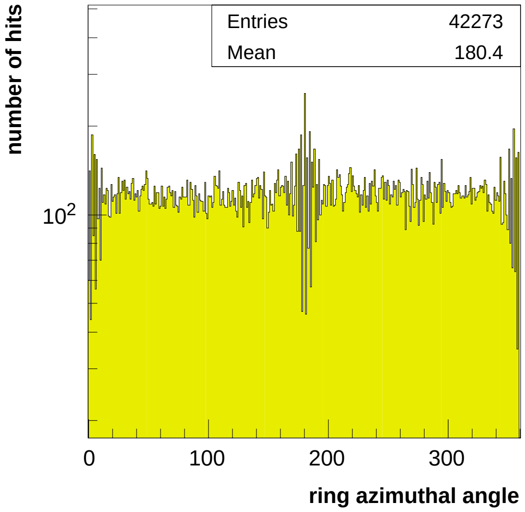

Figure 2.54: Azimuthal distribution of number of hits by 1° bin along the Cherenkov fiducial zone. (3000 events, PC32, 2050 V).

Optimization, yield and stability of PCs

In this section, an outline of the RD phase is given to review the steps achieved in the optimization of the detector towards the assembly of a final prototype of a HMPID module.

During the period 1993 to 1997, 32 CsI photocathodes were produced and evaluated using test beams. They are referred to as PC1 to PC32 in Fig. 2.55. The choice of a parameter convenient to compare their performance is not straightforward since a variable like the photoelectron yield depends on specific experimental conditions like transparencies, efficiencies, etc that might change from run to run. For that purpose, we have taken the QE value at 170 nm, referred as QE(170).

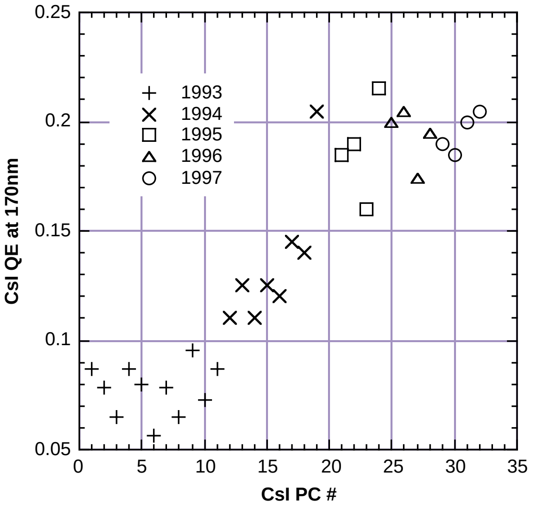

Figure 2.55: CsI QE history. Overview of the QE measured at 170 nm of all the CsI photocathodes produced during the R&D phase.

The following actions, described in chronological sequence, were taken and resulted in an improvement of either the photoelectron yield or the QE(170) performance.

a) At the beginning of our R&D work, CsI layers were deposited on G10/Cu/Au substrates at room temperature (PC1 to PC10), showing low QE and bad quality coatings (Section 2.1.1.5). An improvement was observed (PC12 to PC18) when the post treatment was applied (Section 2.1.1.3).

b) During 1994, PC19 was the first photocathode where the pad PCBs with a Ni/Au layer and polishing were implemented, with the post-treatment applied after CsI evaporation. As seen in Fig. 2.55, a clear improvement of QE(170) was achieved in comparison to the previous PCs made with standard PCBs.

c) Also, during the periods when the PCs were not mounted on the detector for test, they were protected by a tight lid and stored in a setup providing a continuous argon circulation of 15 l/h. Progressively, the mounting on detector was done more carefully in a Jacobex glove box under argon.

d) In 1995, the optical transparency of the second MWPC cathode was improved by replacing a stainless steel mesh (500 μm/square) providing a good field hermeticity in the gap by a cathode made of 100 μm diameter wires spaced by 2mm. A gain of 20% in the transparency, hence in the photon yield, was achieved. This gain is obtained because of the large angles, $\sim 60^{\circ}$, under which the photons cross the wire cathode. The gain uniformity and the protection against charges deposited in the proximity gap were still found satisfactory by using the wired cathode as seen in Fig. 2.51.

e) After PC19, a series of photocathodes were produced to investigate whether the adopted PCB technology and CsI processing were convenient to achieve reproducible results.

f) As seen in Fig. 2.55, the mean performance was kept at a satisfactory mean level over the next 10 PCs with the exception of PC23. Also, the check of PC22 after a 4 months storage period showed a significantly degraded performance. An examination of the PC surface indicated the presence of whitish spots possibly attributed to an exposure to moisture. Both, the transfer procedure from the evaporation vessel to the detector and the tightness of the PCB (through holes) were put under question.

g) An improved technology was tested to guarantee the tightness of the pad PCBs (discussed in Section 3.1.1.1) that was applied to the four large PCs installed on proto-2 (PC29 to PC32). Also, given the size of proto-2, a removable glove box was built to be adapted directly to the back of the detector, allowing for the transfer of each PC from its protective box to the detector without any contact with air. During these manipulation the fractions of oxygen and moisture were kept below 400 ppm.

This first step allowed to demonstrate that the handling, mounting of PCs on a HMPID module of final sizes were achievable under safe conditions and with a simple tooling. The contamination levels could and should still be decreased.

h) Since PC22 was damaged, that was the opportunuity to check whether a second evaporation on the same substrate was feasible after removing the bad CsI film. The removal was done by using pure ethanol and a very soft tissue. The panel was outgased for a week at 60° under argon before the second evaporation. The resulting new QE(170), indicated as PC27 in Fig. 2.55, was found comparable to the first one. That unique test has to be reproduced since, in case of confirmation, the renewing of aged PCs could be done by a second CsI evaporation, avoiding the non negligeable expense of the construction of new pad panels. The new equipment described in Section 3.1.5.2 will be used to pursue this study more conveniently than producing and testing expensive pad panels at the beam.

Stability of the CsI photocathode

Following a first performance evaluation just after production, several photocathodes were periodically re-evaluated at the test beam in order to control their stability versus chemical contaminations as moisture, oxygen. Figure 2.56a shows the evolution of PC19 and PC24, two of our oldest PCs. Even though these PCs were removed and remounted about 10 times from proto-1, under non optimal conditions, long plateaus are observed corresponding to less than 5% QE drop over three years. As discussed in the previous paragraph, the production and the handling of the last PCs, 29 to 32, equipping proto-2 were performed with more care and controls. They show, in Fig. 2.56b, an excellent stability over their first year of operation. These checks will be pursued as well as dedicated tests aiming to quantify the QE loss as a function of the contamination rates using the ASSET system (see Section 2.1.1.6).

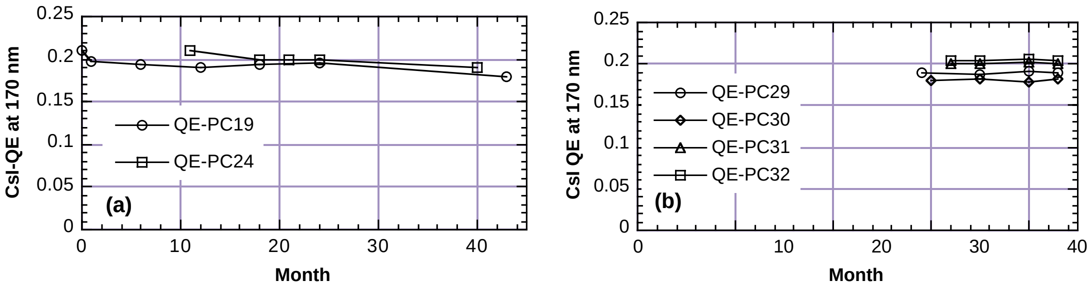

Figure 2.56: QE stability plots. Evolution with time of the QE of several photocathodes.

2.3.2.4 Proto-2: results obtained with single-particle events

Proto-2 was assembled in 1996 and the first large photocathode, PC26, tested at T11 in December 1996. The four final PCs (PC29 to PC32) were processed and tested with small radiators at T11 from June to October 1997. A first test of the detector fully equiped with four PCs and one full-size-radiator tray was performed at the SPS in November 1997. Finally, two SPS test periods were scheduled in April and July 1998, the second one with the complete radiator composed of two trays. Measurements relative to PCs evaluation are reported here while those taken with beam interacting on target are found in Section 2.3.2.6. Figure 2.57 indicates the position of the four photocathodes and of the radiator tray for the test period when only one tray was mounted.

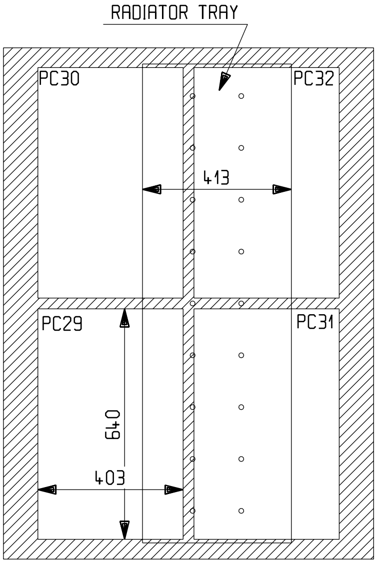

Figure 2.57: Schematic layout of proto-2 showing the position of the radiator tray relative to the four CsI pad panels (PC29 to PC32) when using a single tray at the SPS test runs in November 1997 and April 1998. For the July 1998 runs, the layout with two radiator trays is seen in Fig. 2.26.

Single-particle runs were taken to scan at three beam positions the four PCs at different particle incident angles: 0, ±2.5, ±5, $\pm7.5°$. In addition to the evaluation of the detector, these runs are used as databases to generate by software multiparticle patterns of known density by randomly overlapping single events that are fully characterized. Their analysis is found in Chapter 4.

a) The total time of exposure to the beam was about 30 days. The irradiation rate was typically 5 kHz on a beam spot of 1 cm^2 corresponding to a maximum current of 30 nA/cm^2 at maximum gain. During monitoring, neither microdischarges nor HV trips were observed, indicating a quite stable operation. Such a current density is much higher than the one expected at ALICE.
   CH_4 was mainly used as amplification gas at a flow of 30 l/h. The contamination level was kept at less than 10 ppm for oxygen and moisture. The performance of the C_6F_{14} radiator system is reported in Section 3.1.3.

b) In Fig. 2.58, the measurements of $N_{\rm res}$ and $N_{\rm pad}$ obtained with PC32 over four test periods from its production in August 1997 until July 1998 overlap, demonstrating an excellent stability of the performance for about one year. Three photocathode removal operations were done during this period using the large glove box set-up described in Section 3.2.3.3.

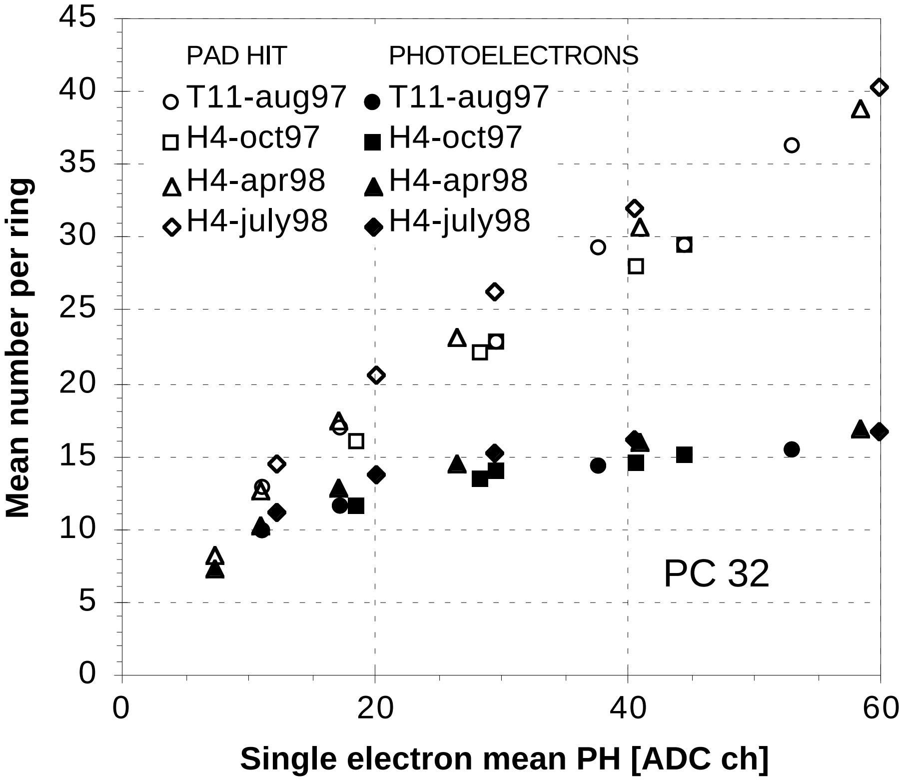

Figure 2.58: Stability of the performance of PC32. Four measurements, obtained over one year's duration, are superimposed. Operating conditions: CH_4, 10 mm C_6F_{14}, pion 350 GeV/c. One ADC channel corresponds to 0.17 fC. Mean $N_{\rm res}$ and $N_{\rm pad}$ per ring as a function of the single-electron mean PH.

c) In Fig. 2.59a, the gain variation A_0 is represented versus the chamber voltage obtained with the beam centred at the middle of each photocathode. While the same gain curves are measured in the quadrants of the chamber corresponding to PC30 and PC32, the curves are shifted by $+30$ V for PC31 and -30 V for PC29, respectively to PC30, PC32. At an operational voltage of 2050 V, that shift corresponds to a 20% variation of the chamber gain A_0. Given the relative situations of PC29 and PC31 on the detector (Fig. 2.57), the gap variation cannot be attributed to an overall deformation of the main frame due to the overpressure but to gap differences of each pad panel resulting in the adjustment procedure (frame machining) described in Section 3.1.1.2. Such a gain difference corresponds to a variation of 120 μm of the nominal 2 mm gap value. The incidence on the clustering is shown below.

d) In Fig. 2.59b, the photoelectron yields, $N_{\rm res}$, and the number of pads hit per ring of the four photocathodes are compared. A mean value of $N_{\rm res} = 14.9 \pm 1.5$ is obtained at $A_0 = 40$ ADC channels. This spread is not correlated to the different gains reported in Fig. 2.59a: PC31 and PC32, achieving the best yields, are located in gaps of low gain. This reflects, in fact, a spread in the QE value, as seen in the plots (c) and (d) of the cluster size and ratio $N_{\rm tot}/N_{\rm res}$ correlating PCs of low QE to PCs of low photon feedback. This spread is actually found acceptable in the context of our pattern recognition efficiency. Finally, proto-2 was operated in July 1998 with CH_4-iC_4H_{10} mixtures. When adding isobutane, the photoelectron yields drops down by 10–20% but associated to a significant decrease of the feedback photon yield at high gain, as shown in Fig. 2.60.

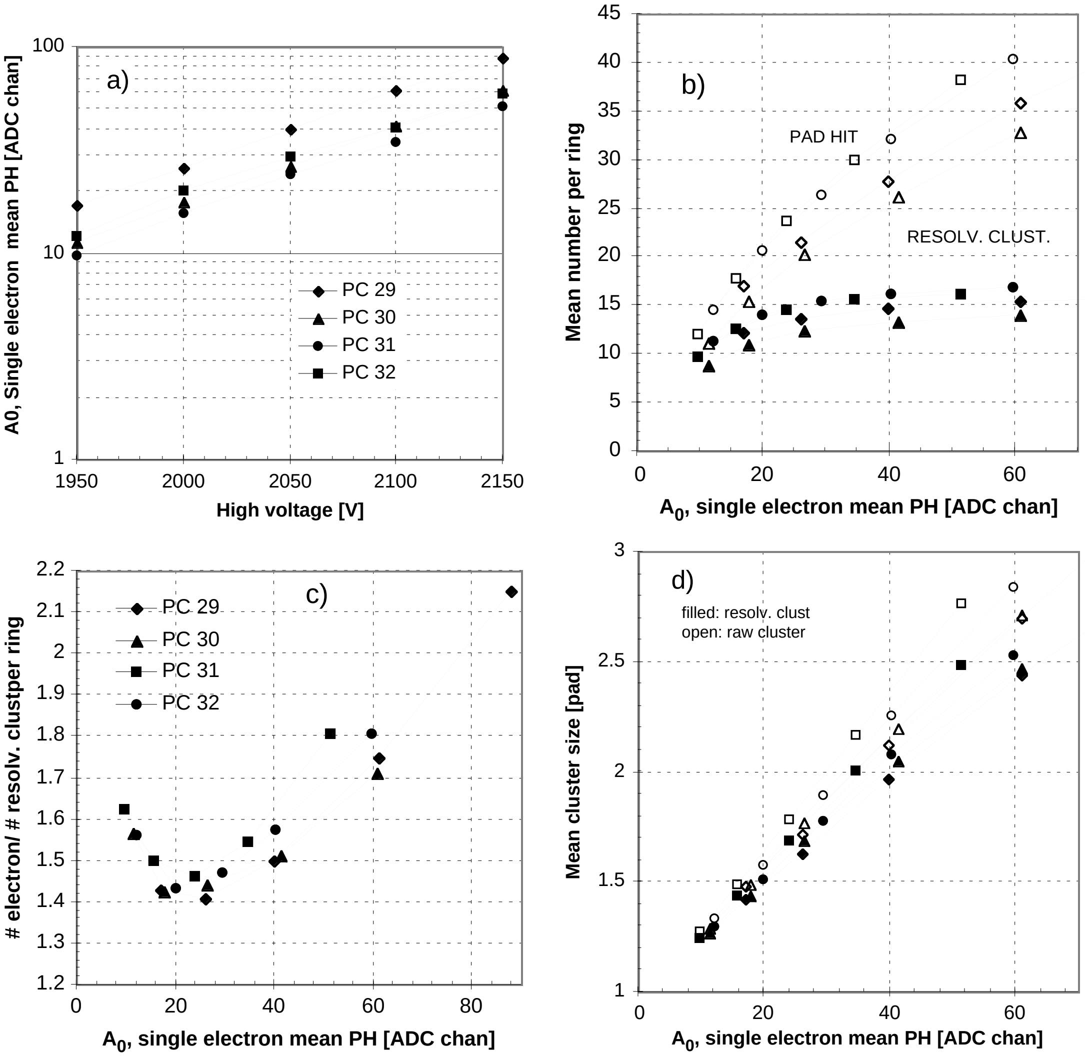

Figure 2.59: Compared performance of the four photocathodes mounted on proto-2. Operating conditions: CH_4, 10 mm C_6F_{14}, pion 350 GeV/c. One ADC channel corresponds to 0.17 fC. a) Mean single-electron PH (or chamber gain) as a function of high voltage measured at the centre of each of the four PCs. As a function of the single-electron mean PH: b) Mean $N_{\rm res}$ and $N_{\rm pad}$ per ring. c) Ratio $N_{\rm tot}/N_{\rm res}$ (feedback photon fraction). d) Mean resolved cluster size.

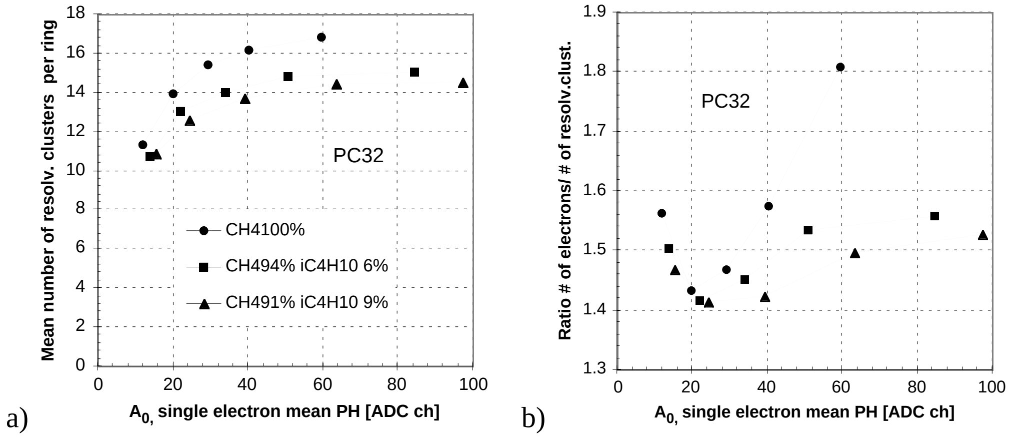

Figure 2.60: Performance comparison using different gas mixtures in proto-2. Operating conditions: PC32, 10 mm C_6F_{14}, pion 350 GeV/c. One ADC channel corresponds to 0.17 fC. As a function of the single-electron mean PH: a) Mean $N_{\rm res}$ per ring. b) Ratio $N_{\rm tot}/N_{\rm res}$ (feedback photon fraction).

2.3.2.5 Study of the angular resolution with single-particle events

The angular resolution is maybe the most important feature of a RICH detector since it is strongly correlated to the particle identification capabilities. We have carried out an investigation of all the aspects influencing the spread of the reconstructed angle distribution, based on a combined analysis of beam test and Monte Carlo events with the support of an analytical estimation of each contribution.

The Cherenkov angle is affected by the following errors:

(1) The *chromatic error*, related to variation of the radiator refractive index n with the photon energy E. It is determined by the dispersion $\mathrm{d}n/\mathrm{d}E$ of the radiator medium index and by the spread of the overall detector response over the effective photon energy range, between the CsI photoelectric threshold and the C_6F_{14} cut-off (Fig. 2.24d).

(2) The *geometric error*, related to the spread of the emission point along the particle path in the Cherenkov radiator. It depends on the ratio RW/GAP between the radiator thickness, RW, and the proximity gap width, GAP; it can be minimized by increasing GAP and reducing RW, provided the number of photoelectrons per ring is sufficient for pattern recognition (Chapter 4).

(3) The *localization error*, related to the precision with which the photon and particle impact coordinates can be measured. It is determined by the detector characteristics (pad size, sense wire pitch) and by the photon feedback.

(4) The track *incidence angle error*, related to the particle angle $\theta_{\rm p}$ and to the precision of the tracking devices. In the following, the $\theta_{\rm p}$ error, assumed to be of the order of 2 mrad at the considered incidence angles, will not be quoted in tables and plots but simply included in the calculation of the total angular resolution.

While the chromatic and geometric error are intrinsic, respectively, to the radiator properties and to the proximity focusing technique, the last two are of experimental nature.

The angle reconstruction procedure defines, between the Cherenkov angle $\theta_{\rm c}$ and each of the described variables, a relation $\theta_{\rm c} = \theta_{\rm c}(E, RW, R, \theta_{\rm p})$ from which the angular resolution, particular to the adopted algorithm, can be analytically estimated as:

$$\sigma_{\theta_{\rm c}} = [\sum_{i=1}^{4}(\frac{\partial\theta_{\rm c}}{\partial v_i}\sigma_{v_i})^2]^{1/2} \, , \tag{2.18}$$

where the variables v_i are: E, RW, R, $\theta_{\rm p}$ and σ_{v_i} are the respective r.m.s. errors.

Angle reconstruction and analytical treatment

Three methods have been used for the Cherenkov angle reconstruction, in real and simulated events. The first one, called β-*method*, provides the intrinsic angular resolution, being based on the knowledge of the particle β which eliminates the analytical dependence on n. The second one, the *loop-method*, is based on the search of the best angle through an iteration routine [67]. Figure 2.34c shows the single-photon experimental distributions of ring radius; the corresponding reconstructed Cherenkov angle distributions, either single-photon or ring averaged (with $\sigma_{\theta_c}^{\text{ring}} = \sigma_{\theta_c}^{\text{single}}/\sqrt{N_{\text{res.cluster}}}$), obtained by means of those two procedures, are shown in Fig. 2.61. Both will be described briefly here and the relative numerical results from the analytical calculation of single contributions to angular resolution will be presented. An extensive discussion about the analytical treatment can be found in Ref. [68].

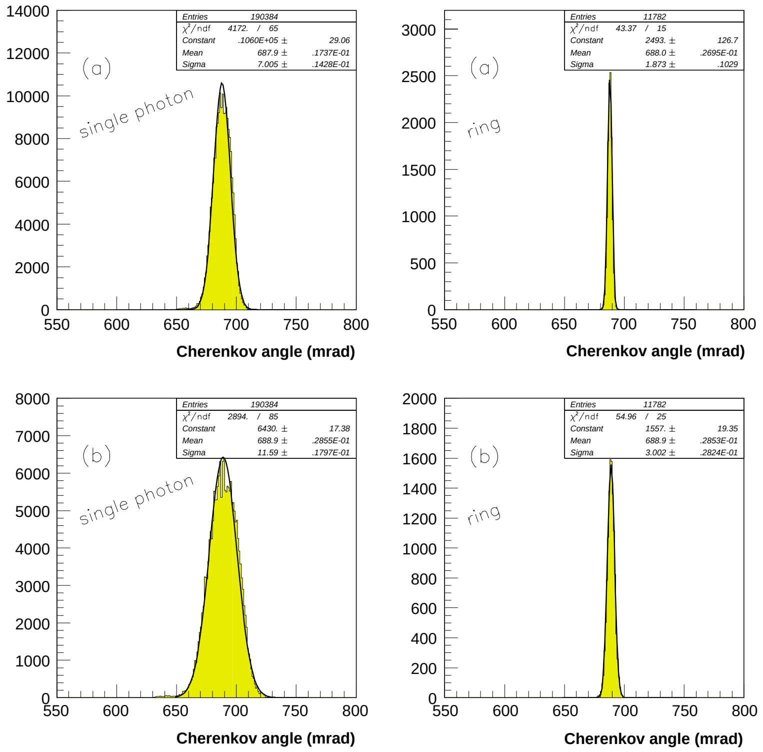

Figure 2.61: Single-photon and ring-averaged, Cherenkov angle distributions, from a) the β and b) the *loop-methods*; SPS beam test (350 GeV/c π), PC32, chamber gain $A_0 \sim 40$ ADC channels.

The third reconstruction algorithm, which produces the same results as the *loop-method*, is based on a photon geometrical backtracing; it will be presented in Chapter 4 with an application to multi-particles events.

Since the photon *emission point* in the radiator, X_{ep} and the photon energy are unknown, in all methods, the angle reconstruction is achieved by fixing them at the most probable values. In particular, X_{ep} is about 5.2 mm for perpendicular tracks in a 10 mm radiator (photons generated in the first radiator half have larger probability of being absorbed due to the longer path in the C_6F_{14}), while the average energy E_{av} is 6.85 eV over the detector response (Fig. 2.24d).

i) The β-*method*. Figure 2.62 illustrates the geometry for the angle reconstruction with perpendicular incidence particles; in the case of oblique tracks an image correction through a detector rotation is needed. The measured ring radius R can be expressed as:

$$R = \Delta R_{\text{rad}} + \Delta R_{\text{qz}} + R_0 \ , \tag{2.19}$$

where $\Delta R_{\text{rad}} = (RW - X_{\text{ep}}) \cdot \tan\theta_c(E_{\text{av}})$ and $\Delta R_{\text{qz}} = QW \tan\theta_{\text{qz}}(E_{\text{av}})$ are constant terms and $R_0 = GAP \cdot \tan\theta_0$. θ_0 can be simply expressed as a function of θ_c by means of Snell's law; then, using the Cherenkov relation $\cos\theta_{\rm c} = (n\beta)^{-1}$, with simple calculations, one can reconstruct the Cherenkov angle as:

$$\theta_{\rm c} = \arcos(\frac{\beta^2}{1+(GAP/R_0)^2}+1)^{-1/2}, \tag{2.20}$$

where GAP and particle β are known and R_0 is deduced from the measured radius through Eq. 2.19.

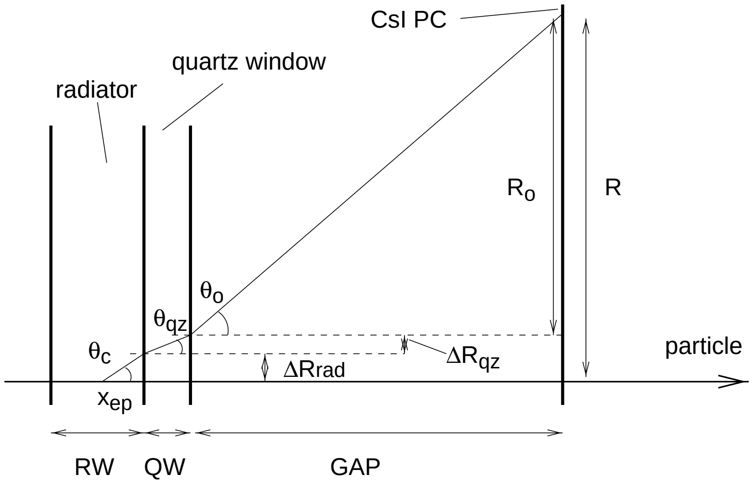

Figure 2.62: Cherenkov photon optical path through the detector and geometry for the β-*method* angle reconstruction.

ii) The *loop-method*. In the first step, the angle $\phi_{\rm c}$, defined by the plane containing the particle trajectory and the photon impact, is calculated and, assuming $\theta_{\rm c} = \theta_{\rm c}(E_{\rm av})$ and β = 1, photon tracking is executed starting from $X_{\rm ep}$ through the media up to the CsI PC, producing an impact point at a distance Δs from the measured point of coordinates ($x_{\rm c}, y_{\rm c}$). Then a new tracking is started after having increased $\theta_{\rm c}$ and $\phi_{\rm c}$ by (d$\theta_{\rm c}$/ds)Δs and (d$\phi_{\rm c}$/ds)Δs respectively, with the derivatives evaluated with a 0.5 mrad variation of each angle. The condition which stops the iteration is $\Delta s \leq 0.1$ mm.

A straightforward vector ray trace with refraction at all surfaces in the detector media gives the following equation for the photon coordinates [69]:

$$x_{\rm c} = Ra_x \ , \tag{2.21}$$

$$y_{\rm c} = Ra_y \ , \tag{2.22}$$

where

$$R = \frac{L}{a_z} + \frac{QW}{\sqrt{a_z^2+(n_q/n)^2-1}} + \frac{GAP}{\sqrt{a_z^2+(1/n)^2-1}} \tag{2.23}$$

and a_x, a_y, a_z are the photon direction cosines in the detector reference system. In the limit case RW, $QW \rightarrow 0$, an explicit solution giving $\theta_{\rm c}$ as a function of the measured quantities ($x_{\rm c}, y_{\rm c}, \theta_{\rm p}$) is obtained:

$$\cos\theta_{\rm c} = \cos\phi_{\rm p}\sin\theta_{\rm p}a_x + \sin\phi_{\rm p}\sin\theta_{\rm p}a_y + \cos\theta_{\rm p}a_z \ , \tag{2.24}$$

with $\phi_{\rm p}$ particle track azimuthal angle, $a_x = x_{\rm c}/nr$, $a_y = y_{\rm c}/nr$, $a_z = \sqrt{1-(x_{\rm c}^2+y_{\rm c}^2)/(n^2r^2)}$ and $r^2 = x_{\rm c}^2+y_{\rm c}^2+GAP^2$.

Evaluation of the r.m.s. errors

After having obtained the partial derivatives $(\partial\theta_{\mathrm{c}}/\partial v_i)$ from the relations Eq. 2.20 and Eq. 2.24, the final step of the analytical treatment is the evaluation of the r.m.s. errors σ_{v_i} which are strictly related to the detector response.

The estimation of the chromatic r.m.s. error, $\sigma_E = (\mathrm{d}n/\mathrm{d}E)\sigma_E^{\mathrm{det}}$, is important in reproducing, with either Monte Carlo simulation or analytical treatment, the measured angular resolution. As explained in Section 2.1.3.1, the assumed value for $\mathrm{d}n/\mathrm{d}E$ is 0.0172 eV^{-1}. σ_E^{det} represents the standard deviation of the detected Cherenkov photon spectrum, resulting from the convolution of all media UV-transmission with the CsI QE (Fig. 2.24d). The shape of such a distribution suggests a triangular response of the detector to UV photons and, therefore, σ_E^{det} can be approximated by $\Delta E/\sqrt{24} = 1.8/\sqrt{24}$ eV. With such values we obtain: $\sigma_E = 6.33 \times 10^{-4}$.

For the geometric r.m.s. error σ_L the calculation is straightforward:

$$\sigma_L = RW/(\sqrt{12}\cos\theta_{\mathrm{p}}) = 2.89\ \mathrm{mm}/\cos\theta_{\mathrm{p}}.$$

The total localization r.m.s. error σ_R includes the indeterminacy of both particle and photon x, y coordinates. The values used to calculate σ_R are: $\sigma_x = 2$ mm and $\sigma_y = 2.5$ mm, both for photons and particles. It is evident that both σ_x and $\sigma_y \to$ (x or y pad-size)/$\sqrt{12}$ (with 8×8 mm pad size). Besides the error introduced by the finite sampling of the charge related to the detector pad segmentation (Figs. 2.19b, Fig. 2.42) further contributions come, for photons, from the large fraction of single pad clusters for which no centroid evaluation is possible, while, for particles, they come from the photon feedback associated to the larger total charge released.

In Table 2.4 are reported the results of analytical estimations of each contribution in the two methods; for comparison, the same errors have been evaluated with the simulation program, described in Section 2.4.1, disabling suitable switches in the code in order to get only the contribution from a particular quantity. The presented values refer to $\beta = 1$ and proto-2 geometry, namely $RW = 10$ mm, $QW = 5$ mm, $GAP = 103$ mm.

Table 2.4: Single-photon Cherenkov angle errors from analytical treatment and simulation

Error	Calculation		Simulation	
	β-method (mrad)	*loop-method* (mrad)	*β-method* (mrad)	*loop-method* (mrad)
chromatic	5.7	9.4	5.9	9.7
geometric	2.5	4.1	2.6	4.2
localization	3.1	4.8	3.1	5

Optimization of the angular resolution in beam tests

The analytical treatment and the simulation have been developed aiming at a better understanding of experimental data and, hence, at the optimization of the detector response in terms of angular resolution. Several studies have been carried out in beam tests, to analyse the angular resolution dependence on:

- the Cherenkov ring radius (proximity gap dependent);
- the chamber gain (high voltage and gas mixture dependent);
- the radiator thickness;
- the particle incidence angle θ_{p}.

In Table 2.5 are reported the single errors ($(\partial\theta_{\mathrm{c}}/\partial v_i)\sigma_{v_i}$) and the angular resolution ($\sigma_{\theta_{\mathrm{c}}}$), from analytical calculation and simulation, for the *β-method*, at several ring radii. In Table 2.6 the same quantities, evaluated with the *loop method*, are shown. It should be borne in mind that the simulation $\sigma_{\theta_{\mathrm{c}}}$ values come from the reproduction of test-beam runs, thus including effects related to the detector operating conditions peculiar to each run, while the calculated values refer to a constant configuration.

In the following all the presented results are relative to the β-*method* since the β value is experimentally known with accuracy.

Figure 2.63 shows the single-photon and ring angular resolution, from measurements and simulation, as a function of the ring radius, confirming the good agreement among measurements, simulation, and analytical treatment. Besides, the results quoted in Table 2.5 and Table 2.6 point out the dominance of the chromatic error over the other contributions, at ring radii $<$ 120 mm; therefore a reduction of the localization error, which could be obtained with a finer detector segmentation, would produce a very small improvement of the angular resolution, not compensating the cost for the increased number of electronic channels.

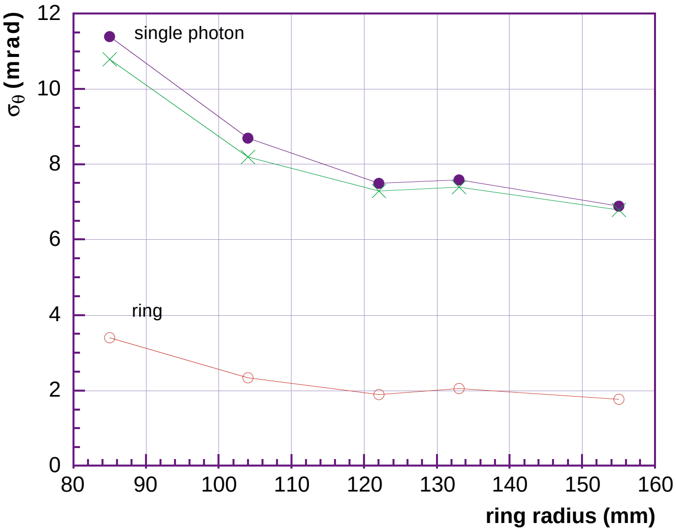

Figure 2.63: Angular resolution as a function of ring radius at $A_0 \sim 40$ ADC channels; circles: measurements; crosses: simulation. Ring radius 85 and 104 mm: data from PS beam-test (3 GeV/c p and π, $GAP = 70$ mm), PC24; ring radius 133 mm: data from PS beam-test (3 GeV/c π, $GAP = 90$ mm), PC32; ring radius 122 and 155 mm: data from SPS beam-test (350 GeV/c π, $GAP = 80$ and 103 mm), PC32.

Table 2.5: Single-photon extracted Cherenkov angle errors from analytical treatment and simulation, in the β-*method*, at several ring radii

ring radius (mm)	Calculation chromatic (mrad)	geometric (mrad)	localization (mrad)	σ_{θ_c} (mrad)	Simulation σ_{θ_c} (mrad)
85	5.76	4.83	5.95	9.7	10.8
104	5.73	3.78	4.66	8.4	8.2
122	5.71	3.26	4.01	7.8	7.3
133	5.7	2.9	3.6	7.43	7.4
155	5.69	2.53	3.12	7.1	6.8

Table 2.6: Single-photon extracted Cherenkov angle errors from analytical treatment and simulation, in the *loop method*, at several ring radii

	Calculation				Simulation
ring (mm)	chromatic (mrad)	geometric (mrad)	localization (mrad)	$\sigma_{\theta_\mathrm{c}}$ (mrad)	$\sigma_{\theta_\mathrm{c}}$ (mrad)
85	9.4	7.9	9.1	15.9	15.6
104	9.4	6.2	7.1	13.8	13.3
122	9.4	5.4	6.1	12.8	12.2
133	9.4	4.8	5.4	12.2	12
155	9.4	4.2	4.8	11.6	11.1

In Fig. 2.64 are reported the single-photon and ring angular resolution, from measurements and simulation, as a function of the chamber gain represented by the single-electron average pulse height A_0, in two gas mixtures. The stability of $\sigma_{\theta_\mathrm{c}}$ with the increase of A_0, at the considered ring radius, could be the result of two opposite effects: the larger feedback contribution, deteriorating the resolution, and the smaller fraction of single pad clusters, improving the resolution. In the mixture with $\mathrm{iC_4H_{10}}$ the single-photon resolution is slightly better than in pure $\mathrm{CH_4}$ probably due to the lower UV-transmission of $\mathrm{iC_4H_{10}}$ reducing the chromatic error and the feedback contribution; however, the ring-averaged resolution is similar to that in pure $\mathrm{CH_4}$ because of the smaller number of Cherenkov photons (Section 2.3.2.2, Fig. 2.37).

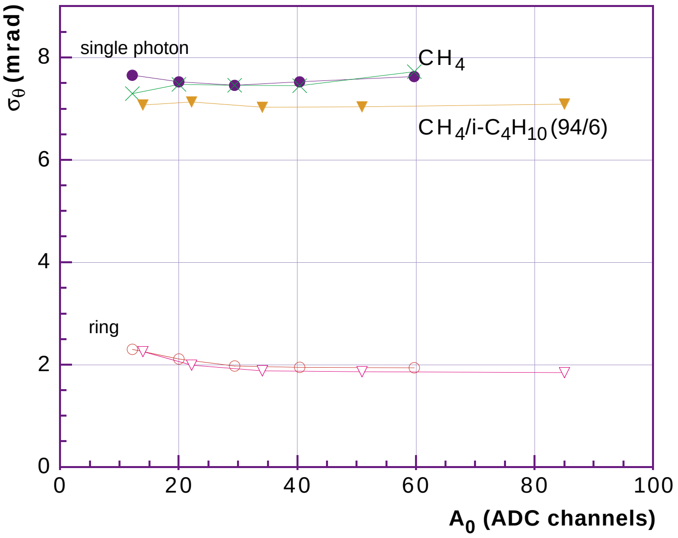

Figure 2.64: Angular resolution as a function of A_0 at $R = 122$ mm, in two gas mixtures; circles and triangles: measurements; crosses: simulation; SPS beam-test (350 GeV/c π), PC32.

In Fig. 2.65 are reported the single-photon and ring angular resolution, from measurements and simulation, as a function of the particle incidence angle θ_p. No significant deterioration of the resolution is observed in the range of θ_p where most of the HMPID expected tracks will fall.

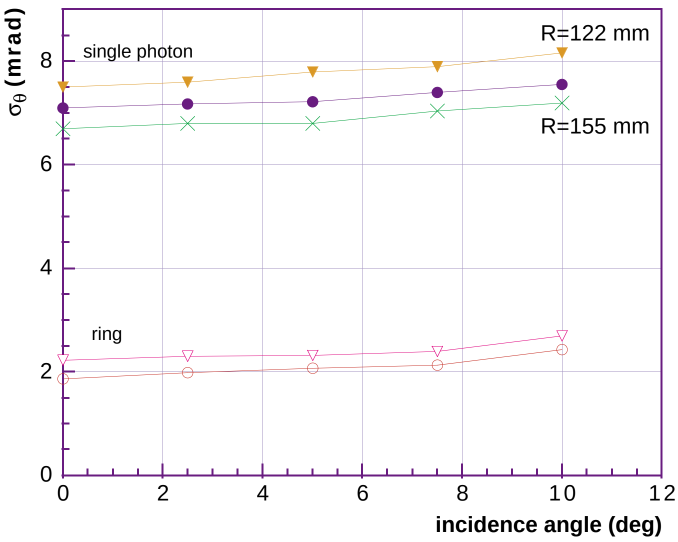

Figure 2.65: Angular resolution as a function of particle inclination at $A_0 \sim 40$ ADC channels; circles ($R = 155$ mm) and triangles ($R = 122$ mm): measurements; crosses: ($R = 155$ mm) simulation; SPS beam-test (350 GeV/c π), $R = 122$ mm: PC30 and $GAP = 80$ mm, $R = 155$ mm: PC32 and $GAP = 103$ mm.

Finally, Fig. 2.66 shows the single-photon and ring angular resolution, from measurements and simulation, as a function of the radiator thickness RW. The small variations of the single-photon σ_{θ_c} are related to the changes of ring radius and radiator transmission with RW, while the ring σ_{θ_c} increases, as expected, at smaller RW as a consequence of the reduction of emitted Cherenkov photons. In general all the observed discrepancies between simulation and measurements could be explained by the difficulty in evaluating correctly the detector rotations used for the angle reconstruction.

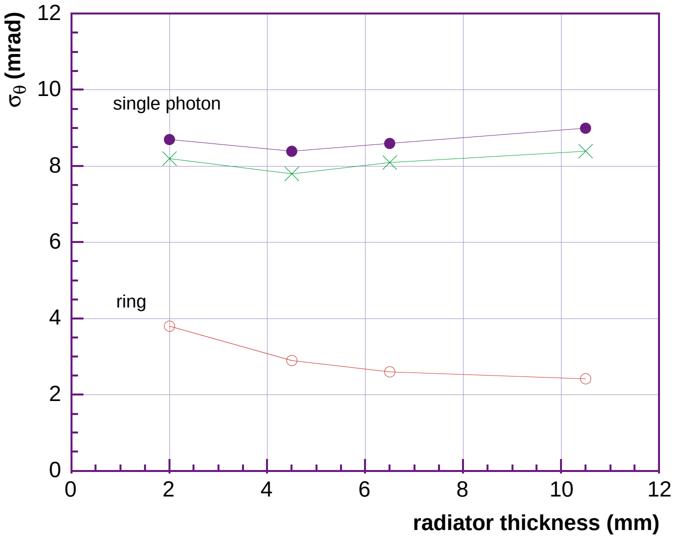

Figure 2.66: Angular resolution as a function of radiator thickness at $R = 104$ mm; circles: measurements; crosses: simulation; PS beam-test (3 GeV/c π), PC24.

2.3.2.6 Proto-2: results obtained with multi-particle events

We present the results obtained by exposing proto-2 to multiparticle events at H4 using a telescope composed of four pad chambers described in Section 2.3.1.2. Two test periods were devoted to this data taking, the first one in April 1998 using a single radiator and the second one in July 1998 with the full radiator (see Fig. 2.57 showing photocathode and radiation implementation). For both periods, PC29 to PC32 were mounted on proto-2.

Track multiplicity and occupancy

The track multiplicity distribution obtained by analysing real events from pion–beryllium interactions is shown in Fig. 2.67.

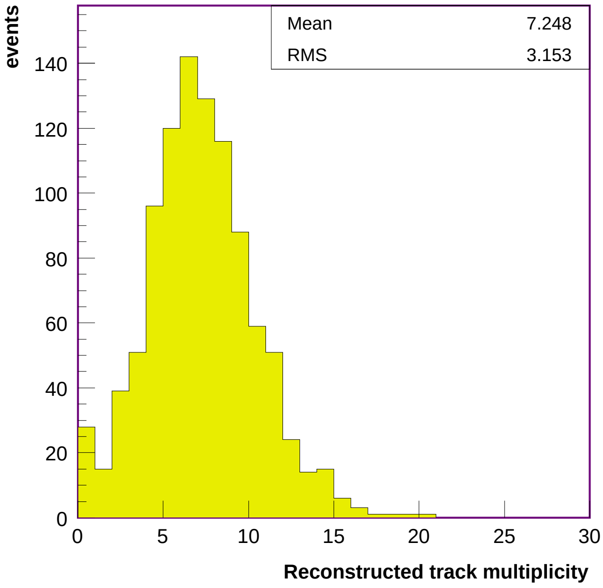

Figure 2.67: Track multiplicity in the HMPID evaluated in π^-–Be events.

The acceptance of the proto-2 is larger than the telescope acceptance, therefore only a fraction of the particles produced are tracked in the telescope. On average, seven secondary particles reach the RICH plane but there are also events with more than 20 tracks. Since no sweeping magnet has been employed in the test, particles hit the proto-2 in a very narrow region around the beam as we can recognize by plotting the distribution of the distance between the impact point of each track on the RICH plane and the beam line (Fig. 2.68).

Consequently, the cathode plane is exposed to a very large track density, as shown in Fig. 2.69. The track density on the HMPID detector has been evaluated by counting the number of tracks contained in annulus regions, 2 cm wide, at a distance d, moving from the beam line to the outer region and dividing it by the chosen fiducial area.

The colour Fig. 2.ii shows a superposition of raw data from 1000 real interaction events. The relative occupancy is shown in Table 2.7.

Table 2.7: HMPID occupancy at different distances from the beam line for two different sets of anode–cathode voltages.

Distance (cm)	2000 V	2100 V
10	10%	15%
30	6%	9%
40	5%	8%

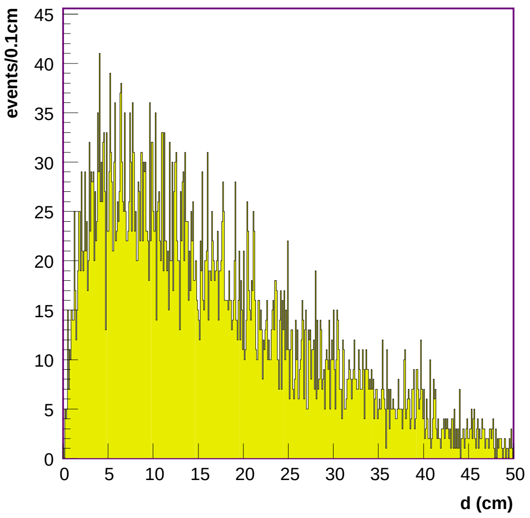

Figure 2.68: The distribution of distances d of track impact points measured on the HMPID cathode plane from the beam line.

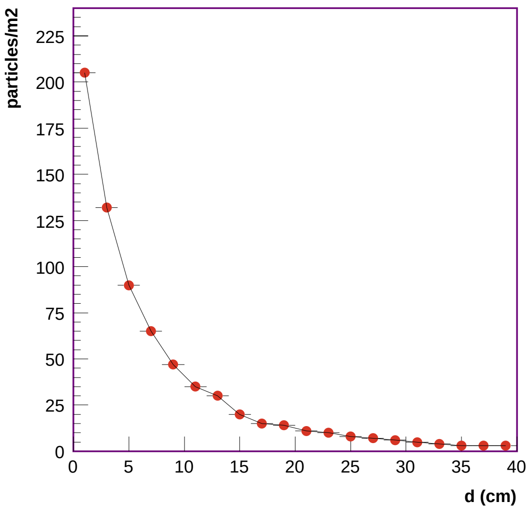

Figure 2.69: Track density on the HMPID cathode plane in real π^-–Be events (see text).

SPS data pattern recognition

The SPS ALICE facility represented a formidable ‘test bench’ for the HMPID prototype in terms of particle density and background as already shown previously. Moreover, SPS data will allow the pattern recognition algorithms to be tested in environmental condition that might also be more severe than those anticipated in the ALICE heavy-ion runs. In order to accomplish this last point, an accurate GEANT simulation of the telescope that takes into account secondary interactions and multiple scattering effects was used to evaluate the tracking capability of the telescope. Tracking errors were accounted for with regard to the spatial resolution of the proportional chambers, and their efficiency according to the specification given in Section 2.3.1.2. Since three pad chambers out of four have a good spatial resolution in the horizontal projection, whilst only one gives a good accuracy in the vertical projection (see Table 2.2 on page 42), tracks are reconstructed by applying the method ‘by view’. In this method, the first step is to reconstruct track projections onto the xz plane and later in the yz plane, z being the beam axis. Track projections are then associated only to those candidate tracks that point back to the target region defined by a box of 15 mm side. Since the pad chamber efficiency is larger than 95$\%$, the reconstruction method requires that every track projection must have a hit in each pad chamber. In Fig. 2.70, the tracking efficiency is shown as a function of the number of tracks generated.

The telescope allows the correct reconstruction, and therefore the association of the respective impact point on the proto-2 plane in almost 85$\%$ of the particle trajectories, also in events with 16 tracks pointing to the proto-2. The average momentum of those particles that, being produced in the interaction of a pion beam of 350 GeV/c on a Be target, impinge the HMPID, is about 40 GeV/c. Therefore the multiple scattering weakly contributes to the accuracy in reconstructing the particle trajectories. The measured angle resolution $\sigma_{\theta_{\mathrm{p}}} = 1$ mrad is mainly due to the geometry of the pad chambers and their specific spatial resolution. The analysis of the real data based on the Hough transform method, so far developed as discussed in Section 4.3, is in progress. The method seems robust enough also when applied to recognize Cherenkov patterns belonging to tracks that cross the proto-2 plane in a very small region.

A fully reconstructed SPS event is shown in colour Figs. 2.iii and 2.iv.

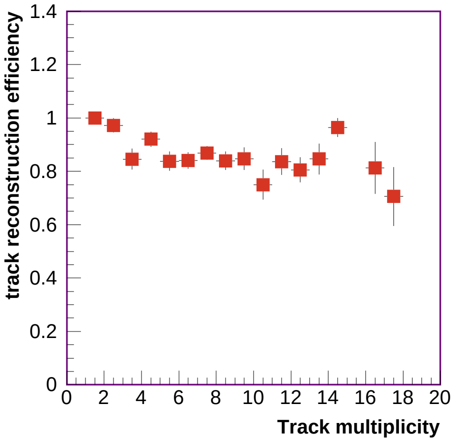

Figure 2.70: Track reconstruction efficiency versus the number of simulated tracks per event.

2.3.2.7 Ageing and 'heavily-ionizing' events

Besides the degradation provoked by contaminants, it has been shown in Section 2.1.1.4 that a CsI photocathode operated in a MWPC may be damaged by the impact of the ion clouds of each avalanche. The ion impact rate expected at the ALICE operating conditions has been evaluated from the GALICE event simulation program, discussed in Chapter 4, which provides the charged primary and secondary track densities and associated photoelectron yields. The ion charge per photoelectron and MIP are taken as 8×10^{-14} and 1.2×10^{-12} C, respectively, at a maximum gain of 5×10^5. According to the densities and rate given for minimum bias collisions in Table 2.8, the total ion charge rate amounts to 5×10^{-11} C/cm^2 s^{-1} at ALICE operating with lead beams.

Table 2.8: Track densities and rates in Pb–Pb collisions

Collisions	track/m^2	photoelect/m^2	rate (kHz)
Central	100	1000	0.1
Minimum Bias	25	250	10

In comparison, the beam rates routinely used at the test beams were equivalent to $3\times\ 10^{-8}$ C/cm^2 s^{-1}. The charge density integrated over a 1 year (10^6 seconds) lead run at ALICE amounts to 0.05 mC/cm^2, was largely overcome during the test exposure without showing any degradation on the photocathodes, agreeing with the laboratory results shown in Section 2.1.1.4.

Integrating over 10 years of operation at ALICE (proton, calcium, lead modes [9], Section 12.5.3) results in a charge density of 1.2 mC/cm^2. For comparison, the irradiation test performed with a laboratory set-up shows a stable QE up to 2.5 mC/cm^2. More ageing tests will be pursued in 1999.

In addition to the class of relativistic tracks, the rate of heavily ionizing events was also evaluated using FLUKA simulation (see Chapter 4). They originate from nuclear reactions and fast neutron interactions occuring in the MWPC gap or its vicinity. As seen in Fig. 2.71, such spectacular reactions were indeed observed in proto-2 during the SPS tests and simulated in GALICE. Neutron interactions correspond to such a local release of energy (MeV range) that they are visible as current pulses, usually self-limited by space charge saturation. However, they represent a potential risk of discharges.

In 1995–96, a relevant information was obtained from the exposure during two periods of four weeks of a CsI-based imaging detector built in our group for the NA44 experiment, using lead beam on target. The CsI photodetectors, part of the Threshold Imaging Cherenkov detector (TIC [11]) were located close to the lead beam dump and were delivering high burst current (100–400 nA). However, the magnetic spectrometer in use at NA44 was designed such that very few charged particles were traversing the gaseous radiator of the TIC without even crossing the photodetectors. Hence, it is expected that a large part of the current was produced by neutrons. During these periods, the performance has been found stable and the detector operation satisfactory.

In conclusion, although the ageing of CsI photocathodes is at the present time neither well quantified nor fully understood, our detector has been found stable under ion rates exposures much larger that the one expected during the ALICE operation.

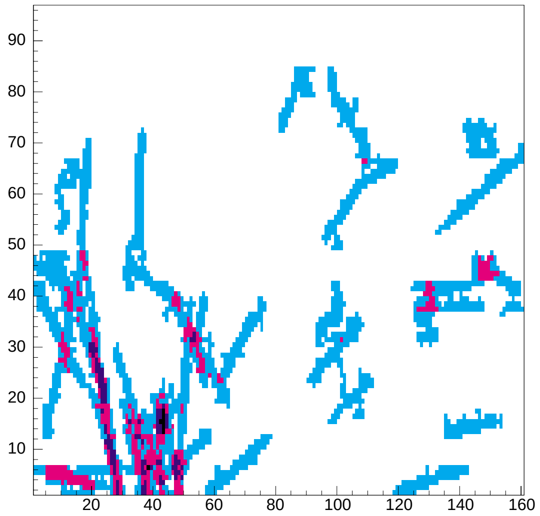

Figure 2.71: Integrated map showing 39 patterns with a cluster size larger than 60 pads. They have been found when analysing 5000 pion–Be events. As seen in Fig. 4.2 on page 155, they correspond to hadronic interactions with the CsI pad plane.

2.4 Event analysis and Monte Carlo simulation

Although the data aquisition is accomplished with a threshold corresponding to a 2–3 sigma of the pedestal variation, mainly for data volume compression, the analysis of each event is preceded by a further cleaning from electronic noise by a 4–6 sigma thresholding. Owing to the good linearity of the FE electronics over the full dynamical range (Section 3.1.4) no corrections of the PH spectrum are required. A typical event is shown in Fig. 2.32 on page 44: it is characterized by clusters of pads relative either to the ionization released by the MIP particle (in the middle) or to the detected Cherenkov and feedback photons (along the ring). As also seen in Fig. 2.32, three different regions can be singled out in such a picture:

1) a MIP region, where the particle is expected to cross the detector;
2) a fiducial area where all Cherenkov photons are detected, determined by particle momentum, detector geometry, UV transmission of traversed media and CsI quantum response;
3) the remaining part of the detector active area, populated mainly by background (electronic noise, feedback photons, cosmic ray ionization, etc.).

Figure 2.34a shows 6000 overlapped events, illustrating the topography of the different fiducial zones. The impact position of particles and photons, for clusters of more than one pad, is evaluated with the centroid finding method, while for single-pad clusters it is assumed to be in the pad centre. Once the MIP centroid has been found, the Cherenkov fiducial zone can be located in the pad plane and the main quantities characterizing the event, inside and outside that region, are estimated. The knowledge of the pad PH, besides a better localization through the centroid method, allows the evaluation of the chamber gain and the single-electron detection efficiency from the cluster PH distribution. Indeed, according to the rather good symmetry of the signal induced on the pads (Section 2.1.2.3), the clusters can be classified into three categories depending on their size and shape (Fig. 2.72):

- class 1: clusters of one, two or three pads (row or L-shaped) when the PH maximum is in the central pad, assumed to correspond to single photoelectrons;
- class 2: clusters of three pads when the PH maximum is not in the central pad, assumed to correspond to two photoelectrons;
- class 3: clusters of more than three pads, assumed to correspond to two or more photoelectrons.

Clusters are first counted as *raw* clusters and after image processing as *resolved* clusters. Figure 2.72 presents the cluster PH distribution for each class, from beam-test events with proto-2 operated with CH_4 at 2100 V. In those conditions the class 1 PH distribution is generally exponential and the single-electron average PH (A_0), namely the chamber gain, can be deduced from the slope of the fit (also reported in the figure). However, it has been deduced from the simulation that a fraction of such clusters is generated by more than one electron, owing to the overlap of a second Cherenkov photon or feedback photon.

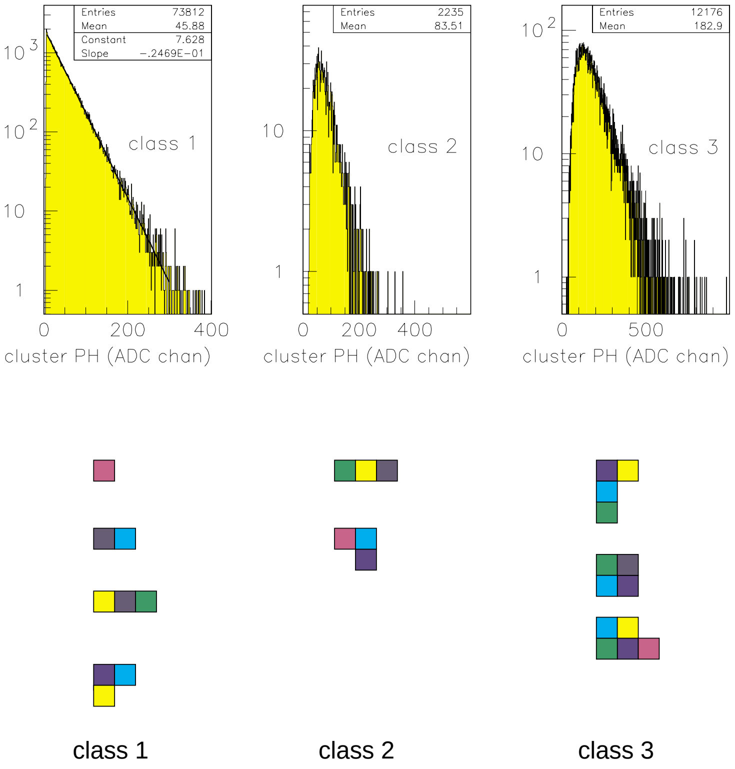

Figure 2.72: (top) The total pulse-height distributions of the three classes of *raw* clusters and (bottom) the geometrical features for each class (the darker the grey tone, the larger the pad pulse height).

The average and the shape of the PH distributions relative to class 2 and 3 clusters, compared to that of class 1, indicate clearly the contribution of two or more photoelectrons. In the majority of the cases those large clusters can be *resolved* into smaller sized clusters: when n local PH maxima are found in the original raw cluster, n resolved clusters are created. The pads in the original raw cluster are associated to a given resolved cluster according to the closeness to the local maxima. When a pad is at the same distance from two maxima, it is associated to both corresponding clusters, with a PH contribution weighted by the PH of the two maxima. Such a procedure improves the localization accuracy of Cherenkov photons: because of the small anode–cathode gap (2 mm) and the larger pad size (8 mm) most of the feedback photons are converted on the same pad hit by the primary photon and the probability that such local maxima are related to Cherenkov photons is quite large.

The main goals of the event analysis are the CsI photocathode response and the Cherenkov angle resolution. The last topic has already been discussed in a previous section. The quantities related to the detection performance are: total number of pads/event, total PH/event, number of raw-resolved clusters/event, raw-resolved cluster size, radius and reconstructed Cherenkov angles (single-photon and ring average). Figure 2.34 shows the respective distributions obtained in the SPS beam test of proto-2 at a chamber voltage of 2100 V. The tool which allows the interpretation of the experimental average values of such distributions is an originally developed Monte Carlo program generating RICH events which can be analysed using the same software adopted for the real beam-test events.

2.4.1 Monte Carlo simulation

The Monte Carlo simulation program *richsim* has been used to obtain very useful information mainly about the CsI photocathode quantum efficiency and to evaluate the many factors affecting the Cherenkov angular resolution. All physical processes, from the Cherenkov emission to the signal induction on the photocathode pad plane, are taken into account. The input parameters are: type of Cherenkov radiator (NaF or C_6F_{14}), its thickness RW and UV-transmission in the 160 to 220 nm range, proximity gap width, O_2 and H_2O contamination (in ppm), CsI QE curve, detector rotation angles, mean pedestal and sigma for electronic noise, chamber gain, photon feedback rate.

Cherenkov photon generation and propagation

The number of photons generated along the particle trajectory in the radiator is drawn from a Poisson distribution with mean N_{av} given by the integral of the Frank–Tamm relation over the energy range established by the CsI photoelectric threshold and the transmission of media traversed by the photons (Fig. 2.24d):

$$N_{\mathrm{av}} = RW \int (\frac{\alpha}{\hbar c}) Z^2 \sin^2 \theta_{\mathrm{c}}(E) \mathrm{d}E \; ; \tag{2.25}$$

α is the fine structure constant, Z is the charge of the particle and θ_{c} is the Cherenkov angle. The emission point in the radiator is uniformly distributed while the Cherenkov photon energy is sampled from a density function

$$f(E) = 1 - \frac{1}{n^2(E)\beta^2} \; . \tag{2.26}$$

Each Cherenkov photon is propagated through the detector, undergoing absorption and interactions at the media boundaries. The transmission T_{we} of the collection and cathode wire electrodes is evaluated on a statistical basis according to the relation:

$$T_{\mathrm{we}} = 1 - \frac{2r}{s \cos{(1 + \tan^2\theta_0 \sin^2\phi_{\mathrm{c}})^{-1/2}}} \; , \tag{2.27}$$

where r is the wire radius, s the wire pitch, θ_0 the Cherenkov photon angle in the proximity gap and ϕ_{c} the Cherenkov photon azimuthal angle.

Photoconversion at the CsI photocathode

The quantum efficiency curve used to reproduce the PC32 beam-test data is shown in Fig. 2.24d. The QE is, by definition, the probability of photoconversion of an incident photon at a given energy; therefore any QE curve includes the reflection losses which, in turn, depend on the photon incidence angle on the photocathode surface. That has to be taken into account when comparing QE measured in the laboratory with perpendicular UV beam and the quantum response of the same photocathode to Cherenkov photons having oblique incidence. Indeed, in the simulation, a suitable correction for that effect is included: the

PC32 QE curve is such that it can be compared to laboratory measurements and the photoconversion probability is calculated as QE$\cdot(1 - R_\theta)/(1 - R_\perp)$. R_θ, $R_\perp$ are the Fresnel reflection probability calculated using a CsI complex refractive index and including a correction for surface roughness.

Table 2.9 reports the photon losses in the proto-2 configuration. Out of 324 Cherenkov photon/MIP produced in the radiator (in the range 5.7–7.8 eV) 21 are converted into photoelectrons.

Table 2.9: Photon losses out of 324 produced per MIP in the radiator (in 5.7–7.8 eV)

Loss mechanism	Number of lost photons
Absorption in C_6F_{14}	48
Absorption in quartz	52
Absorption in CH_4	6
Absorption in wire electrodes	22
CsI inefficiency	175

Generation of signal on pads and photon feedback

Each photoelectron initiates an avalanche on the anode wire which is closest to the photon impact-point inducing a signal on the neighbouring pads. In addition, the signal corresponding to the ionization released by the MIP in the 4 mm sensitive gap is generated as the convolution of the signal relative to each ion pair. The total charge of any single-electron avalanche is sampled from an exponential distribution having a mean deduced from beam-test data. Then a further contribution coming from feedback is added, with the number of generated feedback photons $N_{\rm pf}$ proportional to the total avalanche charge: $N_{\rm pf} = K_{\rm pf}Q$. A feedback rate, $\overline{K_{\rm pf}}$, of 0.05 (for charge measured in ADC channels) reproduces best the experimental data. This value includes corrections not only for the so-called *visible gain* (Section 2.1.2.5) but also for a reflection at the anode wires which enhances the number of the feedback photons directed towards the photocathode. The photons are generated taking as a source the avalanche at the sense wire, with an isotropic angular distribution and sampling the wavelength spectrum described in Section 2.1.2.4. Such photons, if converted on the photocathode, will generate new avalanches and in turn new feedback. The electrostatic model used for the signal induction is based on the single-parameter Gatti formula described in Section 2.1.2.3.

Electronic noise contribution and PH thresholding

The electronic noise is generated on each pad with a Gaussian distribution having a standard deviation determined experimentally. Finally a PH thresholding with pedestal subtraction produces the event that can be analysed by means of the same test beam data-analysis program.

2.4.2 Analysis results: radiator thickness and HV scan

Figure 2.73 shows the analysis results for the radiator thickness scan with PC24, PS 3 GeV/c beam-test. The agreement between real and simulated data is acceptable, also considering that the QE curve for PC24 used in the Monte Carlo is the one obtained from the NaF-runs analysis which produces an approximate estimation of the differential QE (Section 2.3.2.2). The non-linearity of the plotted quantities with the increasing radiator thickness is due to the saturation induced by the geometrical overlapping of the larger number of Cherenkov photons per ring (Fig. 2.33). In addition, enlarging the radiator thickness makes more effective the photon absorption in the higher energy range, close to the C_6F_{14} cut-off. As a result the emitted photon spectrum shifts towards lower energies corresponding to a reduced quantum response of the photocathode.

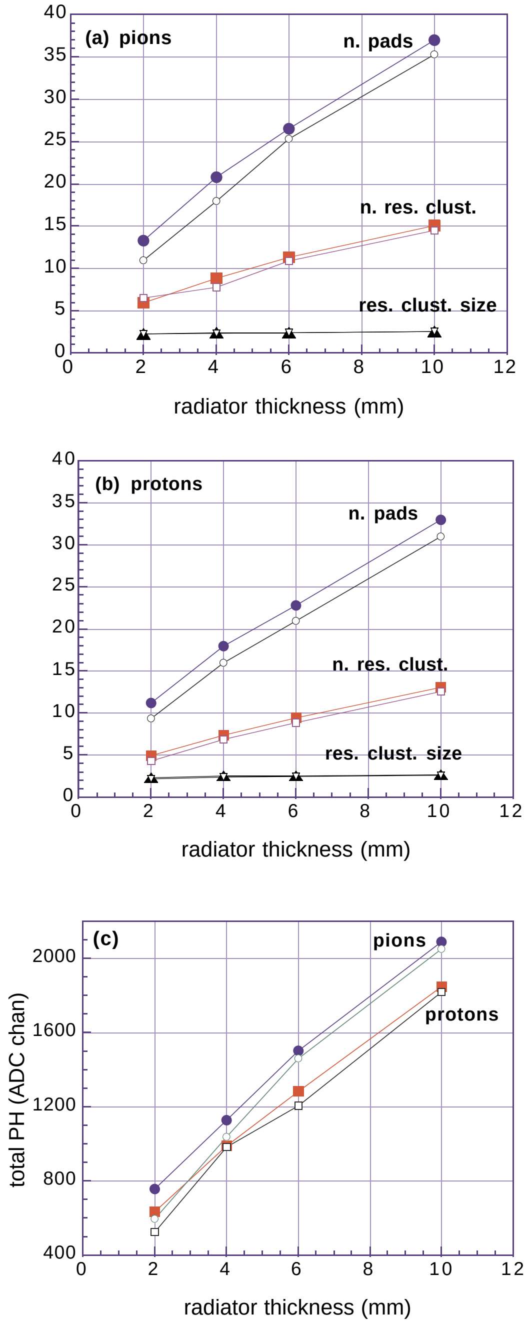

Figure 2.73: Radiator thickness scan in proto-1, PC24, 3 GeV/c PS beam test, chamber voltage 2250 V; full symbols: measurements; empty symbols: simulation. Number of pads, number of resolved clusters and resolved cluster size for pions (a) and protons (b) and total PH per event (c) as a function of the C_6F_{14} thickness.

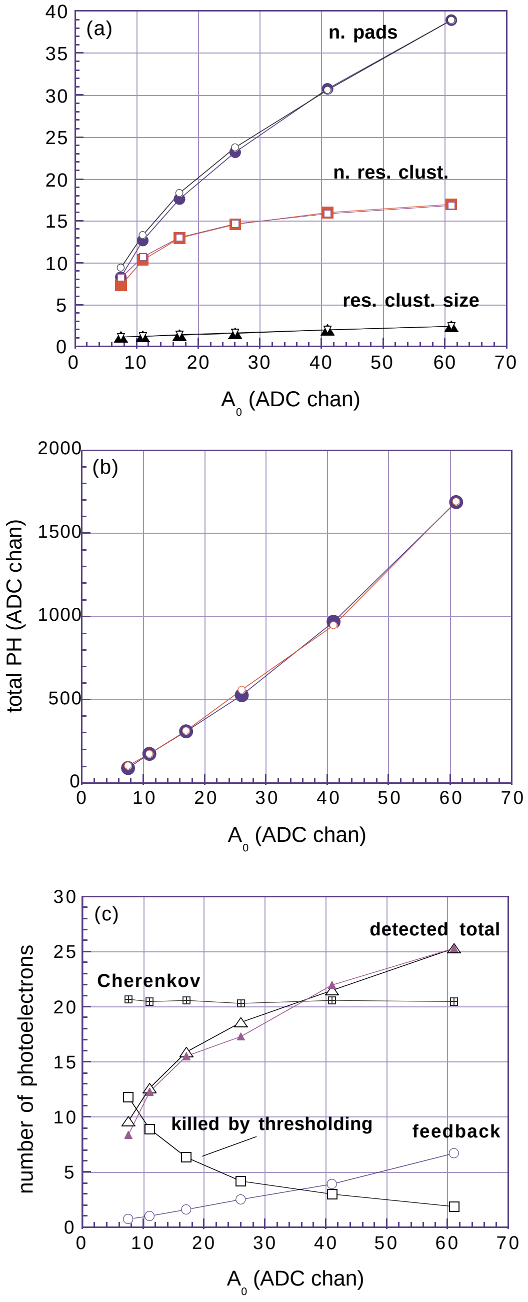

Figure 2.74: Chamber gain scan in proto-2, PC32, 350 GeV/c π SPS beam test; full symbols: measurements; empty symbols: simulation. Number of pads, number of resolved clusters and resolved cluster size (a) and (b) and total PH per event; in (c) the measured total number of detected photoelectrons estimated is compared to the same quantity obtained from the simulation, with an evaluation of the single contributions (detected total = Cherenkov+feedback–killed by thresholding).

In Fig. 2.74 are reported the results of the chamber high voltage scan in proto-2. The variation of the main quantities in plots (a) and (b) can be interpreted in the light of plot (c) where all the contributions to the total number of detected photoelectrons are presented: while the saturation in the number of resolved clusters is due to the plateau of the detection efficiency and the geometrical overlapping, the increase in the number of pads is related to the enhancement of the feedback contribution.

As a concluding remark, the simulation allowed to estimate a factor of merit $N_0 = 45$ cm^{-1} with PC32 and a chamber gain $A_0 = 41$ ADC channels (single electron detection efficiency of 90%).

figure 2.i

figure 2.ii

figure 2.iii

figure 2.iv

3 Detector description

Introduction

This Chapter is composed of two parts. The first part is dedicated to the design and construction of a HMPID module, including all the prototyping and technical work carried out for proto-2 on the main elements of the CsI RICH system, such as the photodetector, photocathode, radiator vessel, C_6F_{14} circulation, electronics and CsI evaporation system. Some specific procedures to produce and assemble them will be described here, as well as the calculations and test results on which their designs were based, optimized and validated.

In the second part, the system aspects of the HMPID detector are described.

3.1 Module production and final prototype

3.1.1 The photodetector

The detector is constructed by stacking a series of independent metallic frames which are designed in such a way that simple machining ensures:

- the parallelism and a controlled thickness of the two anode-to-cathode gaps of the MWPC,
- the parallelism between the radiator trays and the photodetector.

Peralumin is used as the raw material for the frame to guarantee optimum surface quality (porosity, polishing) and flatness during machining. The sealing between the frames is achieved by machining standard grooves for the Viton O-ring joints. In order to minimize the outgassing, care was taken to avoid using composite, organic material and gluing, in favour of metallic components. We shall first describe the production of the pad cathode panel, then the sequence of the frames and the related assembly procedures.

The main representations of the detector are shown in Fig. 3.1 as a cross-section and in Fig. 3.2 as an axonometric projection. In Fig. 3.2, the final HMPID module is represented, based on six apertures for pad panels and three radiator trays. Proto-2 was built according to the same design but reduced to four apertures and two radiator trays, keeping the same dimensions in the other direction (see Fig. 2.26).

3.1.1.1 The pad cathode panel

Besides acting as a substrate coated by the CsI film, the pad-PCB also has to be designed in such a way that all the pads are electrically connected to the external Front End Electronics (FEE), ensuring optimum sealing with respect to the chamber gas.

The first pad-PCBs were designed to solve the FEE implementation, using standard two-layer circuit technology. Pads and traces were etched on a copper-clad G10 foil and protected with a chemical deposit of gold of 0.5 μm thickness. The open ‘through-holes’, traversing the PCB to carry the signal from each pad to the external traces were filled with tin soldering. As shown in Section 2.1.1.5, the CsI films were of poor quality and not efficient.

In order to avoid unwanted contact between the CsI film and copper substrate, it was decided to cover the copper with a 7 μm thick nickel layer which is known to be sufficiently dense. In addition, more care was devoted to surface preparation by using different kinds of polishing.

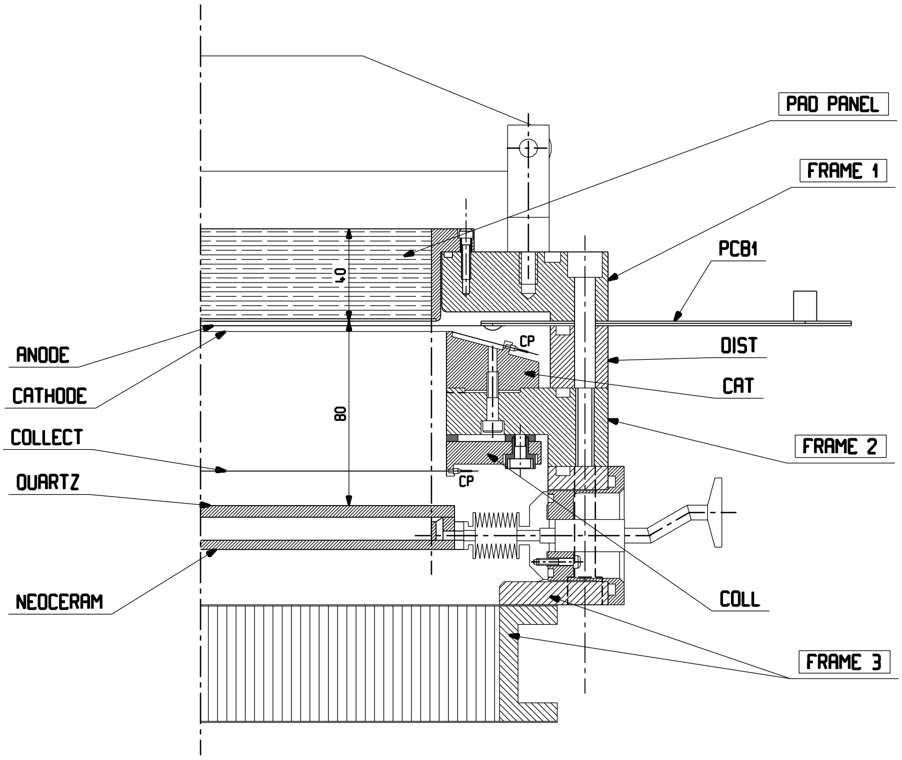

Figure 3.1: Cross-section of a HMPID module in a plane parallel to the anode wires.

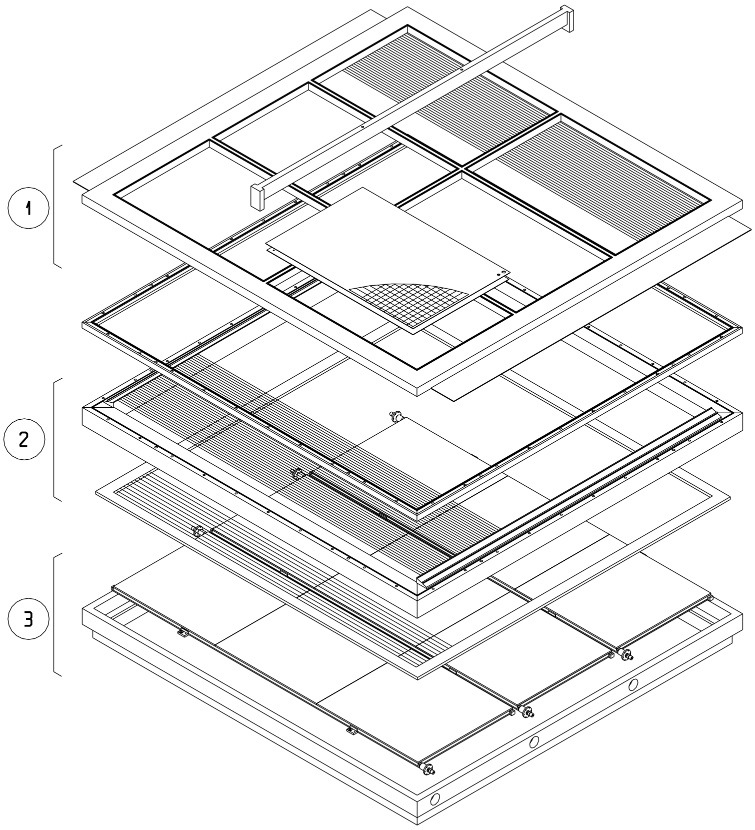

Figure 3.2: Axonometric view of a HMPID module. (1), (2), (3) are the elements described as Frame-1, Frame-2, Frame-3, respectively.

Two main lines of procedure are still under consideration, using two- or three-layer circuits, as shown in Fig. 3.3. Since they may also have several options, we refer to Ref. [1] where details are given and describe here only the main characteristics.

The solution based on three layers avoids having ‘through-holes’ and provides a perfectly gas-tight circuit, but uses more expensive technology (see Fig. 3.3a). First, on a two-sided copper-clad G10 foil, 0.5 mm thick, the pads are etched on one side and connected to traces on the other side by metallized holes. Then, a second circuit one-sided copper-clad G10 foil, 0.2 mm thick, where traces needed for electronic connections have been etched, is glued to the first one in such a way that by blind hole drilling and further metallization, the electrical connections are created between the two circuits. Mechanical and chemical polishing on the pad side are then performed on the circuit. Finally, the nickel and gold layers are deposited either by chemical or electrolytical processes. According to the technology in use, the structure and chemical composition of these layers are quite different and are expected to influence the germination and growth of the CsI film evaporated on them. Microstructural studies are used to characterize these layers. The solution based on two-layer circuits (see Fig. 3.3b) has electrical connections made by open ‘through-holes’ which are filled by glue insertion and protected by a new metallic layer necessary to mask each hole and achieve a smooth surface on the side where the pads are. The rest of the process follows the same steps as mentioned above. Comparable QE performance is at present obtained with both solutions. Given the large number of operations involved in this procedure, the final choice will be made on the basis of the one ensuring the best reliability in the mass PCB production. Further developments will be pursued with a VUV scanning set-up, as described in Section 3.1.5.2.

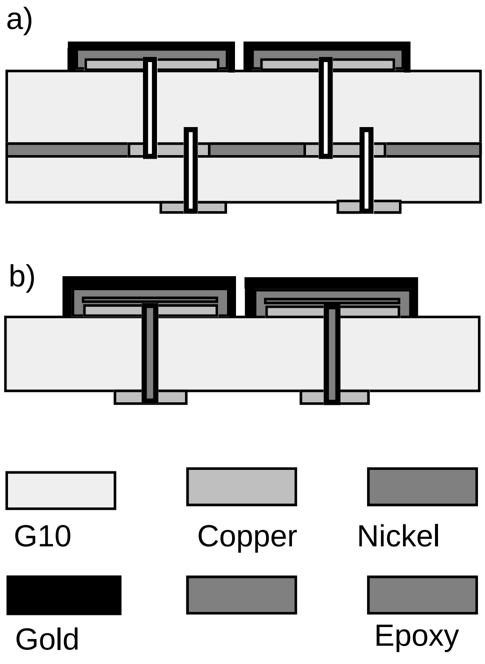

Figure 3.3: Schematic cross-sections of the pad PCB: a) version without through holes; b) version with through holes.

In order to minimize the length of connections between the pads and FE channels and their dispersion, groups of 48 pad channels are made corresponding to a pattern of 8×6 pads in the X and Y coordinates, respectively. This modularity in fact fits to three FE chips and available SMD connectors. The connection is established by soldering flexible Kapton foils on the back of the pad-PCB (see Fig. 3.4a,b). At the other end of the pad-PCB there is an SMD flat connector (ERNI-004863) with 50 contacts, which will be plugged into the FE board to ensure easy dismounting of the FE electronics (see Fig. 3.4b,c).

The last operation is a test that all pads are electrically connected to the SMD connectors.

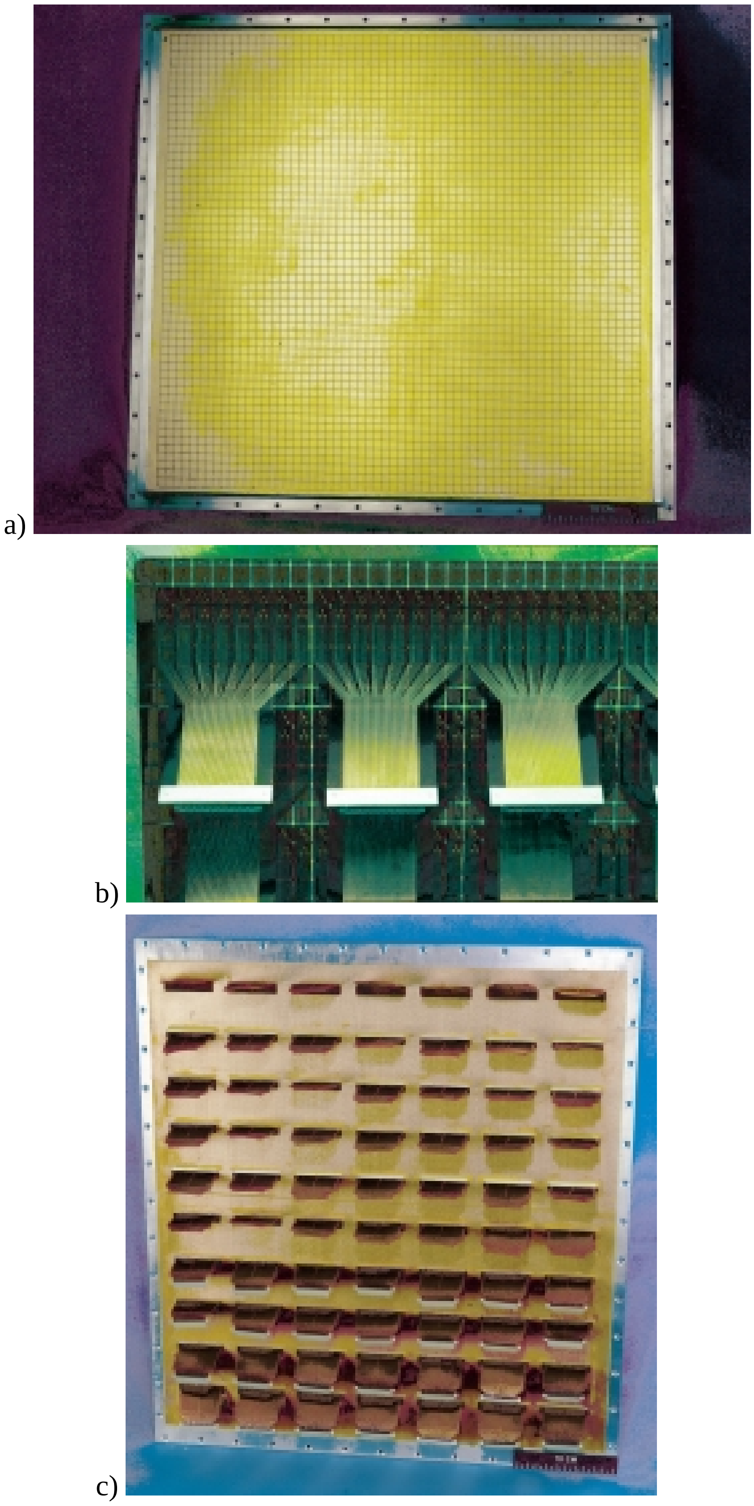

Figure 3.4: a) Pad panel viewed from the side of the pad PCB. The size is of 60×56 pads of 8×8 mm^2 each. One sees the aluminium frame used to tighten the pad panel on the detector.
b) Close-up view of the back of the pad PCB, where Kapton circuits (carrying by groups of 48 the pad signals to the FEE) are soldered.
c) Pad panel viewed from the side of the FE electronics showing the Kapton circuits sticking out of the sandwich panel. Some of the circuits hold the flat connector (48 channels) to be plugged into the GASSIPLEX boards.

Assembly of the pad panel

Since no drastic requirements are imposed with respect to the detector dead zone, the pad panel is assembled as a sandwich composite structure inserted in a metallic frame (see Fig. 3.4a). This technology was selected in order to provide a stiff structure with a minimum of material and efficient gas sealing of the pad panels. The panel structure is schematically shown in Fig. 3.5.

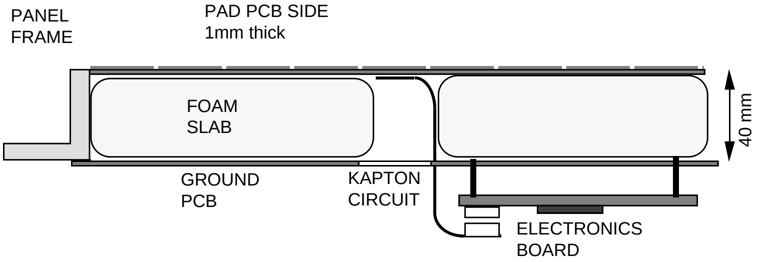

Figure 3.5: Schematic cross-section of the pad panel. The foam is Rohacel-51-HF, 52 g/l. The glue in use is Araldite epoxy AW106-HV 953-4.

The composite structure is made of the pad-PCB and Kapton circuits spaced by a 40 mm thick foam plate from another circuit referred to as the ground-PCB. The Kapton foils are soldered on the pad-PCB in rows, leaving a free space of about 30 mm between them for placing foam strips of that width (see Fig. 3.4b). The grooves thus formed allow the Kapton foils to come out through apertures created in the ground-PCB. The pad-PCB is first glued to the frame on a granite table and the necessary ground connections made with conductive glue. Then, the elements are stacked and glued together under proper load, keeping the pad-PCB in contact with the granite table.

A flatness of $\pm 50\ \mu$m is achieved over an area of 64×40 cm^2. The ground-PCB makes good grounded electromagnetic shielding. The pins necessary for plugging the FEE boards are implemented last.

3.1.1.2 Frames

Frame-1

As shown in Fig. 3.1 and Fig. 3.2, Frame-1 holds the elements forming half of the wire chamber, i.e. the pad cathode and the anode wire plane. A design is described which allows the gap value and the parallelism of the two planes to be controlled within $\pm 50\ \mu$m, allowing the pad cathode to be removed with a simple procedure. For this purpose, Frame-1 consists of a plate with six openings in which six pad cathode panels are mounted from the outside, tightened with screws and sealed with O-rings.

The anode wire plane: installation and HV supply

On the opposite side to the pad panel, the anode wires are stretched between two PCBs glued on opposite edges of the frame (PCB1 in Fig. 3.1). The wires are 20 μm diameter, tungsten rhenium gold plated, 861/60, grade L, quality 4.

As the two PCBs are glued in grooves, further machining is necessary to adjust them to the same level as the frame and ensure a flat surface for the O-ring to run over. As the cathode pads are held at ground potential, the high voltage must be applied to the anode wires. The PCBs are designed such that they act as a high-voltage feedthrough for every wire by using a three-layer configuration.

As shown in Fig. 3.6, 20 μm wires are soldered to pads etched at one edge of the circuits. Then, in order to pass over the frame region, the trace is enclosed between two G10 foils of 1 mm thickness ensuring HV insulation. Another advantage is that the O-ring is in contact with a perfectly smooth surface of the PCB whilst running over all the wires put under HV. Outside the chamber and at each end of the anodic wires, traces are pulled in groups of eight to a well-insulated flat connector. On one side of the chamber, a PCB is used to make the HV distribution. Each wire is fed through a 1 MΩ resistance implemented on small cards grouping eight resistors. All these cards can, in turn, be fed by a single trace linked to the HV supply. All these external components, which are put under HV, are enclosed in a housing that can be flushed with a dry gas (nitrogen) in order to eliminate any external surface-leakage current caused by moisture.

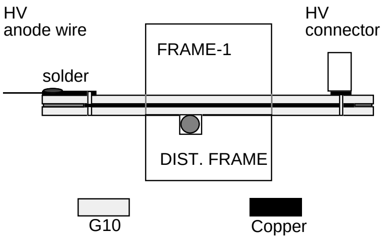

Figure 3.6: Schematic cross-section of the anode wire circuit.

It has been checked that in the case of possible sustained discharges, one or several wires could be disconnected from the HV source without affecting the operation of the remainder of the wire plane. It is therefore foreseen to study a scheme where each group of eight wires is fed by an independent HV line that can be interrupted by a remote-controlled HV switch in case of severe defects. This would allow the chamber to still be operated, losing only a 32 mm wide slice.

The connectors available on the opposite PCB may be used for implementing electronics for reading out fast wire signals, after convenient decoupling by HV capacitances. This facility was used locally during the test period and makes it possible to check that every wire is actually under voltage and to supply a current for controlling the wire stretching (see below).

Support line for anode wires

Given the length of the anode wires of 120 cm, a support line structure is needed to ensure the stability of the wires against the electrostatic force. For assembly reasons, this element can only be implemented between the pad cathode and the wire plane as the second cathode also consists of wires. As shown in Fig. 3.7, the support line is attached along the rod traversing Frame-1 through the middle, perpendicular to the anode wires, permitting the pad panels and the second wired cathode to be removed. This region is, in any case, a nonactive area of the pad cathode, making the inefficiency created by the support line of no importance. The sagitta and the stability of the wire under the electrical field have been studied with a full-length mock-up [2]. The safest solution is to make the gap anode-to-pad slightly smaller than the opposite one in order to have a constant resultant force directed towards the pad cathode, such that the anode wires are pressed against the support line.

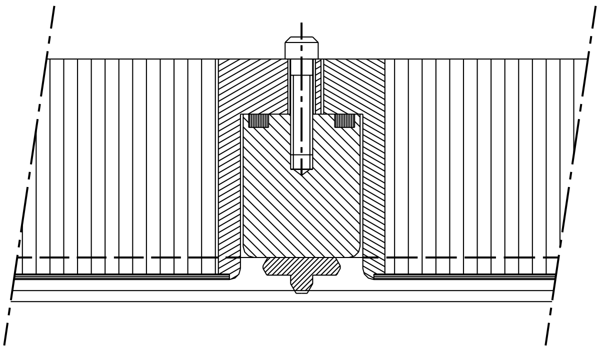

Figure 3.7: Cross-section of Frame-1 showing the implementation of the anode wire support structure. To achieve the necessary electrical insulation, the material in use is a machinable ceramic, Macor.

Soldering of the anode wires

The anodic plane is in fact divided into three parts by the dead zones created by the 30 mm wide aluminium transverse rods of Frame-1. Each part has 96 wires and is terminated at both edges by two field degrading wires of 50 and 100 μm, in such a way that the 20 μm wires overlap the full pad sensitive area. To give the correct spacing the wires are positioned using a comb, stretched by a weight of 40 g and held to the PCB by tin soldering. A flux is used to help the solder to run easily and at the end of the wiring, alcohol is used to remove the flux.

The wires are located in thin triangle-shaped grooves, 0.2 mm deep, machined at the surface of the Macor support line. For optimum safety (against vibrations, etc.), a very small amount of glue (AV144-2/HV 997) was added thus fixing the wires in these grooves.

The wire tensions are measured using CAEN instrument SY502. The tension is obtained by measuring the frequency of each wire fed with a known DC under a known magnetic field.

Adjustment of the anode/pad gap thickness

Once the anode plane has been soldered, the distance between this plane and the upper side of Frame-1 is measured at several points all around the frame. The thickness of each pad panel is also measured at several points between the pad surface and the inner side of its frame. After averaging and adjustments, the difference between these two measurements must be made equal to the nominal distance anode-to-pads, i.e. 2 mm. This is possible by machining, if necessary, the inner side of the pad-frame in the final adjustment.

Frame-2

Frame-2 holds two wire planes and its thickness contributes to the depth of the proximity gap of the RICH (see Figs. 3.1 and 3.2).

One of the wired planes is the second cathode of the photodetector MWPC that is kept at ground potential. It is made of 100 μm diameter gold plated Cu/Be wire, spaced by 2 mm. The wire specification is CuBe2, hard, flash Ni, gold 1 μm. This spacing ensures 95% transparency to the incident Cherenkov photons and acts as an electric screen between the proximity and MWPC gaps. In order to avoid having a new PCB for holding these wires, crimping pins were used to support the stretching tension, fixed at 200 g/wire. Two independent machined bars are used to position and plug in the metallic crimping pins, allowing thus simpler drilling than would be the case of the large frame itself. The reason these bars have an oblique side (see Fig. 3.1) is to create a shape surrounding the edge of the PCB where the 20 μm wires at HV are soldered, such that the distances are much larger than the 2 mm gap. In this zone, the electrical field is kept at a low level, thus avoiding any breakdown from the anodes to surrounding grounds. The PCB is also long enough to avoid any leakage current along the circuit surface.

Once the cathode is wired, the distance between the wire plane and the upper side of Frame-2 is measured all around the frame. Then, the gap between the wired cathode and the anode planes can be adjusted to its nominal value by machining the distance frame, interleaved between Frame-1 and Frame-2, to the necessary thickness.

The second wire plane is the collection electrode which creates a small electric field in the proximity gap in order to drain primary ionization, deposited by the relativistic particles, instead of drifting into the MWPC gap. This electrode is fixed to Frame-2 by means of an independent frame. It is made of the same 100 μm diameter gold plated Cu/Be wire spaced by 5 mm also using crimping pins. It is raised to about 300 V. The gap between the collection electrode and the radiator tray should be kept to a minimum since primary ions created in that interval are repelled against the insulated radiator window and might create deposit.

Frame-3

A light composite panel is fixed on Frame-3 to close the detector (see Figs. 3.1 and 3.2). The three radiator trays are held by locating parts attached to the panel. Details are given in the next section which is devoted to the radiator array. It should be mentioned that the depth of the proximity gap can be increased by inserting a distance frame between Frame-2 and Frame-3.

A photograph of proto-2, installed at the SPS test beam, is shown in colour Fig. 3.i.

3.1.2 The radiator array

This section is dedicated to prototype studies of the large radiator tray to be used in a HMPID module. Smaller devices used at the test beam were described in Section 2.3.1.1.

3.1.2.1 Introduction

The rather high C_6F_{14} and SiO_2 densities, 1.68 g/cm^3 and 2.1 g/cm^3, respectively, and the need to minimize the total amount of material traversed by the incoming particles, required a careful investigation and optimization of the radiator vessel mechanical structure. In addition, since the HMPID performance depends strongly on transparency in the UV spectral range 160–220 nm and long-term stability of the perfluorohexane radiator, the emphasis was put on the choice of material. Indeed, in the definition of the structural mechanical design of the radiator vessel, we benefited from the long-term operational experience of DELPHI and SLD who employed C_6F_{14} in their RICH system [3].

3.1.2.2 Radiator description

The liquid radiator container consists of a tray made of a glass-ceramic material called Neoceram, closed by a UV-grade fused silica plate, as shown in Figs. 3.8 and 3.9.

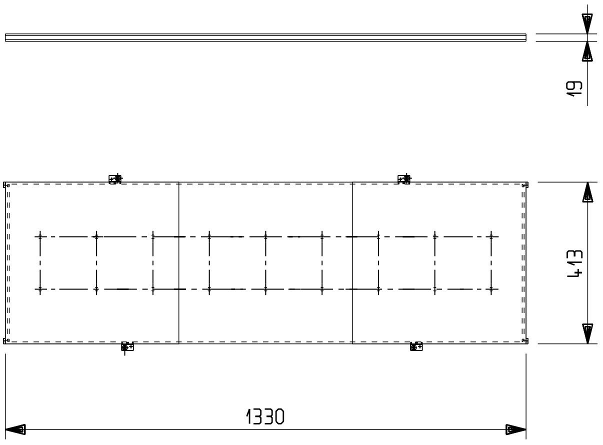

Figure 3.8: Schematic views of a radiator tray. The upper window is assembled by gluing three quartz plates together.

Neoceram, with its thermal coefficient of 0.5×10^{-6} °C^{-1}, ensures that no mechanical stress is induced on the vessel by temperature gradients. The limited size of commercially available fused silica plates and the need to keep the hydrostatic load within reasonable levels determined the thickness and size of the radiator vessel elements: in the current geometry, the quartz window is 5 mm thick, whilst the Neoceram base plate is 4 mm thick. The vessel elements are glued together with Araldite AW106. The liquid radiator inlet and outlet are obtained by gluing two stainless-steel pipes on the opposite sides of the Neoceram tray, the outlet always being at the highest location.

To withstand the hydrostatic pressure, 24 cylindrical spacers are glued to the bottom plate on one side and the quartz window on the other side. Spacers consist of fused silica rods with a diameter of 10 mm placed in two rows of 12 equidistant elements.

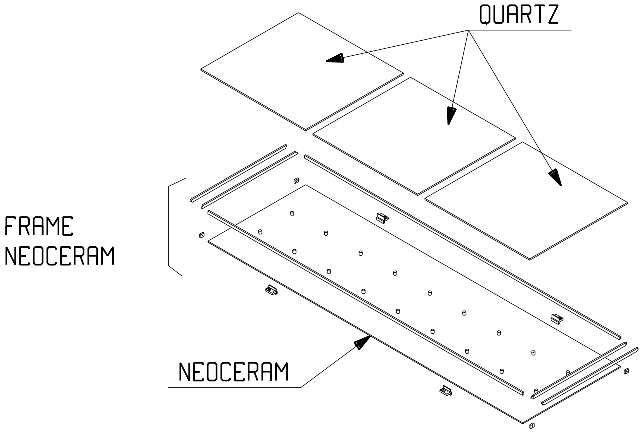

Figure 3.9: Axonometric view of the elements composing a radiator tray. Four carbon fibre feet are used to locate the tray in the detector back plane (Frame-3).

Each HMPID module has three independent radiator trays 1330×413 mm^2, supported by a stiff composite panel made by sandwiching 50 mm of an aramide-fibre epoxy honeycomb material between two 0.5 mm thin layers of aluminium (Fig. 3.10). The radiator vessel and the fluid dominate the bulk of the detector material, estimated to be 17% X_0 (Table 3.1).

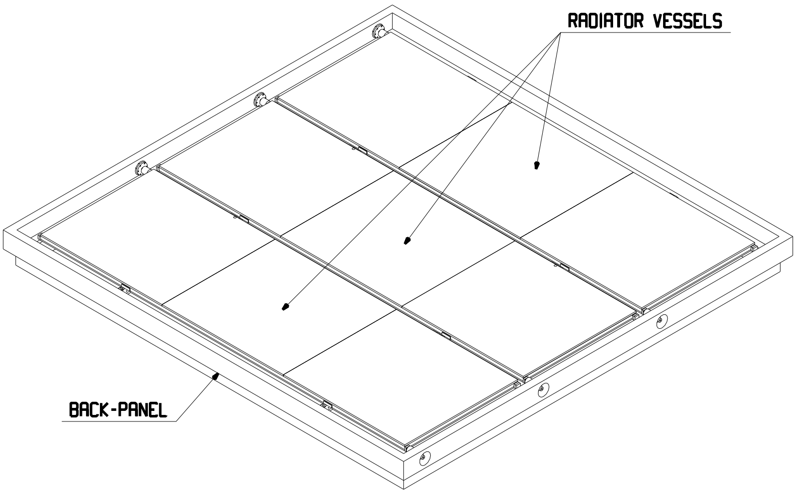

Figure 3.10: Perspective view of the HMPID back panel with the three radiator trays and feedthroughs for the liquid circulation.

Table 3.1: Material budget

	Material thickness [mm]	X/X_0
Honeycomb back panel	50	0.02
Neoceram plate	4	0.03
Quartz window	5	0.05
C_6F_{14}	10	0.05
PC panel + FEE	1	0.02

3.1.2.3 Assembly of a radiator tray

The long-term tightness of the radiator vessels depends critically on the quality of the assembly procedure. After delivery, the Neoceram elements and quartz windows are first visually inspected by looking for unwanted scratches on the surfaces or broken edges. A control of the dimensions and face parallelism is then performed to check that each part has been machined according to the specifications. Quartz windows are also inspected by measuring their UV transmission curve. Damaged or inaccurately machined pieces are rejected. Whilst the quartz plates used in the prototyping phase were always delivered within the specifications, the Neoceram parts needed a specific treatment, since suppliers only deliver large plates.

The procedure adopted for the Neoceram part is as follows:

- a diamond saw cut to almost the final size, within a tolerance of 0.5 mm;
- an accurate finish on a lathe provided a dimensional accuracy better than 0.05 mm.

Before gluing, all elements must be carefully cleaned to remove any trace of pollutants on the surfaces. The following steps are therefore performed:

- liquid soap (ph 5.5) and bi-distilled water washing;
- cerium oxide powder (the smallest size grain for a weak abrasive power) gently moved on the entire surface in order to remove more resistant chemical pollutants that might still be present;
- bi-distilled water washing to remove the cerium oxide powder;
- pure ethyl alcohol washing and drying with nitrogen gas flow.

The radiator is assembled by gluing the Neoceram pieces to the quartz windows in a dust-free room kept at 35°C constant temperature with a relative humidity of less than 50%. An optical table is used for assembly to ensure the right flatness over the whole surface of the radiator.

The lower Neoceram plate is at first glued to the thin Neoceram side walls by using a home-made tool that distributes the Araldite AW-106 at a constant rate to ensure that the glue thickness is 0.15 mm everywhere. On the assembly table there are fiducial marks that allow the surveyors to position the Neoceram pieces before gluing them.

In parallel, the final quartz window is obtained by gluing the three constituent plates using a specially built tool to guarantee a final flatness of the resulting plate (better than 0.05 mm).

Once the Neoceram box is ready, the same assembly table is employed to glue the quartz window on the Neoceram side walls. Finally, each radiator vessel is finished by installing the liquid Freon connections.

The following tests must be performed at the end of the radiator vessel assembly phase in order to ensure that each part works properly.

He leak test

The radiator vessel is mounted in a supporting structure and is flushed for several hours with pure He (flow rate = 10 l/h, 6 mbar overpressure due to an oil bubbler in the outlet line). The tightness test is performed by using a He sniffer with a sensitivity level of ($10 \times 10^{-7}\ \mathrm{atm} \times \mathrm{cm}^3$/s). The entire set of glue joints as well as the inlet and outlet Freon fittings must be completely scanned. A satisfactory result is obtained when no appreciable leak is detected above $3 \times 10^{-7}\ \mathrm{atm} \times \mathrm{cm}^3$/s.

He diffusion rate through the vessel quartz plates

This measurement is performed by keeping the radiator vessel in a sealed box flushed with pure nitrogen (at 50 l/h). The radiator vessel is flushed with He at a rate of 10 l/h. Helium diffuses through the quartz windows. Its content in nitrogen is measured with a He sniffer at the outlet of the nitrogen circulation circuit. If the radiator is He tight, the He content must be below $\sim$ 0.36 ppm.

C_6F_{14} circulation test
The vessel is tested during C_6F_{14} filling and evacuation operations. A visual inspection ensures that the inlet and outlet fittings are free.

Pressurization test
The quartz vessel is filled with C_6F_{14} and left for three days under a hydrostatic load of 103 mbar corresponding to an additional C_6F_{14} liquid column of 20 cm.

3.1.2.4 Full-scale prototype mechanical test

A full-scale prototype of the liquid radiator vessel was made completely in Neoceram, with 16 equidistant spacers, and tested in several hydrostatic loading conditions. Strain, stress and deflection states of the two base plates measured in the test were compared with the Finite Element Analysis (FEA) by means of the IDEAS package, installed on a HP C180 workstation. In Table 3.2, we report the relevant material characteristics employed in the FEA. The adhesive joints were considered to have a minimum thickness of 0.150 mm.

Table 3.2: Material parameters of the radiator vessel components

Material	Young Modulus (N/mm^2)	Poisson coeff.	Density (g/cm^3)
Neoceram	80 000	0.24	2.51
Quartz	70 000	0.17	2.20
Araldite AW106	3700	0.39	1.75
C_6F_{14}	–	–	1.68

An analysis with quadratic SOLID elements was necessary to achieve an accurate evaluation of the effective radiator stress and deformation states, particularly with respect to the plate joints to spacers and ribs.

The study was first performed on the radiator placed vertically in order to limit the computational cost and time by taking advantage of geometric and load symmetries.

The refined mesh adopted for the whole radiator finite element model consists of 22 016 quadratic SOLID elements for a total number of 108 050 nodes. Each plate and the edges, coupled to the shorter side of the radiator, were modelled with two layers of elements. A finer mesh refinement of the glued regions, by means of submodelling, was necessary to improve the analysis of the adhesive behaviour. However, this further mesh refinement has to be related to the effective adhesive film which would otherwise resulte in an overestimated stress state evaluation of the adhesive joints. The study was then extended to the radiator vessel prototype tilted in the most critical load condition in the ALICE HMPID structure (Chapter 1) in order to analyse stresses and deformations and to obtain the necessary information for the design of the radiator vessel in its final configuration.

3.1.2.5 The ALICE HMPID radiator vessel prototype loading

The analysis of the prototype, accomplished with the Finite-Element Method (FEM), was verified using a hydrostatic loading test executed on the radiator placed both vertically and in the most critical load condition.

The test data acquisition was performed by using the BEAM software installed on a personal computer and the UPM100 data logger unit. Two types of strain gauges were used to measure the stress and deformation states: rectangular rosettes were attached to the upper plate at the location of the supports and also close to the edges. The orthogonal strain gages were positioned between the spacers parallel to the radiator sides. Two comparators on both sides of the geometrical centre of the upper and lower plates were used for the deformation measurements.

Tests were executed by overloading the ALICE HMPID radiator vessel prototype, filled with C_6F_{14}, with an extra 200 mm of liquid column corresponding to a maximum pressure of 103 mbar for the vertical position and 131 mbar for the most critical orientation. In addition, stress and deformation data were recorded by overloading the radiator vessel with 100 mm of liquid column. Other measurements were collected during filling and draining operations to check whether the equipment operates properly.

The stress value calculated in the region where the strain gauges localized the largest stress and the plate deflection measured by the comparators are reported in Table 3.3. Their respective FEA predictions are also reported for a comparison.

Table 3.3: Comparison between the test measurements and the FEA evaluation

	Measurement	Finite-element method
Maximum stress σ	12.5 N/mm^2	12.7 N/mm^2
Plate deflection	0.081 mm	0.079 mm

Since the strain gauge measurements confirmed the overall accuracy of the FEA, the FEM has been applied to evaluate the optimal number of spacers in the final radiator tray structure.

Results achieved on each radiator constituent with a tray containing 24(18) spacers are shown in Table 3.4.

Table 3.4: Maximum principal stress (N/mm^2) versus C_6F_{14} hydrostatic pressure in the radiator tray with 24(18) spacers ($h = 0$ corresponds to the full radiator, while $h = 100$ corresponds to an additional liquid column 100 mm high, that takes into account the anticipated overpressures due to the liquid circulation system)

Radiator tray element	$h = 0$	$h = 50$	$h = 100$
Quartz plate	$8.31(11.16)$	$9.00(12.26)$	$9.68(13.36)$
Neoceram plate	$11.6(16.93)$	$12.72(18.63)$	$13.84(20.33)$
Quartz spacers	$7.36(10.91)$	$8.12(12.06)$	$8.88(13.20)$
Neoceram frame	$4.10(4.33)$	$4.47(4.73)$	$4.84(5.13)$

The safety coefficients for a brittle material have to be evaluated in the frame of the maximum stress criteria. In our case, the bending strength concerns the quartz and Neoceram plates (67 N/mm^2 and 100 N/mm^2, respectively), while the quartz tensile strength must be used for the spacers. The ratio between such quantities and the relevant maximum stress represents the ultimate safety coefficient allowed for brittle material in absence of significant flaws and defects.

By considering that flaws and defects could affect the plate and the spacers, and more significantly differences in spacer and rib dimensional tolerances could cause an initial curvature and an unwanted prestress state of the plates, it is prudent to adopt a minimum safety coefficient as large as 7 for both Neoceram and quartz.

As a consequence of the constraints imposed on the plate thickness, a spacer configuration with at least 24 elements is required. A photograph of two radiator trays mounted in a back plane is shown in colour Fig. 3.ii.

3.1.3 The C_6F_{14} circulation system

3.1.3.1 Introduction

A liquid recirculation system was designed and built at CERN for the tests of the prototype at the SPS test beam during 1997 and 1998. The system was required to purify, fill, recirculate and empty two liquid C_6F_{14} radiators independently, remotely and safely.

Movements of the prototype of up to ± 0.6 m horizontally and ± 0.4 m vertically had to be accommodated without interference to the circulation of liquid.

The reference pressure for the circuit was maintained constant and slightly positive with respect to atmosphere. Key pressures in the circuit were monitored electronically. Deviations from nominal conditions automatically interlocked the system into a safe stand-by state.

The liquid distribution to and from the radiators was based on a gravity flow principle — similar to that implemented by the CRID group at SLD [4]. The principle was considered a potential solution for the final ALICE system by virtue of its simple, passive and safe nature. These are important features in view of the inaccessibility of the detector and sub-systems, and the fragility of the liquid radiators.

The prototype system incorporated most of the essential features of a final system, including large volumes, to gain experience with the behaviour of the system and the technology of cleaning relatively large quantities of liquid[1].

3.1.3.2 Liquid and construction materials

Large C_6F_{14} liquid radiator systems have been built and successfully operated for many years by the RICH group at DELPHI [5, 6] and the CRID group at SLD [4]. These groups have great experience in cleaning techniques, compatibility of materials and long-term operation with this liquid. We fully used that knowledge to avoid the pitfalls associated with this chemical.

C_6F_{14} is not available in a high-purity research grade form with a guaranteed UV transparency. It comes in the form of proprietary branded products, which contain a large fraction of C_6F_{14}. The liquid is presently available from several manufacturers (3M, BNFL) but only the 3M product has been used to date.

Two forms are available from 3M: Performance Fluid PF-5060DL and Fluorinert FC-72. Both are manufactured by the same process but the FC-72 is purer as it is refiltered at the final stage until it satisfies more stringent specifications than PF-5060DL (Table 3.5). Note that the C_6F_{14} content could be as low as 90$\%$. FC-72 is promoted as the liquid to use for more demanding applications, whereas PF-5060DL is recommended for use in heat exchangers and as a solvent. For UV applications, it is always necessary to clean the raw liquid (FC-72 or PF-5060DL) since the liquid is filled into drums and stored in contact with air. The liquid chosen for the HMPID system was PF-5060DL — since it is cheaper, and the DELPHI and SLD experience has shown that PF-5060DL can be successfully cleaned with conventional filters. Since the liquid impurities can and do vary from batch to batch, it is has been customary to order a sizeable quantity from the same production batch to ensure uniformity and predictability in its response to cleaning procedures.

Physical properties

The characteristics of PF-5060DL are shown in Table 3.6. Note the high density, volatility and the high solubility of air and water. These characteristics influence the circuit design. The high density causes considerable hydrostatic loading on fragile optical windows, the volatility implies high evaporation losses, which must be recovered; the high solubility of air and water vapour results in over 100 000 vpm oxygen and about 10 000 vpm water vapour in the raw material. Since both of these gases are strongly absorbent in the UV they must be reduced to trace levels to ensure high optical transparency in our application.

---

[1] The circuit was designed together with the CERN DELPHI Gas Group, who later constructed the racks. The HMPID group greatly benefited from the help, advice and facilities of the CERN DELPHI RICH fluid team and the CERN EST/SM group.

Table 3.5: Specifications for 3M fluids

Test	FC-72	PF-5060DL	PF-5060DL 1997 Lot 30097 Drums: 85 87 91 92 95	PF-5060DL 1998 Lot 30184 Drums: 13 16 18
Distillation range (50–60°C)	90% min.	90% min.	98%	96%
Viscosity @ 25°C (cSt)	0.42 ± 0.05	0.42 ± 0.05	0.40	0.40
Density@ 25°C (g/ml)	1.68 ± 0.02	1.68 ± 0.02	1.691	1.684
Dielectric strength	35 kV min.			
Pour point	< -60°C			
Residue (μg/ml)	10 max.			
Cost (CHF/kg)	132 (for 90 kg)	57 (for 100 kg)		

Table 3.6: Physical properties of PF-5060DL

ODP (ozone depletion potential)	0
Average molecular weight	338
Boiling point °C	56
Liquid density (g/ml @ 25°C)	1.68
Liquid viscosity (cSt @ 25°C)	0.40
Vapour pressure (mbar @ 25°C)	309
Solubility of H_2O (ppm by weight @ 25°C)	10
Solubility of air [ml gas/100 ml liquid (FC-72)]	48
Solubility of oxygen [ml gas/100 ml liquid (FC-72)]	65
Thermal expansion coefficient @ 25°C (ml/ml °C $\times 10^3$)	1.6
Refractive index (ND) @ 25°C (FC72)	1.251

Construction materials

The choice of materials to be used in the circuit (including the liquid radiators themselves) is an important issue. Long-term degradation of certain materials in contact with C_6F_{14} has been observed by the DELPHI group [3]. The circuit was constructed using wherever possible metal (stainless steel, aluminium, copper) and glass. All-metal instruments are expensive and often difficult to find. Joints in contact with liquid were metal-metal except where an elastomer joint was unavoidable, in this case Viton was used. Chemical sealants were not used in order to avoid the liquid leaching away components from the compound.

During the construction phase, all welded stainless-steel components were subjected to a standard CERN surface-treatment. The stainless-steel pipe-work installed in the zone had already been chemically cleaned in situ. It was found necessary to pump down these lines via a LN_2 cold trap to remove all vestiges of water vapour. The remaining pipe-work was cleaned with ethyl alcohol and purged dry with nitrogen.

3.1.3.3 Circulation system

The circulation system was divided into a circulation rack, a control rack (outside the test zone) and a distribution rack (in the test zone and fixed to the detector). A schematic diagram is shown in Fig. 3.11.

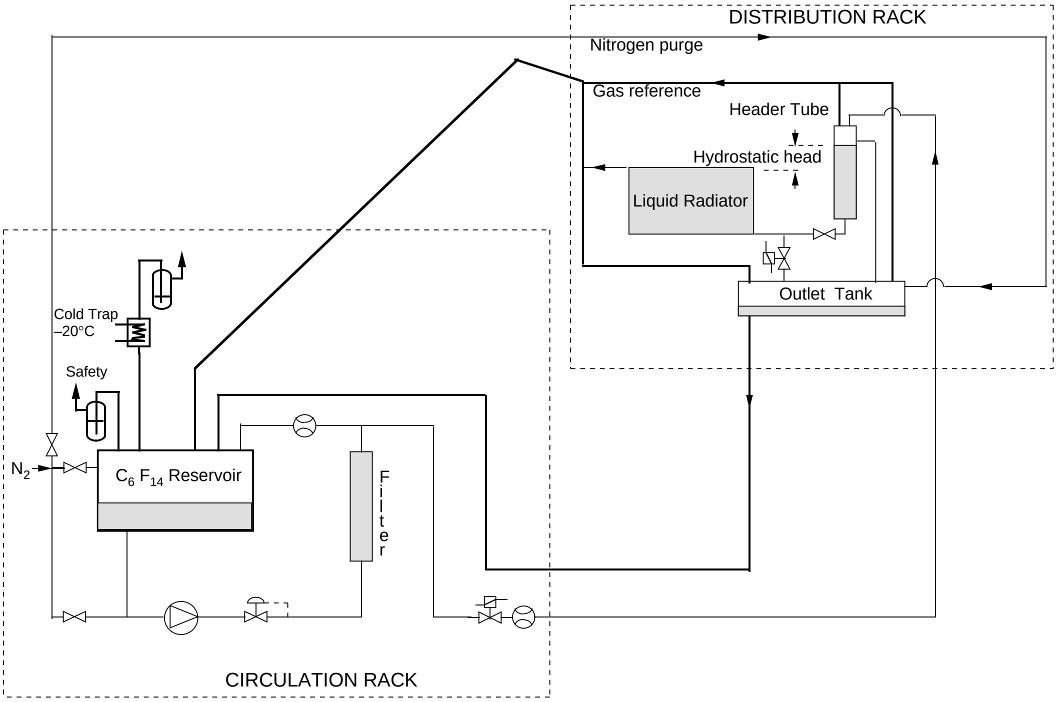

Figure 3.11: Schematic of the circulation system.

Gas reference system

The circuit contains a reservoir partially filled with liquid, the gas volume above the liquid forms the reference pressure for the system. A constant positive pressure is maintained by an oil bubbler purged by a flow of nitrogen gas. The nitrogen is introduced at the most distant part of the circuit at the distribution rack. The distribution rack is connected to the circulation rack by a large-diameter aerial line (without siphons) which acts as the purge gas return. The gas purge maintains all gas pipe-work at the same reference pressure and evacuates impurities out-gassed from the liquid and the materials in the system.

Liquid recirculation, gravity flow

The liquid from the reservoir is pumped via cleaning filters towards each radiator. The liquid first enters a header tube located above the radiator. The top of the tube is connected to the gas reference system; the bottom is connected via a valve to the low point of the radiator. The tube acts as a hydrostatic gravity feed for the radiator. It contains a large-diameter overflow pipe to limit the hydrostatic head (height difference between the overflow and the outlet at the top of the radiator). This head is set to produce the required flow through the filled radiator, taking into account the impedance of the filling line and the radiator. The header tube also traps gas bubbles in the input stream before they pass through the radiator.

Liquid from the radiator outlet falls unimpeded into a large-diameter outlet tube, connected upward towards the gas reference network and downwards toward a large-volume liquid outlet tank. The outlet tube was constructed to eliminate any siphons.

The circulation cycle starts with the progressive filling of the header tube, which in turn generates flow to the radiator. The level in the tube reaches overflow and then remains constant. The radiator filling continues until the radiator overflows into the outlet line and down to the outlet tank. At this point the gravity feed and the flow through the radiator become constant.

From the bottom of the outlet tank the liquid falls into a large diameter return line and back to the system reservoir. The outlet tank must always be above the level of the system reservoir to ensure return flow by gravity. The top of the outlet tank is connected to the gas reference network by lines without siphons.

When the flow to the radiators is stopped, the hydrostatic head drains via the radiator. The radiator then remains full until circulation is restarted.

Safety

The gravity flow system contains passive security to prevent an over-pressurization of the liquid radiator windows. The radiator is decoupled from the high-pressure part of the circuit by a header tube at the input and by a reference gas-filled collector pipe at the outlet. (It is, of course, essential that the reference pressure remains close to the atmospheric one and that the overflow can never be blocked or overloaded.)

In normal operation, the maximum pressure in the radiator is the sum of the reference plus hydrostatic pressure of the liquid column in the radiator itself. In the extreme case that the radiator output becomes blocked, the hydrostatic head is also added. Of course, the aim is to minimize this hydrostatic head.

3.1.3.4 Circulation rack

The circulation rack (Fig. 3.12) was based on the DELPHI RICH circulation system [6]. The system gas reference pressure (P1) was defined by the operational bubbler at +3 mbar. The reservoir volume of 100 litres was typically filled with 35 litres of liquid, which fed a pump (IWAKI MDGM2S220). The liquid height in the reservoir was measured by the hydrostatic pressure at P2 and was used as an interlock to prevent the pump from running dry.

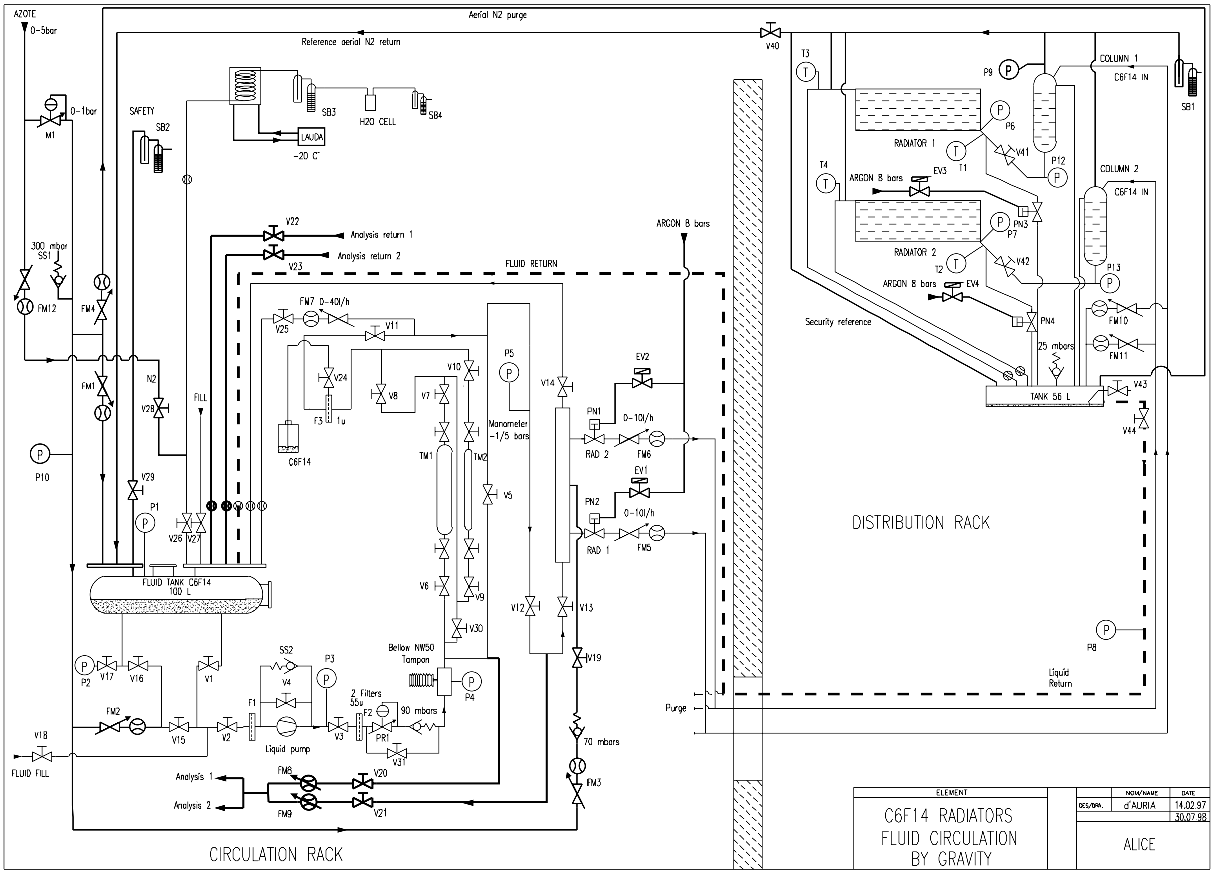

Figure 3.12: Circuit diagram of the recirculation system.

The pump pressure of about 2 bar was regulated down to 1.2 bar before entering the cleaning system (P4). The system was designed to hold two types of filter cartridges: molecular sieve (13X- standard DELPHI) and activated copper (small EST/SM). The cartridges could be used individually, or in series.

All liquid from the filters passed through a mechanical filter (ULTRAFILTER-1 micron). Mechanical filtering was essential to eliminate punch-through dust particles from the filter cartridge.

The filtered liquid at a pressure of 0.6 bar (P5) was divided into a closed-circuit flow back to the reservoir (30 l/h) and an external flow to the two radiators (12 l/h). In this way, the liquid volume was filtered at least once per hour and also the flow to the radiators could be interrupted without significantly altering the operation of the pump. The liquid quality was monitored via analysis lines (before or after the filters). The method used to date was to fill, purge, then seal a valved sample cell which was then disconnected and taken to be measured in a dedicated laboratory UV transparency measurement system.

A flow of 6 l/h to each liquid radiator was set by a manual flow-meter instrumented with an electrical low-flow alarm pick-up. A pneumatic valve (NC) enabled/disabled the flow. Pneumatic valves were used instead of electromagnetic valves in the liquid input and emptying lines to prevent local heating (bubble formation) by the valve body.

After passing through the radiator, the return liquid flow to the circulation rack fell unimpeded into the reservoir via a liquid manifold. The purge gas flow of 20 l/h was exhausted from the circuit via the same manifold. The C_6F_{14} vapour-laden gas passed via a cold trap provisionally cooled to $-20\,^{\circ}$C by a thermostatically controlled bath. The condensate dropped into the liquid manifold and the purge gas and impurities exited the system via the operational bubbler.

Great care was taken, at start-up and after introducing large quantities of raw liquid, to ensure that the water vapour level was well below the dew point at the temperature of the cold trap. As a safety precaution, the coolant temperature was always raised in these circumstances. The water vapour level was monitored provisionally by inserting a hygrometer downstream of the operational bubbler.

As a final security, a safety bubbler (+5 mbar) was located upstream of the cold trap in case of blockage. The liquid loss in the 1997 run was typically 1.0 liquid litres/week. Figure 3.13 shows the variation of the liquid level in the reservoir versus time for the run Table 3.7. The losses were consistent with the losses expected from uncondensed vapour escaping from the system. A recovery system operating at $-40°$C is at present under study and should reduce the loss by a factor of 4.

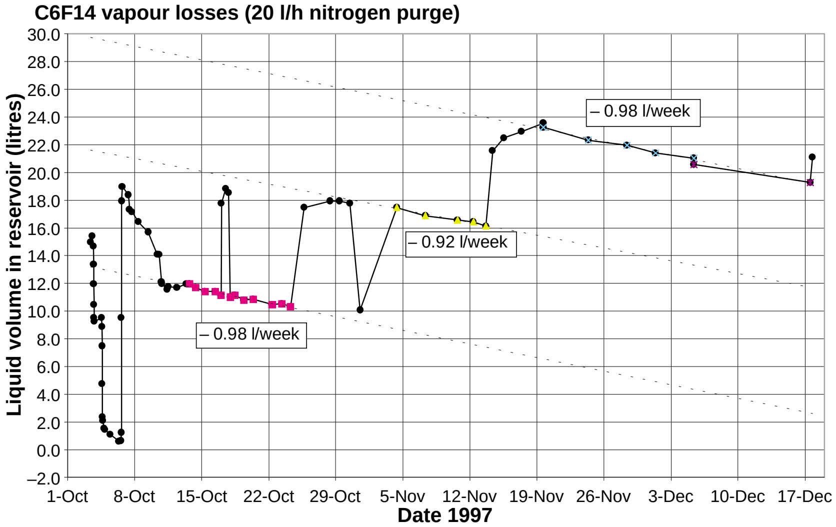

Figure 3.13: Variation of the liquid level in the reservoir versus time.

3.1.3.5 Distribution rack, mini-rack

The distribution rack (Fig. 3.12) was fixed to the detector to ensure that the correct hydrostatic heights were maintained during the detector movements in the test beam. The rack contained the header tubes with the overflow pipe at 12 cm above the radiator outlet corresponding to some 20 mbar hydrostatic head. This was estimated as a realistic minimum value for the final ALICE system.

The height of the liquid column in the tube was monitored by pressure gauges (P12, P13). The input flow to each tube was 6 l/h, the valves (V41, V42) were calibrated before the run to provide 3.5 l/h to a full radiator when the header tube was in overflow. The flow to the tubes could drop by 40% before the radiator flow changed, resulting in very stable running conditions. Note that a flow measurement in the input line is very difficult due to the inevitable pressure drop within the instrument. The pressure at the input to each radiator was monitored (P6, P7). The pressures observed corresponded to the sum of the reference pressure and of the hydrostatic height of liquid in the radiator plus several millibar of dynamical pressure generated by the flow at the input and outlet of the radiator.

The radiator outlet and header overflow pipes were inclined continuously downwards toward the outlet tank and were successfully tested at five times the nominal flow rate. The tank was chosen large (56 litres) for safety reasons — as planned for the final system. The tank had the capacity to contain all liquid in the system without the risk of backing-up into the liquid radiator outlet lines should the return line become blocked. In normal operation the tank contained a shallow layer of liquid. The tank was purged by nitrogen. The gas could rise via several large-diameter lines directly to a gas reference manifold on top of the rack, sweeping away any gaseous impurities liberated from the liquid. The manifold was protected by a safety bubbler (+5 mbar). The pressure at the manifold was measured at P9.

If circulation was stopped for an appreciable time, the shallow layer of liquid in the outlet tank evaporated away. On restarting circulation, liquid entering the ‘dry’ tank generated a large transitory gas flow by displacing part of the nitrogen atmosphere with C_6F_{14} vapour (Section 3.1.3.7).

The radiators were emptied by closing the input valves (PN1, PN2) and opening the valves (PN3, PN4) which linked the radiator filling lines to the outlet tank.

Scanning the detector by remote control necessitated that all lines connecting the rack to the circulation rack were flexible over the first five metres. A pressure probe (P8) was installed in the liquid return line to monitor the return liquid level and give advanced warning in case of anomalies.

3.1.3.6 Control rack and monitoring

The control rack displayed the pressure readings, status of flow-meter flow alarm relays and contained buttons to control the operation of the circuit. The safety interlocks for the system were generated by hard-wired logic due to the simplicity of the system.

Ten pressure probe signals (4–20 mA) were fed into individual digital display multimeters (A puissance 3 -VUP391) possessing two alarm-level relay outputs (hi =AL1 and lo =AL2) and an independent analogue output (4–20 mA).

The multimeters provided the visual display and the alarm relays used in the interlock logic. The analogue output was used to feed a monitoring PC card and a slave display panel fixed on the distribution rack. The signals passed via a LABPC+ card into a PC running LABview system which displayed and stored data. Programmable software alarm levels on the monitored pressures generated alarms and Mobile phone messages to the operator.

3.1.3.7 Operational experience

Tests were carried out in September 1997 using a prototype liquid radiator made from Neoceram. The full system was then transported to the SPS ALICE test beam and installed for the end of September.

The system was first filled and circulated with 10 litres of raw liquid and then emptied to remove particles and impurities leached from the wetted surfaces. Table 3.7 contains an abridged summary of the October 1997 run.

Raw liquid was added at the start-up of each run to allow the maximum cleaning time before data taking started. No further liquid was then added. At the end of data taking the radiators were emptied and the circuit closed down to prevent needless evaporation losses. Isolation valves (V26, V29, V40, V44) were added to facilitate this operation. After close down, the reservoir was pressurized to 100 mbar with nitrogen. The safety bubbler on the distribution rack was then used as the operational bubbler for the continuing purge of this rack.

Table 3.7: October 1997 run summary

	Radiator 2 only
01/10/97	System purged, molecular sieve #1 (MS#1) installed
	Add 18 litres drum 85
	Start closed circuit circulation
	Nitrogen purge flow 20 l/h
03/10/97	Fill return line
04/10/97	Fill and circulate the radiator
05/10/97	Measure T% drum 91
	ECD test – no measurable trace C_6F_{14} in HMPID
06/10/97	Add 18 litres drum 91
07/10/97	Measure T%
	Add MS# 2
09/10/97	Measure T%
10/10/97	Measure T%
	Start recovery system $-5°$C
	Add MS# 3
11/10/97	Recovery at $-20°$C
	Start data taking
17/10/97	Empty radiator
	Fill radiator
18/10/97	Measure T%
19/10/97	Measure T%
22/10/97	Measure T%
25/10/97	Empty radiator
	End data taking
	Measure T%
30/10/97	ECD test – empty radiator – no measurable trace of C_6F_{14} in HMPID
30/10/97	ECD test – full radiator – no measurable trace of C_6F_{14} in HMPID
	Empty radiator, continue closed-circuit circulation
13/11/97	Disconnect liquid filling lines and liquid return line from mini-rack
	Disconnect aerial reference line. Purge mini-rack 15 l/h (safety bubbler)
	Purge liquid in return line back to reservoir N_2 20 l/h
27/11/97	Measure T%
	Drain 0.45 l sample from system
16/12/97	Measure T%
	Close down and seal off system

The system ran stably and safely during the three data taking runs. However, there were some aspects of the operation which were not wholly satisfactory and need attention in the final design. For instance:

- The reference pressure was found to vary when the large external doors to the experimental hall were opened. In cold weather, the sharp drop in ambient temperature caused a drop in the pressure due to condensation of C_6F_{14} vapour. The purge nitrogen flow was maintained at a relatively high value of 20 l/h for the first two runs in order to prevent air from sucking back through the operational bubbler. Insulation or regulation of the temperature of the liquid system in non-regulated environments may be necessary.

- A transient surge in gas flow through the operational bubbler was observed each time liquid fell into the radiator outlet tank when empty (‘dry’). Since the pressure of the operational bubbler was slightly flow-dependent, the reference pressure rose several millibars until equilibrium was reached. It would be advisable to trap a larger volume of liquid at the bottom of each large tank to avoid this effect. Links between all large volumes and the operational bubbler should be in large diameter to prevent pressure build-up due to line impedance in such an event.
- The exchange of filter cartridges was a significant perturbation on the system. A freshly regenerated cartridge of molecular sieve is normally pressurized with 1 bar argon. This excess pressure must be purged before opening the cartridge towards the system. The entry of liquid into the molecular sieve generates heat and gas, which must also be purged beforehand. Valve V24 (Fig. 3.12) was used to bleed off the excess gas. Nevertheless, circulation to the radiators had to be stopped (V11) during this operation.
- Each change of cartridge resulted in a loss of about 1 litre of liquid. The cartridge was positioned above the reservoir to allow draining the liquid back into the reservoir before changing it. However, vapour was lost when filling the cartridge and the liquid absorbed in the molecular sieve pellets was also not recovered. A method to recuperate this loss would be useful.
- The final system will require a pre-cleaning unit to inject clean liquid into the purified bulk liquid, instead of filling new raw liquid directly into the reservoir, as was the case so far.

3.1.3.8 Cleaning and liquid transparency

The liquid used in the HMPID prototype tests originated from the same batch of PF-5060DL (30097). Prior to introducing raw liquid into the system, the sample cell was filled and the transparency measured. The transmission of several raw samples is shown in Fig. 3.14a.

The samples from the batch 30097 are similar, as expected. There is a strong absorption band around 185 nm which later proved difficult to remove. This band is not apparent in the sample from batch 30184. A simulation of the transmission over 1 cm of a gas volume containing 120 mbar oxygen and 10 mbar water vapour is shown for comparison.

The molecular sieve (13X-1001 UETIKON) preferentially removes water vapour but has also a capacity to trap many different impurity molecules. It is the only filter now in use in the fluid systems of the DELPHI RICH. After use in the system, the 13X pellets are discarded and new pellets added to prevent possible reactions when a ‘wet’ filter is regenerated. The new pellets are regenerated at 200 °C for 24 hours under constant argon purge.

Dissolved oxygen in the raw liquid is most efficiently removed with an active filter such as Oxisorb (MESSER GRIESHEIM) or cartridges of activated copper (highly dispersed copper, know also as catalyst copper – EST/SM CERN). The latter produced a dramatic improvement in the transparency of small samples from batch 30097, removing oxygen and the source of the band around 185 nm (Fig. 3.14b). However, problems have been encountered with these filters in the past. DELPHI had problems with batches of PF-5060DL containing non fully fluorinated impurities [7]. These impurities underwent chemical reaction in the filters that degraded the UV transparency of the bulk liquid.

Another method to remove dissolved oxygen is by intensive bubbling of nitrogen through the liquid thereby replacing the dissolved oxygen with nitrogen [4]. However, an efficient recovery system (-40 °C) is required to avoid heavy liquid vapour losses. The provisional system operated at -20 °C so that this technique was not tested. The 20 l/h nitrogen purge of the system produced a slow purging of the out-gassed oxygen.

The cleaning strategy for the first runs was conservative: use only molecular sieve cartridges and nitrogen purging to remove the impurities present in the raw material.

The evolution of the liquid transparency (after filters) for the initial run with one radiator in October 1997 (Table 3.7) is shown in Fig. 3.14c. The cleaning system had to remove impurities in the raw liquid plus those from the newly operational system. The liquid was exposed to only two new cartridges but reached an acceptable level of transparency by the start of data taking. The absorption band around 185 nm was reduced but still significant. The system was then left to run on for a further two months. A significant improvement was observed despite no further change of cartridges.

In preparation for the April 1998 run, the bulk liquid was exposed to three new cartridges since 12 litres of raw liquid were added. The evolution of the liquid transparency (after filters) is shown in Fig. 3.14d. The liquid quality was found to be good throughout the run and better than in October 1997.

After modifications and the introduction of the second radiator into the HMPID before the July 1998 run, a short-term degradation in the liquid quality might have been expected. In addition, 16 litres of raw liquid were added to the system. Again the liquid was exposed to three new cartridges before data taking. The evolution of the liquid transparency (after filters) is shown in Fig. 3.14e. The transparency measured was an improvement on the earlier runs and approached the excellent results obtained with small samples using an activated copper filter.

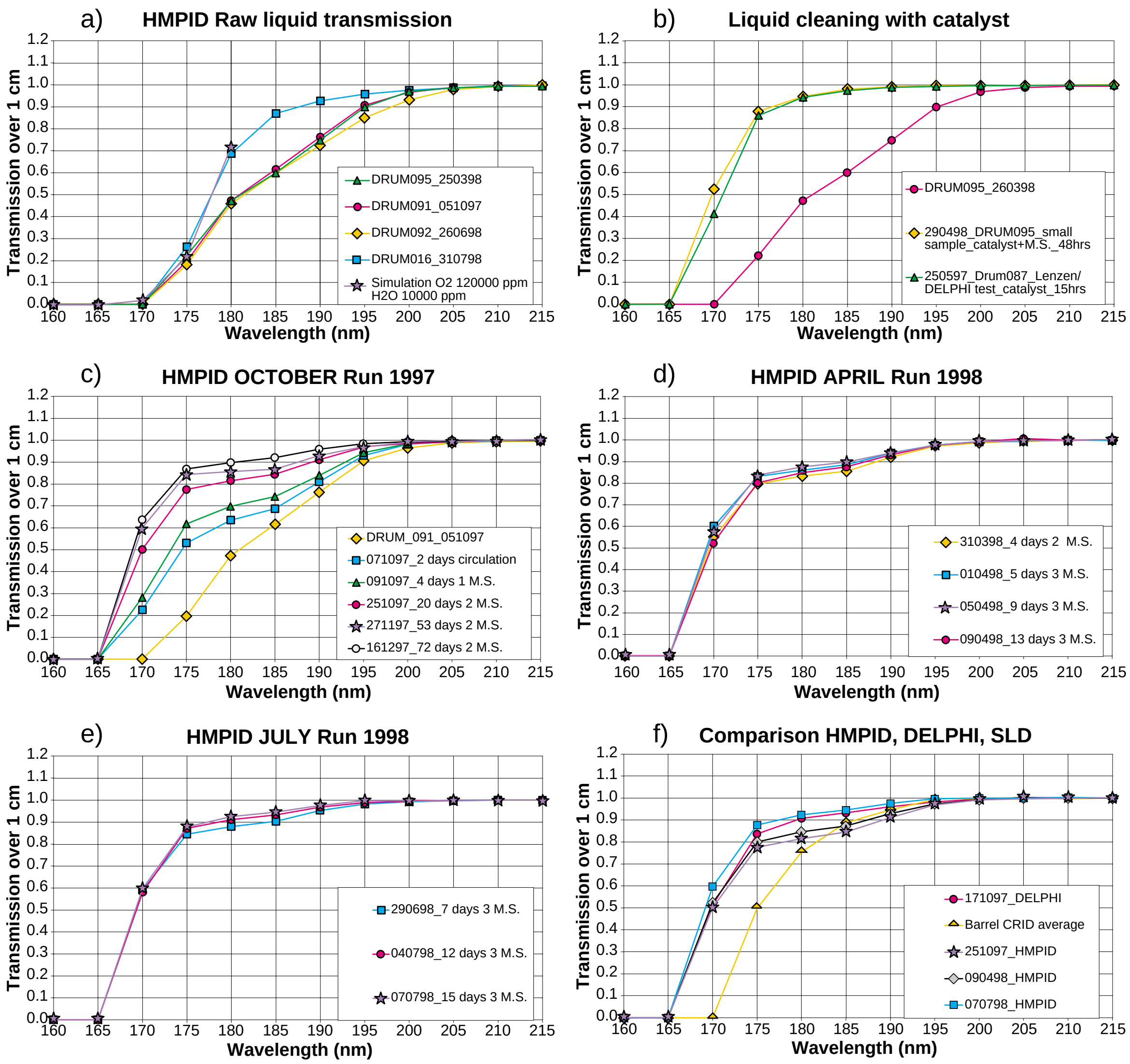

Figure 3.14: Transparency curves for different samples. For details see text.

In summary, the results obtained in the first runs of the prototype liquid system were encouraging. Good-quality transparencies were obtained using safe, passive cleaning methods. The gravity flow distribution system proved safe and stable.

The quantities of liquid involved (35 l) were, however, still small compared with the order of 250 litres required in a large system. In addition, liquid from a single batch had been used while in a large system, mixing of different batches is inevitable.

A comparison of the transparency at the end of each data-taking period is shown together with data from the DELPHI and SLD systems [8] (see Fig. 3.14f). It can be surmised that it will be difficult but not impossible to routinely maintain the quality achieved in the HMPID prototype when the size and complexity of the system increases. Some contingency on the performance side (e.g. number of emitted photons) should, however, be included to allow for a decrease in the average liquid quality in the final system.

3.1.3.9 Future developments

A systematic study of the chemical composition through analysis (GC, IR, etc.) in parallel with cleaning and UV transparency measurements seems essential to improve understanding and predictability in the cleaning process. A multi-cell, automated, on-line UV transparency measurement system is being adapted for use with the prototype and is now near completion.

The future development of diagnostics such as on-line liquid phase measurements of water vapour and oxygen traces would improve the ability to monitor the evolution of the liquid during cleaning. An on-line UV liquid refractometer would complement these instruments.

It is planned to investigate as additional filter materials: silica gel, activated copper catalyst and OXISORB. Passive methods such as using zeolite membranes and liquid out-gassing methods [9] seem promising techniques and merit further study.

3.1.4 The electronics chain

As discussed in Chapter 2, the low interaction rate at ALICE allows an electronics scheme with the following specific features:

- a charge-sensitive preamplifier with a long integrating time > 800 ns,
- analog charge measurement,
- multiplexed operation (MPX),

to achieve optimal single-electron detection efficiency and sub-millimetric localization from the readout of MWPC cathode pad signals.

The HMPID readout electronics is designed to satisfy the system requirements specific to ALICE operational modes:

- maximum trigger interaction rates of $1 \div 10$ kHz and 100 kHz in ion and proton collider modes, respectively,
- a system size of 160 k channels with an occupancy of hit channels expected to be less than 15% per event,
- an implementation on the detectors with a surface density of 16 kchannel/m^2.

The adopted multiplexed analog schematic is composed of two parts:

- an analog part based on the CMOS VLSI front-end chip GASSIPLEX [10], providing 16 analog multiplexed channels,
- a digital part performing the digitization and synchronized zero suppression.

Longer analog sequences can be treated by connecting several GASSIPLEX chips in a ‘daisy chain’ mode.

The development of this system was firstly devoted to the analog part, the chip GASSIPLEX. Most of the R&D work on the detectors was carried out using the first version of GASSIPLEX, referred to as GASSI-1.5, designed in 1.5 μm MIETEC technology. A second version, GASSI-0.7-1, the first chip developed in 1995 at the prototype level using the new 0.7 μm technology from MIETEC, demonstrates a very good noise performance and improved layout features such as a reduced sensitivity to latch-up. The third and final version, GASSI-0.7-2, is presently under completion, the last specifications requested by ALICE, not only from the HMPID but also from the Muon Arm spectrometer being inserted. The basic architecture of this chip is identical and its characteristics and performance will be described later.

During the detector test period, the system aspect of this FEE was investigated using standard readout elements such as the VME modules C-RAMS. In fact, for test-beam purposes, it was possible to operate the system using up to 960 MPX steps — a number much larger than the one foreseen for ALICE operation (48–64) — chosen to minimize the size of the test readout system.

In parallel, the components of the final digital part were designed as ASIC chips to constitute a modular Multi-Chip Module (MCM) based on 48-64 MPX steps needed to keep the MPX dead time compatible with the ALICE trigger rate. The main digital component is a chip referred to as DILOGIC which performs the zero suppression after the digitization effected by a commercial ADC chip.

3.1.4.1 Front-end chip: GASSIPLEX and its operation

The 16-channel GASSIPLEX chip is composed of several functional blocks per channel (Fig. 3.15): a charge-sensitive amplifier (CSA), a switchable filter (SF), a shaping amplifier (SH) and a Track/Hold stage (T/H).

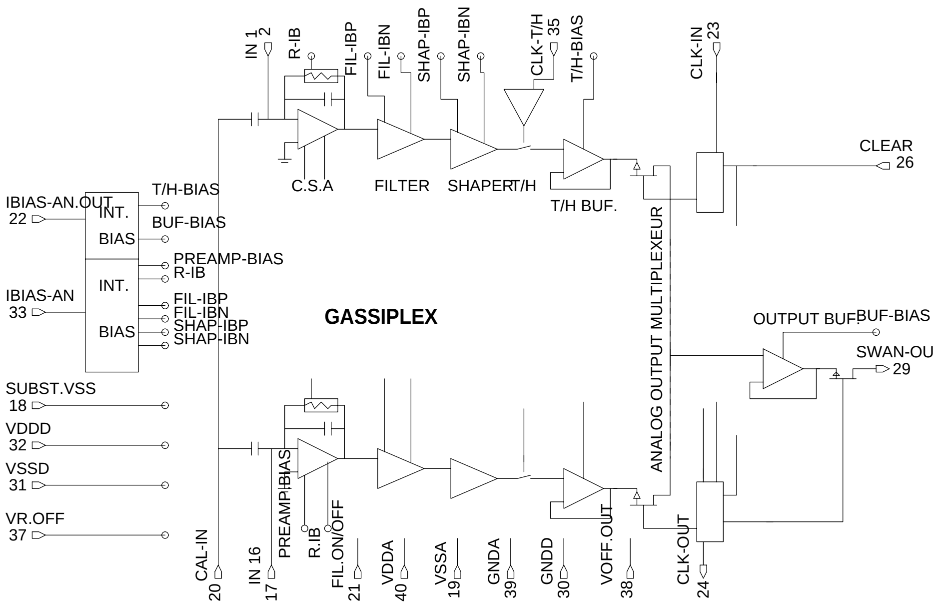

Figure 3.15: Schematics of the functional blocks composing GASSIPLEX-1.5.

As shown by the time diagram in Fig. 3.16, a sequence of control signals performs the multiplexed readout operations:

- a Track/Hold signal (T/H) to store charges in capacitors by opening the switches T/H,
- a train of clock (CLK) pulses, triggered by an external STARTREAD signal, to operate the multiplexed readout of the stored charges on a single output line (SWAN-OUT),
- a Clear (CL) pulse to restore the initial state of the switches.

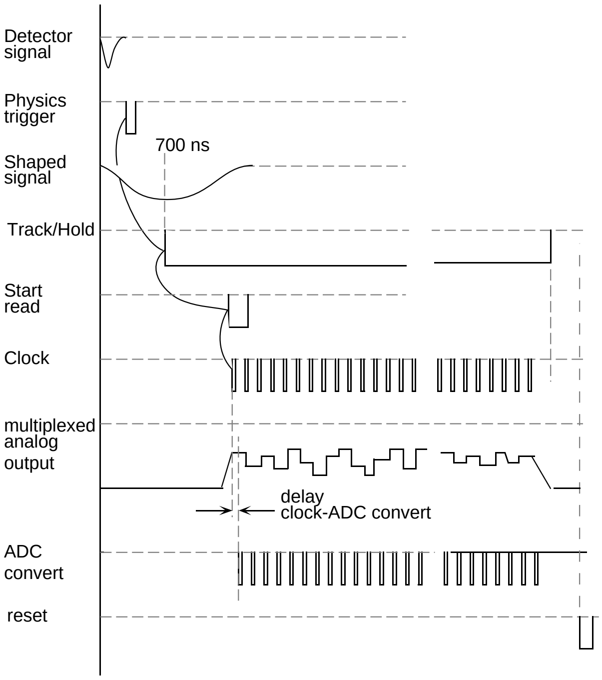

Figure 3.16: Time sequence of the control signals operating the multiplexed readout of GASSIPLEX-1.5.

Test pulses can be sent to all channel inputs through a calibrated capacitance via a common test input line in the 1.5 μm version, whilst sequential channel-to-channel calibration is performed in the 0.7 μm version.

Charge-sensitive amplifier (CSA)

This low-noise amplifier is characterized by a long decay time constant of 30 μs which makes it sensitive to the largest amount of the detector current. This feature and a very good noise figure of the full analog channel, provide an exceptional performance for detecting very low-level signals in MWPC down to a threshold of 0.3 fC. The linear output range of the CSA can be symmetrized.

Switchable filter and shaper amplifier SF,SH

GASSIPLEX is designed to be connected to wire chambers as well as to silicon strip detectors. A switchable filtering stage is necessary to match the different input current shapes of these two kinds of detectors. With solid-state detectors which provide a fast input current (< 100 ns), the filter is by-passed. The input current per channel should not exceed 1 nA. With wire detectors (MWPC), it is known that the slow drift of ions towards the cathode is responsible for a hyperbolic long-tailed current, which lasts for tens of microseconds and consequently disturbs the output baseline as fast differentiation is used. The filter was designed to extract, in several hundreds of nanoseconds, the greatest part of the charge delivered by the detector and to transform the long integrating time of the charge signal into a step function (Fig. 3.17a,b). After the filter, a shaping circuit made of a low-pass followed by a band-pass filter transforms this step function into a semi-Gaussian shape where one-third of the time is taken to reach the peaking time and two-thirds to return to the baseline (Fig. 3.17a,b). A pole-zero cancellation circuit compensates the decay time constant of the CSA, resulting in a very precise return to the baseline in a short time: $\pm 0.5\%$ of the peaking time amplitude in 3 μs and 6 μs for the 1.5 μm and 0.7 μm versions, respectively (Fig. 3.18).

This essential feature sets the front-end occupation time at less than 3 or 6 μs, without analog overlapping of events for versions 1.5 and 0.7 μm, respectively. An external bias resistor permits a slight adjustment (± 100 ns) of the peaking time. This time is 700 and 1200 ns for the 1.5 and 0.7 μm versions, respectively. It provides a natural built-in delay used to wait for the external trigger decision.

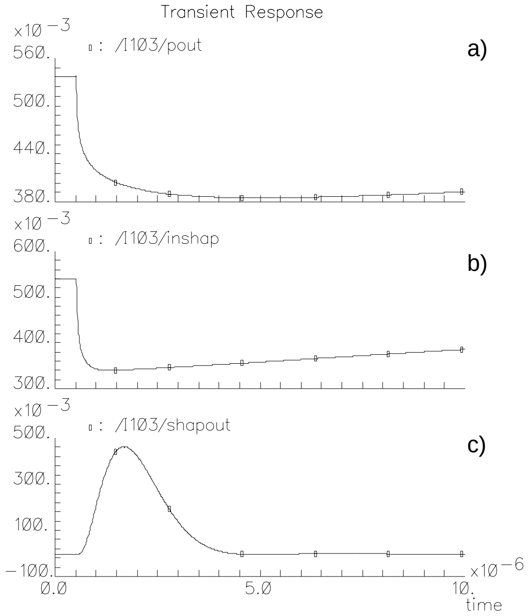

Figure 3.17: Simulated wave forms of the Filter and Shaper stages: a) input current, b) after the Filter, c) after the Shaper.

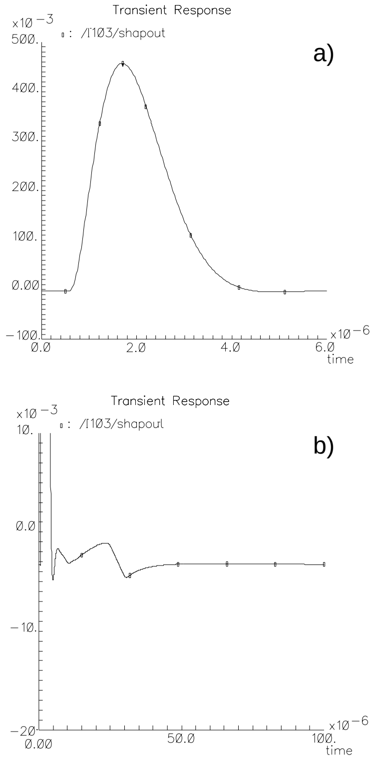

Figure 3.18: a) Shaper waveform (full scale: 6 μs). b) Shaper base line recovery (full scale: 100 μs).

Track and Hold stage (T/H)

In operation mode, all the switches driven by the T/H stage are closed, while those driven by the MPX stage are open in the whole system. When an event occurs, the capacitors associated to hit channels are charged up by the corresponding detector currents. An external trigger signal, synchronous to this event, is used to generate a ‘HOLD’ signal, sent to the whole system, in order to open all switches at a time corresponding to the peaking time of the shaping amplifier (Fig. 3.16). Therefore, the maximum charge signals are stored for those channels with a real signal (hit). Charges corresponding to their pedestal values are stored for those not having been hit.

As long as the HOLD signal is maintained ‘on’, the switches are open and the charges are kept frozen in the capacitors. Charges have a very low leakage rate -1 mV/ms. As soon as the HOLD signal is released, the switches are closed and the charges lost. A fast clear can be implemented according to that feature as the recovery time of the circuit is less than 200 ns.

Multiplexing

The decision to read out an event (charges stored in the capacitors) is independent of the T/H operation. For this purpose, a ‘START READ’ signal is generated from the event trigger logic with any delay convenient to the user. This signal starts a train of MPX clock pulses, issued from an external device, which allows the number and frequency of the clock pulses to be adjusted.

The clock train is also synchronously sent to the readout module where the digitization is performed. The digital conversion and the zero suppression of each analog step is carried out between two clock pulses. The sequencer should make it possible to adjust the delay between the two trains in order for the ADC conversion to be carried out during the flat part of each analog step (see Fig. 3.16).

However, although the two clock trains are issued from the same source, the MPX clock train is propagated through all the GASSIPLEX chips to operate the MPX function. Therefore, this train accumulates some delay (32 ns per chip) with respect to the ADC convert train. If the time between two clock pulses is too narrow, the synchronism is no longer satisfied after a certain number of clock pulses. So, for a large number of MPX steps (> 300), a module has been developed which compensates these delays on the ADC convert train.

CLEAR/BUSY
As soon as the clock train is over and the digitization performed, a CLEAR signal is sent to the GASSIPLEX, repositioning all switches to their initial positions. This signal can be sent after the HOLD signal is released.

Usually, as soon as a HOLD signal has been generated, the trigger logic is vetoed by a BUSY signal to protect the whole system from new events. This protection is released by the computer (via an output register) when all tasks are terminated.

3.1.4.2 GASSIPLEX intrinsic performance

In Fig. 3.19 the linearity and noise figure curves of the two GASSIPLEX versions are shown, respectively. In Table 3.8 the main electronic features of the two GASSIPLEX chips are summarized.

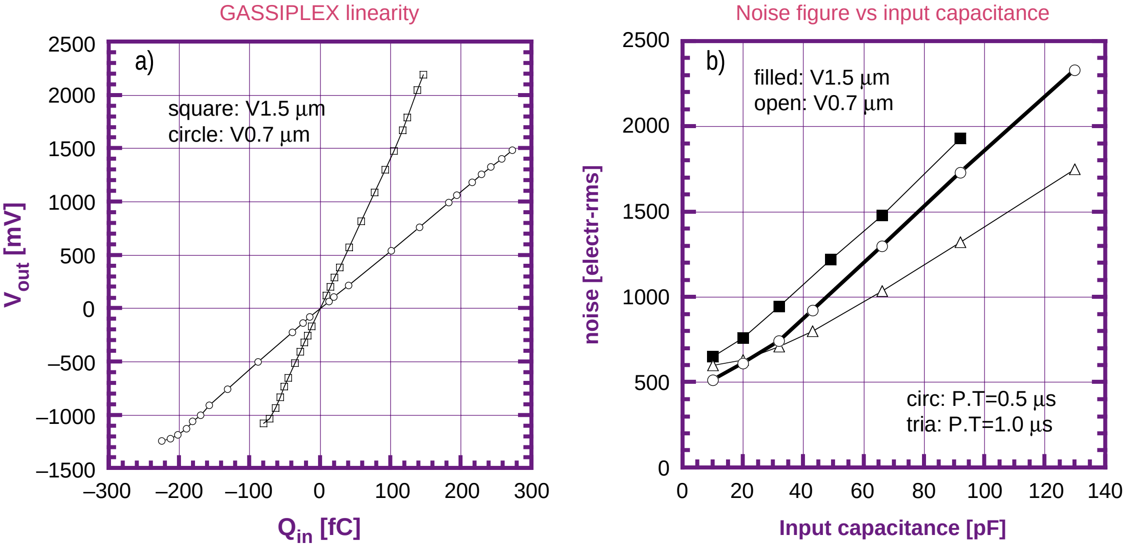

Figure 3.19: GASSIPLEX-1.5: linearity and noise curves.

3.1.4.3 GASSIPLEX system aspect

Pedestal, noise level and threshold definition
GASSIPLEX is an ungated, asynchronous device, which means that its inputs/outputs are always sensitive. Therefore,when the T/H signal is set, each output is raised at a constant DC level in the absence of input signal. This baseline, called ‘pedestal’ is channel-dependent within the chip. Measuring the fluctuation of the pedestal level gives the noise figure of this channel (in practice, as the r.m.s. of a pedestal distribution). Calling PED(i) and SIG(i) the average and r.m.s. values of a pedestal distribution, the operating threshold of the channel (i) is defined as: TH(i) = PED(i) + N*SIG(i), where N is a selectable constant, usually ≥ 3.

This procedure has the essential advantage of attributing the correct threshold value to every channel, regardless of the gain, noise figure and pedestal spreads among the channels and is, in fact, the prime reason to have chosen analog-based operation.

Table 3.8: Measured performances of the GASSIPLEX 1.5 and 0.7 μm versions

		GASSIPLEX V. 1.5 μm	GASSIPLEX V. 0.7 μm
Silicon area	mm^2	$4.2 \times 4.6 = 19.3$	$3.46 \times 4 = 13.8$
VDD/VSS	V	± 3.5	± 2.5
Noise at P.T.* = 500 ns	r.m.s. e	630 at 0 pF	485 at 0 pF
Noise slope at P.T. = 500 ns	e r.m.s./pF	16	15.8
			12.0 at P.T. = 1 μs
Noise at P.T. = 1 μs	r.m.s. e		585
Linear dynamic range	fC	-75 to 150**	-250 to 300
Conversion gain	mV/fC	12.3	4.9
Base line recovery		$< 0.5\%$ μs after 3	$< 0.5\%$ after 3 μs
Range peaking time	ns	400 to 650	400 to 1000
Power consumption	mW/chan	6	6
Analog readout speed	MHz	10	10 max

* P.T. = Peaking Time.

** X 2 when operated in silicon mode.

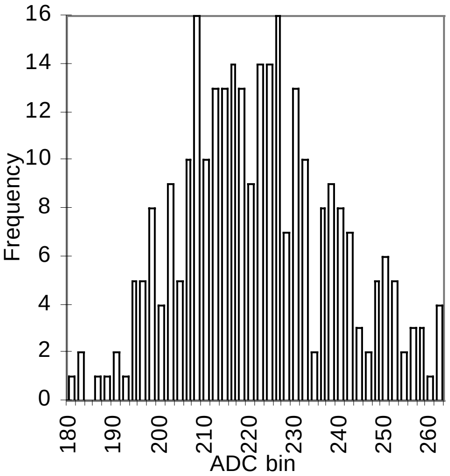

Figure 3.20: Distribution of the mean pedestal value per GASSIPLEX chip taken over a batch of 300 chips.

Usually, the PED(i) have little fluctuation within a chip ($\leq 2\%$). However, a significant spread can be found among chips as can be seen in Fig. 3.20, where a distribution of average values of pedestals per chip is shown. The average of such distributions depends, in fact, on the production batch of the chips. This feature has to be taken into account when a large number of chips are associated in long daisy chains. In order to benefit from the largest dynamical range in a chain, all pedestals should be set at a value as close as possible to the zero-DC level and should have the smallest dispersion. It was therefore necessary to sort out the chips in order to associate them in daisy chains by increasing the mean PED/chip values. The overall adjustment of the mean pedestal value of a chain was then performed independently by the buffer amplifier, at a positive or negative level, depending on the working range of the ADC device in use. As described in Section 3.2.4, that inconvenience will be solved in the final FEE version.

Operation of the system

The schematic of a GASSIPLEX-based operation system is shown in Fig. 3.21. It is composed of the following elements:

1. a trigger/control signal generator used to:
    - set the trigger modes: generator mode for pedestal and calibration measurements, or physics mode to record data from any experimental triggering array;
    - send the T/H and CLEAR signals to the GASSIPLEX chains using level shifters adapting the logic signal levels to those requested in the chip;
    - start the MPX readout sequence.

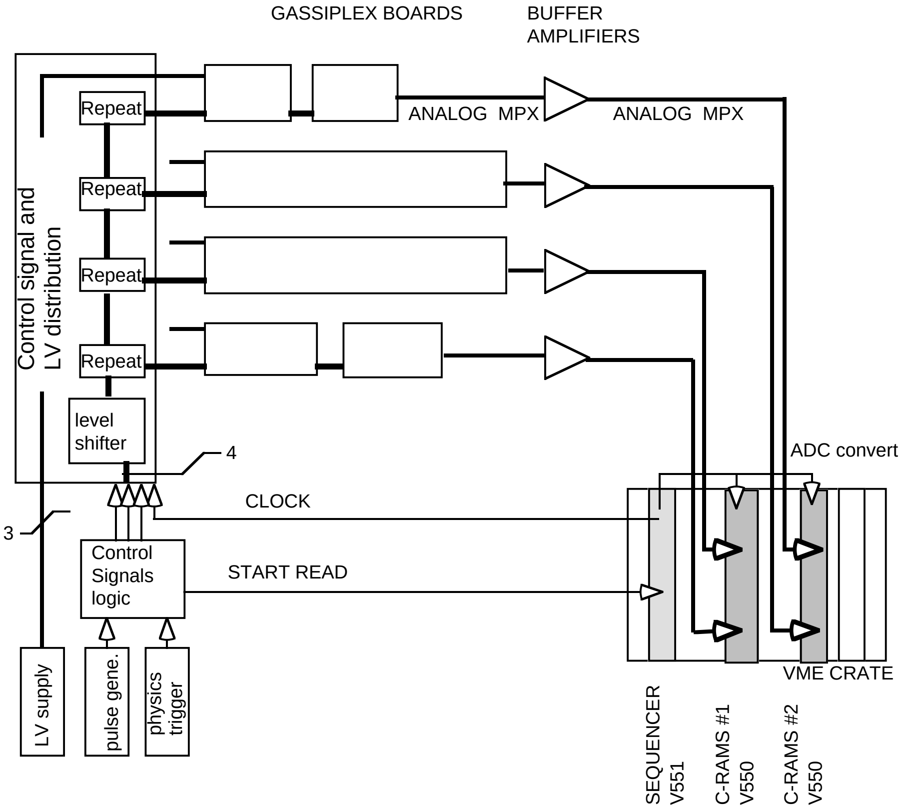

Figure 3.21: Schematic of a GASSIPLEX-based operation system.

2. a multiplexing sequencer used to:
    - send the CLOCK train to the GASSIPLEX chains and the digitizing units;
    - adjust the frequency, the number of CLOCK signals and the delay between the CLOCK trains.

3. digitizer and zero suppressor modules.

During the R&D and test phase, the GASSIPLEX chips were implemented on boards with 3, 6, or 15 chips, easily daisy-chained, using flat cables between the boards. As seen in Fig. 2.26 on page 37, these boards were plugged on the back of the pad panels to form chains of up to 960 channels on proto-2. Each chain was followed by a buffer amplifier driving a low impedance cable transporting the analog MPX signal to the counting room where the digitizers and data acquisition are located.

Element 1 is a specific NIM module designed at Subatech, Nantes [11]. For a large system operating many chains in parallel, a single-level shifter was used, followed by repetitor cards to regenerate the control signals at each chain. Elements 2 and 3 are the CAEN-VME modules V551 and V550, respectively. The maximum rate of digitization/zero suppression is 5 MHz.

In the HMPID system, all these elements will be mounted on the detectors, necessitating the new more integrated versions described in Section 3.2.4.

3.1.4.4 System performance

In order to correctly exploit physics data, the basic state of the system, i.e. the pedestal and noise tables of all channels, must be known and their stability must be under control. This operation is referred to as a ‘pedestal run’ providing the necessary pedestal and threshold tables which are stored in the memories of the digitizer/zero suppressor modules, e.g. V550. At every event, all digitizations, A(i), are compared with the corresponding threshold values TH(i). Only if A(i) $\geq$ TH(i), are the values [A(i)-PED(i)] and their addresses stored in a FIFO memory to be read out by the DAQ system. The pedestal distributions are recorded with a pulse generator as the trigger, in the absence of any other detector signal. This condition can easily be fulfilled under test beam conditions by taking pedestal measurements between particle bursts.

At ALICE, the detectors are irradiated in a DC-mode for periods lasting a few tens of hours without beam interruption. At low interaction rates, pedestal runs could be taken in interaction mode but as few times as possible, implying a good stabilitity of the pedestal values between measurements. In fact, the stability is governed by the level of the input gain temperature coefficient. In Fig. 3.22, we show a set of measurements characterizing the basic state of the FEE equipping proto-2, measured under operation at the SPS test beam. It corresponds to 15 360 pad channels (960 GASSIPLEX chips) readout by eight CRAMS modules. 960 channels were multiplexed per CRAMS input at a clock rate of 1 MHz. One ADC channel corresponds to 0.17 fC. In plot (a) we show the distribution of pedestal values, reflecting the spread discussed before. Plot (b) shows the distribution of sigma values corresponding to an r.m.s. noise figure of 1120 ± 155 electrons; (c) and (d) show the pedestal and sigma channel maps corresponding to 1920 channels. In (e) to (g) are shown the distibutions of the differences between pedestal values measured at different time intervals, demonstrating a good stability over an 18-hour period. Linearity curves obtained by pulsing all channel inputs are shown in (h) for 240 channels, (i) indicating an r.m.s. of the electronic gain of 2%.

3.1.4.5 Preliminary developments of the HMPID electronics

The MultiChip Module (MCM)

In order to satisfy the trigger and data flow rates expected in pp and Pb–Pb operational modes at ALICE, the final electronic system will be organized in a serial/parallel architecture based on a modular array composed of three GASSIPLEX chips (48 channels) and a MCM composed of one ADC and one zero-suppressor chip, referred to as DILOGIC, as shown in Fig. 3.23. The analog part will be still implemented at the back of the pad panels, while the multiplexed analog signals will be now propagated in parallel on a bus PCB to the frame of the module where the MCMs are concentrated on a motherboard. The data transfer to the DAQ is achieved by a serial optical link.

In this section, we shall only describe the R&D made on the first prototype version of the ASIC DILOGIC-1 and the operation of a MCM prototype. The complete system is described in Section 3.2.4.

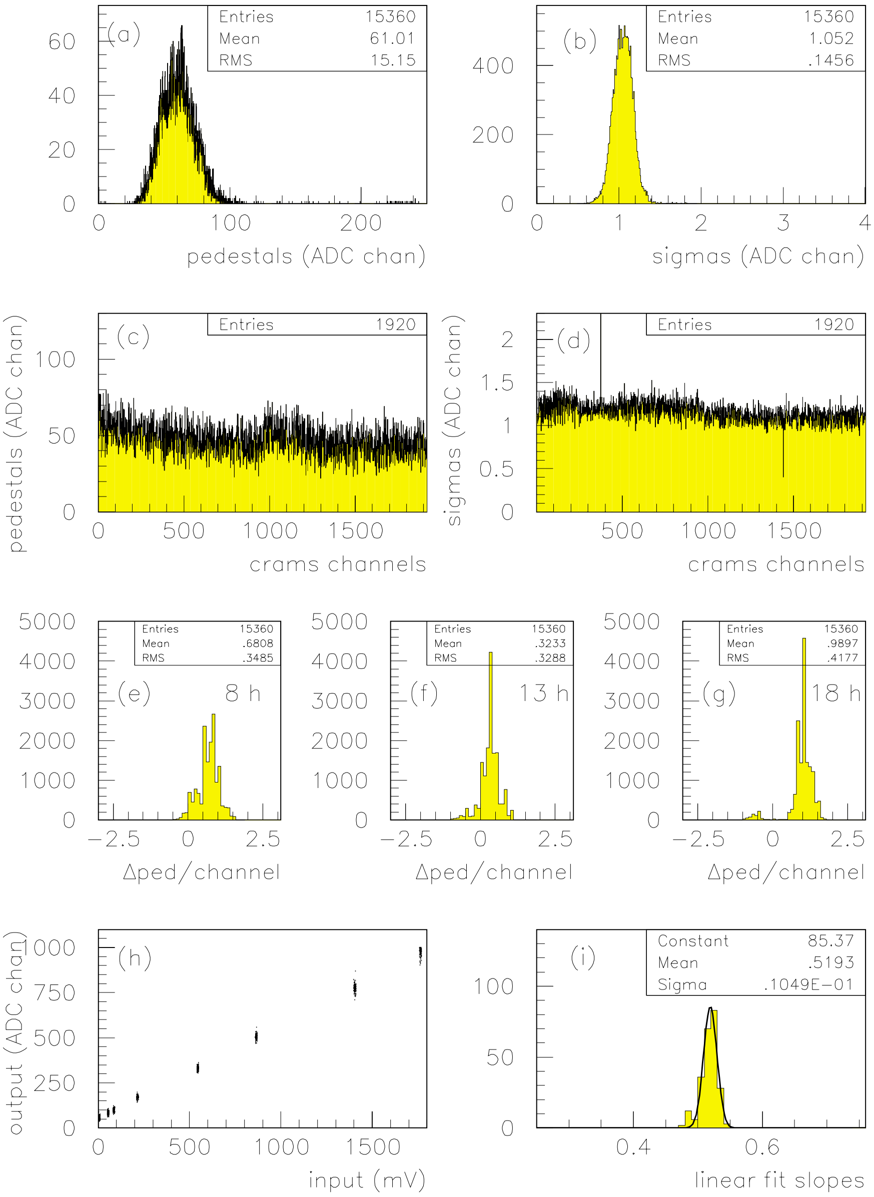

Figure 3.22: Pedestal and noise measurements, pedestal stability and gain calibration of a system of 15 360 GASSIPLEX channels. Measurements taken with proto-2 during a test beam period.

DILOGIC-1

The schematics of the first version, designed with the MIETEC 0.7 μm technology, is shown in Fig. 3.24. It works in pipeline mode with the ADC and channels (16, 32 or 64) read out sequentially. Each ADC conversion is fed into the DILOGIC-1 with the corresponding address to be processed in order to eliminate the empty channels, to subtract the pedestals, to fill the memories with a bit-map of the event and the digitized information of the hit channels, and finally to make an Input/Output connection with the outside world through a dedicated link.

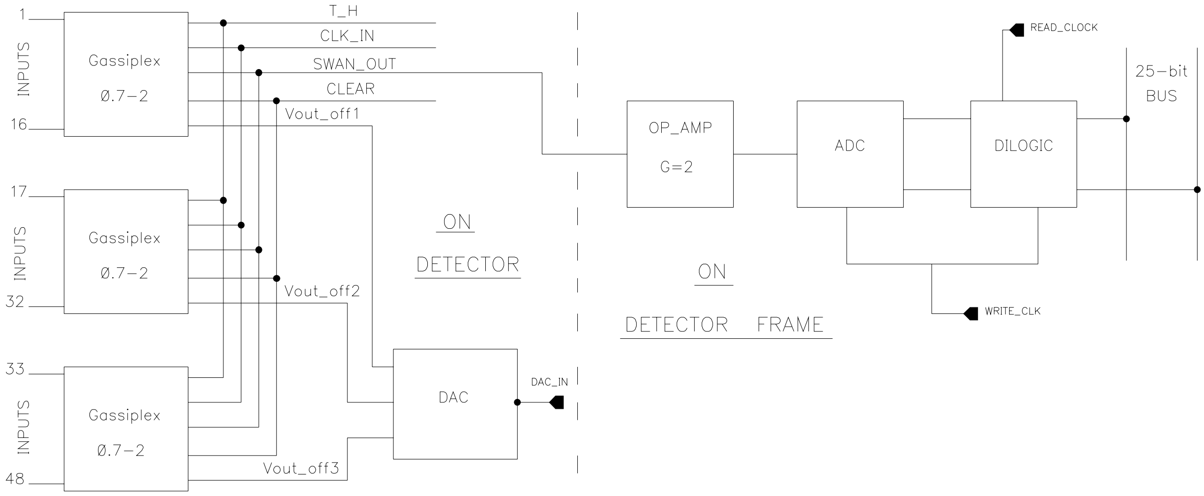

Figure 3.23: Schematics of the Multi Chip Module (MCM) constituting the basic readout cell of the module. It is based on a 48-channel multiplexed operation (3 GASSIPLEX chips). On the right side of the hatched line are the MCM elements implemented on the chamber frames.

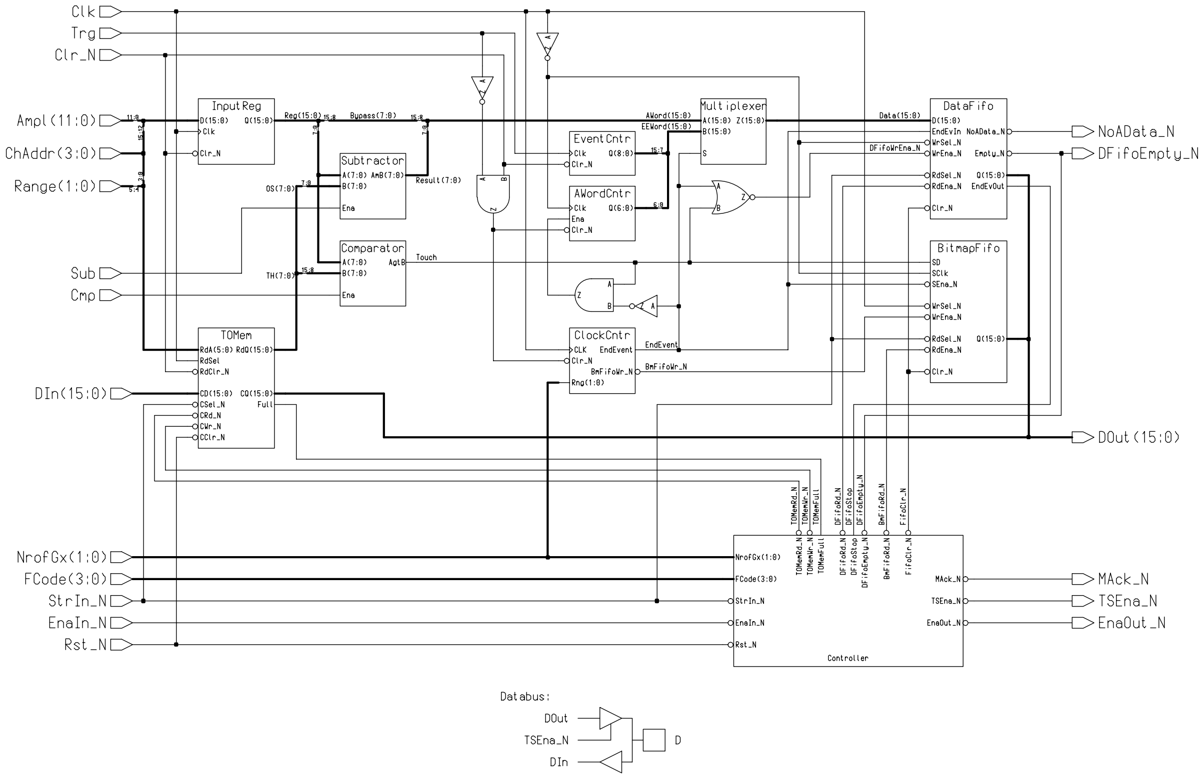

Figure 3.24: Schematics of the DILOGIC-1 performing the zero-suppression in the MCM.

The sparse data scan section is made up of a digital comparator and a subtractor, with an 8-bit range; each one is fed on one side by the analog information and on the other side by the contents of two separate memories filled respectively for each channel by the chosen level of comparison (pedestal + $N_{\sigma noise}$) and the pedestal value. At present, DILOGIC-1 can process up to 64 channels with a single range 8-bit ADC and 16 channels with the 4-range CRIAD- ADC0u7. The BIT-MAP memory (64 words $\times$ 16-bits) is filled with ones for channels above threshold or zeros for channels below the threshold; the analog data memory (512 words $\times$ 16-bits) is filled with the amplitude information and the address of the selected channels. An End-Event word turns off the event readout sequence; it contains the number of the hit channels (7-bits) and the number of the events (9-bits). In this way, DILOGIC-1 needs one more clock compared to the GASSIPLEX multiplexer clock; it can process 16, 32, or 64 channels. Figure 3.25a gives the timing diagram of the write operation and Fig. 3.25b shows the timing diagram of the read sequence.

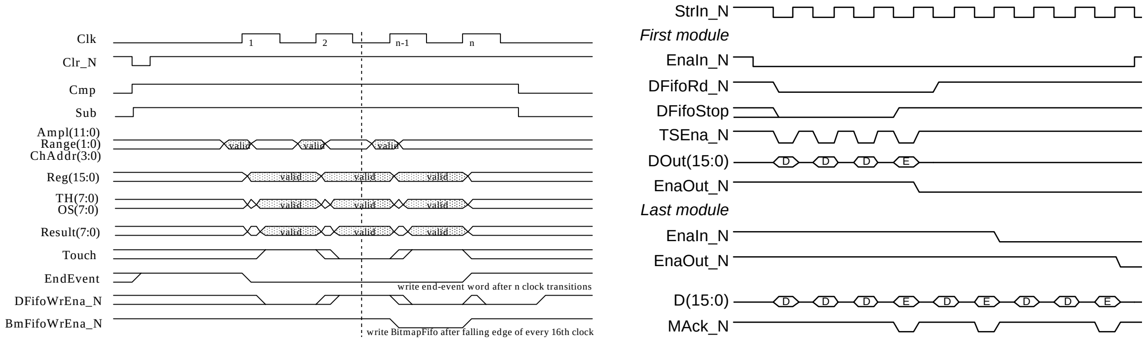

Figure 3.25: Operation of the DILOGIC: timing diagram of the analog write operation (a) and of the analog read sequence (b).

The output of DILOGIC-1 is made of a bi-directional 16-bit bus and a few control lines lines which allow the number of channels to process and the storage mode (with or without zero suppression) to be selected; on the output side, a function code of 4 bits allows the mode of operation shown in Table 3.9 to be chosen. Two flags give, respectively, the content of the data FIFO and the kind of data it contains: analog information + End-Event words or just End-Event words (event empty). A Mack signal comes out in phase with the End-Event word and a Token-in allows the readout of the chip, whilst a Token-out performs the Daisy-Chain to the next DILOGIC. A separate clocking permits an asynchronous operation, write during read.

Table 3.9: Readout controller code

F-code	Function
1000	Pattern readout
1001	Pattern delete
1010	Analog readout
1011	Analog delete
1100	Reset FIFO pointer
1101	Reset daisy chain
1110	Write Th. and Ped. Memory
1111	Read Th. and Ped. Memory
0xxx	Disable Dilogic

DILOGIC-1 was designed for a maximum write clock of 10 MHz and a maximum read clock of 20 MHz with a capacitative load of 50 pF, at a power consumption of 80 mW.

DILOGIC-1 was implemented on an MCM-Digitplex card. The first card was made with four GASSIPLEX (64 channels) and a second card was developed with four GASSIPLEX to fit the HMPID standard which is 48 channels. The results of the tests will be presented in the next section. A new DILOGIC-2 is under development to fit the HMPID requirements and to allow choices in ADC precision up to 12 bits and channel numbers up to 256. It will be described in Section 3.2.4.

MCM-Digitplex

The MCM-Digitplex [12] is a compact on-detector analog-to-digital processor for the readout of particle detectors. Each MCM has on board, a set of GASSIPLEX readout chips, a fast digitizer, digital pre-processing and data buffering. In this way, the MCM-Digitplex is able to select triggered events and provide the addresses and amplitudes of hit channels. A 64-channel prototype was developed, as shown in Fig. 3.26, and the first results obtained from electrical tests. Directly mounted on a custom-made VME digital I/O board and operated at a conversion rate of 5 MHz (limited by the present set-up), the noise level is kept at 700 e r.m.s. at zero pF additional input capacitance with a slope of 15 e/pF.

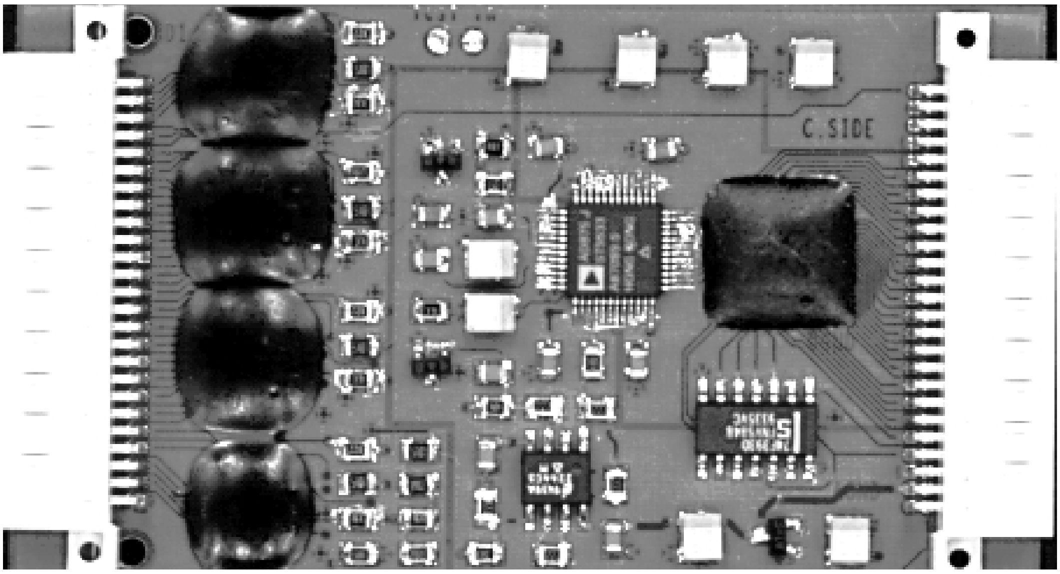

Figure 3.26: Photograph of a MCM-Digitplex board. The GASSIPLEX and DILOGIC-1 are implemented as dies, wire-bounded on the PCB and protected with plastic glue.

A set of 48-channel modules interfacing an 8-module readout bus was prepared and will be tested with the prototype of the HMPID detectors of the ALICE experiment. In the following the functionality of the full set was verified and the performance of a single card is presented.

Performance

In spite of the VME environment, the performance of the analog section was similar to that obtained with a single, shielded GASSIPLEX (Table 3.8): 700 e r.m.s. compared with 650 e r.m.s. The other characteristics are unchanged, particularly the inter–channel crosstalk which is lower than -60 db. The total power consumption of the 64-channel MCM-Digitplex is 1080 mW, which is 16.8 mW/channel; 300 mW are consumed by the discrete components: ADC, address counter and analog buffer.

Figure 3.27 show the measured pedestal spread, noise and data selection obtained on a MCM chip.

The idea to use an on-detector analog-to-digital processor was abandoned in favour of a simple 48-channel analog-multiplexed card. The digitization, the data processing and the memorization were moved out to the frame of the detector and are described in Section 3.2.4.

GASSIPLEX-0.7

The new version (Fig. 3.28) in 0.7 μm technology has a peaking time adjustable from 1.0 to 1.3 μs compatible with the trigger L0 latency. If this value is marginal due to a longer latency time imposed, an earlier fast multiplicity trigger instrumented in the zone generating a pre-T/H of 2 μs duration and sent to the HMPID in a time shorter than the L0 trigger latency might be envisaged. This pre-T/H, if validated by T_0, maintains the Hold on for normal readout; if not validated, the pre-T/H is released and the system is ready to accept the next trigger after 100 ns.

The time for baseline recovery at 1% of the peak amplitude was increased to about 5–6 μs. That value of the occupation time corresponds to a 1% probability of overlapping consecutive events with very dense central Pb collisions. For higher rates in pp mode, the event density is so low that a higher probability of overlapping consecutive events should not create problems in the pattern recognition.

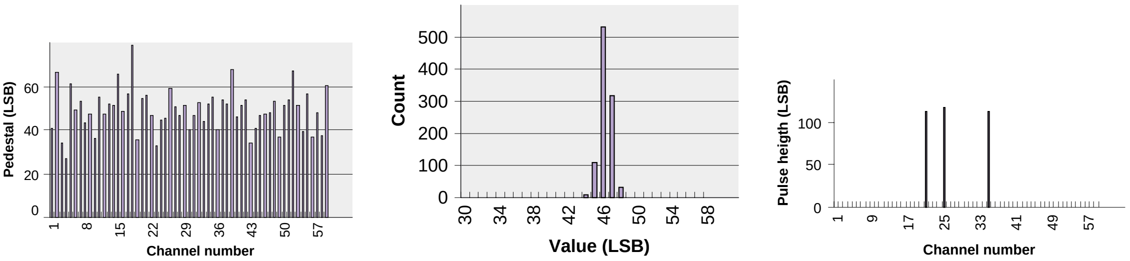

Figure 3.27: (a) Test of the MCM-Digitplex showing the spread of 64 pedestals. (b) Test of the MCM-Digitplex showing a channel noise performance equals to 0.73 LSB (least significant bit). (c) Test of the MCM-Digitplex showing a 3-channel hit configuration obtained with data selection.

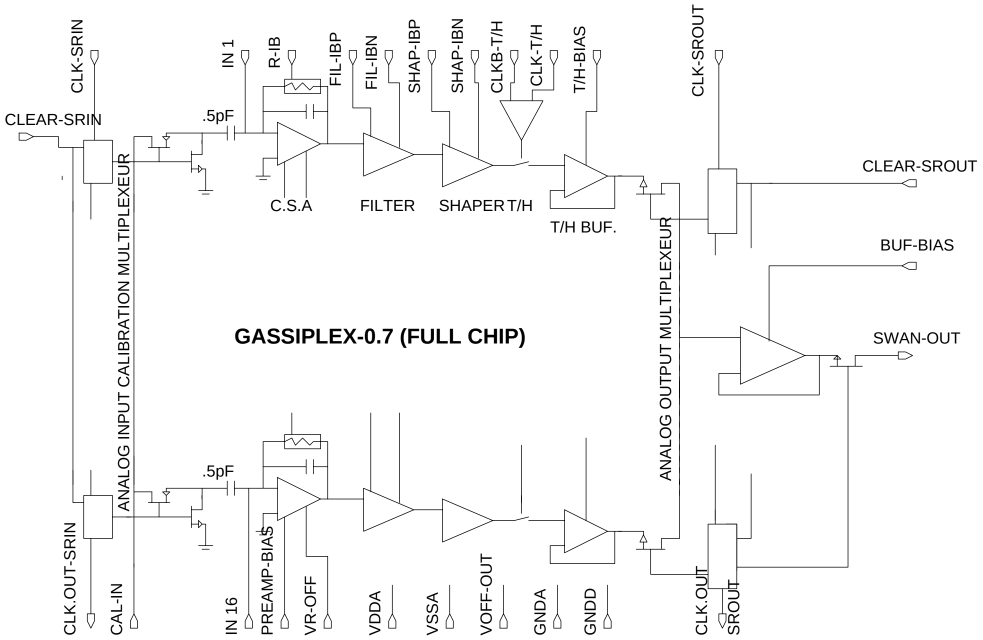

Figure 3.28: Schematics of the functional blocks composing GASSIPLEX-0.7. The calibration block is different from the 1.5 μm version (Fig. 3.15).

3.1.5 The CsI evaporation system

The basic properties of the CsI film were described in Section 2.1.1 and the main procedures to achieve films of high QE performance discussed. The CsI evaporation facility described now was used to process all the PCs studied up to now and will be the one in use for the final production of the HMPID PCs. The station is being extended with another vessel in which the PC freshly evaporated can be translated under vacuum and scanned for local evaluation of its QE.

3.1.5.1 CsI evaporation facility

The CsI evaporation facility is shown schematically in Fig. 3.29 and in colour Figs. 3.iii and 3.iv. The main body is a cylindrical vessel, made of stainless steel, of 0.8 m diameter, 1 m long, lying horizontally on a support and closed by rotatable doors to allow easy access from both ends. All around the vessel, a large number of ports are implemented, equipped with Conflat metallic sealed flanges used to install auxillary equipment such as pumps, pressure probes, electrical and motion feedthroughs, etc.

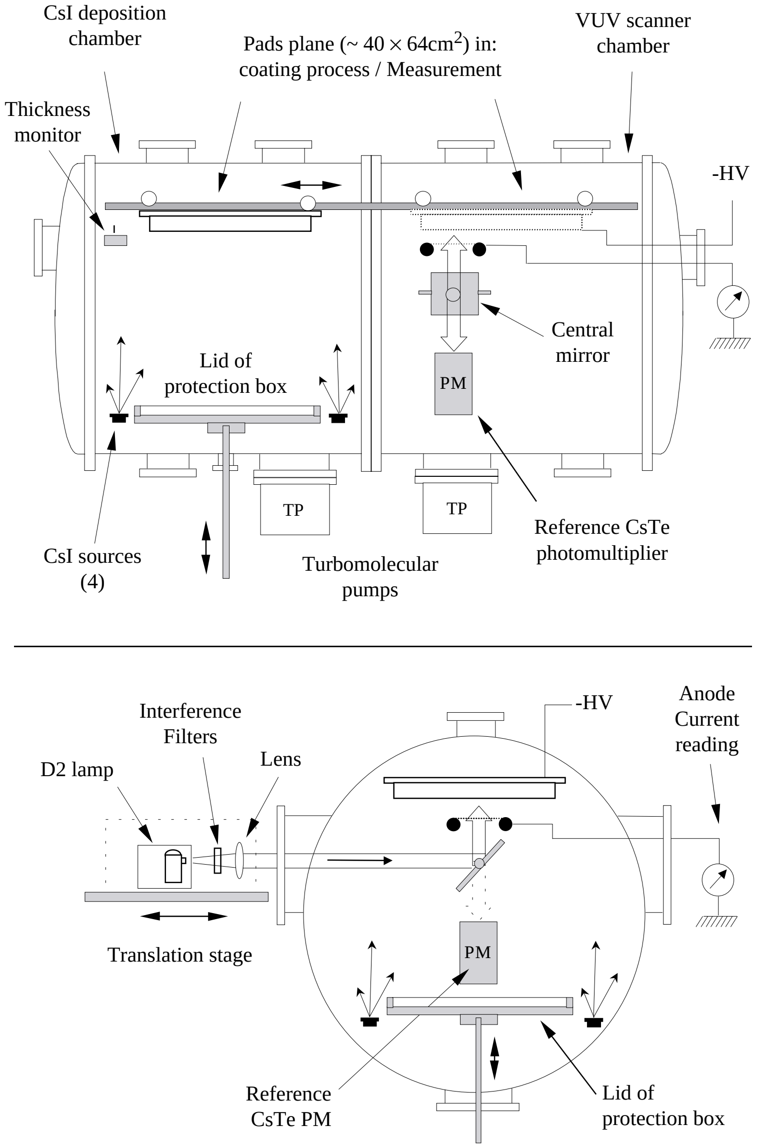

Figure 3.29: Schematic side- and cross-views of the CsI evaporation system. On the top: the evaporation and the QE measurement parts are on the left and on the right side, respectively. At the bottom: principle of the QE evaluation based on the measurement of the photocurrent produced by local irradiation of the CsI PC by a monochromatic UV beam, the intensity of which is obtained from a calibrated PM.

The primary and secondary vacuum are obtained from a 120 m^3/h Alcatel rotary pump and two Leybold Turbovac pumps, for a total evacuation speed of 2500 l/s, respectively, separated by a URB040 Balzers catalyser trap. Resistive heating bands are wound around the cylindrical vessel allowing the system to be heated up to about 100 °C, for outgassing and temperature conditioning.

A pressure ionization gauge SVT AL310 and Pirani/Penning Palzers TPG300 gauges are used to monitor the residual pressure. A Quadrupole Mass Spectrometer Balzers QMS200 is now available to analyse partial pressures of residual gases. The total residual pressure reached after outgassing is 2×10^{-7} Torr and 5×10^{-7} Torr with a pad panel array installed in the vessel.

Manipulation of the pad panel

The side of the pad panel where the FEE connectors are implemented is first enclosed in a box made of a metallic lid tightly fixed to the back of the pad panel. When installed inside the evaporator, a primary vacuum is independently made in this box as the full vessel is evacuated. In this way, we avoid an overlong outgassing time expected from the FEE-instrumented side, and balance the pressure on both sides of the pad panel. Then, although only the clean pad face is exposed to vacuum, a long outgassing time is necessary to reach a total residual pressure of 5×10^{-7} Torr indicating that moisture is still present at the surface of the pad PCB. Further improvement, such as increasing the outgassing temperature, should be investigated in order to reach a lower pressure.

A second metallic lid is installed at the bottom of the evaporator, fixed on a motorized system enabling it to be moved vertically up and down inside the evaporator. This lid is designed in such a way that it constitutes, when put in contact with the pad panel, a tight box to protect the CsI film. After the CsI film has been deposited and the vessel filled with argon at atmospheric pressure, the lid is lifted and kept firmly pressed against the pad panel frame in order to compress the O-ring and ensure a good tightness in the absence of screws.

Then, the so-constituted box is flushed with argon at atmospheric pressure and the evaporator vented at the same time. After opening the evaporator the necessary screws are inserted to tighten the lid on the pad panel definitively, the pressure exerted by the lifting device is released and the CsI pad panel removed from the evaporator under inert gas protection, having never been in contact with air.

CsI evaporation system

Given the diameter of the evaporator, the distance available from the boats to the substrate is reduced to about 50 cm. In order to ensure a uniform thickness of the CsI film over the large area of PCs, four evaporation boats are used. Their locations with respect to the PC are optimized such as to ensure a variation of the film thickness of about 10% over an area of 65×50 cm^2, as seen in Fig. 3.30.

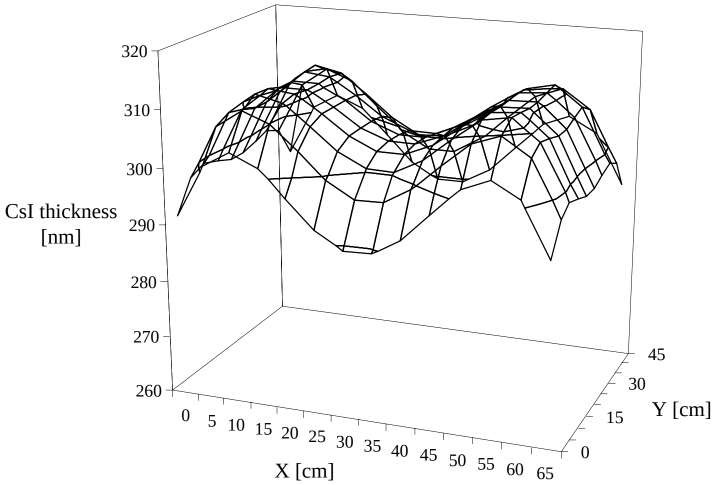

Figure 3.30: Thickness mapping of a CsI film of 60×40 cm^2 area obtained by evaporation from four boats.

The boats are made of molybdenum and heated independently by Joule effect. The CsI loads are calculated such as to ensure the desired film thickness after the complete evaporation of the content of the four boats. The CsI loads are pre-molten in the boats under vacuum in order to have a good thermal contact between the CsI and the boat, and avoid local overheating.

The four boats are evaporated simultaneously under the control of a quartz balance Edwards FTM5 monitoring the evaporation rate and the thickness. During a few seconds, a shutter masks the source in order to collect the beginning of the evaporation, possibly polluted, and is then removed. A slight drop in pressure of about 25$\%$ of the initial pressure is usually observed at the beginning of the evaporation, probably as a consequence of the reduced outgassing of the vessel and the pad panel caused by the freshly deposited CsI layer.

Conditioning

After the installation of the pad panel and the boats in the evaporator, the sequence of operations is as follows:

- pumping and outgassing during 2–3 days at 60 °C until a residual pressure of 2×10^{-6} Torr is reached,
- CsI evaporation on substrate maintained at 60 °C,
- heat conditioning at 60 °C under vacuum during 8–12 hours at a pressure of 2×10^{-6} Torr,
- stop heating for cooling down to 40 °C,
- venting the protection box and the evaporator with argon,
- lift the lid to form the protection box,
- opening of the evaporator and transfer of the pad panel to storage under argon flow.

The transfer of the CsI pad panel to the detector is described in Section 3.2.3.

3.1.5.2 Purpose and description of the VUV scanning set-up

The primary evaluation of the QE of a large PC using Cherenkov measurements at the test beam becomes impracticable with 42 pad panels as foreseen for the completion of the HMPID. So far, a simpler and faster method has been elaborated for evaluating the PC performance just after processing. As schematized in Fig. 3.29 and Fig. 3.31, it is based on the measurement of the direct photocurrent emitted under a local illumination of the CsI PC by a monochromatic and collimated VUV light beam. A cylindrical vessel the same size as the evaporator is appended to it to create a volume large enough to scan the PC.

The set-up is composed of the following elements.

- A motorized linear motion, parallel to the cylinder axis (x-coordinate), which performs first the transfer of the pad panel from the evaporation to the measurement vessel and then moves the panel by steps for the scan.
- Perpendicular to the evaporator axis (y-coordinate), a mechanical structure supports another stage providing the motion of the measurement arm in the y-direction. An expandable and tight connection is made between the stage and the measurement vessel by a tombac of 110 mm diameter, allowing a scan over 50 cm in the y direction.
- The VUV source, a D_2 lamp, its housing and the necessary CaF_2 optics delivering the VUV collimated beam are located on the y-moving stage. The UV beam is propagated through a tube up to a mirror fixed at the other extremity of the measuring arm, reflecting the beam up or down thanks to a remotely controlled action. At the same end of the arm, a wired electrode is fixed which collects the photoelectrons emitted when the mirror is positioned in such a way that the beam is directed towards the PC. Rotating the mirror by 90 degrees directs the beam to a reference phototube allowing the intensity of the incident photon flux to be calibrated. The phototube is a Hamamatsu R1460, 1 inch diameter, MgF_2 window. The CsTe photocathode response was calibrated against a NIST

photodiode in the 150–220 nm range. This array keeps the length of the UV beam and electrical connections fixed while the stage is moved for scanning purposes.

– In addition to the control of the parameters during the CsI film processing phase (pressure, temperature, rate, etc.), the aim of the VUV system is to perform automatic QE measurements by scanning large-area PCs. X/Y motions and positions of the measuring arm and the pad panel and relevant physical parameters (voltages, currents, etc.) have to be monitored. A slow-control monitoring task has been written for that purpose.

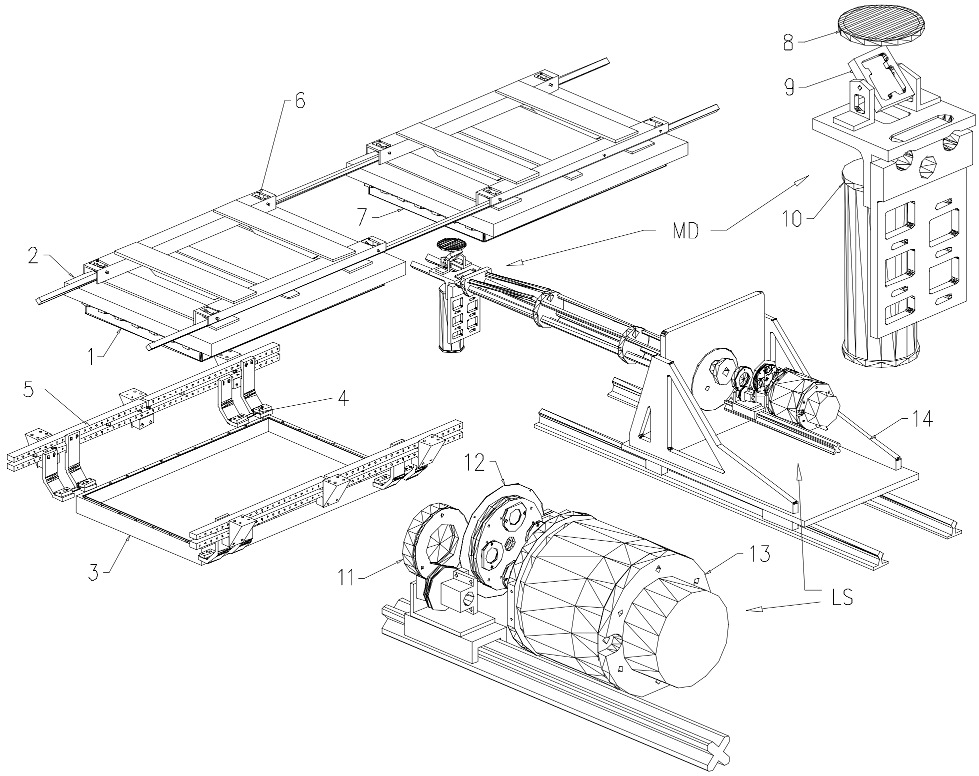

Figure 3.31: Axonometric view of the system used for the linear transport of the pad plane, and the UV-optical arm inside the vacuum vessel. Detailed: LS: The UV-source with interference filter wheel and MD: the photocurrent measuring device.

3.2 HMPID system description

3.2.1 Introduction

In Section 3.1, all the essential elements constituting a CsI RICH module and some auxiliary devices have been described in terms of functionality and performance. For the most critical ones, detailed discussions about their production and assembly procedures were presented and proofs of principle established, showing that they can be used in a large system. The successful test of a full ‘essential size’ prototype described in Section 2.3 has confirmed these remarks. In this chapter, the system aspect of the HMPID detector will be discussed by describing all the sub-systems composing the HMPID detector, at least at the level of a schematic. Next, the production and assembly schemes of each sub-system will be given.

The HMPID detector system is composed of seven modules having in common a number of auxiliary systems. The main sub-systems described are listed in Table 3.10.

Table 3.10: Main sub-systems constituting the HMPID detector

	MODULES
7	CsI RICH chamber with radiator
7	System instrumenting 23 040 pad channels for analog multiplexed readout, digitization and zero suppression
	AUXILIARY
1	Evaporation plant for production of CsI photocathodes
1	Storage plant for CsI photocathodes
1	Test and monitoring system
1	High-Voltage supply system
1	Control signal and trigger electronics system
1	Low-Voltage supply system
1	Data transfer system
1	Data acquisition system
1	Main gas mixture supply with purification and contaminent control systems
1	Main C_6F_{14} supply and system for circulating the liquid through the 7 modules acording to gravity flow scheme
1	Slow-control and monitoring system

The production of the HMPID can be split into four main parts — the radiator array, the chamber modules, the pad panels, the electronics — and two auxiliary systems, the gas and liquid supplies. The production of these items could be carried out independently over a period of time comparable for each of them, ranging from 12 to 15 months if effected in a continuous way. In fact, for more effective sharing of the institute manpower resources, production and testing activities will frequently be interleaved. We present these time schedules in a general diagram shown in Chapter 5.

3.2.2 The CsI RICH modules

The prototype that has been built can be considered as a final version of a HMPID module, even though its size will be increased by one-third. In the framework of a test period spreading over two years under test beam irradiations close to the ones expected at ALICE, all the major components fulfilled both the requirements of stable operation and satisfactory performance. In addition, it has been demonstrated that the numerous operations associated with the production of the module, e.g. the assembly of quartz radiator trays or the processing and mounting of the CsI photocathodes, can be performed reliably using simple procedures and tools. Lastly, over the available lifetime of the detector the performance was found to be stable. Possible improvements that would affect the present design could be oriented towards reducing the material budget of some elements, e.g. the radiator trays.

Therefore, we summarize the main components and assembly procedures of a HMPID CsI RICH module.

3.2.2.1 Components

A module consists of three main frames requiring conventional machining of Peral plates with tolerances of ± 50 μm at several locations. A flatness tolerance of ± 100 μm over the whole frame is required. The elements constituting the detector, the MWPC and the radiator array are associated to each frame and are listed in Table 3.11. Their design is made such that the assembly, mounting and dismounting operations cause no difficulties and ensure the necessary tolerances for reproducible operation, as discussed in Sections 3.1.1 and 3.1.2.

Table 3.11: Main elements constituting a module

No.	Frame	Main elements associated with the frame	Function	Ref.
1	Frame-1		Hold the 6 CsI pad panels Hold the anode plane Hold the digital electronics	3.1.1.2
6		Pad panel	CsI photocathode hold the FEE	3.1.1.1
6		Anode wire PCB	To solder 20 μm anode wires	3.1.1.2
1		Anode support line	To stabilize the anode wires	3.1.1.2
1	Frame-2		Hold the wired cathode MWPC Hold the collection electrode	3.1.1.3
6		Bars for crimping cath. wires		3.1.1.3
1		Collection electrode frame		3.1.1.3
1		Distance frame	To adjust the gap of the MWPC	3.1.1.3
1	Frame-3		Hold the Cherenkov radiators	3.1.1.4
3		Radiator tray	Contains the C_6F_{14} liquid	3.1.2.3
1		Piping array	Connect tray to the C_6F_{14} supply	3.1.2.3

3.2.2.2 Assembly and production test

We summarize the main steps for assembling a module according to the procedures detailed in Section 3.1.1 and 3.1.2. These operations are split into five parts which can be carried out independently (in parallel) and are expected to be performed in comparable periods of time.

Module: Radiator array

- production (external firm) of the quartz plates,
- production (external firm) of the Neoceram parts,
- production (external firm) of the mechanical parts: back plane and spare parts,
- quality control of the back plane and leak test,
- control and transparency test of the quartz plate,
- assembly of the Neoceram elements,
- assembly of the radiator tray with quartz,
- mounting of the trays in the back plane with piping.

Production test of a radiator tray: TEST-RAD-1

Each radiator tray is installed in the back plane which is closed by a panel allowing a tight box to be formed which is flushed with argon. The radiator tray is filled with C_6F_{14} in the vertical position in order to apply the same hydrostatic pressure expected at ALICE. Then, the circulated gas is passed through an analyser allowing traces of electronegative gas with high sensitivity to be measured. A tray is accepted when the trace level is maintained below 0.5 ppm during a fixed period.

The necessary equipment, C_6F_{14} circulation, analysers, etc. are those used during the beam test of proto-2.

Module: Frames and MWPC

- production (external firms) of all mechanical parts and PCBs,
- quality control, final polishing, cleaning of all frames and mechanical components,
- installation on Frame-1 of the PCBs holding the anode wires and frame thickness adjustment by machining,
- installation of support lines and soldering of the anode wires (20 μm),
- test of anode wire tension,
- weaving of the cathode and of the collection electrode using crimped pins,
- distance frame machining for thickness adjustment,
- test of the cathode wire tension.

Module: Pad panels

- production (external firm) of the pad PCBs,
- production (external firm) of all mechanical parts, frames, protective boxes,
- quality control, final polishing, cleaning of all frames,
- soldering of the signal Kapton circuits on the back of the pad PCBs,
- preparation of the sandwich panel elements (foam, 2d PCB, etc.),
- final assembly of the pad panel,
- assembly of the protection box for CsI PC,
- electrical and leak tests.

Production test of a module: TEST-MOD-1

Once all the parts are available, a module is preassembled with the pad panels not yet coated with CsI. The aim of this operation is to certify that the wire electrodes and the pad cathodes satisfy the conditions for stable operation at the maximum voltage. For this purpose, the measurement of the chamber current is a convenient tool as any defective part of the chamber driving a too high current can easily be located by disconnecting a group of eight, or even a single anode wire from the HV supply. In addition, it is foreseen to equip one-third of the anode wire plane with FEE (96 channels) in order to have a better characterization of the behaviour of the chamber in terms of rates and pulse shapes.

The sequence of tests is foreseen as follows:

- After leak test, the module is flushed with CH_4. The radiator trays are filled with C_6F_{14}.
- Traces of contaminants, O_2, H_2O and electronegative gas are measured and monitored for a fixed period.
- Having shortened all pads to ground, the module is put under high voltage. The chamber current, the rates and pulse-height spectra of anode wires signals are recorded as background and under local irradiation by a Ru^{106} or Sr^{90} source.
- Eventual repairs or replacements are performed if a part of the chamber does not satisfy the specifications listed below.

The specifications to be achieved for the acceptation of a module are:

- The fractions, in volume, of contaminating species must be less than 5 ppm for oxygen and moisture, and < 1 ppm for electronegative gas at a CH_4 flux of 30 l/h;
- a total dark current at maximum voltage (2250 V in CH4) less than 1 nA for a third of a module;
- a uniform wire rate map corresponding to the expected local cosmic irradiation;
- a uniform map of the most probable pulse height corresponding to the expected local cosmic irradiation.

Once these specifications have been maintained for a fixed period of time, the module is accepted and the pad panels are ready for CsI evaporation. The next sequence of tests are discussed in Section 3.2.5.

3.2.3 The evaporation system for CsI photocathodes

It is planned to use the evaporation system described in Section 3.1.5 to perform the production of the 42 CsI PCs equipping the seven HMPID modules. That system will be composed of two parts: the one used for the evaporation of the CsI film and the other one, the VUV scanner, in which the CsI PC is translated for evaluation of the QE performance by an automated two-dimensional scanner[2].

The scanning part of the system will be available at the end of 1998. Before launching the PC production, it is foreseen to complete an experimental programme defining and testing the final choices still pending in order that the bulk production is undertaken with a guarantee of achieving the highest yield of optimally performing PCs.

The preliminary programme will be devoted to fixing the following points:

- scan existing PCs for comparison between the Cherenkov and the VUV beam QE evaluations,
- quantify the QE improvement by heat treatment in case of large-area PCs and optimize the post-treatment parameters (see Sections 2.1.1.3 and 3.1.5.1)
- choose the final pad PCB technology (see Section 3.1.1.1),
- optimize the outgassing operation,
- validate the possibility to re-evaporate further CsI films on the same substrate after removal of a non-satisfactory one.

As discussed before, these studies necessitate a statistical analysis from several samples to be conclusive. For time- and cost-based arguments, it is unrealistic to perform these tests using the Cherenkov photon counting technique at a test beam. On the contrary, the VUV scanner is well adapted since the evaporations will be made on the PCB samples only, without assembling the entire pad panel structure needed for FEE implementation. Also, smaller sample sizes will be used, allowing for examination of several samples at a time. At the end of the preliminary programme, expected to last about a year, the evaporation system will be fully completed and the slow-control system ready and checked to operate safely in automated mode for a long production period.

3.2.3.1 Procedures for the final production of the CsI PCs

The final production of the 42 CsI PCs can be launched as soon as the production and test programs, TEST-MOD-1 and TEST-MOD-2 (see Section 3.2.5), of the pad panels and the modules have been completed. The completion of the PC production has to be scheduled as close as possible to the start of the experiment in order to minimize the storage period.

For the time being, the sequence of operations foreseen for the production of a CsI PC repeats the one which was used during the R&D period described in Section 3.1.5.1. Variations in some parameters are expected to result from the preliminary programme but are not expected to affect seriously the main sequence described below.

Evaporation sequence

- premelting of the CsI boats,
- preliminary heating of the pad panel under neutral gas flow to eliminate moisture,
- installation of the pad panel and the boats in the evaporator,
- pumping and outgassing the evaporation system for 2–3 days at 60 °C until a residual pressure of 2×10^{-6} Torr is reached,
- CsI evaporation on substrate held at 60 °C,
- heat conditioning at 60 °C under vacuum for 8–12 hours at a pressure of 2×10^{-6} Torr,
- stop heating for cooling down.

---

[2] The system has been built and operated in close collaboration with the TA1/EP-CERN group. It might be considered as a facility possibly used by other groups, e.g. COMPASS/NA58, also aiming at the production of a large number of CsI PCs.

QE evaluation sequence

- transfer of the CsI PC into the measuring part of the system,
- two-dimensional scan based on 24 measurements, (6×4 X/Y locations) according to the parameters defined by the preliminary programme: wavelengths, photon flux, duration, etc.

Storage sequence

- venting the protection box and the evaporator with argon,
- lifting the lid to form the protection box,
- opening of the evaporator and transfer of the pad panel to the storage under argon flow system (see next section).

The transfer of the CsI pad panel onto the detector is detailed in Section 3.2.2.3.

3.2.3.2 Components

A large part of the evaporation system has already been built (see colour Figs. 3.iii and 3.iv) and will be completed by the end of 1999.

In addition, one has to build a system for storing the PCs, keeping them in their individual protective boxes under constant argon flow. That facility (the CsI-PC storage system) will be of transient or complementary utilization since the PCs will usually be mounted on a module and also kept under argon flow for storage.

The storage facility is composed of a primary argon source with input and output manifold systems to supply each box and to control the contaminant fraction.

3.2.3.3 Assembly and test

As mentionned in Section 2.3.2.3, the mounting of the CsI PC panels was performed on proto-2 by using a large glove box mounted at the back of the module and allowing the transfer of a PC from its protection box to the module under controlled argon environment. To allow for some parallel installation, two glove boxes will be built of the size of a final module. A perspective view is shown in Fig. 3.32, illustrating the sequence of operation for mounting PCs on a module:

- The HMPID module, equipped with blank panels in place of the pad ones, is circulated with argon.
- The glove box is fixed to the module without its closing lid.
- Two CsI PC panels protected by their boxes are hung vertically close to the blanks with the back sides facing the operator and kept under argon flow.
- The glove box is closed with the lid holding the gloves and flushed with argon.
- When the oxygen and moisture fractions are below a fixed value (100 ppm), a blank panel is removed from the module and stored aside, and then a CsI PC panel is removed from its protective box and fixed in place of the blank panel. There is room enough in the glove box to fix two CsI PCs in a single sequence, meaning that three sequences are needed per module, i.e. about 6–8 days.

An equivalent procedure is used to remove CsI PCs from a module in case of opening of a chamber.

3.2.3.4 Production schedule

The production of PCs is segmented in batches of six PCs with an interruption of 15 days for maintenance of the evaporation system. As soon as a batch of six PCs is available, they are installed on a module and ready for test for a period of 1.5 months (see TEST-MOD-3 in Section 3.2.5). The total duration amounts to 16 months, assuming a continuous activity. It is advisable to carry on this programme without interruption in order to minimize the storage period (ageing) before the start of the experiment (Section 2.3.2.3).

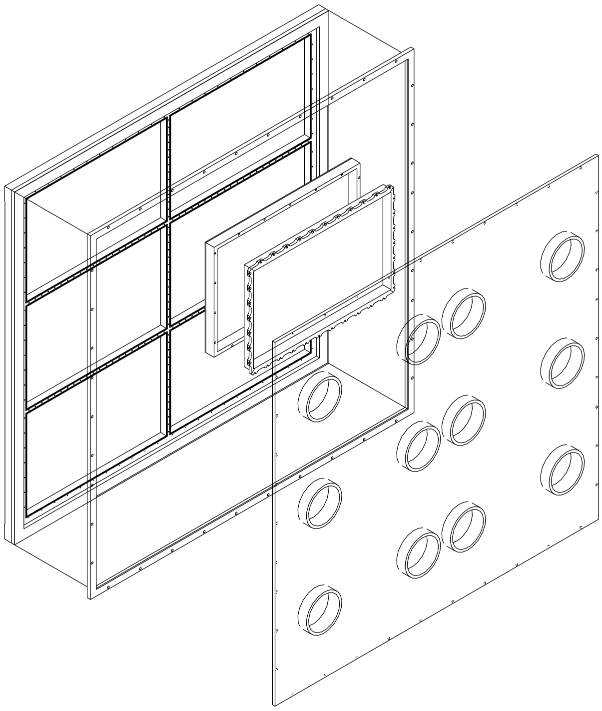

Figure 3.32: Axonometric view of the glove box array used to transfer under controlled argon atmosphere a CsI photocathode from its protective box to the detector.

3.2.4 The readout electronic system

Several modes of operation are expected to be exploited for the physics at ALICE since the LHC collider will be run with protons and with different species of ion beams, i.e. calcium and lead.

The main experimental parameters are shown [13] for three running modes in Table 3.12. Two extreme situations have to be treated by the readout system: a data flow corresponding to a high rate of events of low charged multiplicity in pp mode, changing to a low rate of very high charged multiplicity in Pb–Pb mode.

Table 3.12: Main experimental parameters at ALICE

Collider mode	Unit	pp	Pb–Pb	Ca–Ca
Bunch interval	ns	25	125	125
L0-trigger latency	μs	1.2	1.2	1.2
Max. interaction rate, mini. bias	kHz	100	10	10–100
Max. interaction rate, central	kHz	100	1	1–10
Charged multiplicity in 1 rapidity unit central collision		8	8000	1200
Hit occupancy, mini. bias	%	3–4 10^{-3}	3–4	0.45–0.6
Hit occupancy, central	%	1.5–2 10^{-2}	15–20	2.2–3
DAQ rate central/mini. bias	Hz	1000	40	150
Luminosity half-life time	h	10	10	> 50

The first-level trigger latency (L0) originates from considerations described by the Trigger Group in Ref. [14] and has been fixed to 1.2 μs. As stated in Chapter 1, the evaluation of the hit occupancy is based on the highest expectation of the charged-particle multiplicity, actually model-dependent. The DAQ rate is in fact driven by the large tracking systems, ITS and TPC [13], producing very large event sizes. In case of operation of the TPC, one has to consider a dead time imposed by the 200 μs drift time necessary to collect the primary ionization deposited by an event.

3.2.4.1 Final version: system schematics

Referring to Section 3.1.4.5, the final electronic system is based on a modular array composed of three GASSIPLEX chips (48 channels) and an MCM composed of one ADC and one zero-suppressor chip, referred to as DILOGIC. It has been shown that the modular array and the associated ASICs are operational at the prototype level. Final ASIC versions, described below, are being completed. The final readout system is presented at the schematic phase and the final design is still in progress.

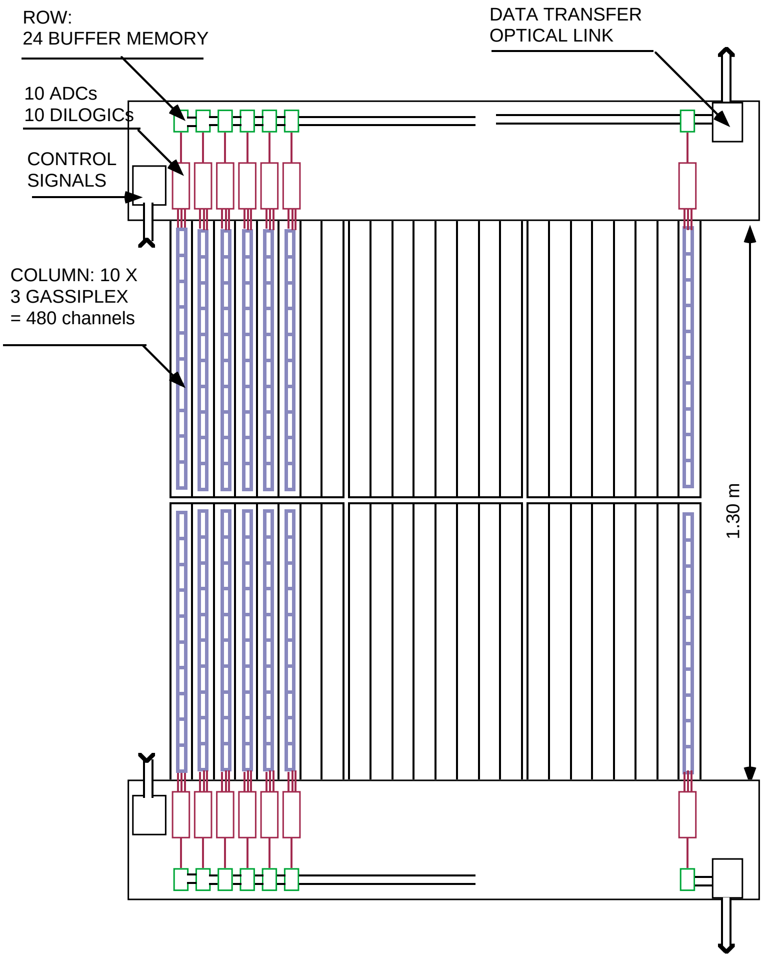

Figure 3.33: Schematics of the implementation of the FE and readout electronics on a HMPID module.

The implementation of the modular arrays to read out the HMPID modules is organized according to a parallel/serial architecture as shown in Fig. 3.33. The module is first subdivided into two halves, each of them in turn partitioned into 24 columns. A column is composed of 10 modular arrays, i.e. 480 pad chanels. Each column is connected to a buffer memory with a capacity to store data from 480 channels needed for pedestal measurements. Finally, the 24 memories are bussed in a row linked to the DDL sender card. The readout sequence of one-half of a module is done as follows:

- parallel multiplexing of all the modular arrays ending with data stored in the DILOGIC FIFOs,
- serial transfer of the data from the 10 DILOGICs into the buffer memory performed in parallel on the 24 columns,

– serial transfer from the row of 24 buffer memories into the DDL sender card,
– transfer from the DDL to the DAQ buffer cards.

Given the specifications of the two final ASICs, the time necessary to read out an event is evaluated in Table 3.13 for two modes of physics and pedestal operation, according to the detector occupancy and conservative readout clock frequencies.

In case of Pb–Pb mode, the total readout time is significantly smaller than the corresponding L0-trigger periods, implying small dead-time loss even in case of event rejection. That is not the case in pp mode where the two durations are comparable in time. However, since the second-level trigger (L1) is available after 2.4 μs [14] and has a much longer period, one could apply a fast clear on the data after 2.4 μs each time there is no L1 signal associated with the L0 one. The pedestal/calibration mode is discussed in the next section.

Table 3.13: Readout time of the HMPID system for various operating modes at ALICE

Operation mode	Unit		pp	Pb–Pb central	Pb–Pb mini. bias	Pedestal
Occupancy	%		0.2	15	3	100
Word/column (480 chan. max)	No.		1	72	15	480/2 = 240
Word/row (24 buf. mem.)	No.		24	1728	350	5760
		freq.	dur. [μs]	dur. [μs]	dur. [μs]	dur. [μs]
MPX, 48 chan.	MHz	7.5	6.4	6.4	6.4	6.4
Transfer colum	MHz	10	0.1	7.2	1.5	24
Transfer row	MHz	20	1.2	86	18	288
Transfer DDL	MHz	25	1	69	14	230
Total	μs		8.7	169	40	550
L0-trig. period	μs		10	1000	100	
L1-trig. period	μs		1000	20 000	4000	

3.2.4.2 Components

1. *Final version: GASSIPLEX-0.7-2*
   This chip has the same architecture as the GASSIPLEX-0.7-1, described and characterized in Section 3.1.4.1. It has been modified as follows:

   i) the peaking time can be adjusted between 1.1 and 1.3 μs, to satisfy the ALICE L0-trigger latency,
   ii) the test/calibration pulse can be sent channel by channel in a sequential mode,
   iii) the dynamic range has been increased by decreasing the sensitivity, to fit the requirements of three ALICE detectors aiming to use the chip in different operational modes: HMPID CsI RICH for single electron detection, Veto-PHOS and DI-MUONS pad chambers for MIP localization. The sensitivity can be adjusted according to the needs, by changing the gain on the internal output buffer or on the external buffer (always necessary by groups of 3–4 chips). Its new characteristics are shown in Table 3.14.

   The prototype of the GASSIPLEX-0.7-2 was developed at CERN [15] and submitted in August 1998 to IMEC for prototype fabrication to be delivered in autumn 1998.

2. *Final version: DILOGIC-2*
   This chip has the same architecture as the first version, DILOGIC-1, described in Section 3.1.4.5.

Table 3.14: GASSIPLEX- 0.7-2 performance

Technology	MIETEC- 0.7 μm
Peaking time	1.2 μs
Peaking time adjust.	1.1 to 1.3 μs
Noise at 0 pF	600 er.m.s.
Noise slope	11 er.m.s./pF
Absolute dynamic range	2 V
Dynamic range at 4 mV/fC	500 fC
Minimum sensitivity	4 mV/fC
Baseline recovery	$< \pm 0.5\%$ after 6 μs
Analog readout speed	10 MHz max.
Silicon area	$3.63 \times 4 = 14.5$ mm^2
Power consumption	8 mW/channel at 10 MHz

Its capacity has been increased in order to handle more input steps and larger digitization sizes. Its main features are:

Zero suppression and pedestal subtraction.
Selectable number of units of 16 channels to be read: 1, 3, 4, 8 4-bit readout protocol.
19 bit × 512 words DATA memory.
16 bit × 256 words bit-map memory.
16 bit × 256 words threshold and subtraction memory.
19 bit bi-directional bus.
15 MHz max. writing speed.
20 MHz max. readout speed.
Full testability.
Silicon area: 47 mm^2 I/O connections: 60 pads.
Power consumption: 100 mW.

Given the maximum capacity of the memories, the chip can be configured by matching the number of inputs and the digitization size of the ADC, e.g. as in Table 3.15.

Table 3.15: DILOGIC-2 configurations

Config.	No. of inputs	ADC	No. of ADC bits
1	64	CRIAD [x]	4 ranges
2	64	linear	12
3	256	linear	10
HMPID	48	linear	12

The DILOGIC-2 has 55 000 equivalent gates, memories not included. The prototype fabrication, using 0.7 μm technology, will be done at IMEC from a block diagram and specifications written at CERN [16]. Delivery of prototypes is expected in February 1999.

3. *Cards and motherboards*

Figure 3.34a shows a perspective view of the hardware implementation of the readout electronics on half of a module and Fig. 3.34b shows the way it is attached to the module. All the components are described below.

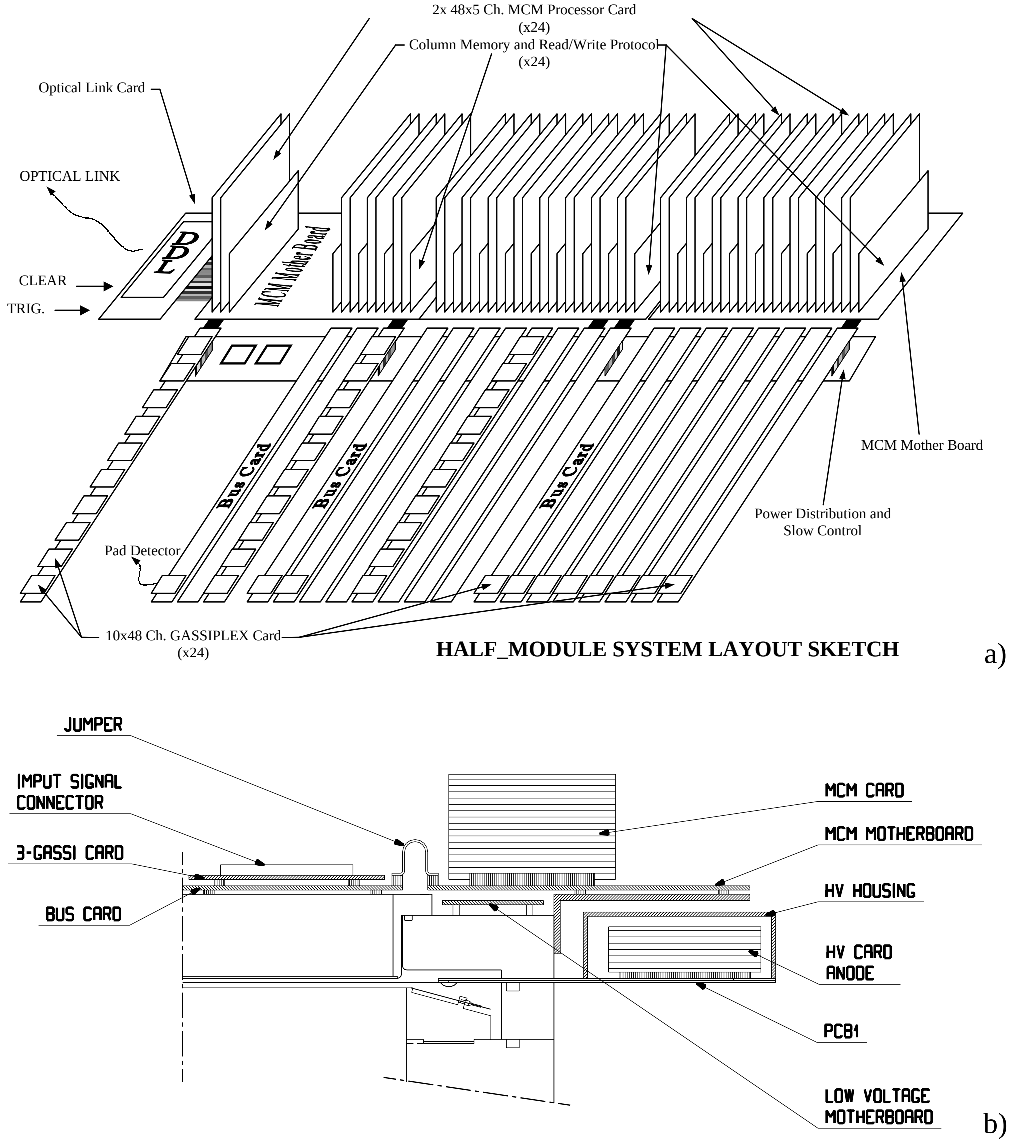

Figure 3.34: (a) Axonometric view of the electronics boards on the HMPID module. (b) mechanical fixation of the electronics boards on the module.

i) 3-GASSIPLEX card:
Ten of these cards are mounted on a motherboard directly attached to the pad-panel back plane, to perform the readout of 10×48 channels in a row. The components of the card 3-GASSIPLEX are, as seen in Fig. 3.35:

- 3-GASSIPLEX chips and the necessary SMD components to make the biasing and the decoupling of the DC pins,
- a multiple DAC to equalize the DC level of the mean value of the pedestals of each chip, avoiding the GASSIPLEX chips sorting as described in Section 3.1.4.3,
- a set of logic buffers to separate each card from the others to avoid the spoliation of a common logic line by a damaged chip,
- a small HV protection card put near the input connector to protect the channels from HV spark.

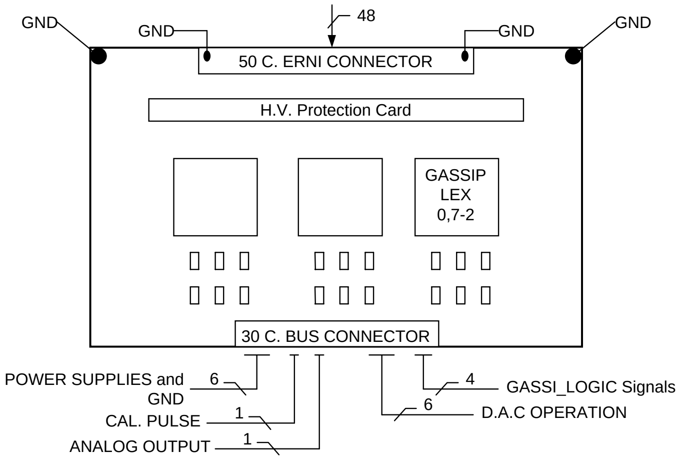

Figure 3.35: Schematic of a 3-GASSIPLEX card.

Finally, two connectors make the connections on one side to the detector pads using the Kapton circuits and on the other side to the column bus card. The connections to the column bus card are done through a standard 2×15 contact connector. The ± 2.75 V supplies and the ground will use six contacts, the GASSIPLEX logic signals and the DAC operation will need respectively four and six contacts, while the calibration pulse as well as the 48-channel multiplexed output will use one each. The other contacts are reserved.

ii) Column bus card:

As seen in Fig. 3.34a, this multilayer board supports ten 3-GASSIPLEX cards and distributes the common functions: LV supplies, grounding, DAC operation, GASSIPLEX logic signals and calibration. The analog multiplexed outputs are separated to be processed individually on the MCM processor cards. This bus card has two separated connections: one to the MCM motherboard and the other to the power and slow control board.

iii) MCM processor card:

The MCM processor cards, shown schematically in Fig. 3.36, are mounted on the MCM motherboard attached to the frame of the detector. One card processes 240 channels using five groups, each composed of an analog buffer which adjusts the front-end sensitivity at the operating value, a fast 10-bit ADC (or 12-bit), a DILOGIC-2 and some active components. Two connectors make the connections on one side to five 3-GASSIPLEX cards and on the other to the Column Memory and Read/Write protocol card (CMRW). Two MCM processor cards are connected to the CMRW card which stores data from one column; 24 of these cards collect the data corresponding to a half-module.

There are three main operations: reading–writing pedestals, data aquisition and testing.

The pedestals have first to be measured when the detector is not active.

Collected for each column in the CMRW card, they are sent to the control room to be processed and sent back to the threshold and subtraction memory of each DILOGIC-2. Each channel will need one DILOGIC clock cycle to read or write a pedestal because 16 bits are needed per channel.

The data aquisition is performed as follows.

When a trigger occurs, all the necessary clocks are generated by the clock generator fed by a common half-module oscillator. The sequence is: GASSIPLEX multiplexing clock, ADC clock, address-generator clock, DILOGIC-2 write-clock. The DILOGIC-2 processes the data given by the ADC and stores the good data in its FIFO memory.

The write sequence takes 6.4 μs. After that time, the DILOGIC memory of each column is emptied in the CMRW card, during this process the empty end-of-event word, which closes the reading of each event in a DILOGIC-2, is discarded. The CMRW card will be filled only with good data.

Then the data are ready to be sent to the control room by the DDL.

The testing can be divided in three parts: the front-end electronics, the digitization and the DILOGIC-2.

The front-end electronics can be tested by the calibration signal and the DAC by its effect on the output DC level of the 3-GASSIPLEX.

The injection of a calibrated signal also allows the digitization to be tested. The DILOGIC-2 can be tested in a separate mode. After having been put in test mode, its bi-directional output bus allows a sequence of data to be injected to test the threshold and subtraction circuit, the write protocol, the read protocol and the differents memories.

iv) Column memory and read–write protocol card:

This card, as seen in Fig. 3.34a, collects the data coming from each column and makes the connections with the DDL through a 32-bit bus. Its memory capacity is at least 512 words of 32 bits, which is the necessary number of words to read/write the pedestals and the necessary number of bits to process all the operations.

Around the memories, a few components will take care of the read/write protocol of the three main operations.

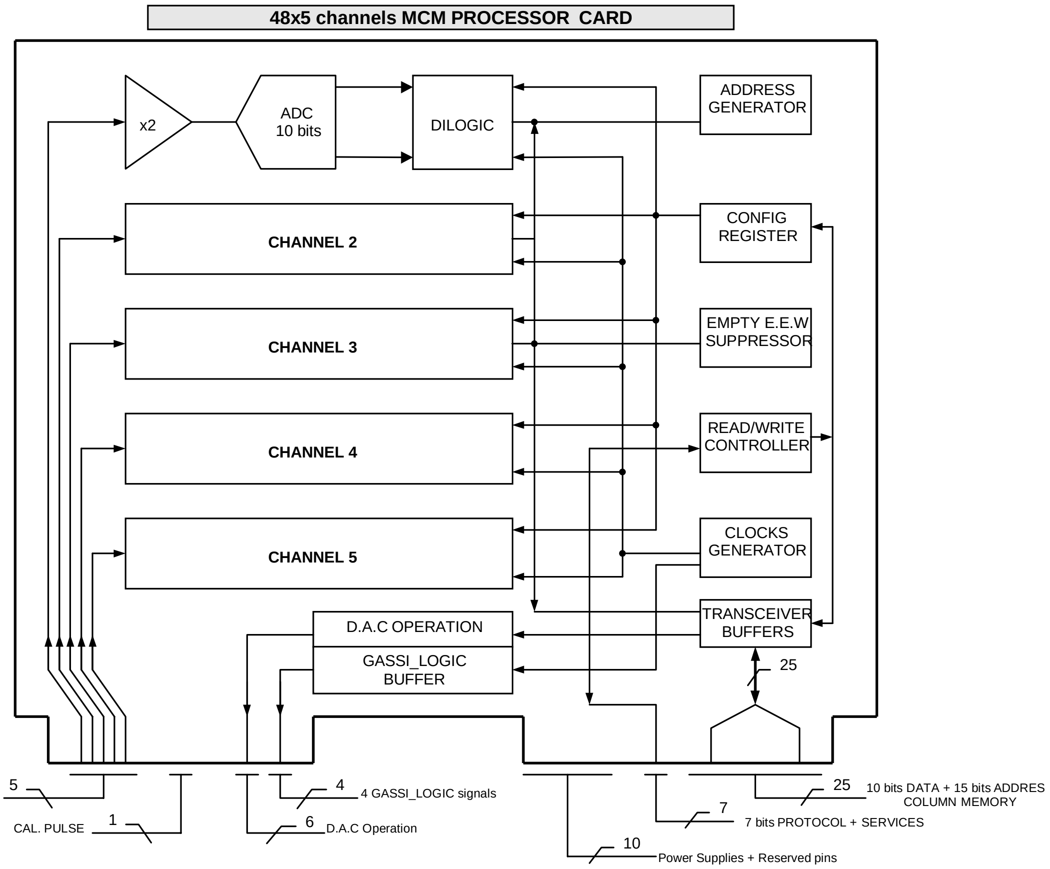

Figure 3.36: Schematics of the functional blocks of a MCM-processor card performing digitization and zero suppression of 5×48 channels.

3.2.4.3 Assembly and tests

The only components that are not available on the market are the two ASICs, GASSIPLEX-0.7-2 and DILOGIC-2. It is foreseen for them to be produced in the same foundry, MIETEC.

GASSIPLEX-0.7-2

After some prototyping production, it has been decided to mount the GASSIPLEX die in a plastic package without previous testing on wafer. This kind of package, of a very low price (1.2 CHF/chip), is actually well controlled and has a performance comparable to a more expensive ceramic one.

After delivery, two operations have to be done: the chip acceptance and the burn-in tests. The first one could be done in an automatic way by the same firm that makes the packaging, provided the firm gets material and procedures from us. The second one is foreseen to be done by the collaboration, using two specialized boards on which 256 chips are mounted on sockets. Burn-in and chip characterization are done on the same batch.

It is possible also to give this work to a specialized firm which will make the tests on a specification basis.

DILOGIC-2

This will be encapsulated in a plastic package and tested by a specialized firm.

FEE card assembly

The assembly of all cards and boards is sub-contracted as industrial support to firms that are specialized in surface-mounting components.

The tests of all cards is done in the collaboration, using a dedicated test set-up. The acceptance test is finalized on the module.

Table 3.16 summarizes the main elements constituting the FEE readout system. The data transfer and DAQ systems are described separately in Section 3.2.8.

Table 3.16: Components of the readout electronics

ASIC chips	No.
GASSIPLEX-0.7-2	10 080
DILOGIC-2	3360
CARDS and BOARDS	
3-GASSIPLEX card	3360
Column bus card	336
Power/slow control board	42
MCM processor card	672
MCM motherboard	42
CMRW protocol card	336
TEST BOARDS	
Burn-in	2
Digital test	2

3.2.5 The test and monitoring systems

Several tests have been performed during the production period, meant essentially to provide green lights for pursuing the construction of the modules:

– the radiator trays are declared leak-tight but the UV transparency must be evaluated,

- the photodetector chambers are leak-tight and stable at the operating voltage but the single-electron detection efficiency and gain homogeneity must be measured,
- the QE of the CsI PCs have been previously evaluated in vacuum but the response must be checked for single-photon counting in the gaseous MWPC,
- the FEE components are individually checked but the system behaviour must be evaluated when mounted on a module.

Therefore, to answer these questions, an intermediate test is still needed to ensure that the response to single electrons is adequate over the whole module before starting the CsI evaporation programme. In fact, this request is similar to the one related to the need of a monitoring facility aimed at following the evolution with time of the QEs in a module when the CsI PCs are installed.

The method that was routinely used for single-electron studies with the prototypes was to illuminate the pad cathode, coated with CsI or not, with a pencil beam of UV light generated by an ORIEL deuterium lamp, a quartz optical fibre and a collimating device. The trigger signal needed to read out the pad FEE is given by the anode wire signal provided a sensitive enough amplifier is selected.

Two systems are under development to provide means to test the response of a module to single electrons and to monitor in a simple way the QE in a module.

Test of the response of a module to single electrons: TEST-MOD-2

Two methods are being investigated to generate a low enough rate of single electrons into a large module. The first is to use a Neodym YAG laser emitting at 266 nm, creating along the beam path in the gas primary ionization essentially composed of single electrons given the low energy transfers. Adjusting the energy of the light pulse at a low enough value allows a density of primaries to be created such that they are well separated along the path of the beam. The laser provides the trigger needed to read out the pad FEE. The geometry of the light beam propagating into the chamber has to be optimized in such a way that an optimum scan of the whole chamber can be performed per laser shot.

The second method is to install a set of quartz tubes traversing the proximity gap. A small UV lamp is moved inside these tubes, illuminating the pad plane and generating single electrons by photoelectric effect at the pad surface. This equipment can be easily removed since the pad panels are as yet uncoated with CsI.

The goals of the test are:

- having implemented all the FEE elements previously tested on a module, to evaluate in a real operationnal mode the FEE system response, i.e. noise figure, preamp gain calibration, pedestal stability, readout protocols, etc.;
- by using one of the methods to generate single electrons, to record at various chamber gains PH spectra corresponding to delimited pad zones in order to produce a map of the chamber gain (i.e the mean value, A_0, of each PH spectrum) per pad panel (see Sections 2.1.2.4 and 2.3.2.4).

In case of too large a gain discrepancy between panels, the distance pad-plane-to-anode wires could still be readjusted by proper machining of the pad-panel frame. In case of satisfactory results, the module and the FEE are ready for the last operation, that is the CsI evaporation on the pad panels.

Monitoring of the QE

The system under development consists of a feedthrough allowing to transmit a quasi-monochromatic UV pencil beam to illuminate a CsI-coated pad and to count the single-photoelectron rates at several adjacent anode wires. A part of the UV beam is deviated on a calibrated solar-blind photomultiplier (Hamamatsu R1460) ensuring the normalization of the incident photon flux and therefore of the single-electron rate. PH spectra will be recorded as well in order to make the measurements at the same chamber gain. Laboratory tests will be performed to check the relation of the QE to the counting rate and the reproducibility and stability of the method.

If the method is found relevant, several devices could be installed along the frames of the module.

Final test: TEST-MOD-3

Following the production schedule of the CsI PCs (see Table 5.1), we are planning to perform a final test of every module fully equipped, possibly at the ALICE test beam line, T10 at the PS East Hall. As described in Chapter 2, such a test provides in one go all the information listed at the beginning in real operational conditions. In addition, it provides an essential characterization of the performance of the whole detector, QEs, gain, transparencies, photoelectron yield, that is of prime importance as input parameters for the pattern recognition and simulation programs as discussed in Chapter 4. Last, we have experienced while testing proto-2 at the SPS that a full scan of a module using single-particle events can be performed in 4–5 days, not including the filling and purification of the radiators. All elements necessary for the development phase are available in our laboratory, including the expensive Neodym YAG laser.

3.2.6 Control signal and trigger electronics

The control signals needed to operate the FEE will be generated on board by the MCM processor card at arrival of the TRIGGER signal. They are:

1) TRACK & HOLD
2) CLOCKS train (multiplexing)
3) CONVERTS train
4) CLEAR to the Gassiplex chips

When operating in pedestal mode, the signal sequence stays exactly the same but the trigger signal is supplied by a pulse generator driven by computer.

During the MPX sequence, a signal will be available to the trigger logic of the experiment to participate in the generation of the BUSY.

A RESET signal, driven by the trigger logic and/or by computer will reset the full system (FEE + MCM processor) forcing it to a defined state.

It will also be used to initialize the system (e.g. when switching on power supplies).

Finally the same signal can be used, after the occurrence of a trigger, to abort the readout sequence.

3.2.7 Low-voltage system/high-voltage system

3.2.7.1 Final schematics

Low-voltage supply

The operating low voltages of GASSIPLEX are $\pm$ 2.75 V. Each column of 30 chips is supplied separately by voltage regulators (24 couples in total) mounted on the power and slow-control board, fed in turn by a main double power supply corresponding to a half-module board. The choice of a double supply is needed to ensure that both polarities are fed at the same time when the system is powered on.

The voltage regulators on each column have to be able to sustain 3 W each; a protection circuit has to be implemented to detect the over-current in case of latch-up and switch off the supplies of the column concerned by this latch-up. Two other power supplies are needed for the digital electronics (see Table 3.17). The LV supply units have to be located outside the L3 magnet.

Table 3.17: Elements of the low-voltage system

	Voltage (V)	Current (A)		No. of units	Power W/2.5 m^2
Analog part: GASSIPLEX					
Column: 10 3-GASSI cards	± 2.75	0.8	switch.		
Half-module	± 2.75	20	switch.	14	220
Digital part (half-module)					
MCMs, memories, etc.	+ 5	20	switch.	14	200
ADCs, buffers	± 5	4	linear	14	80

High-voltage supply

At the moment, it is foreseen to supply one-third of a module with one HV channel in order to keep some flexibility in adjusting the operating voltages. Also, it allows parts of the module to be operated in case of malfunctioning of a sector. A more elaborate system (see Section 3.1.1.2) is under study allowing for a finer segmentation (by groups of 16 wires) of the HV distribution, which is attractive but necessitates cost evaluation.

The CAEN 2 channels NIM HV-unit N471A is currently under consideration, providing all remote control facilities (ramping, limits, etc.) and allowing for direct monitoring of very small current down to the nanoampere level. The specifications of the LV units are listed in Table 3.18

Table 3.18: LV units

	Unit supplying		
	GASSIPLEX	DIGITAL	ADCs, buffers
Regulation	Switching	Switching	Linear
Voltage [V]	± 5	$+5$	± 5
Adjustment [%]	± 10	± 5	± 5
Current, max. [A]	25	25	5
Noise ripple [mV, pp]	< 20	< 30	< 5
Overvoltage protection	y	y	y
Overcurrent protection	y	y	y

3.2.8 The data-transfer system and data-acquisition systems

3.2.8.1 The data-transfer system

The trigger level 0 provides the track and hold signal to the GASSIPLEX readout system at a rate of 1200 Hz maximum (see Table 3.19) and with a fixed delay of 1.2 μs. The trigger level 1 can then either dispose of the event or confirm it. In the first case, the readout system is reset. The trigger level 1 has a fixed delay of 2.7 μs and the readout system reset takes ≤ 0.3 μs. This reset will therefore not introduce any additional dead time to the detector dead time of 5 μs.

In the latter case the readout is initiated in parallel in the 14 half-modules of the detector. The data are then transferred to the DAQ system by several standard ALICE Detector Data Links (DDL) [17]. The logical interface of the DDL can be seen in Fig. 3.37a. There is one DDL dedicated to each half-module. The data are transferred from the row of 24 buffers of the half-module to the DDL Source Interface Unit (SIU) at a speed of up to 25 MHz. The SIU will be mounted directly on the readout card on the detector as shown in Fig. 3.37b. It is the same clock which will drive the transfer from the buffers and the DDL SIU.

Table 3.19: Expected rates for different modes of operation

Collision mode	Pb–Pb	Ca–Ca		pp
Luminosity	10^{27}	2.7×10^{27}	10^{29}	10^{30}
Interaction rate (Hz)	8000	8000	3×10^{5}	10^{5}
L0 rate (Hz)	1000	1000	3000	1200
L1 rate (Hz)	800	800	2800	1000
L2 rates				
TPC $\mu\mu$	40	~ 3	–	–
TPC MB	40	40	–	500
NO TPC low p_T	660	–	650	–
NO TPC high p_T	165	–	30	–

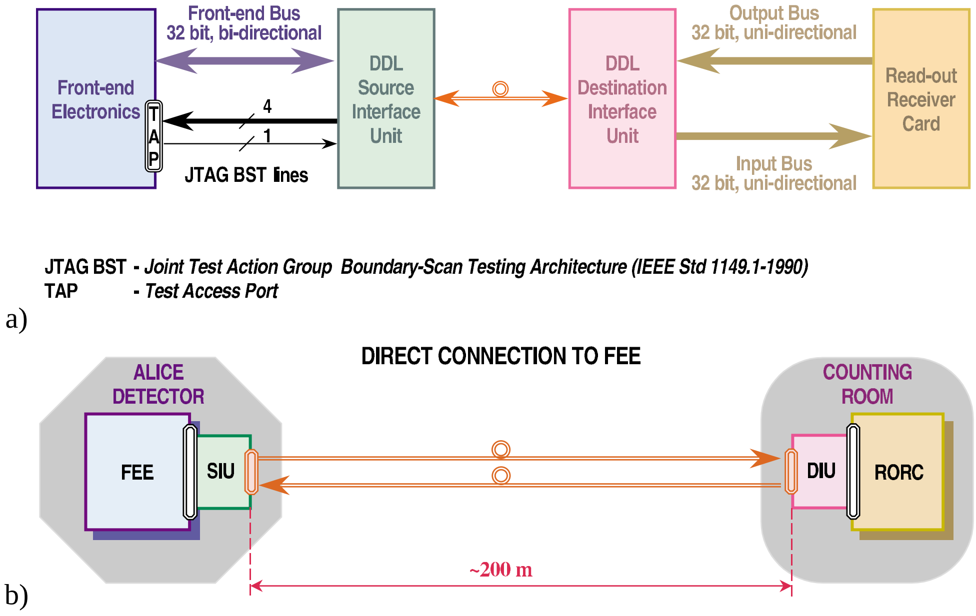

Figure 3.37: (a) DDL logical interface. (b) Direct connection between the front-end electronics on the detector and the DDL.

The DDL is also used to load pedestals and thresholds from the DAQ system to the memories of the DILOGIC chips and to set up and to control the DILOGIC chips.

The physics data transferred by the DDL are buffered in the ALICE readout receiver board (RORC) [18]. The RORC has several functions:

- to be the mothercard for four DDL Destination Interface Units (DIU)
- to act as the transmitting memory for the commands and the data transferred by the DDL to the readout system;
- to act as a remote master for the front-end control and test;
- to act as the receiving memory for the physics data transferred by the DDL to the DAQ;
- to detect the end of the data blocks and manage the data blocks received through the DDL;
- to interface with the trigger system (clear the BUSY status data when a complete data block has been received from one detector).

Once the data have been transferred in the RORCs, they are under the control of the DAQ system. The RORC includes enough buffering to store several tens of events from the HMPID. From this point in the acquisition chain, the data are processed completely asynchronously from the trigger levels 0 and 1.

A prototype of the DDL DIU and of the RORC have been developed and are working properly. A prototype of the DDL SIU is currently under design and will be ready by the end of 1998. Its main characteristics correspond to the needs of the HMPID. A test of integration of the HMPID readout system and of the DDL will be done in 1999. The specifications of the DDL will be frozen after a successful integration test has been done with the HMPID and the other major ALICE detectors. The production will be started one year before the assembly of the HMPID.

The data-transfer system of the HMPID will consist of a single Front-End Digital Crate (FEDC) including four RORCs and one Local Data Concentrator (LDC) (see Fig. 3.38). This crate will also contain the RORCs of the CPVeto detector. A standard computer (workstation or PC) is also included in the system. It makes it possible to work independently during the integration and installation phases and to run interactive programs to perform local test or debugging after the installation.

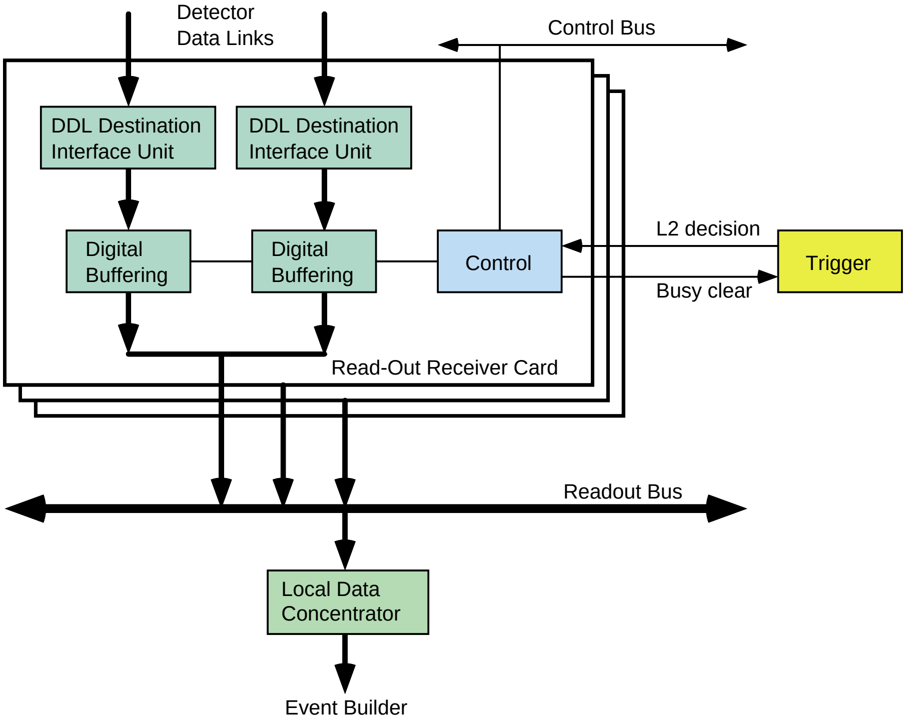

Figure 3.38: Front-end digital crate architecture.

The current prototypes of the data transfer system use VME crates and the LDC is implemented as a single-board computer running the UNIX operating system. The implementation will most probably evolve with the technology but the main functionalities will remain.

3.2.8.2 Data-acquisition system

The main functions of the data-acquisition system when it takes part in a global run with the other ALICE detectors are [14]:

- to validate or discard the event fragments depending on the trigger level 2 decision;
- to read out the data fragments from several RORCs and assemble them into one sub-event;
- to send the sub-event to the computer designated by the event-building and distribution system as event builder to build the complete ALICE event.

The data-acquisition system allows data to be taken in stand-alone mode as well. In this case, the LDC records the data locally instead of sending them to the event-builder computer. This facility can be used for the tests during the preparation and the installation phases of the experiment. During the production phase, it will also allow calibration runs to be made independently of the other detectors and acquire the pedestals needed for the readout electronics. In this case the DAQ will acquire data from all the channels and will prepare pedestal tables which will be loaded at the beginning of the runs.

A prototype of the DAQ system is currently in use for the test beams. It includes a first version of the DAQ software.

3.2.8.3 Components

The modules needed for the data transfer are listed in Table 3.20.

Table 3.20: Data transfer units

Data transfer units	Quantity
DDL	14
RORC	4
FEDC	1
LDC	1
Work station	1

3.2.9 Gas mixture distribution system

3.2.9.1 Design parameters and final layout

The HMPID detector comprises a total gas volume of 1.4 m^3 and operates with 100% methane as nominal gas. This volume is split into seven chamber modules of $1400 \times 1400 \times 100$ mm^3, i.e. 0.2 m^3, each of them supplied individually with gas. In order to protect the very sensitive CsI PC plates there are three basic requirements that need to be met by the gas system:

- The modules must be protected against oxygen and water vapour at all times both during construction and operation, thus giving the requirement that all circuits be purged before the initial module connections are made. Particular attention must be paid to oxygen and moisture analysis of the incoming gas.
- Possible leak of the radiator trays filled with C_6F_{14} and enclosed in the chamber volume must be detected as electronegative contaminant.
- The modules must be permanently supplied with either the operating gas, or, purged with an inert gas (e.g. clean nitrogen or argon), a manually operated supply must ensure the purging of the system during unattended operator closures.

The proposed design consists of a single-pass gas system that distributes the gas to each module at a flow rate of 30 l/h (four volume changes per day) and at a pressure of 7 mbar (above atmosphere). The design parameters are given in Table 3.21.

The primary pressure regulation, purifier and system purge will be located in the surface gas building (SG). The final distribution and flow control to the individual modules will take place on the shielding plug area in the access shaft (PX24), which is accessible during LHC machine operation. Return gas will be exhausted into the dedicated gas extraction system located in the shielding plug area. An overview of the system can be seen in Fig. 3.39.

Table 3.21: Design parameters of the gas system

Total volume	1.3 m^3
Number of modules	7
Module volume	0.185 m^3
Gas mixture*	100% CH_4
Volume exchanges/day	4
Total flow rate	210 l/h
Working pressure	7 mbar

* The system has a provision to supply binary mixtures.

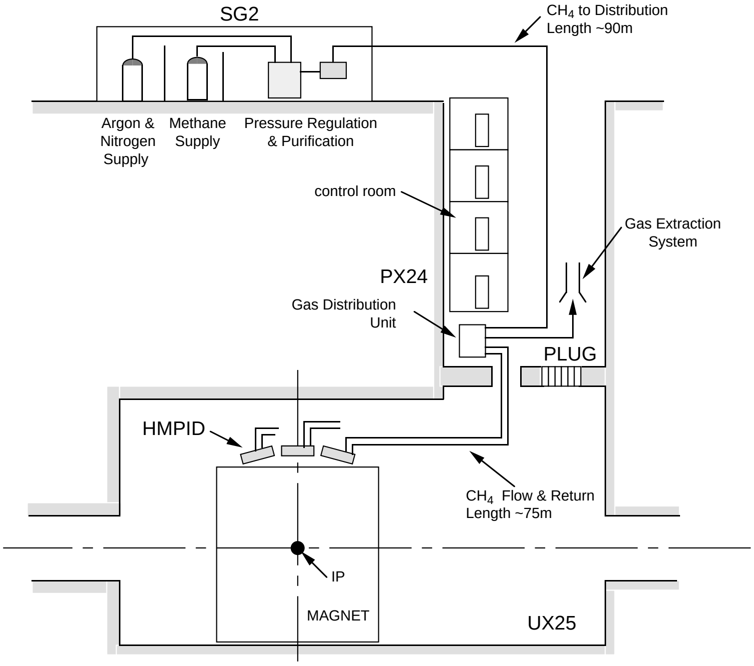

Figure 3.39: Schematic of the gas distribution system.

3.2.9.2 Components

Gas supplies

The methane gas is supplied from standard batteries, each battery having a capacity of approximately 108 m^3; two batteries will be installed in parallel, in the gas storage room of the surface gas building. Automatic changeover and primary pressure regulation will ensure an interruption-free supply of gas to the panel in the mixing room, at a nominal pressure of 5 bar.

Argon gas for purging and inerting is supplied from a liquefied argon storage dewar, with reserve batteries which will ensure an interruption-free supply at a nominal pressure of 5 bar.

Pressure regulation and mixing unit

Although the module gas at the present time is 100% methane, a standard LHC gas mixing unit is proposed which will allow a second gas component to be added if required. An argon supply is also incorporated which is used to keep the system purged during stand-by. A three-way valve is incorporated into each supply line which will allow a small volume of gas to flow via the exhaust keeping the lines clean (see Fig. 3.40).

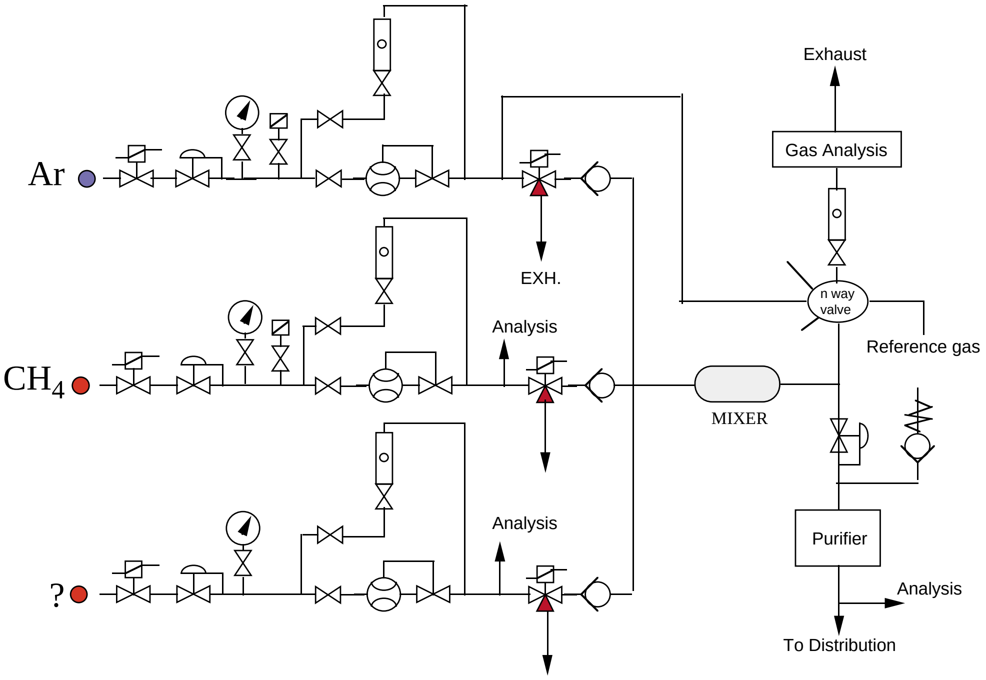

Figure 3.40: Gas mixer unit located at the surface level.

The flow of component gases is metered by mass flow controllers, which have an absolute precision of 0.3% in constant conditions. Flows are monitored by a process control computer. In the event of a second component being added the mixing unit can either work in a constant ratio mode, or alternatively may be derived from comparison of the running mixture with a reference gas mixture in an analysis instrument. The medium-term stability in constant flow conditions is better than 0.1%: absolute stability will depend on the absolute precision of the analysing instrument.

Normal flow rates are typically about 30% of full-scale flow. Detector filling and purging would generally be at maximum flow rate, resulting in a volume exchange time of 0.6 hours.

Gas analysis & purification

The quality of methane 35 as supplied from the CERN stores is considered adequate as far as impurities are concerned. However, since the risk associated with the connection of a gas cylinder having impurities above the limit is non-negligible, inline purifier cartridges for the removal of oxygen and moisture will be installed. The size of the cartridges will be such that a one-year operating cycle can be achieved without change. A 0.4 micron filter is installed in the purifier outlet to trap dust.

Sampling points will be incorporated into the downstream side of each of the component gases of the pressure regulating/mixing unit, for the online measurement of oxygen and moisture in the incoming gases.

On the distribution rack, sampling points on the return gas flow from each of the seven modules will monitor gas for impurities of oxygen and moisture along with monitoring for traces of C_6F_{14}.

Flow distribution

Final pressure regulation and flow distribution to the seven modules will take place in the shielding plug area. Gas arriving from the surface building will pass through a pressure regulator, before being distributed and passing through individual throttle valves, Fig. 3.41. A safety relief device is incorporated into the manifold to prevent over-pressure of the modules, this device will either be a simple relief valve or a rupture disc depending on the pressure limits.

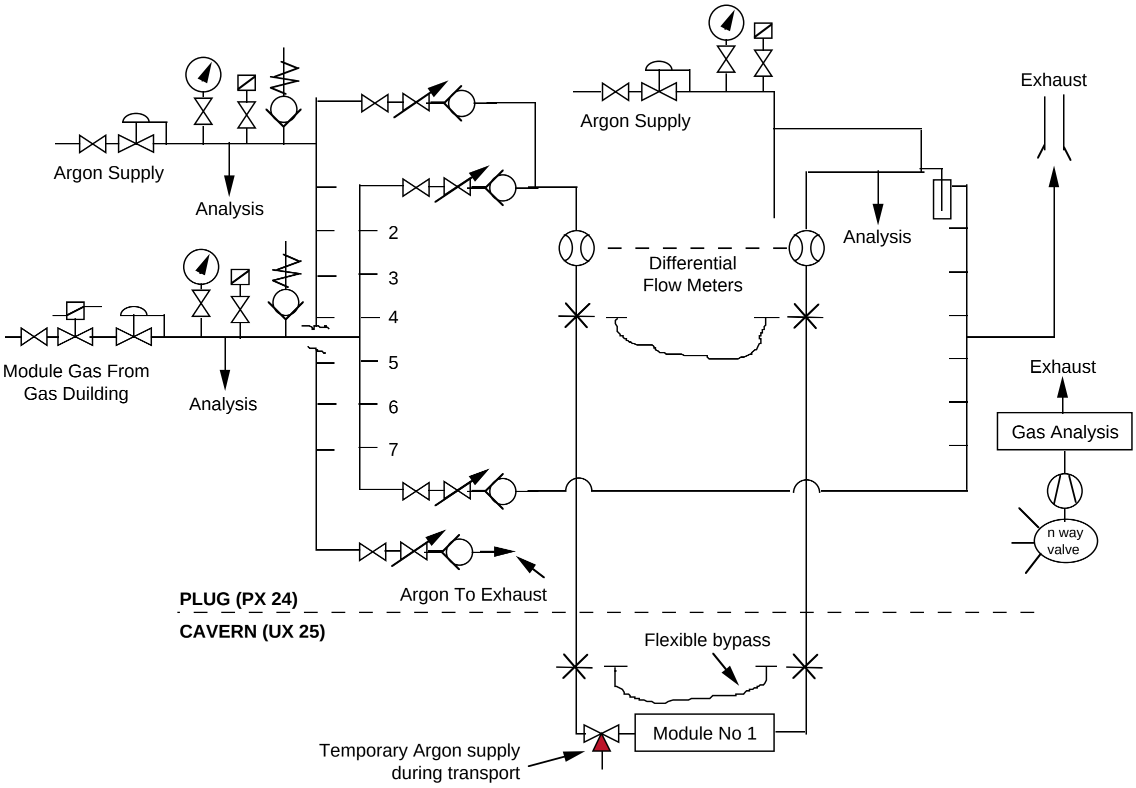

Figure 3.41: Schematics of the gas distribution system.

Differential flow monitors are incorporated into the flow and return lines, which will allow easy adjustment of individual channel flows using the throttle valves, and will allow the detection of leaks by comparing flow-rate changes.

The return gas from the modules will pass through bubblers, to allow visual control of flow, before venting into the dedicated flammable-gas extraction system.

To prevent excess stressing of the modules due to fluctuations in atmospheric pressure in case of a loss of the primary gas supply, a system of back-filling with argon gas is proposed. This allows one to fill or ballast with gas to keep the modules at a slightly positive over-pressure. Since gas is fed in near to the exhaust outlet no dilution of the module gas will occur.

Sampling points are installed in both gas flow and return lines for the detection of oxygen and moisture and the return gas will also be monitored for traces of C_6F_{14}.

Purging

A flexible bypass will be provided to allow purging with argon of each gas circuit before the modules are installed. In case of a major methane leak any individual module may be isolated and purged. Quick connectors will be provided on a patch panel located on the HMPID support structure to allow removal of individual modules. A three-way valve will be incorporated to allow an argon gas cylinder to be connected to maintain purging during transport.

Distribution pipework

All tubes, valves and fittings within the system will be made of stainless steel. The tubes will be butt-welded together to reduce the possibility of contamination and leaks to a minimum. Existing gas pipes at point 2 will be re-used as far as possible. Table 3.22 shows an overall view of the main piping parameters. At the shielding-plug end they will be modified to link up with the new position of the distribution rack. In the experimental area (UX25) they will be extended into the L3 solenoid magnet and onto the HMPID frame. A patch panel, equipped with self-sealing quick connectors will allow disconnection for removal of the modules.

Table 3.22: Main piping parameters

	No.	Diam.	Length	Velocity	Re	Dp
SG2-distribution	1	22/20	90 m	0.371	220	0.154
Distribution-module	7	10/8	75 m	0.132	80	0.710
Module-exhaust	7	16/14	75 m	0.075	45	0.076

Reserve pipes will be installed, to avoid re-opening of the magnet doors in the future.

Power supply purging

The high-tension connectors located on each side of the module must be purged with a neutral gas to eliminate any risk of methane chamber gas coming into contact with the components. For economic reasons nitrogen will be used for this operation: the gas will be supplied from a manifold in the shielding-plug area (PX25). In case of breakdown of the nitrogen flow, automatic shut-down of the chamber gas system will be put into action.

Safety

The gas return from each module will be monitored for traces of water vapour, oxygen and C_6F_{14}, which will give a good indication of leaks. In the event of abnormality the chamber gas supply will be shut off and the module will be purged with argon; in addition, the corresponding liquid radiator will be isolated and purged with nitrogen at a higher pressure than the module gas volume. In case of failure of the module gas supply, or any other reason why the supply of gas is interrupted, argon will be fed into the outlet side of each module to maintain a positive pressure with respect to atmosphere.

The internal volume of the ALICE solenoid magnet will be continuously monitored for traces of flammable gases; in the event of an alarm resulting from a leak of flammable gas, all primary supplies of flammable gases will be shut off at the primary supply level.

3.2.10 The C_6F_{14} circulation system

3.2.10.1 Introduction

The distribution system is designed to supply Perfluorohexane (C_6F_{14}) liquid to each of the twenty-one radiator modules at a constant flow of up to 3 l/hr. The maximum working pressure of 120 mbar above atmospheric pressure, for each radiator must not be exceeded (see Table 3.23). A circulation scheme is proposed which will eliminate any possibility of over-pressure taking into account the various geometrical positions of the radiator modules. A gravity feed system was constructed and successfully tested for the HMPID prototype, and has been described in Section 3.1.3. The circuit was designed such that priority was given at all times to the supply of liquid to the radiator modules. The full-sized system will follow very closely that design. An overall layout of the system is shown in Fig. 3.42.

The system can be split into three distinct units:

1. The tank and purifier unit will be installed in an area which will be accessible at all times during LHC operation, and will be located in the Pit PX24 on the radiation shielding plug.
2. The distribution rack will be located in the experimental hall on the platform at 3.32 metres above beam height, close to the ALICE solenoid magnet. This rack will house the intermediate tank, header tubes and lower tank. The pumps that return the liquid to the top tank will be installed below this rack.

Table 3.23: Maximum Radiator working pressure

Maximum Radiator height	98 mbar
Outlet tube height	8 mbar
Vapour column to exhaust	12 mbar
Bubble	2 mbar
TOTAL	120 mbar

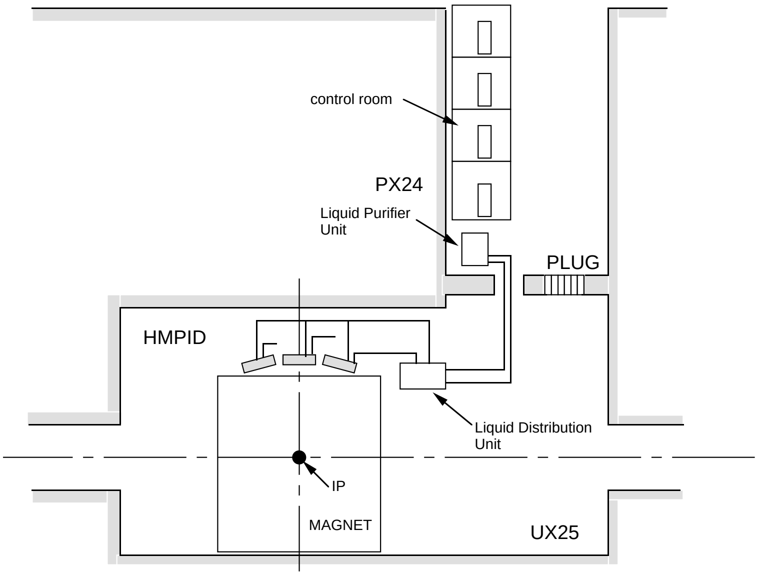

Figure 3.42: Overall view of the liquid system.

3. The pipe distribution to the modules proper, which is located on the HMPID support frame, within the ALICE solenoid magnet.

3.2.10.2 Design

Principle of operation

The liquid distribution system has been designed to have as few active components as possible, especially in areas which will not be accessible during LHC operation. The system is designed using a gravity flow principle with the priority flow given to the radiator modules, excess flow cascades to the lower tank. In case of power or other system failure, all liquid in the circuit, except for the radiators, will drain automatically into the lower tank. Manual valves will allow the radiator units to be drained and sealed-off if required. The lower tank has a capacity capable of holding the entire contents of the system, including operational losses during one year of operation. The liquid volume in the circuit is calculated to be of the order of 250 litres. A schematic diagram of the liquid distribution system can be seen in Fig. 3.43.

From the lower tank the liquid is pumped to the upper tank at a constant flow rate of 210 l/h, against a calculated pressure head of 6 bar. The constant flow is achieved by the use of a mass-flow-meter controlling a bypass valve on the pump; a safety relief bypass valve is also mounted in parallel to protect the pump from overpressure. A filter installed at the inlet protects the pump. Perfluorohexane is a high-density, low-viscosity liquid and not recommended for applications where a high degree of lubrication is required, therefore, special care is required in the choice of pumps. Two pumps, which are of the well proven magnetically coupled gear type, are mounted in parallel to provide redundancy.

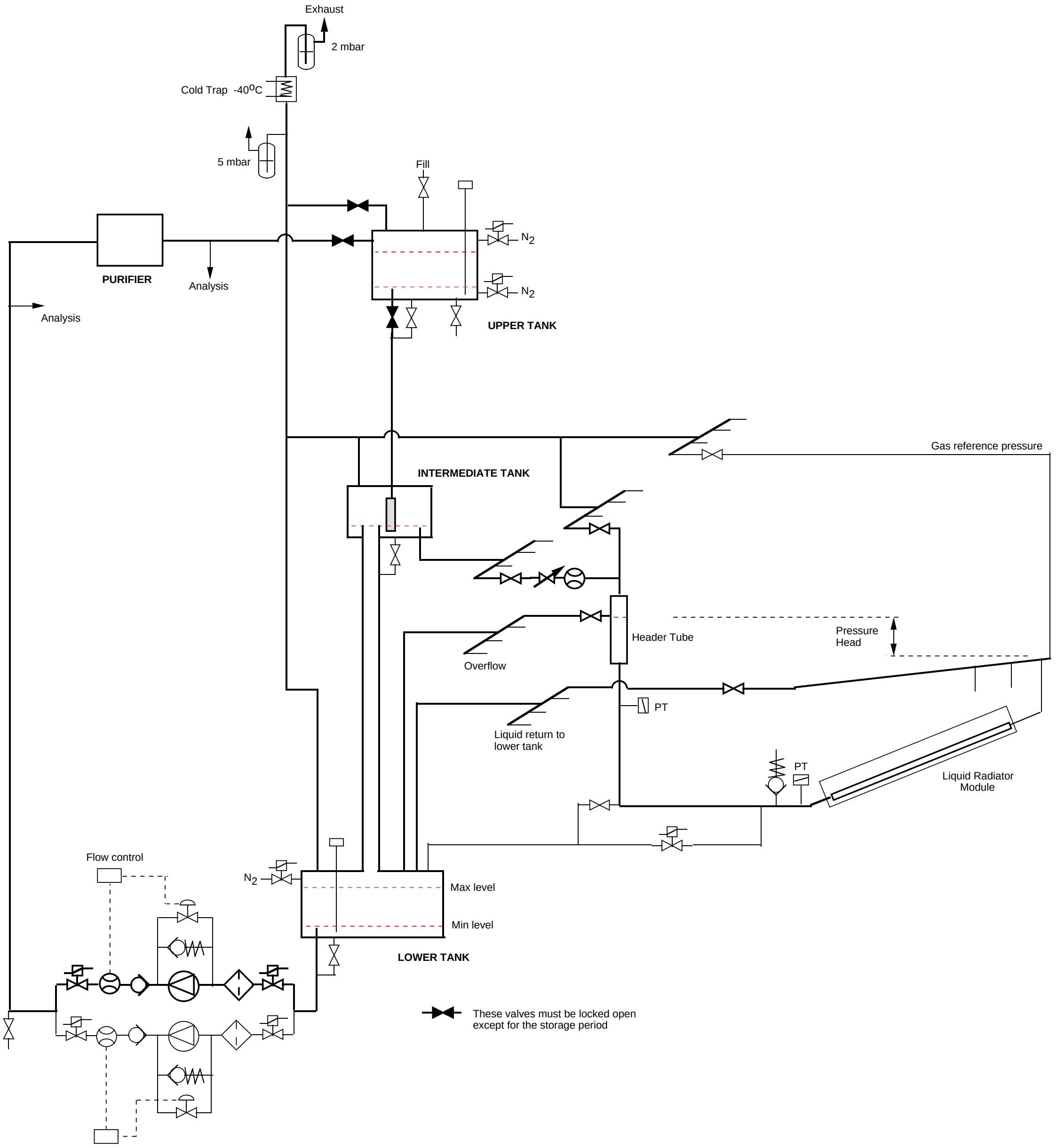

Figure 3.43: Liquid distribution system.

Liquid flows from the upper tank, by gravity, into the intermediate tank. A phase separator is installed in the outlet of the line, and sufficient depth of liquid is allowed for in the bottom of the tank to allow outgassing of the liquid. From this tank the liquid is distributed to the twenty-one header tubes, at a total flow rate of 130 l/h. The excess flow leaves the intermediate tank via the overflow to the lower tank.

The flow of liquid from the intermediate tank via a distribution manifold to each header tube is regulated by a flow meter and manual throttle valve at 6 l/h. The height of each header tube is a function of the orientation and height of its respective Radiator and of the pressure losses in the inlet pipes.

Owing to the hydraulic pressure in the individual header tubes the liquid flows to the radiator module. The flow rate is controlled in the range of 1–3 l/h, by the pressure drop in the entrance tube. The radiators are filled from the bottom thus displacing the nitrogen purge gas through the outlet situated in the upper part of each Radiator. Excess liquid from the header tubes leaves via the overflow to the lower tank. A solenoid valve is installed in the circuit which will allow individual radiators to be shut off if required. A general view, showing the pipe layout on the HMPID support frame, can be seen in Fig. 3.44.

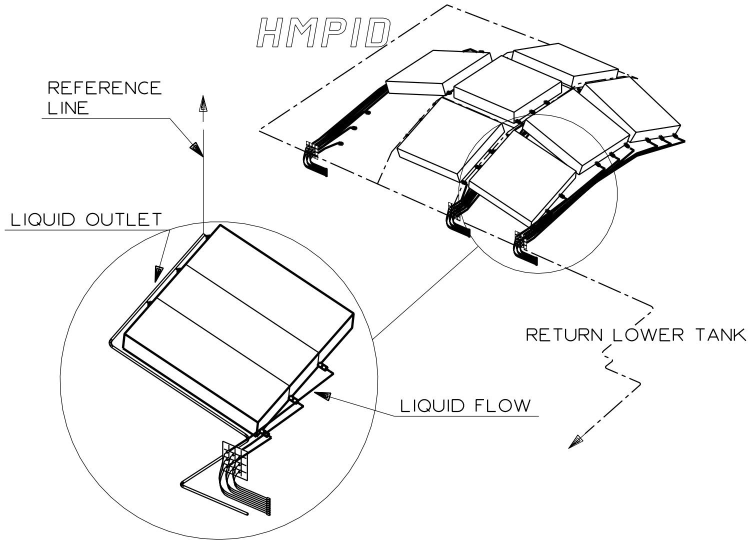

Figure 3.44: Pipe layout on support frame.

A manifold has been designed to collect the liquid as it exits from each group of three radiators. As a means of ensuring that liquid does not back flow into a radiator, the outlet from each radiator will enter the manifold above the liquid level.

The collector tube diameter is such that the liquid occupies only a small section of the tube. Each outlet manifold has also a gas reference pressure line connected to the main exhaust line which avoids pressure oscillations in the output pipes. The geometry of all return pipes is such that they have a constant slope back to the lower tank.

Each radiator may be isolated and drained if required by the bypass valve. Large-diameter valves are installed in the output lines so that each set of three radiator modules may be isolated in case of a component failure.

Setting-up and purging

After the installation of the liquid circulating system and before the tadiator modules are connected to the system, all circuits and tanks are to be purged with nitrogen to remove oxygen and moisture. The system will be designed to allow vacuum pump-out and back-filling with nitrogen. For this operation the safety bubblers will temporarily be removed.

Once purging has been completed the system will be put into operation to thoroughly rinse and outgas the circuit. Only liquid from the same batch that has been pre-cleaned will be transvased into the system, in quantities for one year of operation.

3.2.10.3 Components

Materials

Stainless steel will be used for all tubes, valves and fittings within the system to reduce the possibility of contamination and leaks to a minimum; as far as possible only welded joints will be used. In places where it is necessary to dismount parts for maintenance, compression fittings will be used. The tubes and fittings will be supplied from the manufacturer degreased and passivated since cleaning will be difficult after installation.

All parts of valves and other instruments which have contact with the liquid must be of stainless steel to avoid contamination of the liquid.

‘O’ ring type joints will be avoided as much as possible; where they are found to be necessary, elastomers made of Viton will be used.

Purifier
On-line purification will be carried out on the full liquid flow as it is pumped from the lower to the upper tank. Two purifier columns are installed in parallel such that in the event of one becoming saturated or blocked, the flow of liquid will be diverted through the second column, see Fig. 3.45.

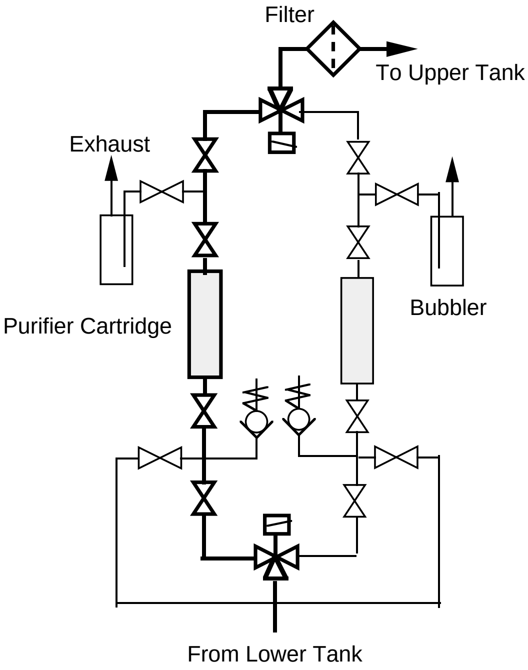

Figure 3.45: Purifier unit.

Zeolite 13X has been found to be satisfactory for removing water vapour and other impurities in the liquid. After filling, the columns are purged and filled with clean nitrogen at a pressure of 1 bar. Precautions are required when changing columns since an exothermic reaction takes place when replacing the nitrogen purge gas with the process liquid, resulting in formation of important quantities of gas. Only when there is a steady flow of liquid leaving the column and the temperature has returned to ambient can the purge liquid be shut off and the column isolated. Safety relief valves are installed to protect from overpressure.

Quality monitoring
The liquid quality will be continuously monitored. Sampling lines before and after the purifier will send liquid to an array of diagnostic devices. It is intended to measure the UV transparency, refractive index, oxygen and moisture content in the liquid phase on-line.

On-line monitoring of the oxygen and moisture content of the reference gas is also planned. The moisture level will be used to interlock the cold trap in the exhaust line. The dew point temperature of $-40°$C corresponds only to a moisture content of about 100 ppm, if values above this are detected the cold trap will be heated to avoid freezing.

Liquid recovery
In the event that all the liquid in the system must be changed or recovered, drain valves are installed below all low points which allows the liquid to be drained to the lower tank.

To keep the oxygen and moisture to a minimum due to the effects of outgassing or air trapped when modifications are carried out, the system is continuously purged with nitrogen at a flow rate of 60 l/h, which is exhausted to the atmosphere. At the present time there are no restrictions to exhausting this product to the atmosphere, however, since this product has a known greenhouse effect, long-term legislation may require it to be recovered. For economic reasons this liquid must be recovered, since, at normal operating temperatures the vapour has a saturation of approximately 25% volume in nitrogen, which would result in the loss of 3.6 litres per day.

To recover the liquid, we propose to install a cold trap in the exhaust line, which will have a working temperature of $-40\ ^\circ\mathrm{C}$. This will reduce the vapour content in the exhaust outlet to less than 1% resulting in a maximum loss of 0.15 litres per day.

Safety

The pressure in the radiator, even when empty, will be 13 mbar due to the vapour column of 23 metres, In the case of a leak in a radiator, vapour will migrate into the gas volume which will have a maximum working pressure of 7 mbar. If traces of C_6F_{14} are found in the methane gas outlet the entire module will be closed down and sealed off. The gas volume will be purged with argon. Since there are three radiator units in each module, which are interconnected by the gas reference line, all three units in the Module must be isolated and drained to the lower tank. In the event of a bockage of the radiator output line, the maximum pressure in the most inclined radiator will rise from 120 to 140 mbar.

3.2.11 The slow control system

The ALICE detector control system (DCS) is characterised in Ref. [14] and will be described in detail later in the ALICE Computing Technical Proposal. The signals to be measured for the HMPID are listed in Table 3.24.

Table 3.24: Main parameters of the detector control system for the HMPID

Systems Subsystems	Location	Controlled parameters	Number	Type	Parameters	Control
Gas supply	PX24	Primary flows	20	Analog	Flow	Read
	PX24	Primary pressures	10	Analog	Pressure	Read
	Detector	Temperatures	20	Analog	Temperature	Read
	PX24		5	Serial IF	Complex	Read
	PX24	Safety switch	1	Binary	Voltage	On„ Off
	PX24	Purity control	2	Serial IF	Complex	Read
	UX25	Gas pressure MWPC	14	Analog	Pressure	Read
	Detector	Temperatures	80	Analog	Temperature	Read
	UX25	Gas flow MWPC	7	Analog	Flow	Read
Radiator	UX25	Circulator valves	80	Binary	Voltage	ReadWrite
	PX24	Pumps & circulators	32	Binary	Voltage	On„ Off
	PX24	Liquid flow	64	Analog	Flow	Read
	PX24	Pressure	10	Analog	Pressure	Read
	Detector	Temperature	80	Analog	Temperature	Read
	PX24	VUV transp. Syst.	1	Serial IF	Complex	Read
	PX24	Safety system	1	Binary	Voltage	On„ Off
Other system	PX24	VUV transp. Syst.	1	Serial IF	Complex	Read
HV	PX24	Chamber voltage	12	Analog	Voltage	ReadWrite
	PX24	Chamber current	14	Analog	Current	Read
	PX24	Current limits	14	Analog	Thresholds	ReadWrite
LV	PX24	Readout electronics	42	Analog	Voltage	ReadWrite
	PX24	RO sign. Cntrl	42	Binary	Voltage	On„ Off
	PX24	FEE	42	Binary	Voltage	On„ Off
	PX24	MWPC FEE supply	28	Analog	Voltage	ReadWrite
	PX24	FEE current monitoring	28	Analog	Current	Read
	PX24	Current limits	28	Analog	Thresholds	ReadWrite
	PX24	chamber	42	Analog	Voltage	ReadWrite
	PX24	chamber	42	Analog	Current	Read

The validation of design choices for the overall ALICE DCS will be performed for a liquid circulator system of the HMPID but an adaptation to other applications is envisaged.

For this purpose a small test and evaluation station is being set. The system is entirely based on standard industrial components following the recommendations of the relevant working groups. The realisation of this first stand-alone system for the control of a detector sub-system will cover all layers of the proposed DCS architecture:
Supervisory Software: LabView/BridgeView
Control Software: Siemens Step7, equivalent to IEC1131
PLC programming libraries
Controller station: Siemens S7 + TCP/IP
Field instrumentation: Temperature sensors, Switches, Valves

figure 3.i
figure 3.ii

figure 3.iii
figure 3.iv

4 Detector performance

4.1 Introduction

In Chapter 2 we have discussed in detail the technical performance of the RICH. In the following we shall try to demonstrate that given the basic technical performance studied and optimized in single track tests, we are able, in the very dense environment of ALICE, to extract the Cherenkov angle of emission with satisfactory precision. It is important to remember that the range for π/K positive identification of the HMPID is limited to momenta $\gtrsim 1$ GeV/c for pions and kaons and even higher for protons (because of the threshold effect for Cherenkov photon emission). In the low magnetic field of ALICE, tracks with these momenta are almost straight so that the maximum angle of incidence is limited to $\sim\ 10°$. This means that most of the patterns will be closed ellipses, a feature that eases the pattern recognition.

In the first part we shall describe the ALICE environment in which the detection will take place. To do so we have simulated the complete response of the ALICE experiment including the material budget of all detectors, using the GEANT and FLUKA packages, and an event generator which produces the highest rapidity density expected in Pb–Pb collisions, i.e. 8000 charged particles per unit of rapidity. By applying a detailed simulation of the RICH response, described in Chapter 2, we can then generate the pad map of hits on the RICH modules. This simulation gives an upper limit on the occupancy we can expect and therefore sets the requirements for the pattern recognition performance described afterwards.

In the second part we describe a pattern recognition algorithm that allows to extract the Cherenkov signal in the conditions of occupancy as generated by the simulations.

In the third part we shall describe the matching of tracks from the TPC to the HMPID. The pattern recognition depends critically on the capability to track particles through the tracking detectors of ALICE — the Inner Tracker System (ITS) and the Time Projection Chamber (TPC) — and to extrapolate the tracks, with sufficient precision up to the HMPID (more than two metres away).

In the fourth part we review further work on the optimization of the design, using the described tools of simulation, tracking and pattern recognition.

All the results presented in this chapter have been obtained, using the tracking precision and the material budget quoted in the ALICE Technical Proposal [1].

4.2 Simulation of the RICH response in the ALICE radiation environment

4.2.1 Particle multiplicities at the HMPID and secondary interactions

The detector modules will be installed at a radius of 4.8 m and will cover one unit of rapidity with a 16% coverage in azimuth.

For the highest anticipated charged particle multiplicities of 8000 particles per unit of rapidity in central Pb–Pb collisions at $\sqrt{s} = 5.5$ TeV/nucleon, the predicted densities of charged pions and kaons with momenta above $1\,$GeV/c (signal particles) is $\sim\ 5$ m^{-2} at the position of the RICH. The flux of lower-momentum primary particles and secondary particles produced in detector elements below the RICH and in structural elements like the front absorber, the vacuum chamber and support structures is of the order of 100 m^{-2}. These particles have, in general, a much larger angle of incidence than those concerned by the HMPID ($p \gtrsim 1$ GeV/c), which have $\theta_{\rm in} \leq 10°$. The distribution of the angles of incidence as a function of the particle momenta is shown in Fig. 4.1.

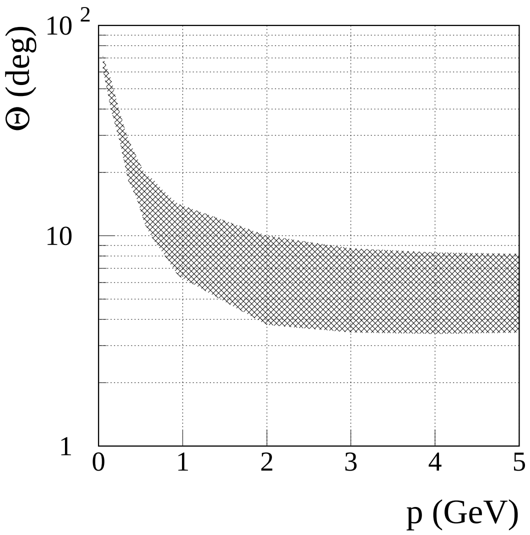

Figure 4.1: Variation of the primary particles angle of incidence in function of momentum. The band represents the 1 σ spread in angle at a given momentum.

The radiation and hadronic interaction lengths of the RICH radiator (vessel material + liquid) is 13% and 3.7%, respectively. Together with the hydrogen content of the gas gap, this makes the RICH sensitive to neutral particles. The fluxes of gammas and neutrons are, respectively, one and two orders of magnitude higher than that of charged particles.

In order to evaluate and optimize the RICH performance it is mandatory to estimate the contribution of the charged and neutral particle background to the overall occupancy. This task has been performed using the GEANT 3.21 based implementation of the RICH response simulation [2], and the FLUKA based ALICE simulation of the radiation environment [3, 4]. The two programs are combined to calculate the expected occupancy of the RICH.

4.2.2 GEANT description of the RICH

To simulate the performance in the ALICE radiation environment, a description of the RICH has been implemented into the ALICE GEANT 3.21 based detector simulation code, GALICE [5]. The program uses the GEANT routines GGCKOV and GTCKOV for the generation and tracking of Cherenkov photons.

The modelling of the RICH response, including the important photon feedback contribution, is based on the stand-alone code *richsim* that has been described in Chapter 2 and in Ref. [6]. In addition to the original code we explicitly track feedback photons and take into account the response of charged tracks with a large angle of incidence ($\tan\theta_{\mathrm{inc}} > \mathrm{padsize}/\mathrm{gapsize}$). Through the simulation of hadronic and electromagnetic interactions in the RICH, the GEANT implementation allows us to evaluate the detector response to gammas and neutrons.

4.2.2.1 Geometry

The RICH geometry defined for GEANT comprises the layered structure of the active part and the frames of the modules. The active part includes dead regions due to spacers and boundaries between radiator modules. The wire grid is not part of the geometry but its absorption effect is taken into account during tracking. The backplane of the RICH, i.e. photocathode, pad-plane and electronics, is implemented as one volume with tracking medium attributes including the Cherenkov photon detection efficiency and the average material thickness. The cathode segmentation is assumed to be 162×162 pads per module and a pad size of 8×8 mm^2 is taken into account at the signal generation level.

4.2.2.2 Background processes

The production of background events from gamma conversions or hadronic interactions in any of the detector planes is taken into account automatically by GEANT during tracking. By setting the kinetic energy threshold for the tracking to its lowest value (50 keV for gammas, electrons and positrons), we got the best possible description of the background in a high-radiation environment. The background due to feedback photons has been described as explained in Section 2.4.1.

4.2.2.3 Signal generation

The signal generation described in Section 2.4, has been complemented by specific tracking of background tracks and photons.

Background particles may have any angle of incidence and the ionization along their path may induce charges over many pads. In such cases the signal generation is followed over the whole path within the MWPC gap.

An example of a simulated background event is shown in Fig. 4.2. In this event a 350 GeV/c charged pion has undergone a hadronic interaction in the RICH backplane. One of the produced secondary particles travels nearly parallel to the cathode plane and produces a long track.

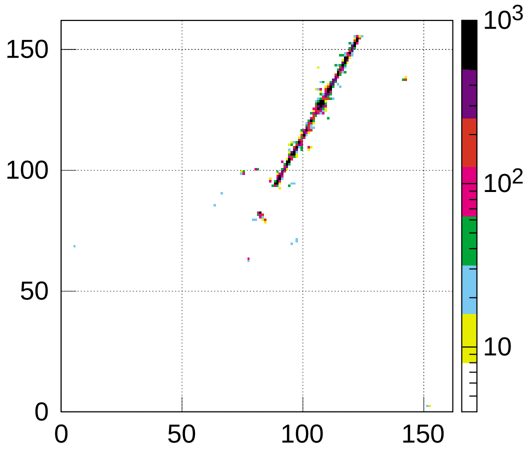

Figure 4.2: Simulated RICH response to a hadronic interaction in the backplane.

4.2.2.4 Electronics noise and zero-suppression

In the output produced by GALICE, the induced charge per pad is stored separately for each hit. From this information the *digit* of each pad is obtained by summing up the individual contributions from all hits and then adding random noise and applying zero suppression. This procedure allows, in case of overlapping hits, to determine in an analysis program the individual contributions to the hits and evaluate their influence on occupancy, pattern recognition and angular resolution.

For the simulation results presented here we added random noise with a r.m.s. of 1 ADC channel (in the following we use the unit ADC chan, where 1 ADC chan = 0.17 fC). The pad-to-pad variation of the noise r.m.s. is 0.12 ADC channels. A threshold of 5 ADC channels is applied.

4.2.2.5 Comparison with test beam data

A comparison of the simulation results of the RICH response to 350 GeV/c pions with results from test beam data, relevant for the evaluation of the occupancy (number of clusters, cluster size and integrated pulse height), is shown in Table 4.1. The overall agreement of the simulation with the test is very good.

Table 4.1: RICH response to single pions when comparing data and simulation for a single-electron mean pulse-height of $A_0 = 43$ ADC chan.

	Data	Simulation
Photon fiducial region		
Resolved clusters	16	15.5
Cluster size	2.0	1.9
Total charge (ADC chan)	968	928
MIP region		
Cluster size	5.5	5.3
Cluster charge (ADC chan)	982	1096
Outside fiducial and MIP		
Clusters	1.5	1.45
Cluster size	1.5	1.8
Total charge (ADC chan)	100	83

4.2.3 Background simulation

Charged and neutral background particles for the HMPID are produced in structural elements (absorber, beam-pipe flanges) and other detectors, although they are not in the direct path of the primary particles reaching the detector. GEANT and FLUKA simulations have been performed to calculate the expected flux of background particles. Both simulations use a coarse description of the ALICE geometry outside the RICH, representing the material budget to our best knowledge. The GEANT simulation includes a detailed description of the RICH and its response, as described in the previous section. The present version of FLUKA does not provide any generation or tracking of Cherenkov photons. Hence, the simulation of the detector response is not possible within the same program. The momentum vectors from FLUKA are used as an input to GALICE, where the detector response is simulated in a second step.

FLUKA [3] was run with the EMF option for explicit electromagnetic shower evolution. Close to the material surfaces, the gamma and electron kinetic energy cuts were set to 50 and 100 keV, respectively. Higher cuts were used in shielded regions in order to decrease the calculation time. Neutrons were produced and tracked down to thermal energies. All other particles were tracked down to a kinetic energy of 1 MeV.

The same kinetic energy cuts were used in the GALICE simulations except for neutrons which are only tracked down to a minimum kinetic energy of 10 keV. The GEANT/MICAP interface [7] has been used to simulate the RICH response to low-energetic neutrons resulting from the FLUKA simulation.

The primary particle flux has been simulated by sampling from pion and kaon pseudorapidity distributions obtained from the HIJING event generator, as described in Ref. [8]. The normalization was adjusted to obtain 8000 charged particles per unit of rapidity in the central region.

4.2.4 Results

4.2.4.1 Charged and neutral particle fluxes

A breakdown of the charged and neutral particle fluxes at the radial position of the RICH, as obtained with FLUKA, is shown in Table 4.2. The flux of primary pions and kaons amounts to $32.2\,\mathrm{m}^{-2}$ and $1.4\,\mathrm{m}^{-2}$, respectively. A similar contribution to the charged particle flux comes from electrons and positrons ($43\,\mathrm{m}^{-2}$). The proton flux is low ($3.7\,\mathrm{m}^{-2}$), but a potential increase in occupancy may result from their stronger ionization loss. Only 8% of the charged particles enter the RICH from above, i.e. backscattering from the L3 magnet.

Table 4.2: Neutral and charged particle fluxes from a central Pb–Pb collision at $R = 4.8$ m

Particle	Flux (m^{-2})	Flux from below (m^{-2})
All $\pi^{\pm}$	40.7	39.6
Primary $\pi^{\pm}$	32.2	32.2
Primary $\pi^{\pm}$ ($p > 1$ GeV/c)	4.6	4.6
All K$^{\pm}$	1.40	1.40
Primary K$^{\pm}$	1.33	1.33
Primary K$^{\pm}$ ($p > 1$ GeV/c)	0.59	0.59
$\mu^{\pm}$	14.1	12.3
Electrons	28.7	25.8
Positrons	15.0	12.6
Protons (secondary)	3.69	3.27
All charged	103.5	95.0
All γ	1490	1030
primary γ	120	120
γ ($E_{\gamma} > 1$ MeV)	560	390
All neutrons	9100	4970
Neutrons ($E_{\mathrm{kin}} > 100$ keV)	3100	2060
Thermal neutrons	205	130

The γ flux amounts to $1500\ \mathrm{m}^{-2}$. Most of the γ's are products from secondary interactions. About 30% of the total flux is shining from the L3 magnet back onto the RICH.

The total neutron flux amounts to 9100 m^{-2}, out of which 34% are neutrons with kinetic energies above 100 keV and 2% are thermal neutrons. The fast neutrons can create a signal by knocking out a proton from the methane gap. Nearly the same amount of neutrons reach the RICH from below as from above.

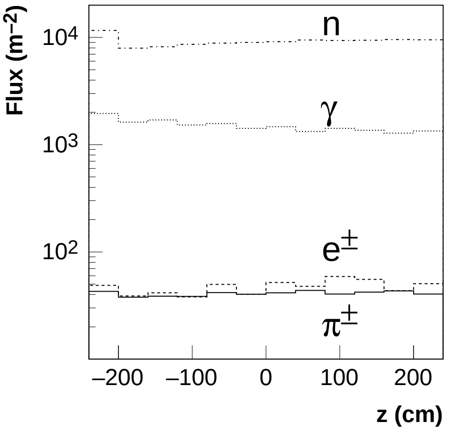

Figure 4.3: Charged and neutral particle fluxes as a function of the z coordinate along the beam axis, as simulated with FLUKA. The absorber of the muon spectrometer is on the positive side.

The fluxes of charged particles, gammas and neutrons as a function of the position along the beam axis (z) are shown in Fig. 4.3. Some asymmetries with respect to the interaction point ($z = 0$) can be observed due to the presence of the front absorber (from the muon spectrometer) and of the ITS services.

4.2.4.2 Event displays

The map of hit pads of one module for a central Pb–Pb collision is illustrated in Fig. 4.4. The single-electron mean pulse-height for this event is 20 ADC chan. and the proximity gap distance corresponds to a saturation ring radii of 155 mm. Under these conditions 9.3% of the pads have a signal above the threshold. To get an impression of the influence of the background hits, we show in Fig. 4.5 the hit pattern produced by primary charged pions alone. In this case the occupancy amounts to only 4%. Figure 4.6 shows the ring pattern created by pions with momenta above 1 GeV/c.

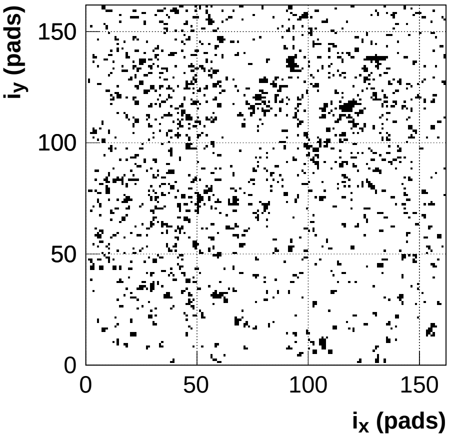

Figure 4.4: Simulated full event (Pb–Pb central collision) as seen by a RICH module.

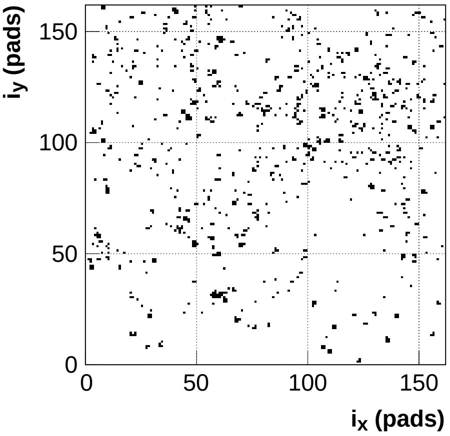

Figure 4.5: Same as Fig. 4.4, but for primary charged pions only.

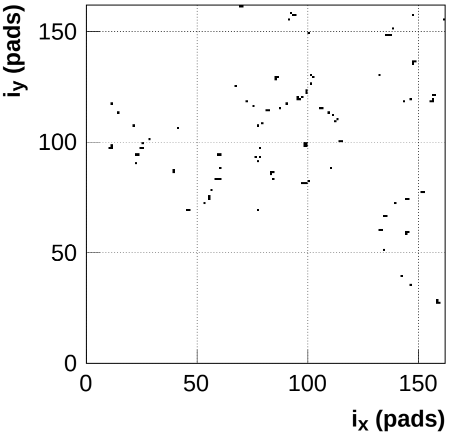

Figure 4.6: Same as Fig. 4.4, but for primary charged pions with $p > 1$ GeV/c only.

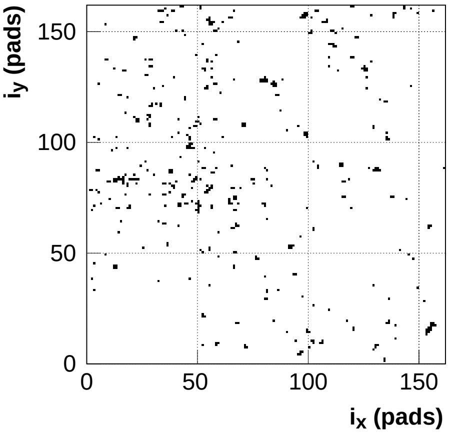

Figure 4.7: Same as Fig. 4.4, but for gammas only.

The pattern produced by gamma conversions in the RICH alone is shown in Fig. 4.7. As for hadronic interactions, backscattering from the cathode plane can produce track segments as can be seen in the lower right part of the picture. Conversions in the quartz window can produce pairs of MIP clusters, which are likely to overlap. Conversion in the radiator or in front of it can produce double rings (see Fig. 4.8).

As will be shown in the next section, the contribution of neutrons to the overall occupancy is small. Locally, however, the knock-out of a proton by a fast neutron can lead to a substantial release of charge creating a large pad cluster, as can be seen from Fig. 4.9.

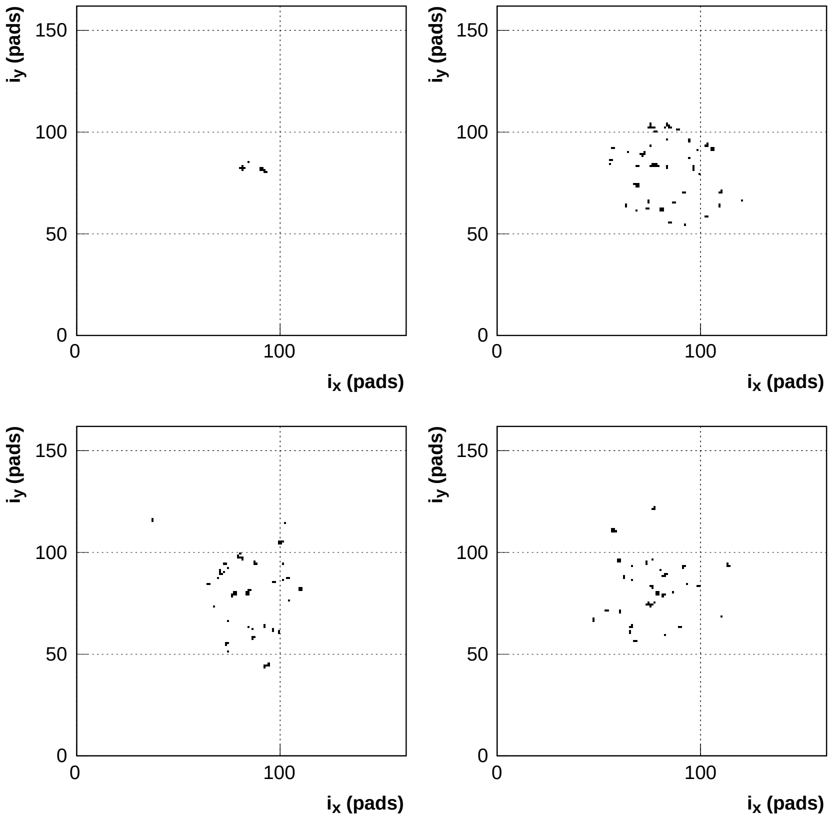

Figure 4.8: Examples of single gamma interaction in the RICH radiator ($E_\gamma = 100$ MeV).

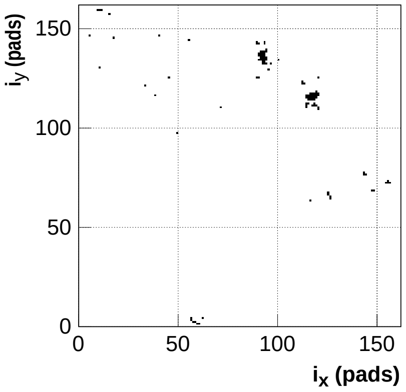

Figure 4.9: Same as Fig. 4.4, but for neutrons only.

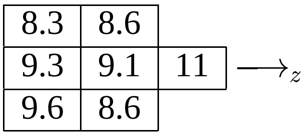

8.3	8.6		
9.3	9.1	11	$\longrightarrow z$
9.6	8.6		

Figure 4.10: Simulated occupancies (%) of the seven RICH modules for one central Pb–Pb collision (single electron mean pulse height: 20 ADC chan).

4.2.4.3 Occupancy

The occupancies for each of the seven RICH modules as obtained from one simulated central Pb–Pb event (single-electron, mean-pulse-height 20 ADC chan) are shown in Fig. 4.10. The average occupancy amounts to 9.23% at a mean single-electron pulse height of $A_0 = 20$ ADC chan.

The effect on the occupancy caused by the change of the single-electron mean pulse height from 10 ADC chan to 40 ADC chan is demonstrated in Table 4.3. Decreasing the amplification will also decrease the number of signal hits. Hence, the choice of the amplification has to come from an optimization of pattern recognition efficiency and resolution.

Finally, we show in Table 4.4 the relative contributions of the different particle species to the occupancy. The values were obtained by observing the decrease in occupancy when the respective particle was taken out of the total flux. Half of the occupancy results from pions and decay muons. Primary pions and kaons alone give an occupancy of 3.2%.

Table 4.3: Simulated mean occupancy as a function of the single-electron mean pulse height A_0

A_0 (ADC chan.)	Mean Occupancy (%)
10	5.6
20	9.2
30	11.2
43	12.7

Table 4.4: Simulated contributions of individual particle fluxes to the mean occupancy

Particle	Contribution in $\%$
pions	37
μ^+, μ^-	13
photons	22
e^+, e^-	23
neutrons	4

4.3 Pattern recognition

In the following we present the status of the pattern recognition algorithm that has been developed specifically for the HMPID. A geometrical reconstruction of the photon angles has been developed using sets of samples of controlled density, in order to transform the coordinate space of clusters in the pad plane to a Cherenkov angle parameter space. This method, based on the approach initially reported in Ref. [9], is very general and is valid for any track incidence on the RICH surface. The signal obtained in this manner has been treated in the frame of a ‘Hough-like’ pattern recognition method to determine for each track the corresponding mean Cherenkov angle. The development of the pattern recognition is important at the present stage because it serves to validate the design and allows further optimizations of the construction.

4.3.1 Data sample used for pattern recognition

Different sets of data have been used in the current analysis. The main ones have been obtained as a superposition of single-track (beam) events, so that one obtains samples of known densities. The events are obtained by randomly superimposing a fixed number of single ring events on a pad map of the dimensions of the ALICE prototype module. In such a way, sets of respectively 10, 20, 30, 40 and 50 overlapped events per square metre have been formed, the last density being representative of the maximum expected pad occupancy in the ALICE environment. Only results obtained with the superposition of tracks perpendicular to the radiator will be presented in here, but sets of data under angles of incidence varying from 2.5 to 7.5 degrees are also available and will be analysed in the near future. Since special care was given to the study of the importance of the photon feedback on the pattern recognition, events measured at different anode voltages have been used. In addition, the influence of the ‘ring’ radius has been studied using different gaps. The different samples are summarized in Table 4.5. Another set of data has been

Table 4.5: Samples of data, collected at the SPS with a 350 GeV/c pion beam, used for the analysis

Sample	‘ring’ radius (mm)	Density (m^{-2})	RICH-HV (V)
1	155	1, 10, 20, 30, 40, 50	2100
2	155	1, 10, 20, 30, 40, 50	2050
3	155	1, 10, 20, 30, 40, 50	2000
4	122	1, 10, 20, 30, 40, 50	2100

obtained from GALICE, as explained in the preceding section, for pattern recognition studies of simulated, multiple-track ALICE events.

Figure 4.11 shows overlapped events corresponding to sample (1), for different particle densities.

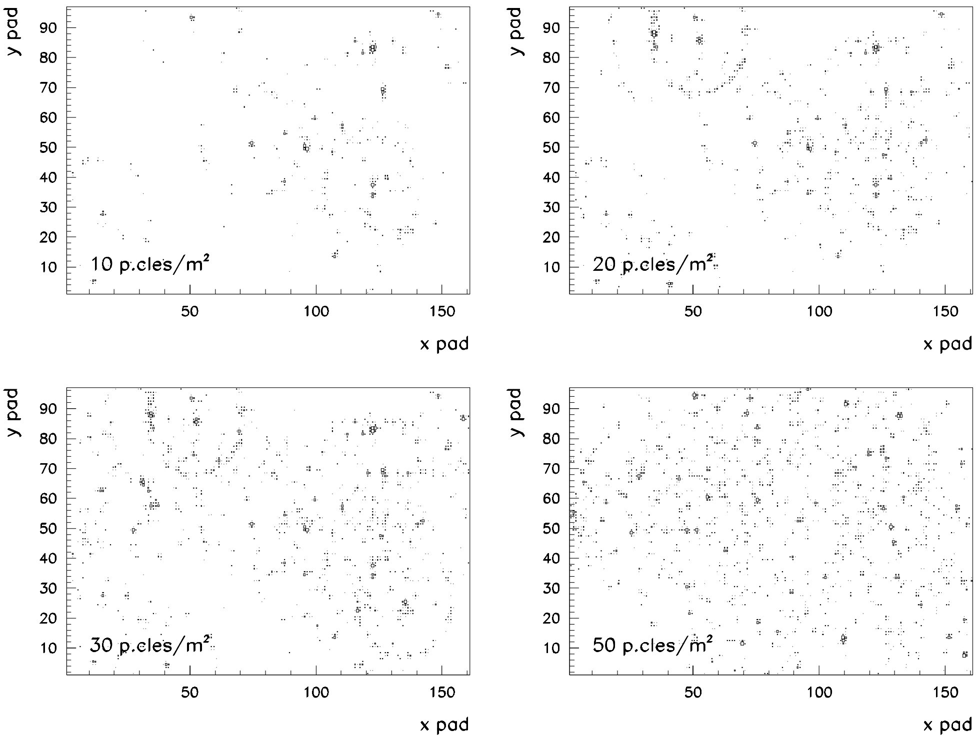

Figure 4.11: Overlapped events at different particle densities.

The occupancy for different radii and anode high voltages as a function of the number of overlapped events is shown in Fig. 4.12. The pad occupancy on the cathode plane depends on the ring radius, the HV setting on the MWPC and is proportional to the particle density. A particle density of 50 particles/m^2 corresponds to an occupancy of $\sim$12%, equivalent to the largest occupancy obtained in Section 4.2.4.3 from the GALICE simulation, where most of the particles have low momenta and large angles, therefore emitting a smaller number of photons in the detector than in the case of the test beam tracks.

The fact that the occupancy is higher at smaller radii is understandable in terms of 'edge effects'. The larger radii get a smaller number of full rings into the detector active area than is the case for smaller radii.

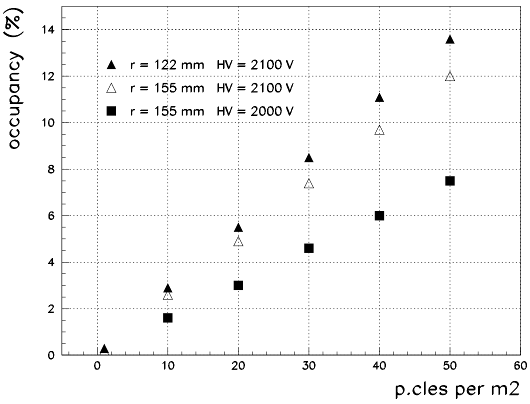

Figure 4.12: Occupancy on the photocathode for different conditions of gap size and anode voltage.

4.3.2 The signal from the HMPID readout: the pad hit and the clusters

The signal recorded by the pad readout of the MWPC consists of the following information:

- the coordinates of the pads where a signal (after zero suppression) has been recorded. We call them *hit pads*;
- the amount of charge induced on each hit pad, obtained by the analog readout of the electronics.

Because of the nature of the induction process (the characteristic spread), the pad size (8×8 mm^2), and the fluctuation of the charge in the avalanche, the signal produced by a single-track ionization in the gas or by Cherenkov photons converted in the CsI layer on the cathode will result in a 'cluster' the size of which may vary from one to several pads.

4.3.3 Cluster centroids and deconvolution

The map of hit pads is first analysed for clusters by an algorithm that recognizes, as such, groups of adjacent hit pads that share one common edge. In a second pass, the identified clusters are analysed looking for the existence of possible multiple-charge maxima in a single cluster, indicating that the recognized cluster represents, in fact, an overlap of two or more clusters. In cases where multiple maxima are observed, a deconvolution algorithm is applied, resulting in so-called 'resolved clusters'. Finally, a charge-weighted centroid is defined for each identified resolved cluster. Although this procedure allows a better localization of the photons, it does not mean that clustering can be usefully applied in high-occupancy environments; this point will be addressed in Section 4.3.6.

4.3.4 Reconstruction of the 'Cherenkov signal'

In the most general case of multiple tracks on the HMPID we have:

- a large-sized map of hits with a very complex pattern where individual RICH patterns can hardly be identified by eye (see Fig. 4.11);
- a map of 'impacts' of tracks as extrapolated from the TPC to the HMPID cathode plane;
- a number of real impacts corresponding to large charge clusters close to the extrapolated impact points [10].

In order to extract the Cherenkov signal, for a chosen track, from the described cluster distribution and track-impact information, we proceed as follows:

- we define a *'fiducial zone'* on the detector plane where Cherenkov photon clusters emitted by the chosen track of known momentum and incidence angle may be observed;
- we associate to each cluster (or pad) in the fiducial area a 'Cherenkov angle' of emission in the radiator as if it were produced by the track.

The latter task is performed using a backtracing algorithm described in the next section.

4.3.4.1 Geometrical backtracing

The backtracing reflects the fact that from a cluster centroid we try to reconstruct the angle under which the photon causing it could have been emitted if it had belonged to the chosen track. To be able to start backtracing we have to make the following assumptions:

1. the origin of 'photons' resulting in the same reconstructed angle is chosen to be one point on the track path through the radiator. The coordinates of this point vary with the angle (because of the absorption in the radiator) and are close to the middle of the radiator;

2. all the ‘photons’ are assumed to be of the same energy, corresponding to the mean energy of the photons producing photoelectrons in the HMPID RICH: 6.85 eV;

3. no assumption is made on the β of the particle.

The reference system has the origin at the entrance point of the Minimum Ionizing Particle (MIP) in the detector. As illustrated in Fig. 4.13, we define:

(x_p,y_p) = MIP impact coordinates projected onto the photocathode
(θ_p,ϕ_p) = MIP polar and azimuthal angles
(x,y) = photon impact coordinates projected onto the photocathode
(θ,ϕ) = photon polar and azimuthal angles
r_w, q_w, t_{gap} = radiator, quartz and gap widths
n_f, n_q, n_g = freon, quartz and methane refractive indices.

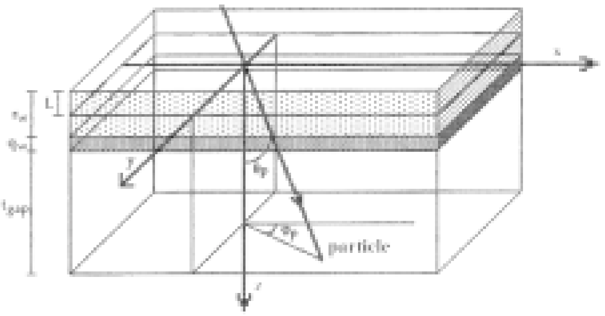

Figure 4.13: Reference system used in the backtracing.

The azimuthal angle ϕ for the photon can be evaluated, assuming an average emission depth L (at the middle of the radiator):

$$\tan\phi = \frac{y - L\tan\theta_p \sin\phi_p}{x - L\tan\theta_p \cos\phi_p} \; . \tag{4.1}$$

Using this value of ϕ and defining a and R as

a = [(r_w-L) + q_w + t_{gap}]tanθ_p
R = *distance MIP — photon cluster on the photocathode* ,

the following equation has to be solved:

$$R^2 = [a\cos\phi_p - b\cos\phi]^2 + [a\sin\phi_p - b\sin\phi]^2 \; . \tag{4.2}$$

In Eq. (4.2) b is a function of the polar angle of the photon according to

$$b = (r_w - L)\tan\theta + q_w \frac{n_f \sin\theta}{\sqrt{n_q^2 - n_f^2 \sin^2\theta}} + t_{gap} \frac{n_f \sin\theta}{\sqrt{n_g^2 - n_f^2 \sin^2\theta}} \; . \tag{4.3}$$

Therefore, the solution of Eq. (4.2) taking into account Eq. (4.3) provides the value of θ for the current photon of the MIP.

Finally, the Cherenkov angle η_c for the photon is calculated by:

$$\cos\eta_c = \sin\theta_p \cos(\phi - \phi_p) + \cos\theta_p \cos\theta \; . \tag{4.4}$$

4.3.5 Analysis of single beam events

Single-beam events at the SPS have been processed in order to obtain the Cherenkov angle resolution in the absence of background coming from other tracks. In Fig. 4.14a the distribution of extracted Cherenkov angles per cluster, using the described method, is shown for data sample (1) (see Table 4.5): there is a clear signal with negligible background). The Gaussian fit of the distribution gives a $\sigma_{\eta_c} \sim 12.8$ mrad.

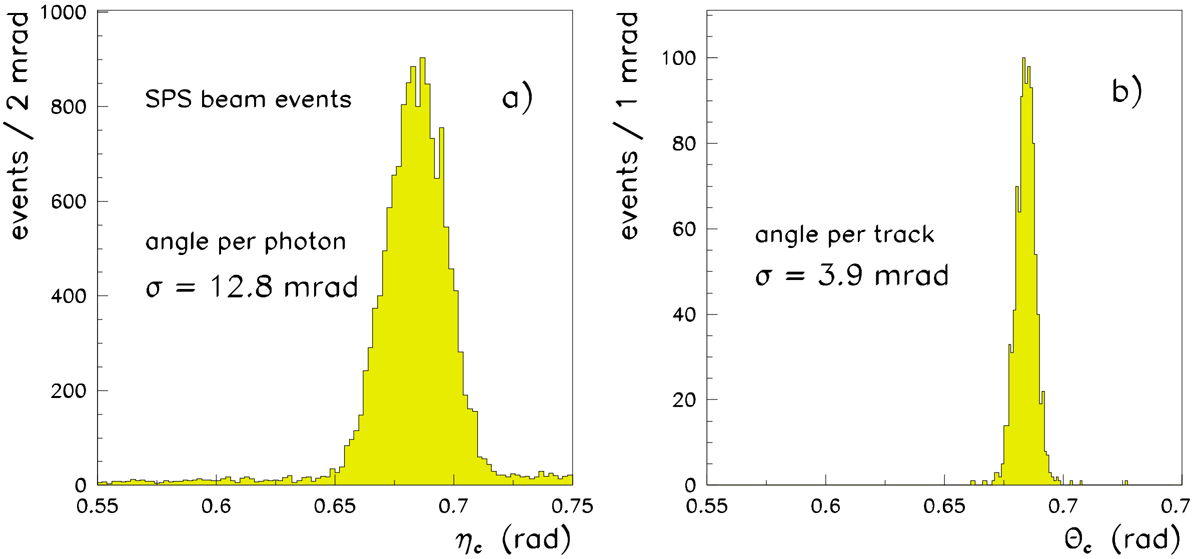

Figure 4.14: Photon angle distribution (a) and track Cherenkov angle distribution (b) for beam events at the SPS in data sample (1).

By averaging the η_c for all the photons, the mean Cherenkov angle per track θ_c is obtained: the distribution, shown in Fig. 4.14b, indicates this resolution to be 3.9 mrad. The distribution in Fig. 4.14b has been obtained considering only photons with η_c angle ranging between 0.550 and 0.750 rad. This fiducial area has no special meaning — it is meant to shorten the computing time.

To determine the baseline parameters we show in Fig. 4.15 the resolved cluster multiplicity, cluster size, and charge spectrum for the case of single-event patterns.

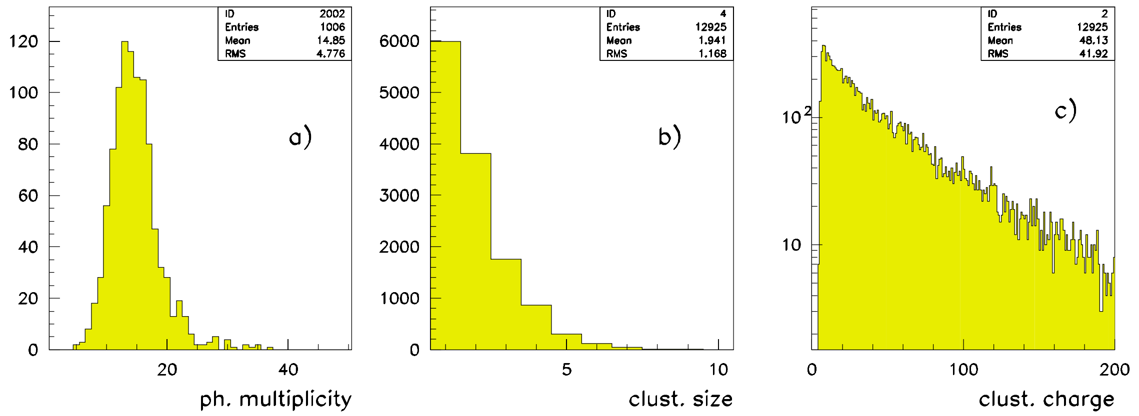

Figure 4.15: Photon cluster multiplicity (a), cluster size (b), and charge (c).

4.3.6 Analysis of overlapped data sets

Pad or cluster centroid backtracing

Although at first sight it seems advantageous to use the cluster centroid method in the backtracing algorithm (better localization) it has been observed that this method, even at moderate densities, leads to a reduction of the Cherenkov signal. The reasons for that are obvious — partially overlapping clusters from different tracks will merge into single clusters thereby reducing the overall number of clusters, and hence leading to a wrong centroid determination. For these reasons, we have analysed multi-ring events taking into the backtracing algorithm only the hit pads, assuming as photon-pad location the middle of the pad itself.

Fiducial region

Starting from the MIP position and knowing the detector parameters, a wide fiducial region is defined, around the MIP impact where all the photons relevant to that track could eventually be found. In the present analysis we have chosen to backtrace all pad hits corresponding to photon angles between 0.550 and 0.750 rad.

As an example, we can see in Fig. 4.16a the map of all backtraced photons (the MIP impact position is always in the origin), i.e. the assumed fiducial band: the picture corresponds to a density of 10 particles/m^2 from sample (1).

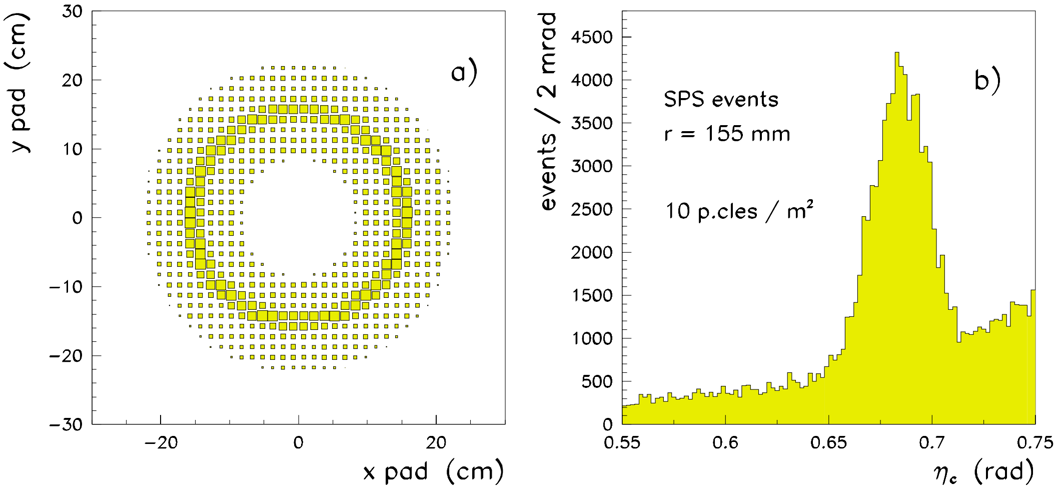

Figure 4.16: Fiducial band around the MIP (a) and photon angle distribution (b) at 10 particles/m^2 for sample (1).

The η_c distribution in Fig. 4.16b shows two distinct components: the peak around the Cherenkov angle, produced by photons belonging to the tracks analysed, and a continuous background belonging to photon pads produced by other tracks and falling in the analysed fiducial zone. The increasing profile of the background distribution is expected and is mainly due to the fact that at larger η_c values, a larger surface of the plane is covered for equal η_c bins. The shape of the background distribution is a challenge to the pattern recognition — biasing the peak value of the distribution towards higher angles. We therefore have to carefully treat the background in the analysis.

4.3.6.1 Background treatment

The background has been parameterised with an analytical form:

$$F_{bkg}(\eta_c) = [\tan\eta_c(1+\tan^2\eta_c)]^\alpha + A + B\tan\eta_c \;, \tag{4.5}$$

where $\alpha = 5.52$, $A = -7.80$ and $B = 22.02$. This parametrisation fits equally well all the studied densities.

With this analytical form, each photon has been weighted according to the following procedure. For each analysed track (MIP impact) the corresponding η_c distribution is calculated. In this distribution we calculate the number of photons N_{bkg} in a sampling band far from the signal (i.e. with η_c between η^1_{bkg} = 0.720 and η^2_{bkg} = 0.760 rad).

So the expected amount of background photons at any η_c can be estimated by means of Eq. (4.5), as

$$R_{bkg}(\eta_c)\mathrm{d}\eta_c = \frac{F_{bkg}(\eta_c)N_{bkg}}{\int_{\eta^1_{bkg}}^{\eta^2_{bkg}} F_{bkg}(\eta'_c)\mathrm{d}\eta'_c}\mathrm{d}\eta_c \; , \tag{4.6}$$

In Eq. (4.6) $\mathrm{d}\eta_c$ is 1 mrad and $R_{bkg}(\eta_c)\mathrm{d}\eta_c$ is the expected amount of background photons in a 1 mrad bin at the angle η_c. In Fig. 4.17 we show the fitted background (dashed line) compared with the real background shape at several particle densities. The white distribution in each case corresponds to the photon η_c spectrum obtained for all analysed MIPs.

If $N_{ph}(\eta_c)\mathrm{d}\eta_c$ is the η_c spectrum for the MIP under study, then in order to take into account the background, each photon in each bin should be weighted by

$$W_{bkg}(\eta_c) = 1 - \frac{R_{bkg}(\eta_c)}{N_{ph}(\eta_c)} \; . \tag{4.7}$$

The dark distributions in Fig. 4.17 have been obtained by entering each photon with the corresponding weight calculated by Eq. (4.7). In this way the background contribution has been taken into account so that, a priori, no systematic biasing of the signal will occur in the pattern recognition.

4.3.6.2 Extraction of the mean Cherenkov angle

The determination of the mean Cherenkov angle per track is the main goal of the pattern recognition. The η_c signal observed in Fig. 4.17 shows that there is no drastic deterioration of the width of the signal distribution, but the mean Cherenkov angle is influenced by the presence of the background signal. In the following we will shortly review the steps in the pattern recognition that we have developed. Our basic approach is to apply a Hough transform method which has been modified to accomodate the fact that the signal in the η_c coordinate has a natural width given by all the features described in Chapter 2. To account for that width we apply a *sampling band* approach that consists in sliding a window of a width comparable to the width of the signal over the η_c spectrum. At each step in the sliding, the number of pads found within the window is counted. When the window reaches the region for which the number of counted photon-pads is the largest, the content of the window is called the *'Hough selected photon pads'*. Using that information and the known background weights, an iterative averaging procedure is used to finally determine the value of the mean Cherenkov angle associated to that track.

The Hough Transform method

The pattern recognition for the HMPID, on the track level, has been implemented using the Hough technique to extract the mean Cherenkov angle per track as a parameter to be estimated in a transformed parametric space [11, 12].

The Hough Transform method (HT) is an efficient implementation of a generalized *template matching* strategy for detecting complex patterns in binary images. This is achieved by analysing the parameters which characterize these patterns and looking for local maxima in a *feature parameter space* [13]. The main advantage of the Hough transform is that it is relatively unaffected by topological gaps in curves

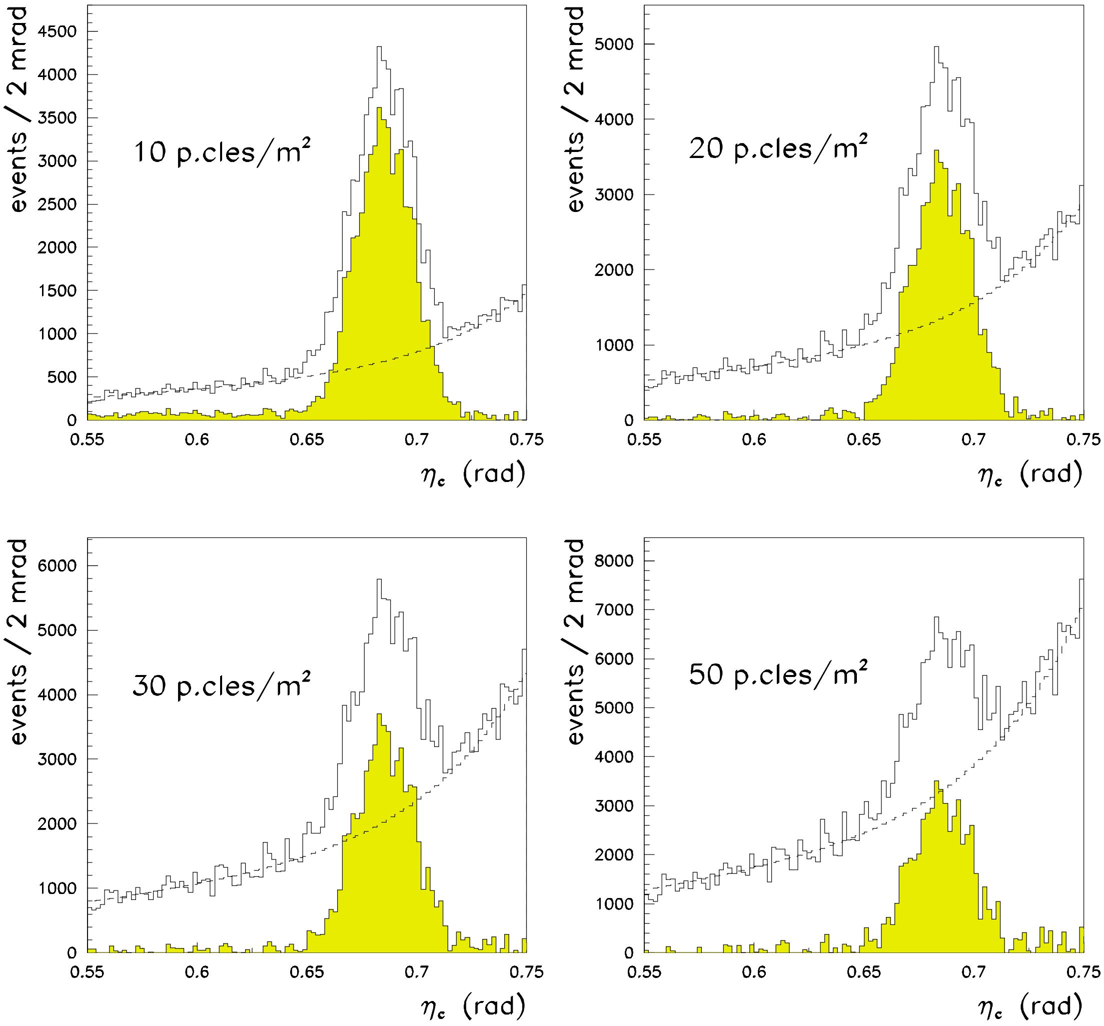

Figure 4.17: Distributions of η_c per photon-pad at different particle densities, with estimated (dashed) and subtracted (dark) background for sample (1).

and by high-noise background in spot-like images [14]. In general, let us assume that we transform a Cartesian space into a feature space:

$$\mathbf{x} \rightarrow (\mathbf{a}, T(\mathbf{x}, \mathbf{a})) \ , \tag{4.8}$$

where **a** is a parameter vector and T(**x**,**a**) its relative transform. For each thresholded contribution of T(**x**,**a**) in the parameter space, a Hough counting takes place in the so-called *'Hough Counting Space'* (HCS):

$$HCS(T(\mathbf{x}, \mathbf{a})) := HCS(T(\mathbf{x}, \mathbf{a})) + w \ , \tag{4.9}$$

where w is a given weight to be assigned to the *feature vector* **a** which, in the simplest case, is assumed to be unitary. The *incrementation strategy* of Eq. (4.9) can be also further refined by applying an incrementation function:

$$w = w(\mathbf{x}, \mathbf{a}) \ , \tag{4.10}$$

which implements a weighting policy in such a way as to use other relevant information associated with a given feature point [15]. The Hough estimator for the feature vector is given by the bin value in HCS which provides the highest occurrence in the parameter space.

For the HMPID analysis we have

$$(x, y) \rightarrow ((x_p, y_p, \theta_p, \phi_p), \eta_c) \ . \tag{4.11}$$

If we assume **a** = (x_p,y_p,θ_p,ϕ_p) to be already known, the transform will reduce the problem to a solution in a one-dimensional mapping space. The HCS in this case represents the photon Cherenkov angle η_c spectrum and, indeed, a Hough estimator for the Cherenkov angle θ_c of the particle is chosen as the highest peak provided by all the photons which fall in that angle bin. Thus, the HCS accumulates the contributions from several Cherenkov photons according to expression (Eq. 4.9). The analysis procedure can be easily extended and made more effective if the weight function (Eq. 4.10) is used to take into account other factors like the background evaluation or the charge contribution for each Cherenkov photon.

The transformation which provides the parameter η_c for a given vector **a** has already been described in Section 4.3.4.1 as the *geometrical backtracing algorithm* to extract the Cherenkov angle associated to each photon pad. Each MIP cluster is excluded from this transformation and for each MIP cluster a scanning in the *MIP reference system* is done in such a way as to get the η_c values ranging from 0.550 to 0.750 rad. It should be noted that this kind of approach allows independence from the topological shape and size of the specific Cherenkov pattern cut in the plane of the detector (i.e. circular, elliptic, parabolic). This is due to the fact that the particle identification happens in the Cherenkov photon angle space, instead of the Cartesian one.

HT method modified with correlation bands

The basic HT method applied to the HMPID has been enhanced in such a way as to be less influenced by the background caused from several noise sources [16].

For each photon there is a spread in the Cherenkov angle to be taken into account, which makes it harder to achieve a good resolution σ_{η_c} in the Cherenkov angle identification. In order to enhance statistically as much as possible the signal in the η_c spectrum, the incrementation expression (Eq. 4.9) has been modified.

The following integration in the η_c space over a *sampling band* b has been applied:

$$HCS'(\eta_c) = \int_{\eta_c - \frac{b}{2}}^{\eta_c + \frac{b}{2}} HCS(\eta_c')\mathrm{d}\eta_c' \ , \tag{4.12}$$

which, in the discrete case, where $\mathrm{d}\eta_c = 1$ mrad (i.e. $\eta_c(k)$ = k $\mathrm{d}\eta_c$, k integer), transform into the correlation:

$$HCS'(\eta_c(k)) = \sum_{i=\eta_c(k)-\frac{b}{2}}^{\eta_c(k)+\frac{b}{2}} HCS(i) \ . \tag{4.13}$$

The HCS has been calculated using $w = W_{bkg}(\eta_c)$, defined by (Eq. 4.7), as the incrementation function. The optimum sampling band in the correlation has been determined at 40 mrad for the smallest σ_{η_c} value.

The information extracted from the pattern recognition, for each analysed MIP, is the number of hit pads falling into the Hough selected band: we call those *'Hough selected photon pads'* and their number will be indicated by N_{ph}^{Hough}. In Fig. 4.18a these selected photon pads are shown in the case of a 10 m^{-2} particle density; in Fig. 4.18b the evolution of the N_{ph}^{Hough} distribution with the particle density is also reported.

In the pattern recognition the band selection performed by the Hough method, as described in Section 4.3.6, takes into account the background: this determines θ_c^{Hough} and N_{ph}^{Hough}. Beyond that, we can alos make use of the different η_c angles for the *Hough selected photon pads* and their background-related weights.

This information is used to calculate the average weighted angle as:

$$\langle\theta_c\rangle = \frac{1}{W_{tot}} \sum_{i=1}^{N_{ph}^{Hough}} W_{bkg}(\eta_c(i))\eta_c(i) \qquad W_{tot} = \sum_{i=1}^{N_{ph}^{Hough}} W_{bkg}(\eta_c(i)) \ . \tag{4.14}$$

In Fig. 4.19 the θ_c distributions at three different densities are shown, with the bottom right plot resuming (white triangles) the behaviour of the corresponding sigmas (*'angle resolution'* per MIP) versus particle density.

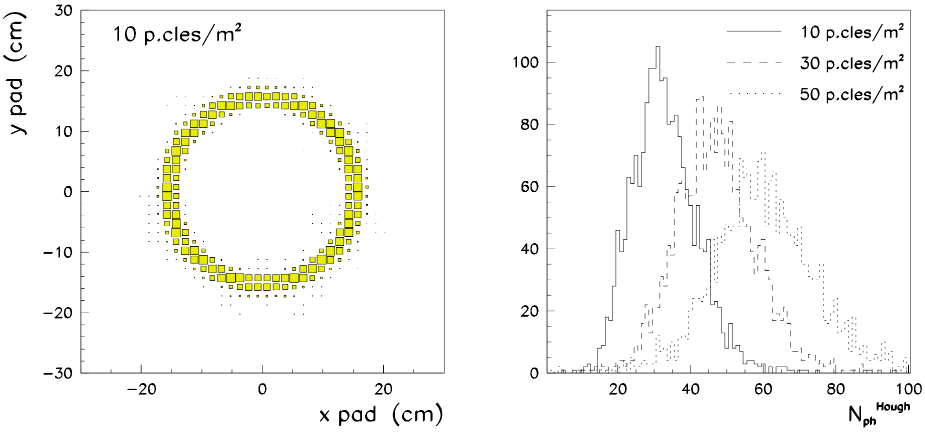

Figure 4.18: Hough selected photon pads at 10 particles/m^2 and multiplicity distributions at different densities for sample (1).

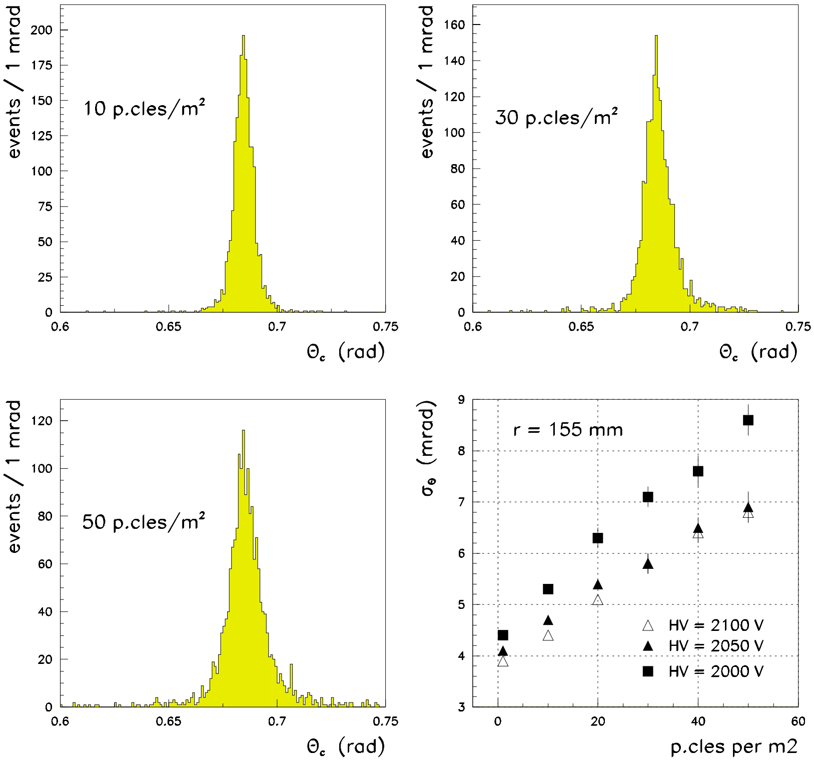

Figure 4.19: Final Cherenkov angle distributions per MIP at different densities for sample (1) and corresponding sigma evolution compared with those for samples (2) and (3).

The same analysis has also been applied for samples (2) and (3) in Table 4.5, i.e. overlapped beam events collected at the SPS H4 beam in 1997 and 1998, lowering the RICH HV from 2100 V to 2050 V and 2000 V: the results are summarized in Fig. 4.19.

No significant difference is observed for the two higher HV values, while a degradation is observed at 2000 V, probably due to some photon losses at that voltage.

A *'ring reconstruction efficiency'* can be extracted as the fraction of *'good reconstructed rings'* with respect to the total number of MIPs: a well-reconstructed ring means that the corresponding Cherenkov angle falls within ± 15 mrad (i.e. $\sim \pm 2\sigma$ of the angle distribution at the highest density) from the central value 0.686 rad. Figure 4.20 shows the evolution of this efficiency versus the particle density.

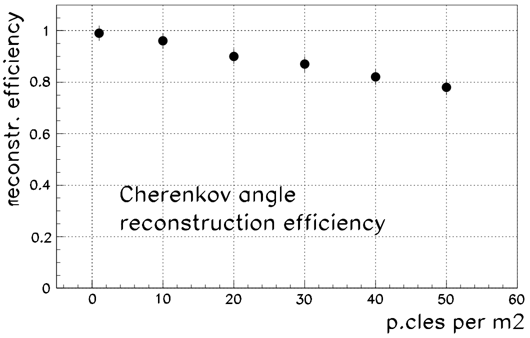

Figure 4.20: Ring reconstruction efficiency versus particle density for sample (1).

The same analysis has been applied to the event sample (4), the main aim being to study the dependence of the pattern recognition performance on the size of the single pattern (i.e. the ring radius). The behaviour of the σ_{θ_c} versus the particle density is reported in Fig. 4.21a, where the results from sample (1) and sample (4) are compared.

The better resolution obtained for smaller R reflects the fact that the overlap of different patterns is smaller for smaller rings, hence the underlying noise background contribution is smaller. This result needs to be confirmed in the more general case of 'realistic' event simulations. In Fig. 1.4 the θ_c distribution at 50 particles m^{-2} for sample (4) is shown, with the corresponding Gaussian fit of the peak.

The analytical relation between the Cherenkov angle resolution and the corresponding momentum limit for 3-σ $\pi-$K separation is plotted in Fig. 4.21b: it can be noted that in the best case the performance of the method provides a 3σ $\pi-$K separation up to more than 2.5 GeV/c for the most violent events anticipated in ALICE. Assuming the mean multiplicity of the recorded events to be about half the maximum value, the present analysis sets the 3σ $\pi-$K value to $\sim$3 GeV/c.

4.3.7 Recognition of Cherenkov patterns in the GALICE environment

The particle identification strategy of the HMPID will address only particles with a momentum larger than 1 GeV/c. With this in mind, the Hough transform method will never be applied to all particles in an event, as is the case in the analysis done so far, but it will concern limited regions in the HMPID plane where high-momentum particles are tracked by the TPC and the ITS.

As an example, we show the present pattern recognition applied to a well-defined hadron in the GALICE environment. The top part of Fig. 4.22 shows the map of hit pads belonging to one module of the HMPID, as simulated in GALICE for a Pb–Pb interaction.

In this high-density environment, Cherenkov patterns are not recognizeable by eye. This is also true in the region enclosed by the box shown in the right-side part of the hit map. This box delimits a window opened around the hit point of a pion of 1.23 GeV/c, that impinges the HMPID plane at an incident angle of 0.98°.

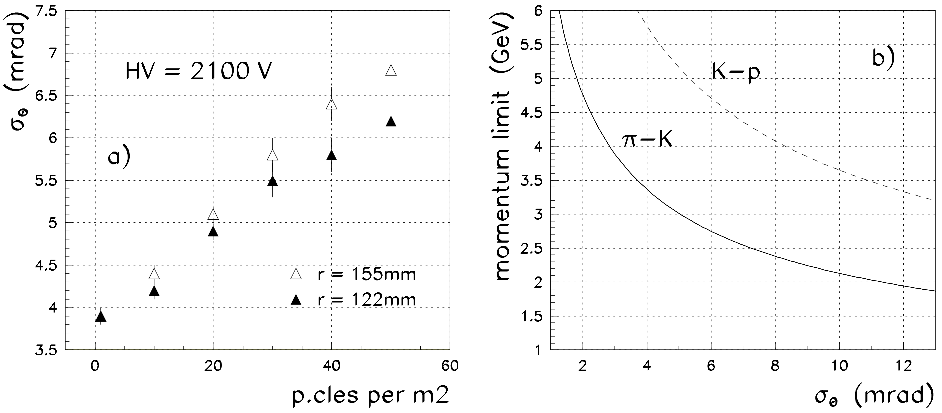

Figure 4.21: a) Cherenkov angle resolution vs. particle density at different radii; b) momentum limit vs. σ_θ.

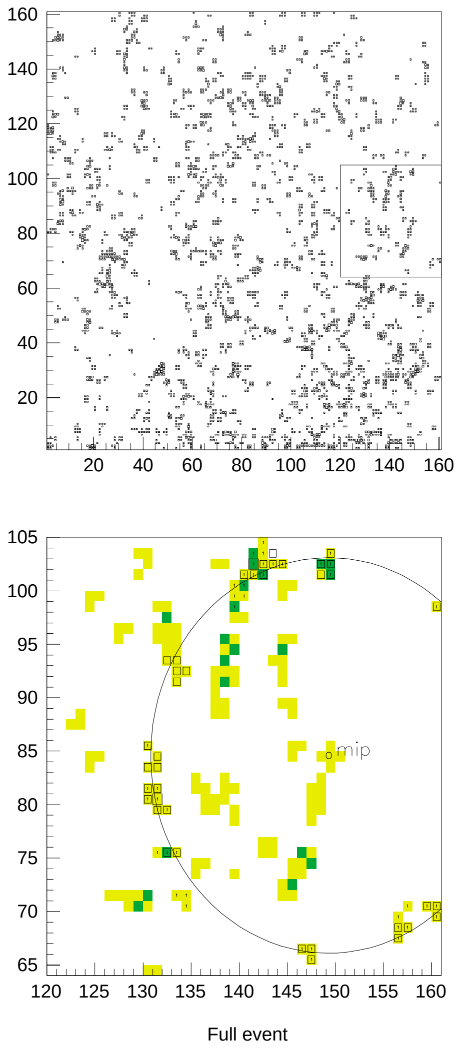

Figure 4.22: Top: hit map of one HMPID module in ALICE generated with the GALICE package for one Pb–Pb event. Bottom: zoom of the region enclosed by the box in the top map with the Cherenkov pattern (ring) associated to the Hough method.

In the lower part of Fig. 4.22, the particle hit point is indicated with *'mip'* while the pads belonging to clusters initiated by the Cherenkov photons emitted by the selected particle are indicated as open boxes. The Hough Transform method has been applied to the set of clusters contained in the window.

Open boxes indicate pads of clusters initiated by Cherenkov photons associated in the pattern recognition to the particle that crosses the region in the point 'mip'. Pads with a darker colour show overlap among clusters. Hough reconstructed pads are indicated with '1'. As shown, the method is able to recognize almost all the relevant clusters belonging to the Cherenkov photons. Indeed 30 pads out of 40 are associated to the right clusters, only one cluster has been completely missed due to the fact that it belongs to a huge unresolved cluster. The final result is a correct identification of the pion. A systematic analysis of GALICE events is in progress.

4.4 Matching of tracks with clusters on the HMPID pad plane

The pattern recognition of the Cherenkov patterns and the precision in the extraction of the Cherenkov angle rely heavily on the precise knowledge of the momentum of the particles, their angle of incidence, and impact point. In particular, it is of primary importance to demonstrate that, at the expected pad occupancy, we are able to correctly match the reconstructed tracks with the impact points at the HMPID pad plane, bearing in mind that the total charge allows to distinguish a MIP cluster from a photon cluster.

The tracking through the ITS and TPC and the extrapolation to the HMPID have been performed [10] by using simulated particles, with momenta ranging from 0.5 to 5 GeV/c. The points generated in the ITS and TPC detectors have been fitted in order to extract the kinematic parameters to be used for the extrapolation to the HMPID. After the calculation of the impact coordinates and direction cosines of the fitted track on the RICH module, the relevant quantities have been compared with those of the simulated track after its full evolution through the ALICE apparatus. These quantities have also been studied as a function of the track momentum.

4.4.1 Track simulation

Tracks have been generated with a flat momentum distribution, ranging from 0.5 to 5 GeV/c in the rapidity range $|\eta| < 0.4$. The evolution of the track through the ALICE subsystems (6 silicon layers in the ITS, 75 space points in the TPC region and the final set of RICH modules) has been determined by GEANT routines.

Multiple scattering in the beam pipe, silicon layers, TPC gas mixture and also in mechanical supports, cooling systems and in electronics has been taken into account (total equivalent to $\sim 8\%$ X_0) according to the detector design reported in the ALICE Technical Proposal [1] (see Table 4.6, where is shown the averaged material budget corresponding to the interesting momentum range for the HMPID as well as to ITS spatial acceptance). About 5000 tracks (over all momenta) have been processed, in an uniform magnetic field of 0.2 T within the RICH acceptance.

4.4.2 Track reconstruction

The fitting routines take into account the hits, both in the ITS and in the TPC detectors, according to the specification reported in the Technical Proposal [1].

In the fitting model the tracks are supposed to be helices [17] with a common vertex at (0,0,0), polar and azimuthal emission angles λ and ϕ_0, respectively, and a radius of curvature $R\ (\mathrm{cm}) = p \cos\lambda / KB$ $(K = 0.003, B = 0.2$ T and track momentum p in GeV/c). All the hits (points in the fit) have been weighted, taking into account the detector spatial resolution and the multiple scattering error propagation through the different layers.

In Fig. 4.23 we report the distributions of the residuals between simulated and reconstructed track kinematic parameters. After reconstruction, angular resolutions of less than 1 mrad have been found,

Table 4.6: Averaged material budget in the tracking volume

	Radius (cm)	X/X_0 (%)		Radius (cm)	X/X_0 (%)
ITS			TPC		
Beam pipe	3.0	0.17	Inner vessel	52	0.27
Si pixel 1	3.9	0.64	CO_2	52–78	0.14
Si pixel 2	7.3	0.64	Inner cage	78	0.52
Si drift 1	14	0.64	Working gas	78–250	0.56
Si drift 2	24	0.64	Outer cylinder	250	1.33
Si strip 1	40	0.64	Air	250–480	0.75
Si strip 2	45	0.64			
Outer shell	50	1.00			
Air	3–52	0.16			

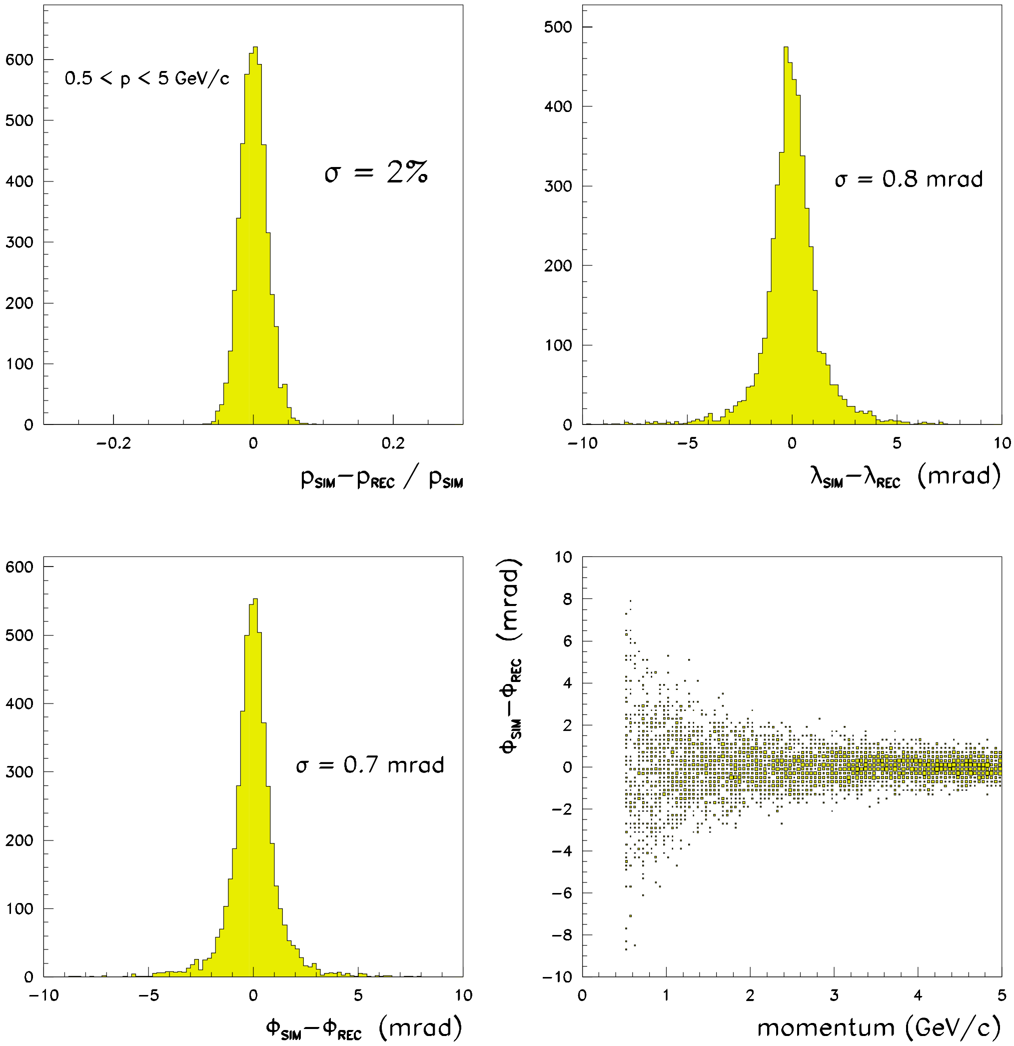

Figure 4.23: Residuals of simulated and reconstructed kinematic parameters.

while the average $\Delta p/p$ (over all momenta) is about 2%. These values are compatible with the tracking resolution estimates reported in the Technical Proposal. The $\Delta p/p$ versus p behaviour will be discussed later in this Chapter.

The track fit residuals have been calculated for each detector layer; in particular, it is interesting to look at the residuals on the last pad row of the TPC, which is the end of the track measurement region. Figure 4.23 reports the distribution of the difference in $r\phi$ and z coordinates between the fitted crossing point and the 'data' point; they refer to the whole sample, while Table 4.7 resumes the values of the sigmas of these distributions as a function of the track momentum.

Table 4.7: Sigmas of the residual distributions at the end of the TPC

Momentum range (GeV/c)	0.5–1	1–1.5	1.5–2	2–3	3–4	4–5
$r\phi$-residuals (μm)	410	300	220	210	180	170
z-residuals (μm)	1060	660	450	320	230	210

4.4.3 Extrapolation to the HMPID

4.4.3.1 Evaluation of the tracking errors at the HMPID

A reconstructed track can be extrapolated from the last measured point in the TPC up to the HMPID modules by using the fitted kinematic parameters. Track-by-track impact coordinates and momentum vector components at the HMPID have been extracted: these have to be compared with real points and momenta provided by GEANT for the same detector module.

In the actual experiment the extrapolated impacts and directions are the starting point for the matching of track hits in the HMPID with the tracks in the TPC. It is useful to remember that the uncertainites in this determination are expected to be greatly amplified with respect to the fit residuals found at the end of the TPC: not only because of the fit error propagation along the 250 cm path from the TPC to the HMPID, but also because of the multiple scattering in the outer wall of the TPC vessel ($\sim 1.3\%\ X_0$).

To estimate the final expected resolution on the impact and angles onto the RICH, we have to look at the distributions of the differences between extrapolated crossings and the 'data' point. Figure 4.24 shows the distribution of the difference $\Delta(r\phi) = (r\phi)_{real} - (r\phi)_{extrap}$ and the same for Δz calculated at the RICH for all momenta (between 0.5 and 5 GeV/c).

The widths of these distributions provide the expected extrapolation error for $r\phi$ and z coordinates of the track impact onto the RICH modules. The same calculation has been performed for the polar and azimuthal angles λ and ϕ of the track. The following error estimates have been extracted:

$$\sigma_{r\phi} = 3.3 \text{ mm} \qquad \sigma_{\phi} = 1.9 \text{ mrad}$$
$$\sigma_{z} = 2.1 \text{ mm} \qquad \sigma_{\lambda} = 0.7 \text{ mrad}$$

4.4.4 Evaluation of the matching efficiency

We have investigated the probability of a fake match between the extrapolated track and the corresponding hit in the HMPID; this can occurr due to the high hit density expected in the RICH modules in Pb–Pb events at the LHC.

A fake match occurs when another hit falls closer to the tracking prediction than the real impact of the track. The particle densities simulated as shown in Section 4.2 using the full ALICE detector material budget have reached a maximum density of 100 particles/m^2. The amount of 'mismatches' computed as a function of track momentum is reported in Table 4.8.

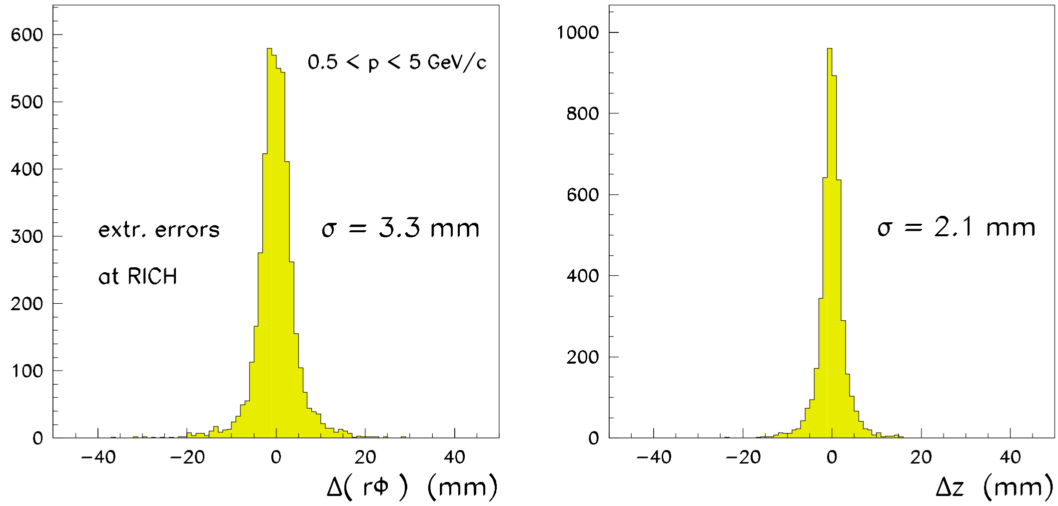

Figure 4.24: Distributions of difference between extrapolated and real impacts at the RICH.

Table 4.8: Estimated probabilities for fake matches between the track and the hit in the HMPID for a density of charged particle impacts of 100 m^{-2}

Momentum range (GeV/c)	0.5–1	1–1.5	1.5–2	2–3	3–4	4–5
Fake match prob. (%)	4.6	1.4	0.8	0.4	0.3	0.2

The results show that the probability of mismatches between tracks and the corresponding hit in the HMPID is tolerable at the estimated tracking impact resolutions.

4.5 Optimization of the detector

In the preceding sections we have discussed the tools developed to determine and study the influence of different parameters on the performance of the HMPID in the ALICE environment together with the results obtained so far. It is important to realize that the optimization in the realistic environment is not necessarily the same as the optimization in a clean environment. For instance, the result that the resolution is better for smaller radius would not have been reached on the basis of low particle density events. The pattern recognition performed on overlapped events clearly shows the importance of the occupancy in worsening the angular resolution of the Cherenkov angle distribution and, hence, the upper momentum limit of particle identification of the HMPID.

We have reached a satisfactory resolution in a particularly hostile environment. However, we believe that further optimization of the design in some respects is still possible. This optimization would consist of decreasing all the elements that contribute to the occcupancy, such as:
– reducing the material budget of the HMPID modules;
– reducing the photon feedback contribution to the noise;
– studying the possibility to use a detector gas mixture with the minimum content of hydrogen atoms;
– determining the optimum single-electron mean pulse height — a compromise between the localization accuracy, the achievable single-electron detection efficiency, and resulting Cherenkov angle resolution;
– determining the optimum size of the proximity gap for best performance in a high-occupancy environment.

These optimizations will be discussed in the following.

4.5.1 Optimization of the constructive elements of the detectors

The analysis of the origins of the noise hits in the HMPID shown in Table 4.4 clearly indicates that it is useful to carefully analyse any possibility to reduce the material budget of the thickest object in the module, i.e. the radiator.

As has been shown in Chapter 2, the resolution of the mean Cherenkov angle has almost no dependence on the thickness of the radiator, because the loss of emitting medium is compensated by the better resolution per photon and by the higher transparency of the thinner radiator. A decrease of $\sim 20\%$ in the thickness seems worth studying in high-density environments.

4.5.2 Reduction of the photon feedback

The photon feedback effect has been described in detail in Chapter 2 and it is obvious that it contributes significantly to the overall occupancy. As an indication, the photon feedback contributes $\sim$ 15% of the overall occupancy in the simulated events at a HV of 2100 V. It is therefore important to achieve the lowest feedback keeping a high single-electron efficiency. Two possible ways of further improvement are: the continuation of the study of the HV dependence of the mean Cherenkov angle resolution in high-occupancy environments and the study of optimized gas mixtures that would allow for the lowest feedback and for the lowest possible hydrogen content, to lower the rate of neutron interactions in the gas.

4.5.2.1 Gap size

We have started to analyse the effect of decreasing the gap length in the HMPID. However, the final decision on the exact value will depend on the optimization of two factors: the best resolution achievable and the best efficiency. A larger ring pattern means that for the particles falling in the edge region of the HMPID, i.e. when the track impact is closer to the edge than the value of the ring radius, a number of photons of the pattern will be lost because of the detector size. This problem will have to be addressed in detail and it is clear that, all other conditions being equal, one would favour a smaller ring radius. It is comforting to see that, under the present conditions of the tests and pattern recognition, the smaller size also results in the best angular resolution, as shown in Section 4.3.6.

5 Installation and organization

5.1 ALICE experimental area

The ALICE detector will be installed at Point 2 of the LHC accelerator. The Point 2 experimental area was designed for the L3 experiment. The main access shaft, 23 m in diameter, provides a 15×7 m^2 installation passage and space for counting rooms. The counting rooms are separated from the experimental area by a concrete shielding plug (see Fig. 5.1). The experimental cavern is 21.4 m in diameter and will be re-equipped with 2×20 t cranes having a clearance of about 3 m over the L3 magnet.

The L3 magnet provides a 11.6 m long and 11.2 m diameter solenoidal field of up to 0.5 T. The end-caps have a door-like construction. The door frames will support large beams traversing the L3 magnet, from which the ALICE central detectors will be supported.

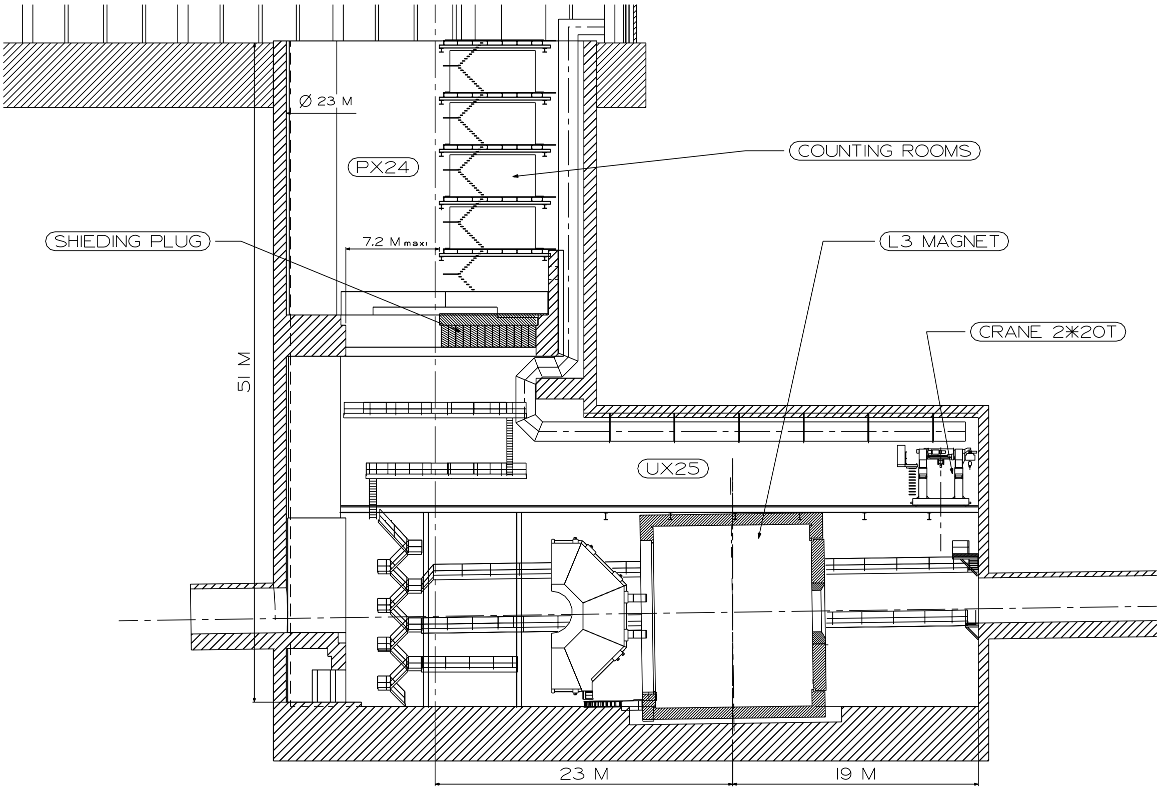

Figure 5.1: General layout of the basic underground structures at point 2, showing the L3 magnet and the counting rooms. PX24 is located at middle-height of the pit.

5.2 Installation and maintenance of the HMPID

The ALICE central detectors will be mounted in a cylindrical space frame construction (see Fig. 5.2), which will be fixed on the large support beams.

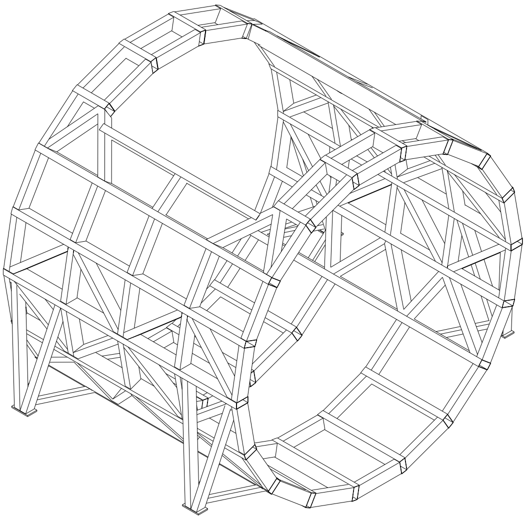

Figure 5.2: Space frame support structure. The openings in the top and bottom are to minimize material in front of the HMPID and PHOS, respectively.

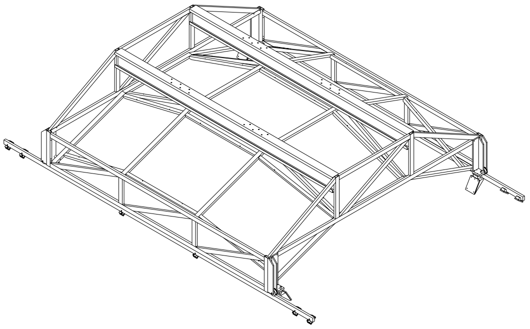

Figure 5.3: Support cradle for the seven HMPID detector modules to roll on top of the space frame.

All seven HMPID modules will be mounted in a support cradle (see Fig. 5.3), which will be fixed on rails at the top of the space frame. The space frame and the support cradle will be equipped with stiffening rods only outside the acceptance area of the HMPID in order to minimize the influence of multiple scattering. To improve access during maintenance and installation operations, a special installation platform (see Fig. 5.4) will be temporarily attached to the space frame and to the magnet, in order to allow the detector to be moved out of the L3 magnet.

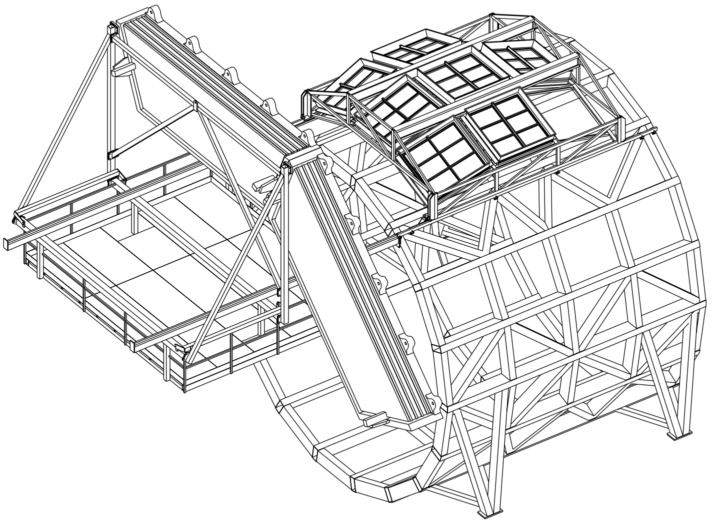

Figure 5.4: Installation platform fixed on the space frame and on the L3 magnet to allow installation and maintenance operations.

All services will be guided through slits between the magnet door and the barrel (see Fig. 5.5). In this way the magnet doors can be opened without removing the services. The HV and LV power supplies will be located in racks in the UX25 experimental area close to the L3 magnet. All power supplies will be remotely controlled from the counting rooms.

The gas and liquid systems have been described in Chapter 3. The gas supply will come from the gas building on the surface. The recirculation and purification unit will be located on the shielding plug in PX24. As described in Section 3.2.10, the liquid radiator system is divided into two parts. The purification system will also be located in PX24, whereas the recirculation system has to be on the same horizontal level as the detector to minimize the hydrostatic pressure in the radiator. As shown in Fig. 5.6 it will be installed on the wall of UX25 outside the L3 magnet. All pipes connecting the detector with the gas and liquid systems will be carried out in stainless steel.

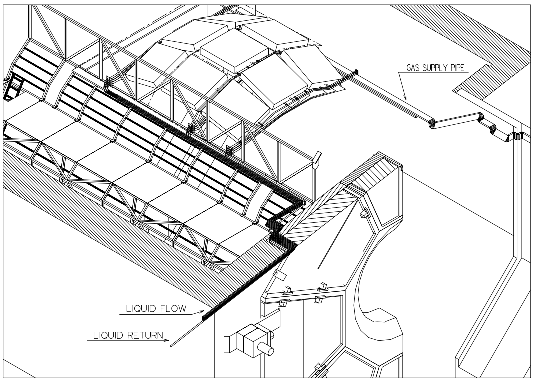

Figure 5.5: Layout of the HMPID services for the detector gas and liquid radiator in the L3 magnet volume.

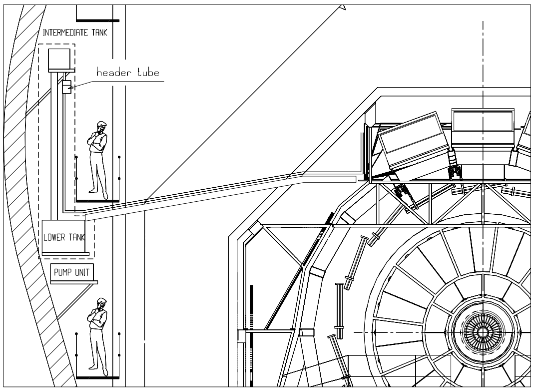

Figure 5.6: Relative position of the liquid radiator recirculation system and the HMPID detector. The difference in height will be optimized to minimize hydrostatic pressure in the radiator.

The overall ALICE planning foresee a pre-assembly phase of all the central detectors to take place in the SKL2 hall at Point 2, between mid 2003 and mid 2004.

This will allow an early preparation of the different detector services, and the installation procedure to be analysed and corrected before integrating the detectors into the L3 magnet.

The different pre-assembly and installation phases for the HMPID detector are as follows (see also Table 5.1).

Pre-assembly phase

i) installation and first commissioning without detectors of the gas and liquid systems,
ii) commissioning of the support cradle and final equipment on the space frame in the UX25 area,
iii) installation and first commissioning of cables and electronic equipment.

Pre-installation in experimental area

i) Calibration of the liquid circulation system using detector modules.
The aim of this operation is to adjust the flow rates of the 21 radiators at their nominal values. The modules have to be located at their final positions on the support cradle because the flow settings are pipe-impedance-dependent. In addition, the cradle has to be tested inside the L3 magnet where the control elements of the liquid circulation are installed. These adjustments can still be done with several detector modules not yet equipped with the CsI photocathodes, to avoid the circulation of protection gas.
ii) Commissioning 'in situ' of the gas and liquid circulation systems.

Final installation

The final installation can start in year 2005, once all detector modules are available with CsI photocathodes. The gas and liquid systems must be operational in the experimental area since the CsI photocathodes have to be flushed permanently with argon. The seven detector modules are mounted on the support cradle equipped with a temporary gas flushing system.

The complete detector and support cradle can now be lowered into the UX25 area and lifted onto the rails of the installation platform. Then the detector will be rolled into its final position on top of the space frame and connected to all the services. After the gas system has been connected to the detector, the temporary gas flushing system will be disconnected, and the final commissioning of the system can be started.

After all the barrel detectors are mounted into the space frame and the cabling is completed, they will be aligned with respect to the LHC beam. The relative positions will be measured by means of photogrammetry.

Maintenance

The maintenance access to the HMPID, once installed inside the L3 magnet, is rather limited and only the perimeter of the support cradle can be reached during a short access. Therefore, during repair or maintenance interventions the complete detector will be moved out onto the installation platform. Although most services (cooling, gas and cables) can be made flexible and absorb the displacement without being disconnected, this is not possible for the liquid C_6F_{14} system. This implies that, once the HMPID is installed on the spaceframe and connected to the C_6F_{14} system, the spaceframe cannot be moved.

5.3 Milestones and construction programme

An overall time schedule for the HMPID is shown in Table 5.1.

During 1999, the programme will be to finalize the digital part of the electronics, once the evaluation of the ASIC prototypes is completed, and to carry out the optimization programme of the CsI processing using the improved evaporation station (Section 3.1.5) and the ASSET system (Section 2.1.1.6).

As from the beginning of year 2000, the main orders should be placed (quartz, mechanics) in order to start the production of the modules staged over two years. It is envisaged to interleave testing periods after the construction of each module to allow the implementation of possible modifications. For the same reason, orders of components should be staged as well.

The final design, testing, and production of the auxiliary systems will be carried out in parallel with the construction of the modules.

Once the detector modules are commissioned, the production of the CsI photocathodes can be launched. This production has to respect the estimated time duration, i.e. 16 months, and should be completed as close as possible to the start of the experiment in order to avoid any unnecessary standby periods of the photocathodes that could initiate ageing. It is foreseen to have the modules equipped with CsI PCs and tested by the end of 2004 ready for final installation at the beginning of 2005.

Table 5.1 is based on the following technical milestones:

- end 1999:
  finalize the ASIC design and the readout electronics
  finalize the CsI PC optimization programme
- middle 2001:
  all radiator trays produced and tested
- beginning 2002:
  finalize the gas and liquid system design

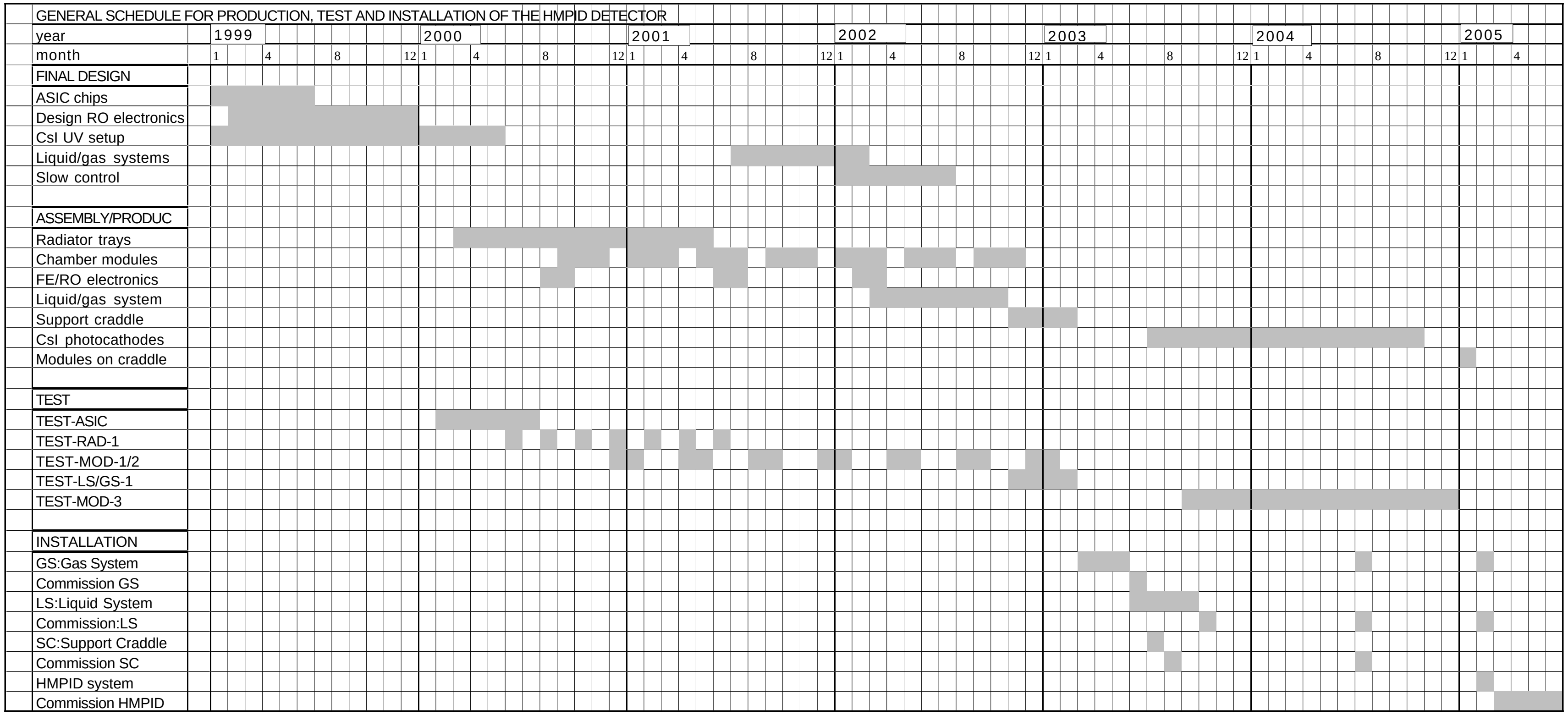

Table 5.1: General schedule for production, test, and installation of the HMPID detector

- end 2002:
  all chamber modules produced and tested without photocathodes
  auxiliary systems ready
- middle 2003:
  start the production of the CsI photocathode
- end 2004:
  all modules tested with photocathodes
  liquid circulation commissioned
- beginning 2005:
  commissioning the detector in ALICE

5.4 Safety aspects

The HMPID has been the subject of a recent Initial Safety Discussion (Ref. TIS/GS/WW/98–034). The outcome of this ISD was that the concept of the detector did not include any major safety risks. However, the operating gas will be flammable CH_4 with a total mass of 1.3 kg inside the detector. As discussed in Chapter 2, it is not possible to replace this gas since it provides the necessary photoelectron yield under stable operational conditions. The experimental zone will be equipped with a flammable-gas detection system. Two systems currently exist in the LEP point 2 area:

1) The standard industrial pelister type, which is used to monitor the surface gas buildings, the gas racks on the plug PX24, and also in the underground area UX25.
2) The SDN air sampling system, which extracts air from critical volumes near the gas-filled detectors.

5.5 Organization

5.5.1 Participating institutes

The following four institutes will share the fabrication and commissioning of the HMPID detector:

- INFN, Sez. Bari and Dipartimento di Fisica, University of Bari, Bari, Italy
- CERN, Geneva, Switzerland
- Institute for Nuclear Research (INR), Moscow, Russia
- Instituto Superior Técnico (IST), Lisbon, Portugal

In the design, construction and testing, the following ALICE members have participated:

- INFN, Sez. Bari and Dipartimento di Fisica, University of Bari, Bari, Italy
  N. Colonna, D. Cozza, D. Dell'Olio, L. Dell'Olio, D. Di Bari, D. Elia, N. Facchini, R. Fini, A. Grimaldi, L. Liberti, E. Monno, E. Nappi, F. Posa S. Stucchi and G. Tomasicchio
- CERN, Geneva, Switzerland
  H. Beker, M. Davenport, A. Di Mauro, D. Fraissard, E. Gaummann, B. Goret, Ch. Gregory, G. Lecoeur, A. Ljubičić Jr., P. Martinengo, R. Monnin, A. Morsch, G. Paić[1], F. Piuz, J. Raynaud, J.C. Santiard and T.D. Williams
- Institute for Nuclear Reasearch (INR), Moscow, Russia
  A. Kurepin, V. Razin, A. Reshetin, K.A. Shileev
- Instituto Superior Técnico (IST), Lisbon, Portugal
  J. Barbosa, R. Carvalho and J. Seixas

In addition, the following people have provided valuable help in specific sections of this Technical Design Report: C. Lourenço, G. Rubin, K. Šafařík, D. Swoboda and P. Vande Vyvre.

---

[1] also Ohio State University, Columbus, USA.

5.5.2 Responsibilities

The proposed sharing of the responsibilities in the construction and operation of the HMPID detector is shown in Table 5.2.

Table 5.2: Sharing of responsibilities

Institution	Responsibilities
INFN, Sez. Bari and Dipartimento di Fisica, University of Bari	Radiator system (part) C_6F_{14} system Readout electronics and auxiliary equipment On-line software and off-line analysis
CERN	Modules (part) CsI photocathodes Gas system On-line software and off-line analysis
INR, Moscow	Radiator system (part) Modules (part) Support cradle
IST, Lisbon	Off-line analysis

The four institutes will jointly participate in the testing activities and related data analysis.

5.5.3 Cost estimate and resources

The evaluation of items foreseen to cost more than 200 kCHF was done following CERN tendering procedures. Other costs have been based, whenever possible, on industrial quotations. In Table 5.3, the cost evaluation is presented in such a way that the cost of the seven modules can be compared with the incompressible expenses on auxiliary systems.

Table 5.4 shows the cost of the major functional components of the HMPID. The manpower from participating institutes needed for construction amounts to approximately 65 man years.

Table 5.3: Cost evaluation per type

Items	Cost [CHF]
Seven modules	1392
Auxiliary systems	529
Industrial and contract-labour support	109
Spare material	121
Total	2151

Table 5.4: Cost evaluation per function

Items	Cost [CHF]
Radiator and liquid circulation systems	668
Modules, CsI photocathodes, gas system	624
Electronics and auxiliary equipments	575
Installation	54
Spare material	121
Industrial and contract-labour support	109
Total	2151

References

Chapter 1

[1] ALICE Collaboration, Technical Proposal, CERN/LHCC 95–71.
[2] X-N. Wang, preprint hep-ph/9804357.
[3] X-N. Wang and M. Gyulassy, Phys. Rev. Lett. **68** (1992) 1480.

Chapter 2

[1] T. Ypsilantis, communication at the 1979 IEEE Nucl. Sci. Symposium;
G. Comby et al., Nucl. Instrum. Methods **176** (1980) 313;
D.F. Anderson, IEEE Trans. Nucl. Sci. NS28 (1981) 842.
[2] J. Seguinot et al., Nucl. Instrum. Methods **A297** (1990) 133;
G. Charpak et al., Nucl. Instrum. Methods **A307** (1991) 63.
[3] Detector R&D Proposal-P35, CERN/DRDC 92–3, CERN/DRDC 92–16.
[4] *Experimental Techniques of Cherenkov Light Imaging*, Proceedings of the First Workshop on Ring Imaging Cherenkov Detectors, Bari, Italy, June 1993, Eds. E. Nappi, T. Ypsilantis (North Holland).
[5] RD-26 status reports: CERN/DRDC 93–36, CERN/DRDC 94–49, CERN/DRDC 96–20.
[6] A. Breskin, Nucl. Instrum. Methods **A367** (1995) 326;
A. Breskin, Nucl. Instrum. Methods **A371** (1996) 116;
J. Seguinot et al., Nucl. Instrum. Methods **A371** (1996) 64.
[7] *Techniques and Results of Cherenkov Light Imaging in High Energy Physics*, Proceedings of the Second International Workshop on Ring Imaging Cherenkov Detectors (RICH95), Uppsala, Sweden, June 1995, Ed. T. Ekelof (North Holland);
New Developments in Photodetection, Proceedings of the First Conference on New Developments in Photodetection, Beaune, France, June 1996, Eds. P. Besson et al. (North Holland).
[8] HADES, Proposal for a High Acceptance Di-Electrons Spectrometer, GSI, Darmstadt, 1993.
[9] ALICE Collaboration, Technical Proposal, CERN/LHCC 95–71.
[10] COMPASS proposal, CERN/SPSLC/96–14.
[11] C.W. Fabjan et al., Nucl. Instrum. Methods **A367** (1995) 240;
A. Braem et al., CERN-PPE/97–120, August 1997.
[12] G.F. Carruthers, Appl. Opt. **14** (1975) 1667.
[13] A. Akkerman et al., J. Appl. Phys. **76** (1994) 4656.
[14] A.H. Sommer, Photoemissive materials (Wiley NY, 1968).
[15] J. Vávra et al., Nucl. Instrum. Methods **A387** (1997) 14.
[16] P. Maier-Komor et al., Nucl. Instrum. Methods **A362** (1995) 183.
[17] C. Coluzza, Nucl. Instrum. Methods **A387** (1997) 24.
[18] D.F. Anderson et al., Nucl. Instrum. Methods **A326** (1993) 611.
[19] G. Malamud et al., Nucl. Instrum. Methods **A343** (1994) 121.
[20] Ph. Miné et al., X-LPNHE 94–05, August 1994.
[21] L.B. Leob, Basic processes of gaseous electronics, (Univ. of California Press, Berkeley 1955), p. 601;
R.W.L. Thomas and W.R.L. Thomas, J. Phys. B2 (1969), 562;
G. Charpak et al., IEEE Trans. Nucl. Sci. NS-30 (1983) 134.

[22] A. Breskin et al., Nucl. Instrum. Methods **A344** (1994) 163.
[23] A. Breskin et al., Nucl. Instrum. Methods **A367** (1995) 342.
[24] A. Breskin et al., Nucl. Instrum. Methods **A367** (1995) 342.
[25] A. Di Mauro et al., Nucl. Instrum. Methods **A371** (1996) 137.
[26] D.F. Anderson et al., FNAL TM-1753, 1991;
D.F. Anderson et al., Nucl. Instrum. Methods **A323** (1992) 626.
[27] H. Brauning et al., Nucl. Instrum. Methods **A327** (1993) 369.
[28] C. Lu et al., Preprint Princeton/HEP/94–10.
[29] J. Almeida et al., Nucl. Instrum. Methods **A367** (1995) 337.
[30] P. Krizan et al., Preprint IJS-DP-7087, 1994.
[31] P. Krizan et al., Nucl. Instrum. Methods **367** (1995) 257.
[32] S. Sgobba et al., CERN-EST/SM/MB 98-07-13.
[33] C. Coluzza et al., Nucl. Instrum. Methods **A343** (1994) 152.
[34] J. Almeida et al., Nucl. Instrum. Methods **A361** (1995) 524.
[35] V. Peskov, Private communication.
[36] J. Vávra, Nucl. Instrum. Methods **A371** (1996) 33.
[37] R. Arnold et al., CRN/HE 90-05, CRN Strasbourg, France.
[38] E. Gatti et al., Nucl. Instrum. Methods **163** (1979) 83.
[39] I. Endo et al., Nucl. Instrum. Methods **188** (1981) 55.
[40] G.A. Erskine, Nucl. Instrum. Methods **198** (1982) 325.
[41] H. Van Der Graaf et al., Nucl. Instrum. Methods **217** (1983) 330.
[42] E. Mathieson et al., Nucl. Instrum. Methods **A227** (1984) 277.
[43] E. Mathieson et al., Nucl. Instrum. Methods **A270** (1988) 602.
[44] F. Piuz et al., Nucl. Instrum. Methods **196** (1982) 451.
[45] G. Alkazov et al., Nucl. Instrum. Methods **89** (1970) 155.
[46] H.D. Morgan et al., J. Chem. Phys. **60** (1974) 4734.
[47] R. Arnold et al., Nucl. Instrum. Methods **A279** (1988) 255.
[48] F. Piuz, Nucl. Instrum. Methods **A371** (1996) 96.
[49] G.H. Mount et al., Astrophys. J. **214** (1977) L47.
[50] C. Lu et al., Nucl. Instrum. Methods **A343** (1994) 135.
[51] A. Amoruso et al., J. Quant. Spectr. Dadiat. Transfer **56** (1996) 145.
[52] J. Seguinot, Ecole J. Curie de Physique Nucleaire, Mabuisson, France, September 1988.
[53] E. Fokitis et al., Measurements of the refractive index of DELPHI RICH radiators in liquid phase down to 185 nm, in preparation.
[54] E. Chesi et al., Nucl. Instrum. Methods **A283** (1989) 602.
[55] F. Piuz et al., Proceedings of the Experimental Apparatus for High Energy Particle Physics and Astrophysics Conference at San Miniato, Italy, June 1990, Eds. P. Giusti et al. (World Scientific, Singapore) p. 121; CERN/PPE 91–7 rev.
[56] T. Francke et al., Nucl. Instrum. Methods **A310** (1991) 146.
[57] F. Piuz et al., Nucl. Instrum. Methods **A333** (1993) 404.
[58] E. Nappi et al., Nucl. Instrum. Methods **A315** (1992) 113.
[59] A. Braem et al., Nucl. Instrum. Methods **A343** (1994) 163.
[60] A. Di Mauro et al., Nucl. Instrum. Methods **A343** (1994) 323.
[61] A. Di Mauro et al., Nucl. Phys. **A566** (1994) 619c.
[62] J. Almeida et al., Nucl. Instrum. Methods **A348** (1994) 216.
[63] H. Berger et al., Nucl. Instrum. Methods **A360** (1995) 411.
[64] F. Piuz et al., Nucl. Instrum. Methods **A367** (1995) 332.
[65] T. Scognetti, PhD Thesis, University of Bari, Italy, 1994.
[66] M. Hempstead et al., Nucl. Instrum. Methods **A306** (1991) 207.

[67] R. Arnold et al., Nucl. Instrum. Methods **A270** (1988) 289.
[68] A. Di Mauro, Internal Note ALICE 98–34.
[69] T. Ypsilantis et al., Nucl. Instrum. Methods **A343** (1994) 30.
[70] A. Di Mauro and A. Morsch, Internal Note ALICE 98–33.

Chapter 3

[1] T.D. Williams et al., Printed Circuit Board for CsI-photocathodes, Internal Note ALICE, in preparation.
[2] P. Majewski, MWPC for the RICH detector for the ALICE experiment at LHC. MSc thesis, University of Warsaw, 1996.
[3] E. Albrecht et al., Perfluorocarbon effects on composite and polymeric materials used within RICH detectors, DELPHI note 95-21;
J. Vávra, Nucl. Instrum. Methods **A367** (1995) 353.
[4] K. Abe et al., IEEE Trans. Nucl. Sci **40** 4, 1993; SLAC-PUB-5888, 1992.
[5] G. Lenzen et al., Nucl. Instrum. Methods **A343** (1994) 268.
[6] W. Adam et al., Nucl. Instrum. Methods **A338** (1994) 28.
[7] S. Ilie and G. Lenzen, DELPHI Internal Report, DELPHI 93–33 RICH 54.
[8] K. Abe et al., SLAC-PUB-7705, 1997.
[9] 3M Fluorinert Product Manual.
[10] J.C. Santiard et al., CERN-ECP/94–17.
[11] C. Drancourt et al., SN954, Instruction book, SUBATECH, Nantes, 1995.
[12] J.C. Santiard, CERN/LHCC/96–39.
[13] ALICE Collaboration, Technical Proposal, CERN/LHCC 95–71.
[14] O. Villalobos et al., Internal Note ALICE 98–23.
[15] J.C. Santiard, GASSIPLEX, version 0.7μm, Internal Note ALICE, in preparation.
[16] J.C. Santiard, DILOGIC-2, Internal Note ALICE, in preparation.
[17] G. Rubin, ALICE Detector Data Link (DDL), Internal Note ALICE 98–21.
[18] G. Rubin et al., Internal Note ALICE 97–14.

Chapter 4

[1] ALICE Collaboration, Technical Proposal, CERN/LHCC 95–71.
[2] F. Carminati, Proc. Int. Conf. on Monte Carlo Simulation in High Energy and Nuclear Physics, Tallahassee, Fl, Eds. P. Dragovitsch, S.L. Linn and M. Burbank (World Scientific) 1994, p. 45.
[3] A. Fasso et al., Proc. IV Int. Conf. on Calorimeters and their Applications, World Scientific, Singapore, 1994, p. 493.
[4] http://www.cern.ch/alice/Projects/offline/Simulation/fluka
[5] http://www.cern.ch/alice/Projects/offline/Simulation/galice
[6] A. Di Mauro and A. Morsch, Internal Note ALICE 98–33.
[7] J.O. Johnson and T.A. Gabriel, A user’s guide to MICAP, Technical Report TM-10340, ORNL, 1988.
[8] K. Eggert and A. Morsch, CERN/AT 95-01(DI) and Internal Note ALICE 95–05.
[9] J. Bächler et al., Nucl. Instrum. Methods **A343** (1994) 273.
[10] D. Di Bari, D. Elia, E. Nappi and G. Paić, Internal Note ALICE 97–39.
[11] P.V.C. Hough, Method and means for recognizing complex patterns, U.S. Patent 3069654 (1962).
[12] R.O. Duda, P.E. Hart, Commun. ACM **15** (1972) 11.
[13] D.S. McKenzie and S.R. Protheroe, Pattern Recognition **23** (1990) 283.
[14] E. Nappi et al., Comp. Phys. Commun. **66** (1991) 293.

[15] D.H. Ballard, Pattern Recognition **13** (1981) 111.
[16] T. Ypsilantis and J. Seguinot, Nucl. Instrum. Methods **A343** (1994) 30.
[17] N. Chernov and G. Ososkov, Comp. Phys. Commun. **33** (1984) 329.